

DISSERTATION

AB INITIO STUDIES OF GRAPHENE-METAL INTERFACES

Ausgeführt zum Zwecke der Erlangung des akademischen Grades eines Doktors der
technischen Wissenschaften unter der Leitung von

Ao. Univ. Prof. Dipl.-Ing. Dr. techn. Josef Redinger
und Dipl.-Ing. Dr. techn. Florian Mittendorfer

E 134

Institut für Angewandte Physik

eingereicht an der Technischen Universität Wien
Fakultät für Physik

von

Dipl.-Ing. Andreas Garhofer

0426308

Nattergasse 1-3/2/41, 1170 Wien

Wien, am 31.07.2013

Abstract

Graphene (Gr) is a two-dimensional allotrope of carbon consisting of a single layer of carbon atoms in a honeycomb arrangement with unique electronic properties due to the special character of its electronic structure. The strong σ -bonds of graphene are responsible for stability of the lattice structure while the π -bonds determine the transport properties and the low-energy electronic structure, which show linear dispersion near the Fermi level at particular points in the Brillouin zone (Dirac points). The isolation of graphene in 2004 has led to a remarkable surge of interest in the scientific community. It was originally produced by exfoliation but high quality graphene sheets of large size can be produced via epitaxial growth on metal substrates. Moreover, graphene supported on a ferromagnetic material, such as nickel, has been proposed as a promising system for spin-filtering devices. In addition, moiré forming graphene grown on transition metals with large lattice mismatch forms suitable templates for the growth of regular arrays of nano-sized entities, such as metallic clusters, which offers potential applications for nanotechnology. However, the interaction of graphene with a metallic surface is still not well understood on a fundamental level. Experimentally the Gr-metal interaction has either been classified as “weak” interaction, e.g. on Au, Ag, Cu, and Ir with merely shifted graphene π -bands, or as “strong” interaction, e.g. on Ni, Co, Rh and Ru, with strongly perturbed graphene π -bands compared to free-standing graphene.

In this thesis, density functional theory (DFT) calculations of different Gr-metal systems are presented, reflecting the various interactions at the Gr-metal interfaces. For these systems it is crucial to include long-range van der Waals (vdW) interactions. Commonly used (semi-)local functionals based on the local density approximation or the generalized gradient approximation, which lack vdW interactions, have to be augmented either by force-field or density dependent corrections (vdW-DF functional). A systematic evaluation of many-body interactions, which naturally include vdW, can be achieved on the basis of the adiabatic-connection fluctuation-dissipation theory in the random phase approximation (RPA). As shown in the present thesis, for graphene on Ni(111) the vdW-DF functionals can be tuned to reproduce the highly accurate, but also computationally very demanding RPA calculations. The calculations show that even for the “strongly” inter-

acting systems such as Gr/Ni(111), the adsorption energies are in the typical range of physisorption. Two minima of the adsorption energy are present: one “physisorption” minimum at a typical vdW distance of about 3-4 Å and another “chemisorption” minimum in the proximity of the surface at 2.2 Å.

Additionally the calculations show significant influence of the substrate on the growth of the graphene sheet: while single vacancies and Stone-Wales defects yield high formation energies in free-standing graphene, the presence of the nickel substrate stabilizes the defects and lowers the energetic barriers to heal the defects.

Despite the small lattice mismatch Gr/Ni(111) does not only grow epitaxially, but scanning tunneling microscopy (STM) measurements also indicate the presence of a rotated graphene phase. This can be explained on the basis of DFT calculations, which show that the presence of a nickel surface carbide Ni₂C phase leads to a weakly coupled graphene layer.

In contrast to Gr/Ni(111), graphene on Ir(111) is characterized by a weak interaction and a large lattice mismatch leading to a moiré structure with large Gr-substrate distance and a small corrugation of graphene. Neither atomic force microscopy (AFM) nor STM can unambiguously assign the minima and maxima in the moiré, e.g. the measured contrast in AFM depends on the proximity of the probing tip to the graphene surface. The DFT calculations allow to identify the correct assignment of minima and maxima and to trace the origin of the contrast inversion.

The role of the mismatch versus chemical interaction is highlighted in a study of an artificially modified system obtained by the intercalation of a strongly interacting nickel monolayer at the weakly interacting Gr/Ir(111) interface. The intercalation leads to a pronounced buckling of graphene due to locally strongly enhanced Gr-substrate interactions for specific adsorption configurations. An analysis of the intercalation process shows that the diffusion of nickel atoms through graphene is facilitated by vacancies in the graphene sheet and the intercalated nickel atoms agglomerate at the step edge.

In the opposite example, the intercalation of a weakly interacting material (Ag) in a strongly interacting Gr/Re(0001), the intercalated layer diminishes the interaction strength as seen in a reduced buckling. The calculation of the electronic structure reveals that the graphene layer is not completely decoupled but hybridizes with silver *d*-states.

Zusammenfassung

Graphen (Gr), eine zweidimensionale Modifikation von Kohlenstoff, besteht aus einer einzelnen Lage bienenwabenförmig angeordneter Kohlenstoffatome. Wegen seiner speziellen elektronischen Struktur hat es einzigartige elektronische Eigenschaften. Während die starken σ -Bindungen für die Festigkeit der Gitterstruktur verantwortlich sind, bestimmen die π -Bindungen die Transporteigenschaften und die elektronische Struktur bei geringen Energien durch eine lineare Dispersion der Energiebänder in der Nähe des Fermi-niveaus an speziellen Punkten der Brillouin Zone (Dirac-Punkte). Zusätzlich könnte Graphen auf einer ferromagnetischen Oberfläche wie Nickel ein aussichtsreiches Spinfiltersystem bilden. Darüber hinaus sind Graphen-Moiré-Strukturen die bei Systemen mit großer Gitterfehl-anpassung vorkommen, gut geeignet um Nanopartikel, wie metallische Cluster, in einer periodischen Anordnung herzustellen, wodurch sich auch Anwendungen in der Nanotechnologie ergeben könnten. Die Wechselwirkung zwischen Graphen und einer metallischen Oberfläche ist aber noch nicht ausreichend erforscht und wird von experimenteller Seite entweder als “schwache” Wechselwirkung wie z.B. auf Au, Ag, Cu, und Ir klassifiziert, wobei die π -Bänder von Graphen nur etwas verschoben sind, oder als “starke” Wechselwirkung auf Ni, Co, Rh und Ru, durch die die Graphen π -Bänder stark modifiziert werden.

In dieser Dissertation werden Dichtefunktionaltheorie (DFT) Rechnungen für Gr-Metall Systeme vorgestellt, um den Einfluß der verschiedenen Wechselwirkungen in Gr-Metall Grenzflächen aufzuzeigen. Für all diese Systeme ist die Berücksichtigung von van der Waals (vdW) Wechselwirkungen extrem wichtig. Die am häufigsten verwendeten (halb-)lokalen Funktionale, basierend auf der lokalen Dichtenäherung und der Gradientennäherung, beinhalten keine vdW Beiträge und müssen daher um kraftfeldartige (Grimmekorrekturen) oder dichteabhängige Beiträge (vdW-DF Funktional) erweitert werden. Eine natürliche Einbeziehung der vdW Wechselwirkungen kann aber am besten durch eine direkte Berechnung der Vielteilchen-Wechselwirkungen erreicht werden, z.B. mit Hilfe der *adiabatic-connection fluctuation-dissipation theory* in der *random phase approximation* (RPA). Die Ergebnisse der sehr genauen, aber auch sehr rechenintensiven RPA Methode die zeigen, dass die Adsorptionsenergien auch für “stark” wechselwirkende Systeme wie

Gr/Ni(111) im Bereich von Physisorptionsenergien liegen, können auch durch optimierte vdW-DF Funktionale reproduziert werden. Für Gr/Ni(111) gibt es zwei Minima in den Adsorptionsenergien: Ein “Physisorptions”-Minimum in einem typischen vdW Abstand von etwa 3-4 Å, und ein “Chemisorptions”-Minimum bei einem kleinerem Gr-Ni Abstand von etwa 2.2 Å.

Außerdem zeigen die Rechnungen einen eindeutigen Einfluss des Substrats auf das Wachstum von Graphen: Während einzelne Leerstellen und Stone-Wales Defekte in freistehendem Graphen eine hohe Bildungsenergie aufweisen, werden diese Defekte durch das Nickelsubstrat stabilisiert und die Energiebarrieren zur Ausheilung der Defekte stark reduziert.

Obwohl die Gitterkonstanten von Graphen und Nickel sehr ähnlich sind, wurden in Rastertunnelmikroskop (RTM) Experimenten nicht nur epitaktisches Wachstum von Gr/Ni(111), sondern auch verdrehte Graphenphasen beobachtet. Dies konnte durch das Auftreten eines Nickel-Oberflächenkarbids erklärt werden, auf dem DFT Rechnungen nur noch sehr schwache Graphen Bindungen zum Substrat zeigen.

Im Gegensatz zu Gr/Ni(111) ist Gr/Ir(111) durch eine große Gitterfehlانpassung und eine schwache Wechselwirkung gekennzeichnet, was zu einer Moiréstruktur mit großem Gr-Substrat Abstand und einer kleinen Korrugation von Graphen führt. Die Maxima und Minima in der Moiréstruktur können weder mit Rasterkraftmikroskopie (RKM) noch RTM eindeutig zugeordnet werden. Zum Beispiel hängt der gemessene Kontrast in RKM von dem Abstand zwischen Spitze und Oberfläche ab. Die richtige Zuordnung und der Grund für das Auftreten einer Kontrastumkehr können anhand von DFT Rechnungen identifiziert werden.

Die Bedeutung der Gitterfehlانpassung im Verhältnis zur chemischen Wechselwirkung wird mittels eines künstlich modifizierten Systems untersucht, das durch die Interkalation einer stark wechselwirkenden Nickellage in die Gr/Ir(111) Grenzfläche hergestellt wurde. Durch die lokal verstärkte Gr-Substrat Wechselwirkung in spezifischen Bereichen des Moirémusters, ist Gr/Ni/Ir(111) sehr stark gewellt. Eine Analyse des Interkalationsprozesses zeigt, dass die Diffusion von Nickelatomen durch das Graphen hindurch von Fehlstellen ermöglicht wird und sich die Nickelatome an Stufenkanten ansammeln.

Im umgekehrten Fall der Interkalation eines schwach wechselwirkenden Materials - Ag - in eine stark wechselwirkende Grenzfläche - Gr/Re(0001) - wird zwar die Wechselwirkung zwischen Graphen und Substrat vermindert, was zu einer kleineren Welligkeit führt, die Berechnungen der elektronischen Struktur lassen aber erkennen, dass Graphen nicht vollständig vom Substrat entkoppelt ist, sondern noch mit Silber d -Zuständen hybridisiert.

Contents

List of Figures	13
List of Tables	17
I Introduction	19
0.1 Motivation and Outline	21
1 Graphene	25
1.1 Introduction	25
1.2 Properties of Graphene and Applications	26
1.3 Electronic Structure of Graphene	26
1.3.1 Structure in Real Space	27
1.3.2 Structure in Reciprocal Space	27
1.3.3 Tight-binding Approach	27
1.4 Production of Graphene	32
1.5 Graphene-Substrate Interaction	32
II Theoretical Background and Methods	41
2 Theoretical Background	43
2.1 Basic Hamiltonian	43
2.2 Born-Oppenheimer Approximation	44
2.3 Simple Models in Solid State Physics	45
2.4 Hartree and Hartree-Fock Method	47

2.5	Post Hartree-Fock Methods	48
2.6	Density Functional Theory	50
2.7	Exchange Correlation Functional	51
2.8	Performing a DFT Calculation in Practice	53
2.9	Including van der Waals Interactions in DFT	55
2.9.1	Force-field Corrections	56
2.9.2	The Adiabatic-Connection Fluctuation-Dissipation Theory in its Random Phase Approximation (RPA)	58
2.9.3	vdW-DF	60
2.10	Quasiparticle Energies in the <i>GW</i> Approximation	64
III	Results	67
3	Graphene on Ni(111)	69
3.1	Structure of Gr/Ni(111)	71
3.1.1	State of the Art	71
3.1.2	Interface Lattice Constants	75
3.1.3	Adsorption Energies for different Functionals	76
3.1.4	Influence of the Adsorption Configuration	81
3.1.5	Relaxation Effects	84
3.1.6	STM Simulation	85
3.2	Band Structure	86
3.3	Computational Methods	89
3.4	Conclusion	90
4	Defect Structures and Defect Healing	91
4.1	Single Vacancies	92
4.2	Single Vacancies in Nickel-supported Graphene	95
4.3	Stone-Wales Defects in Pristine Graphene	98
4.4	SW Defects on Nickel-supported Graphene	102
4.5	STM Measurements of defective Graphene	104
4.6	Computational Methods	105

4.7	Conclusion	105
5	Surface Carbide induced Changes on Gr/Ni	109
5.1	Nickel Carbide on Ni(111)	110
5.2	Graphene on Nickel Carbide	112
5.2.1	DFT Calculations	112
5.2.2	STM Results	114
5.3	Surface Phase Diagram	117
5.4	Growth Model	120
5.5	Computational Methods	122
5.6	Conclusion	123
6	Graphene on Ir(111)	125
6.1	Lattice Mismatch and Moiré Unit Cell	126
6.2	Electronic Structure and imaging Contrast	130
6.2.1	Contrast Inversion in CC STM	130
6.2.2	Contrast Inversion in AFM	133
6.3	Methods	142
6.4	Conclusion	142
7	Graphene on intercalated Ni/Ir(111)	145
7.1	Graphene adsorbed on one Monolayer Ni/Ir(111)	146
7.1.1	Experimental Background: STM Results	146
7.1.2	DFT Calculations	147
7.1.3	Band Structure of Gr/Ni/Ir(111)	152
7.2	Intercalation Mechanism of Gr/Ni/Ir(111)	154
7.2.1	Experimental Evidence: Intercalated Nickel at Gr/Ir	154
7.2.2	Adsorption and Intercalation of a Single Nickel Atom	157
7.2.3	Preferred Configurations of Intercalated Nickel	162
7.2.4	Multilayer Nickel Intercalated in Gr/Ir(111)	164
7.2.5	Intercalation Mechanism	165
7.3	Computational Methods	169

7.4	Conclusion	170
8	Silver intercalated in Gr/Re(0001)	173
8.1	Band structure and Core Level Shifts	174
8.2	Computational Methods	180
8.3	Conclusion	182
9	Summary and Conclusion	183
	List of Abbreviations	187
	Bibliography	189
	Acknowledgments	203
	Curriculum Vitae	205

List of Figures

1.1	Primitive cell of honeycomb graphene lattice with primitive vectors.	28
1.2	First Brillouin zone of graphene with reciprocal primitive vectors.	28
1.3	Tight-binding band structure of graphene.	30
1.4	The effective (cyclotron) mass of electrons and holes as a function of their concentration n	31
1.5	Density of states per unit cell in the tight-binding approximation.	31
1.6	Summary of the interactions between transition metals and graphene.	34
1.7	C1s CL BEs of monolayer graphene on various transition metal substrates.	35
1.8	Electronic structure of Gr/Ni(111) before and after the intercalation of 1 ML Au.	39
2.1	Exchange enhancement factors F_x as a function of the reduced gradient density s for different functionals.	63
3.1	Fermi surface projections onto (111) plane for Co, Ni, Cu, and graphite.	70
3.2	Adsorption sites on a fcc(111) surface.	72
3.3	Adsorption sites of graphene on Ni(111).	73
3.4	Adsorption energy per carbon atom as a function of the Gr/Ni distance for different functionals.	77
3.5	Adsorption of graphene on Ni(111) for various vdW functionals.	79
3.6	RPA adsorption energies separated into the exchange- and correlation contributions for Gr/Ni(111) in the top-fcc and top-hcp configuration.	80
3.7	Adsorption energy per carbon atom as a function of the Gr/Ni distance for various adsorption sites (optB88-vdW, RPA Ni lattice constant).	81

3.8	Adsorption energy per carbon atom as a function of the Gr/Ni distance for various adsorption sites (optB88-vdW, optB88 Ni lattice constant).	82
3.9	Adsorption energy per carbon atom as a function of the Gr/Ni distance for various adsorption sites (optB86b-vdW, RPA Ni lattice constant).	83
3.10	Adsorption energy per carbon atom as a function of the Gr/Ni distance for various adsorption sites (optB86b-vdW, Ir lattice constant).	84
3.11	Simulated STM image of graphene on Ni(111) in several configuration. . .	86
3.12	PBE band structure and differential charge density of Gr/Ni(111).	88
4.1	TEM image, atomic structure, and STM image of a single vacancy.	93
4.2	Free-standing graphene with a SV in the most stable configuration.	94
4.3	Graphene with a single vacancy at the top-site.	97
4.4	Graphene with a single vacancy at the fcc-site.	98
4.5	Flat, sine-, and cosine-like SW-structures in perfect graphene.	99
4.6	Schematic representation of the energies involved in the removal and the formation of a SW defect.	101
4.7	Calculated reaction pathway for the healing of a SW defect in pristine graphene.	102
4.8	Configuration of Gr/Ni(111) with SW defect.	103
4.9	Calculated reaction pathway for the healing of a SW defect for nickel-supported graphene.	104
4.10	STM images of graphene grown at different temperatures.	106
4.11	STM image of a graphene grain boundary and comparison of an experimental and simulated STM image of single carbon vacancy.	106
5.1	Clock reconstruction of the surface carbide Ni ₂ C.	111
5.2	STM/FFT images and DFT simulations of the surface carbide.	113
5.3	STM/FFT images of graphene on Ni ₂ C.	115
5.4	STM/FFT images and line profiles along protrusions and depressions. . . .	116
5.5	Free surface energies (LDA) of Ni(111), Gr/Ni(111), Ni ₂ C/Ni(111), and Gr/Ni ₂ C/Ni(111).	118

5.6	Free surface energies (optB88-vdW) of Ni(111), Gr/Ni(111), Ni ₂ C/Ni(111), and Gr/Ni ₂ C/Ni(111).	119
5.7	Proposed steps in the formation of rotated graphene grains.	121
6.1	DFT structure of the Gr/Ir(111) moiré unit cell.	128
6.2	STM and combined STM/AFM images of Gr/Ir(111).	131
6.3	Experimental and calculated CC STM images of Gr/Ir(111) and DOS for all high-symmetry regions.	132
6.4	Experimental frequency shift and tunneling current as a function of the tip-sample distance.	134
6.5	Frequency shift and tunneling current of CH AFM measurements at two different distances d_1 and d_2	135
6.6	DFT simulations of AFM measurements using a 5W-tip model.	136
6.7	Interaction energy, force, and frequency shift as a function of the tip-Gr distance using a 10W-tip model.	138
6.8	Distances appearing in relaxed AFM simulations.	140
7.1	STM images and line profiles of Gr/Ni/Ir(111).	148
7.2	DFT structure, simulated and experimental STM and C1s core level shifts of Gr/Ni/Ir(111).	150
7.3	Calculated and ARPES band structure with different amount of nickel intercalated.	153
7.4	STM images with low and high nickel coverages after annealing.	155
7.5	Adsorption and intercalation positions for nickel at a stepped graphene covered Ir surface.	158
7.6	Gr/Ir(111) structure with intercalated nickel atoms at various adsorption sites.	161
7.7	STM images of Gr/Ni/Ir(111) to Gr/Ir(111) step, and multilayer layer intercalated nickel.	163
7.8	Schematic structural profiles of Gr/Ni/Ir(111).	166
7.9	Energies of the initial state, transition state, and final state for a nickel atom diffusing through graphene for various systems.	168

7.10 Transition state of nickel diffusing through Gr/Ir(111). 169

8.1 ARPES bandstructure of Re, Gr/Re, and Gr/Ag/Re. 175

8.2 Experimental C1s core level energies and DFT band structures of Ag/Re. . 177

8.3 Calculated C1s core level energies. 178

8.4 DFT band structures for Gr/1 ML Ag, Gr/Ag/Re (1 × 1), and Gr/Ag/Re
in supercell. 181

List of Tables

1.1	Comparison of d -band center of transition metals and the Gr-metal separation.	37
3.1	Literature values of the preferred adsorption site, BE, and Gr-Ni distance of Gr/Ni(111).	74
3.2	Experimental and calculated lattice constants of graphene and Ni(111). . .	76
3.3	BEs and Gr-substrate distance for different adsorption configurations. . . .	85
3.4	Energies of graphene states close to the Fermi energy at the K -point. . . .	88
4.1	Formation energies and activation barriers of unsupported graphene with a SV.	96
4.2	Formation energies and activation energies for a SW-defect in free-standing graphene.	100
6.1	Experimental and calculated lattice constants of Gr and Ir.	126
6.2	Comparison of DFT heights and corrugation of Gr/Ir(111).	129
7.1	Experimental and calculated lateral lattice constants of Ir and Ni.	149
7.2	BE of a nickel adatom adsorbed on Gr/Ir(111).	157
7.3	Binding energies of intercalated nickel atoms on Gr/Ir(111).	160

Part I

Introduction

0.1 Motivation and Outline

The most exciting phrase to hear in science, the one that heralds the most discoveries, is not “Eureka!” (I found it!) but “That’s funny ...“

– Issac Asimov (1920-1992)

Probably every one who is capable of writing with a pencil has already produced lots of (multi-layer) graphene in his life. Although pencil cores are called ”lead“¹ and also the German word for pencil ”Bleistift“ allows the assumption that pencils are made of lead, graphite is the actual material pencil cores are made of. Graphite is formed by the stacking of identical layers, where in each layer carbon atoms are arranged in a honeycomb lattice. A stack of multiple layers is naturally formed by pressing a pencil against a sheet of paper. But it took more than 400 years to isolate a single sheet of graphite, called *graphene*, which was not expected to exist due to its two-dimensional nature [1]. It was rather serendipity than premeditation that led to the discovery with far-reaching consequences. The original production of graphene was merely based on a repeated peeling of highly oriented pyrolytic graphite with a scotch tape. For the isolation and further groundbreaking experiments with graphene, Konstantin S. Novoselov and Andre K. Geim awarded the Nobel Prize in Physics in 2010. In fact, a similar method proposed in 2012 [2] uses a pencil lead to make few-layer graphene in a fast and low cost production with high yield.

The unique electronic and mechanical properties of graphene and many potential applications initiated enormous amounts of scientific activities [3–5]. The crystallographic quality of graphene is high and it is stable under ambient conditions despite its true two-dimensional nature. Moreover it has a very unusual electronic structure – the π and π^* -bands touch at a single point in the Brillouin zone, and show a linear dispersion relation close to this so-called Dirac points. This specific dispersion relation mimics that of massless fermions in quantum electrodynamics, except that the so-called Dirac fermions in graphene move with the Fermi velocity v_F instead of the speed of light c . Because of this relativistic behavior graphene shows an anomalous quantum Hall effect [3, 6]. Further-

¹An enormous deposit of solid graphite (the only one ever found in solid form) was discovered in Borrodale, England in the 16th century and was misleadingly thought to be a form of lead and therefore called plumbago.

more, a high mobility and low conductivity as well as extraordinary mechanical properties make it interesting for applications in electronic devices, solar cells, display screens etc. Chapter 1 gives a brief introduction to the properties of graphene.

While the production of graphene via mechanical exfoliation methods is a time-consuming process where only small sample sizes can be achieved, large graphene sheets of high-quality can be obtained by the epitaxial growth of graphene on metals. However, the interaction with a substrate can decisively change the electronic properties of graphene. A detailed understanding of the Gr-metal interaction is crucial, e.g. for the coupling of graphene on metal substrates in nanoscale electronic devices, but is still missing at the current state of research. From an experimental point of view the interaction was either described as “weak” – for almost unperturbed graphene π -bands, or as “strong” – for clearly perturbed graphene π -bands [7]. The d -band model is often stressed to give an idea why the interaction on some metals is stronger than on others, but cannot cover the whole physics behind. Therefore, a well-founded theoretical analysis is required to reveal the physics of Gr-metal interactions. Basic concepts of the Gr-metal interaction are discussed in section 1.5.

A theoretical treatment of graphene on metal surfaces must provide an accurate description of both, the surface and the complex Gr-metal interactions. Solving the Schrödinger equation for the full many-body wave function is in practice impossible for a system with a particle number N of the order $N \approx 10^{23}$ [8]. In solid state physics and surface physics, density functional theory is the most widely used method because it combines computational efficiency with a reasonable accuracy (e.g. of total energies). In DFT one uses the electron density instead of the full many-body wave function and maps the problem of interacting electrons onto a system of non-interacting electrons in an effective potential [9]. In principle the ground-state energies are exact in DFT, however all is hidden in the exchange-correlation functional E_{xc} , which is not known exactly but must be approximated. While bulk systems with delocalized electrons are in general well described in the local density approximation (LDA), the generalized gradient approximation (GGA) gives better results for systems with strongly varying electron densities such as surfaces or molecules. However, both approximations are lacking non-local contributions, which are important for the systems covered in the present work. Different

approaches have been suggested to include non-local van der Waals (vdW) interactions in the framework of DFT, e.g. force-field corrections, vdW-DF functionals, or the random phase approximation (RPA) which goes beyond DFT and gives highly accurate energies but comes along with a high computational demand. The theoretical methods used in this work are presented in chapter 2.

In this thesis, DFT calculations are performed to study various Gr-metal systems. In chapter 3 the interaction for graphene adsorbed on Ni(111) is discussed. The potential use as a spin-filtering device and the almost perfect lattice matching makes this system interesting for applied research as well as a perfect model system to study the Gr-metal interactions. Gr/Ni(111) has been usually classified as strongly interacting system, because graphene π -bands hybridize with nickel d -states. However, RPA calculations reveal that although graphene is chemisorbed on Ni(111), the adsorption energies are in the range of physisorption. Common (semi-)local functionals fail to describe this system but an optimized vdW-DF functional can reproduce the RPA calculations allowing the treatment of larger systems which is computationally not feasible with RPA.

Intrinsic point defects have low equilibrium concentrations in free-standing graphene due to high formation energies. The influence of a substrate on the stability of single vacancies and Stone-Wales defects is studied in chapter 4. The presence of a substrate significantly lowers the formation energies and the barriers to heal the defects.

Because of the small lattice mismatch, graphene usually grows epitaxially on Ni(111). However in STM experiments, also moiré structures were observed, indicating a rotated graphene phase on nickel. DFT calculations presented in chapter 5 show that the presence of surface nickel carbide Ni_2C leads to a weakening of the Gr-Ni interaction enabling different rotation domains.

Contrary to Gr/Ni(111), graphene is weakly adsorbed on Ir(111) where the linear dispersion of the graphene π -band is restored [10]. A large lattice mismatch leads to a moiré pattern with a small graphene corrugation [11]. While the assignment of the topographic features is hindered by an experimentally observed contrast inversion in AFM/STM measurements, the DFT calculations allow to identify the correct structure and to trace the origin of the inversion (chapter 6).

In chapter 7 the strongly interacting nickel is intercalated in Gr/Ir(111) to study

an artificially lattice mismatched Gr/Ni interface. vdW-DFT calculations yield a large buckling of Gr/Ni/Ir(111) due to a modulated interaction strength depending on the local adsorption configuration. The intercalation mechanism comprises two steps: diffusion of nickel through the graphene film enabled by vacancy sites and subsequent diffusion to the step edges.

The reverse case of a weakly interacting material (Ag) intercalated in strongly interacting Gr/Re(0001) is topic of chapter 8. Despite the fact that the intercalation of the noble metal leads to a decoupling with a recovered Dirac cone, there are still signs of an interaction between graphene and the substrate in terms of a band gap in the graphene π -band.

In summary, the manifold interactions occurring at different Gr-metal interfaces can be accurately described with the theoretical methods used in the thesis and are in good agreement with the experimental findings, which is proven for various Gr-metal systems (chapter 9).

Chapter 1

Graphene

1.1 Introduction

Graphene is a one-atom thick sheet of carbon atoms, which are arranged in a tightly packed honeycomb lattice. It is a basic building block for graphitic materials of all other dimensionalities. It can be wrapped up into zero-dimensional fullerenes or rolled into one-dimensional nanotubes [4] or form three-dimensional graphite, which consists of stacked graphene layers, weakly bound by vdW forces. The isolation of graphene in 2004 [1] was a surprise for the scientific community, as it has been assumed that a two-dimensional material cannot exist. According to the Mermin-Wagner theorem a truly two-dimensional crystal is not stable [12]. Meyer et al. [13] found intrinsic microscopic roughening on suspended graphene that could explain the stability of graphene. In 2002, ab initio calculations showed that a graphene sheet is thermodynamically unstable with respect to other fullerene structures for small sizes (< 20 nm) but becomes the most stable one for sizes larger than 24000 carbon atoms [14]. The flat graphene is also known for its tendency to roll up and buckle [15, 16]. Thus, it is disputable whether graphene is a truly two-dimensional structure or not [4, 17, 18].

1.2 Properties of Graphene and potential Applications

Graphene has many unique properties not found in any other material which makes it interesting for basic research as well as for many potential applications. It is not possible to give a complete overview on all the topics regarding graphene, because of the enormous research activities in the last years. The most important early findings were reviewed in a 2007 article Geim et al. [4]. The electronic properties were summarized in a review article Castro Neto et al. [5].

For this thesis, the extraordinary electronic structure is the key quality of graphene, which will be discussed in the next section. A remarkably high electron mobility at room temperature, an unexpected high opacity, a very high stiffness, and the occurrence of an anomalous quantum Hall effect [3, 6] are some examples of the astonishing characteristics of graphene.

Various potential applications for graphene are currently under development, and many more have been proposed. Examples are solar cells, flexible, thin, yet durable display screens, electric circuits, various chemical, medical and industrial processes enhanced or enabled by the use of new graphene materials.

1.3 Electronic Structure of Graphene

Atomic carbon has the electronic configuration $1s^2 2s^2 2p^2$. Two electrons occupy the inner $1s$ orbital and the other four are valence electrons. In the carbon allotrope graphene, the $2s$, $2p_x$ and $2p_y$ orbitals hybridize so that each carbon atom is bonded to its three neighbors by strong sp^2 bonds of σ -type. The σ -bonds are responsible for the stability of the lattice structure in all allotropes. Due to the Pauli principle, the corresponding bands are completely filled and form a deep valence band [5]. The remaining electron in the p_z -orbital, oriented perpendicular to the honeycomb lattice, contributes to a π -orbital. As each p_z -orbital contains one electron, the π orbital is half-filled. The π -electrons determine the low-energy electronic structure of graphene and their nature can be understood on the basis of e.g. a tight-binding approximation (see section 1.3.3).

1.3.1 Structure in Real Space

The periodicity of the hexagonal lattice is described by a Bravais lattice formed by two base vectors \mathbf{a}_1 and \mathbf{a}_2 (Fig. 1.1). There are two identical carbon atoms A and B within each unit cell forming two identical sublattices. The nearest neighbor distance a_b , i.e. the distance between two adjacent carbon atoms A and B is 1.42 Å [19]. The length of the basis vectors, which is also the lattice constant a can be calculated as

$$a = |\mathbf{a}_1| = |\mathbf{a}_2| = \sqrt{3} \cdot a_b \approx 2.46 \text{ \AA} \quad (1.1)$$

Each atom of type A is surrounded by three neighboring atoms of type B, when sitting at an A atom at relative positions

$$\delta_1 = a_b (0, 1) \quad \delta_2 = \frac{a_b}{2} (\sqrt{3}, -1) \quad \delta_3 = \frac{a_b}{2} (-\sqrt{3}, -1), \quad (1.2)$$

while the six second-nearest neighbors are located at relative positions

$$\delta'_1 = \pm \mathbf{a}_1 \quad \delta'_2 = \pm \mathbf{a}_2 \quad \delta'_3 = \pm (\mathbf{a}_2 - \mathbf{a}_1), \quad (1.3)$$

for atoms of both sublattices A and B.

1.3.2 Structure in Reciprocal Space

The reciprocal lattice of graphene is shown in Fig. 1.2. The hexagonal symmetry of the direct lattice is also apparent in the first Brillouin zone in reciprocal space. However, there are two inequivalent points at the corner of the hexagon, K and K' , which are called Dirac points for reasons that will become clear later. The M -point is in the middle of two corners.

1.3.3 Tight-binding Approach

The band structure of graphene was first studied using a tight-binding approximation [20], which is still a common practice to get an insight in graphene's band structure. Following the review of Castro Neto et al. [5], the tight-binding Hamiltonian in second quantization formalism for p_z electrons for electrons hopping to both nearest- and next-nearest-neighbor atoms has the form

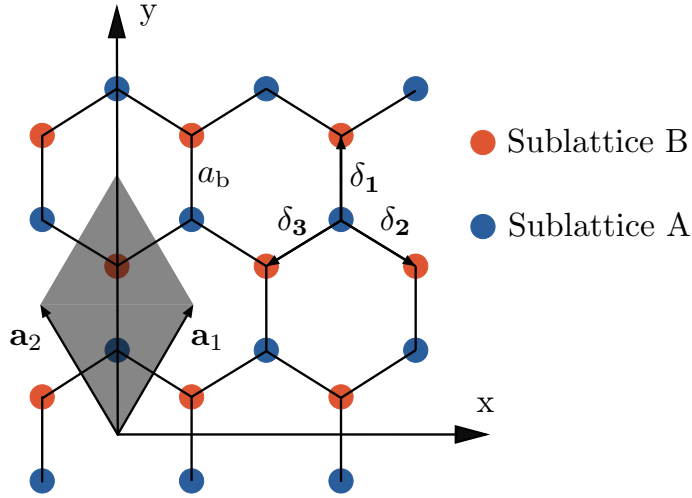


Figure 1.1: Graphene consists of a two atom basis superimposed onto a hexagonal lattice. The primitive cell (grey area) is spanned by the primitive vectors $\mathbf{a}_1 = \frac{a}{2} (1, \sqrt{3})$ and $\mathbf{a}_2 = \frac{a}{2} (-1, \sqrt{3})$ where a is the lattice constant. Any lattice point \mathbf{R}_i can be reached by adding an integral number of primitive vectors. The basis consists of two carbon atoms A and B, given by the vectors $\mathbf{r}_A = \frac{1}{3} (\mathbf{a}_1 + \mathbf{a}_2)$ and $\mathbf{r}_B = \frac{2}{3} (\mathbf{a}_1 + \mathbf{a}_2)$. The nearest-neighbors of type A atoms are given by the vectors δ_1 , δ_2 , and δ_3 , respectively.

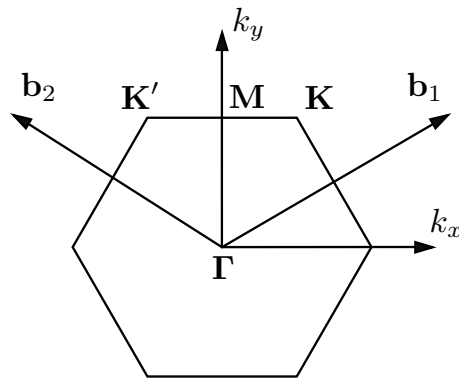


Figure 1.2: First Brillouin zone of graphene with reciprocal primitive vectors $\mathbf{b}_1 = \frac{2\pi}{a} (1, \frac{1}{\sqrt{3}})$ and $\mathbf{b}_2 = \frac{2\pi}{a} (-1, \frac{1}{\sqrt{3}})$. The coordinates of the high symmetry points are $\Gamma = (0, 0)$, $\mathbf{K} = (\frac{2\pi}{3a}, \frac{2\pi}{\sqrt{3}a})$, $\mathbf{K}' = (-\frac{2\pi}{3a}, \frac{2\pi}{\sqrt{3}a})$ and $\mathbf{M} = (0, \frac{2\pi}{\sqrt{3}a})$.

$$H = -t \sum_{\langle i,j \rangle, \sigma} (a_{\sigma,i}^\dagger b_{\sigma,j} + \text{H.c.}) - t' \sum_{\langle\langle i,j \rangle\rangle, \sigma} (a_{\sigma,i}^\dagger a_{\sigma,j} + b_{\sigma,i}^\dagger b_{\sigma,j} + \text{H.c.}), \quad (1.4)$$

where $a_{\sigma,i}$ ($a_{\sigma,i}^\dagger$) annihilates (creates) an electron with spin σ on site \mathbf{R}_i on sublattice A (an equivalent definition is used for sublattice B), $t \approx 2.8$ eV is the nearest-neighbor hopping energy (hopping between different sublattices A and B), and t' is the next nearest-neighbor hopping integral (hopping in the same sublattice). The value of t' is not well known but ab initio calculations of Reich et al. [21] find $0.02t \leq t' \leq 0.2t$ depending on the tight-binding parametrization. Taking this Hamiltonian, the energy bands can be written as [20]

$$E_{\pm}(\mathbf{k}) = \pm t \sqrt{3 + f(\mathbf{k})} - t' f(\mathbf{k}), \quad (1.5)$$

$$f(\mathbf{k}) = 2 \cos(k_x a) + 4 \cos\left(\frac{1}{2} k_x a\right) \cos\left(\frac{\sqrt{3}}{2} k_y a\right),$$

where the plus applies to the conduction band and the minus to the valence band, respectively. If t' equals zero (only nearest-neighbor hopping allowed) the spectrum is symmetric with respect to zero energy. For finite values of t' , the electron-hole symmetry is broken and the π - and π^* -bands become asymmetric (Fig. 1.3, 1.5). The π - and π^* -bands touch each other at six points exactly at the Fermi energy, but only two of them are independent (K and K'), the rest are equivalent by symmetry.

The band structure with both, t and t' is shown in Fig. 1.3. On the right side a, close up of the band structure close to one of the Dirac points, shows the characteristic *Dirac cone*. This dispersion can be obtained by expanding the full band structure, Eq. (1.4), close to the K or K' -point. For a wave-vector $\mathbf{k} = \mathbf{K} + \mathbf{q}$, with $|\mathbf{q}| \ll |\mathbf{K}|$ [20],

$$E_{\pm}(\mathbf{q}) \approx \pm v_F |\mathbf{q}| + O[(q/K)^2], \quad (1.6)$$

where \mathbf{q} is the momentum relative to the Dirac points and v_F is the Fermi velocity, given by $v_F = 3ta/2$, with a value $v_F \simeq 1 \times 10^6$ m/s [20].

This dispersion relation is different to the usual case, $E(\mathbf{q}) = q^2/(2m)$, where the Fermi velocity $v = k/m = \sqrt{2E/m}$ is a function of the energy (m is the electron mass). For graphene p_z electrons, the Fermi velocity is a constant and the energy is linearly dependent on the wave vector in the vicinity of the K -points.

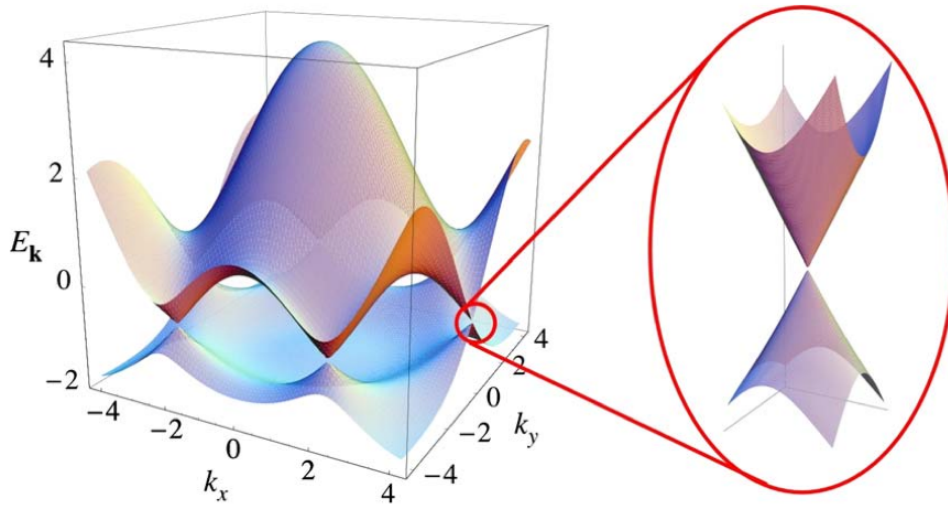


Figure 1.3: Tight-binding band structure of graphene including nearest-neighbor and second-nearest neighbor hopping terms, t and t' , respectively. The energy is displayed in units of t with $t = 2.7$ eV and $t' = -0.2t$. Taken from Castro Neto et al. [5]

Since the unit cell of graphene contains two equivalent atoms, the wave function can be written as an effective 2-spinor-structure. In momentum space, the wave function for the momentum around \mathbf{K} has the form

$$\psi_{\pm, \mathbf{K}}(\mathbf{k}) = \frac{1}{\sqrt{2}} \begin{pmatrix} e^{-i\theta_k/2} \\ \pm e^{i\theta_k/2} \end{pmatrix}, \quad (1.7)$$

where θ_k is the angle in momentum space. One can show that this wave function obeys the two-dimensional Dirac equation¹

$$-iv_F \boldsymbol{\sigma} \cdot \nabla \psi(\mathbf{r}) = E \psi(\mathbf{r}), \quad (1.8)$$

with Pauli matrices $\boldsymbol{\sigma} = (\sigma_x, \sigma_y)$ [22]. The phase factors of the two components are interchanged for the wave vector at K' . Hence, the electron and holes are called *Dirac fermions*, and the corners of the Brillouin zone are called *Dirac points* [22].

The effective (cyclotron) mass, defined within the semiclassical approximation [23] for the Dirac fermions is calculated as [3]

$$m^* = \frac{\sqrt{\pi}}{v_F} \sqrt{n}. \quad (1.9)$$

¹For a detailed derivation see Castro Neto et al. [5]

where n is the electron density, which is zero at the Dirac point. Thus, massless Dirac quasiparticles have been expected in graphene, which were indeed confirmed by experimental observations [3] (Fig. 1.4).

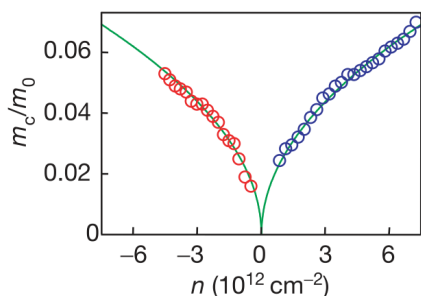


Figure 1.4: Effective (cyclotron) mass of electrons and holes as a function of their concentration n . The circles are the experimental data; solid curves are the best fit to Eq. (1.9). Taken from Novoselov et al. [3]

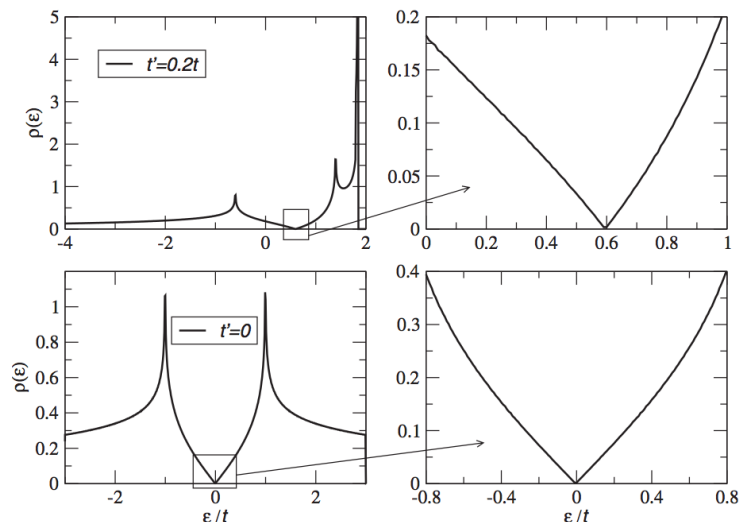


Figure 1.5: Density of states per unit cell in the tight-binding approximation, for $t' = 0.2t$ (top) and $t' = 0$ (bottom). The close-up at the Fermi level on the right side shows that for $t' = 0$ the DOS can be approximated by $\rho(\epsilon) \propto |\epsilon|$. Taken from Castro Neto et al. [5]

The density of states (DOS) per unit cell, derived from Eq. (1.4) for both $t' = 0$ and $t' \neq 0$ is illustrated in Fig. 1.5. Both cases show semimetallic behavior [20]. Thus, graphene is a semi-metal or zero-gap semiconductor. For $t' = 0$, an analytical expression for the DOS was derived by Hobson and Nierenberg [24]. Close to the Dirac point, the dispersion is approximated by Eq. (1.6) and the expression for the DOS becomes

$$\rho(E) = \frac{2A_c |E|}{\pi v_F^2}, \quad (1.10)$$

where A_c is the unit cell area. The linear dependency of the DOS is in contrast to carbon nanotubes, which show a $1/\sqrt{E}$ singularity due to their one-dimensional nature of their

electronic structure [25, 26].

1.4 Production of Graphene

In 2004, graphene was isolated and characterized for the first time by micro-mechanical alleviation of highly oriented pyrolytic graphite, commonly referred to as the Scotch tape method of mechanical exfoliation [1]. The drawback of the exfoliation of graphene is the small sample size, typically less than 1 mm^2 , and the time consumed by isolating monolayer graphene flakes. Aside from graphene also free-standing atomic planes of boron nitride, mica, dichalcogenides and complex oxides were obtained by using the same method [27].

Silicon carbide (SiC) has been widely used to grow monolayer and few-layer graphene of very high quality with the advantage that the graphene resides on top of a wide band gap semiconductor. Many important properties of graphene were first measured using a SiC substrate. While graphene on silicon carbide is advantageous for many electronic applications, a major drawback is the inability to remove graphene from the silicon carbide substrate. Another method to produce high quality sheets of graphene is the epitaxial growth on metal substrates. It has been known for a long time that monolayers of graphite can be grown epitaxially on metal surfaces, e.g. on Ni(111) [28]. After the 2004 paper of Novoselov et al. [1], a revival of interest in graphene on transition metal surfaces occurred. For example, graphene grown on iridium is very weakly coupled to the substrate with a small corrugation and can be prepared highly ordered, as will be discussed in section 6. High-quality sheets of few-layer graphene with sizes more than 1 cm^2 have been synthesized via chemical vapor deposition (CVD) on thin nickel films with methane as a carbon source. These sheets have been successfully transferred to various substrates [29].

1.5 Graphene-Substrate Interaction

While many properties of the free-standing graphene layer result from the linear dispersion at the Dirac-point, adsorption on substrates can alter its electronic properties significantly. For example, the weak interaction of graphene adsorbed on the (0001) surface of insu-

lating hexagonal boron nitride is enough to destroy the characteristic band structure of graphene, because of the symmetry breaking induced by the substrate and opens a gap of ≈ 50 meV [30]. A similar effect is even present in the bulk allotrope graphite. Even when the interaction is sufficiently weak to leave the conical points essentially unchanged, it can lead to a large shift of the Fermi energy away from the conical points [30] [31].

From an experimental point of view, graphene on transition metals are classified either as “weak” or “strong” interacting systems [7]. A third category can be defined as graphene on bulk-carbides (Fig. 1.6). A strong interaction on a pure metal commonly involves [32]: (i) formation of a large domain structure, (ii) a strongly perturbed graphene π -band, in particular a shift to a higher binding energy (BE) of 1-3 eV and opening of a gap, (iii) the smallest Gr-metal distance around 2.1-2.2 Å, much smaller than the interplane distance in graphite, which is clearly observed for nickel and cobalt. For these two elements, graphene is well lattice matched and can adsorb in a single adsorption geometry, i.e. the honeycomb lattice has the same registry with the metal substrate atoms across the surface. (iv) If a moiré-pattern is formed, a large corrugation of the graphene layer with a buckling of more than 1 Å is observed. The moiré pattern is a consequence of the lattice-mismatch between graphene and the substrate so that graphene is forced to occupy different adsorption sites in the different regions of moiré cell. A large corrugation in strongly interacting Gr/metal systems indicates large variations in the carbon-metal interaction, depending on the position of the carbon atoms relative to the substrate metal atoms [32]. For all elements the weakest interaction and largest Gr-metal distances (3.6-3.8 Å for Re, Ru, and Rh) are found if the carbon-hexagon is centered above surface metal atoms². The strongest interactions are either found for one carbon at a metal top-site and the other in a three-fold hollow³ (for Ru and Re) or in a bridge adsorption position⁴ (for Rh).

The different bonding strength at different regions in the moiré cell gives rise to a slight variation of C1s core level (CL) shifts [34]. A comparison of C1s peaks for graphene on several lattice mismatched metals shows that for weaker interacting systems, the peak is shifted to higher energies (Fig. 1.7). Furthermore, only one peak is observable for the

²This position is called *ATOP* region [33] and corresponds locally to a hcp-fcc adsorption configuration according to Fig. 3.3

³This configuration corresponds locally to a top-fcc and top-hcp adsorption positions in Fig. 3.3

⁴Corresponding locally to a bridge-top adsorption position in Fig. 3.3

Ti carbide	V	Cr	Mn	Fe	Co ^S d=2.1 ^e c=0 π=?	Ni ^S d=2.1 ⁿ c=0 π= 2 eV ^o	Cu ^M d=3 (3.3) [†] c=? π= intact ^u
Zr	Nb	Mo	Tc	Ru ^S d=2.1-3.6 ^{b,c} c=1.5 ^b (0.82 ^o) π= 2.6 eV ^d	Rh ^S d=2.2-3.8 ^f c=1.6 ^g π=?	Pd ^M d=2.5 ^d c=? π=?	Ag d=3.3 ^v c=? π= intact ^w
Hf carbide	Ta carbide	W carbide	Re ^S d=2.1-3.8 ^o c=1.6 ^o π=?	Os	Ir ^{S/M} d=3.4-4 ^{h,k} c=0.3 ^l π=intact ^m	Pt ^M d=3.3 ^{q,r} c=? π= intact ^s	Au ^M d=3.3 ^x c=? π= intact ^y

Figure 1.6: The interaction of graphene with transition metals is divided into three groups. First, elements where graphene was not observed to grow on pure metals but may grow on their bulk-carbides, colored in blue. Strong and weak Gr-metal interactions are colored in red and yellow, respectively. 'S' or 'M' in the upper right corner of each element-box indicates if graphene forms single or multiple rotational domains, 'd' denotes the Gr-metal separation in Å. The corrugation is given by 'c' in Å, and the amount of downward shift of the π -band by π , where 'intact' means that the Dirac cone is preserved. Taken from Batzill [32].

two weakly interacting systems Gr/Pt(111) and Gr/Ir(111), while two peaks are found for the strongly interacting systems Gr/Rh(111) and Gr/Ru(0001). The double peak can be assigned to the stronger and weaker interactions within a moiré cell with large corrugation. Two peaks were also found for graphene on Re [35].

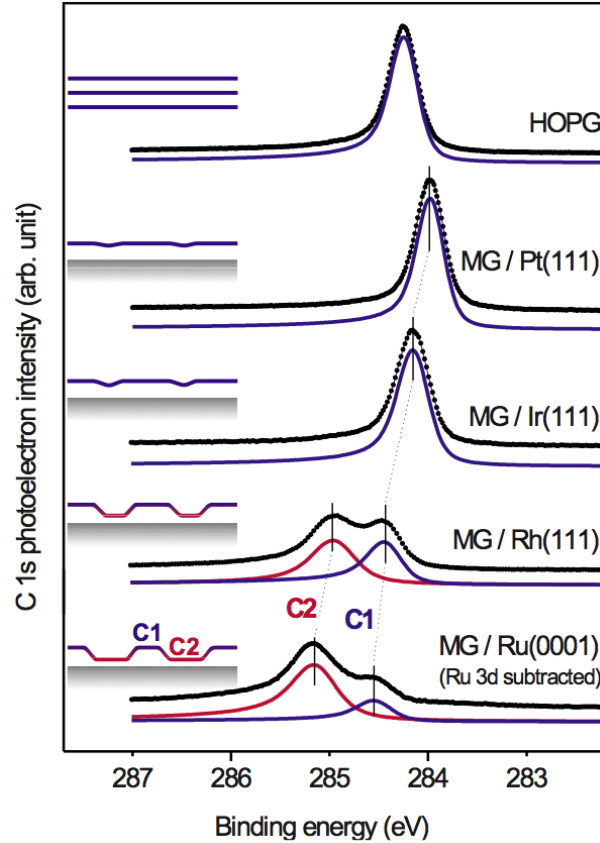


Figure 1.7: C1s core level BEs of monolayer graphene on various transition metal substrates. With decreasing Gr-metal interaction a shift toward lower BEs is measured. For systems with a strongly corrugated graphene moiré pattern, two BE peaks are observed corresponding to the strongly and weakly interacting regions within the moiré unit cell. Taken from Preobrajenski et al. [34]

A characteristic feature of a weakly interacting Gr-metal system (yellow in Fig. 1.6) is a Gr-metal distance of more than 3.3 Å and an almost undisturbed graphene π -band with the Dirac cone at the K -point intact. However, the Fermi level can be shifted (as much as 0.5 eV) which is due to charge transfer, as a consequence of differences in the work function [32]. Pd was marked between strong and weak interaction in Fig. 1.6 based

on a separation of 2.5 Å calculated with the LDA-DFT [36]. Yet, with the results of more recent RPA calculations [37] which predict a typical Gr-metal distance for weakly interacting systems of 3.3 Å, one would categorize Gr/Pd(111) as weakly interacting system. Interestingly, Gr/Ir(111) is the only weakly interacting system where single rotational domain structures are found [32].

The chemical reason for different interaction strengths for various transition metals can be given in a crude simplification by analyzing the d -band position relative to the Fermi level with the so-called d -band model [38]. This model was originally developed to understand the bonding strength of adsorbates (mainly molecules) on transition metals and mainly applies for covalent bonding situations. The interaction of graphene with a transition metal is often characterized by weak vdW interactions, therefore the application of the model to Gr-metal system is very limited. Within this model, a stronger bonding is predicted for a decreasing occupation of the d -band, because the anti-bonding state is pushed to higher energies and partly above the Fermi level. A stronger bonding is also predicted when going from $5d$ to $3d$ transition metals, caused by a stronger Pauli repulsion due to a stronger overlap of the adsorbate-metal orbitals. The center of d -bands for various transition metals are compared with the respective Gr-metal separation in table 1.1. From this comparison one can conclude that metals with their d -band center less than ≈ 2 eV below Fermi level are strongly interacting, whereas if the d -band center is further below ≈ 2 eV the metal interacts weakly with graphene [32].

However, the model is not suitable to explain different interaction strengths within the moiré unit cell for lattice mismatched systems. Furthermore, abrupt changes from weak to strong interaction from one metal to a neighboring in the periodic table (e.g. from Ir to Rh) cannot be explained with this model. Moreover, this model does not apply to interaction cases dominated by dispersive interactions. Therefore, more advanced electronic structure calculations are required to understand the bonding of graphene with transition metals. In recent years, even large moiré-structures which are coupled by weak vdW interactions can be successfully treated with DFT calculations. Graphene on iridium as an example of a weak interaction system with a large moiré unit cell is subject of section 6 in this work.

Graphene on noble metals such as Au, Ag, and Cu is not easily synthesized. Due to the weak Gr-metal interaction for these materials, graphene grows polycrystalline on these

	$(E_{d\text{-center}} - E_{\text{F}})$ [eV] [38]	$d_{\text{Gr-metal}}$ [Å]
Co(0001)	-1.17	2.1
Ni(111)	-1.29	2.1
Cu(111)	-2.67	3.3
Ru(0001)	-1.41	2.1
Rh(111)	-1.73	2.2
Pd(111)	-1.83	2.5
Ag(111)	-4.30	3.3
Re(0001)	-0.51	2.1
Ir(111)	-2.11	3.4
Pt(111)	-2.25	3.3
Au(111)	-3.56	3.3

Table 1.1: A rough classification of strongly and weakly interacting Gr-metal systems can be done by comparing the d -band center of transition metals used as substrate for graphene and reported values of Gr-metal separation (the smallest Gr-metal distance was chosen for strongly corrugated moiré-structures where the strongest interaction is found). A d -band center shifted to lower energies (< -2 eV) is correlated to a large Gr-metal distances and thus a weak Gr-metal interaction. Smaller shifts of the d -band center (> -2 eV), on the other hand correspond to a small Gr-metal separation and a strong interaction. Reprinted from Batzill [32].

substrates, which makes it difficult to perform measurements. However, by first growing graphene on a strongly interacting metal substrate and then subsequently intercalate the metal of choice between the metal substrate and graphene, the required experiments can be performed [32]. This approach has been demonstrated, e.g. by the intercalation of Au, Pt, Pd, Ni, Co, In, and Ce between graphene and ruthenium and for noble metals (Cu, Ag, Au) as well as Fe and alkali elements (Na, K, Cs) for graphene grown on nickel. The intercalation of noble metals often results in a decoupling of graphene from the substrate and the recovery of the Dirac cone, e.g. angle-resolved photoelectron spectroscopy (ARPES) measurements one monolayer (ML) Au intercalated in Gr/Ni(111) (Fig. 1.8) showed that quasi-free-standing graphene with a linear dispersion relation at the Dirac points is formed, because the hybridization of Ni $3d$ -states with graphene π -bands is suppressed [39]. However, the intercalation of a noble metal does not always lead to quasi-free-standing graphene, e.g. a band gap was observed for Au intercalated between (the strong interacting) graphene and ruthenium [40]. Furthermore, the intercalation of a noble metal (Ag) underneath Gr/Re(0001) restores the linear character of the graphene π -band, but also a significant hybridization between Ag-bands and the π -bands of graphene is observed, which will be discussed in section 8. In contrast, the intercalation of strongly interacting nickel, in weakly interacting Gr/Ir(111) is studied in section 7. The nickel layer is stretched to the iridium lattice constant resulting in a moiré-structure with strong corrugated graphene caused by different interaction strengths in different regions of the moiré [41] similar to Gr/Ru, Gr/Rh, and Gr/Re.

Also from a theoretical point of view the Gr-metal interaction was divided into two categories. In 2009, Khomyakov et al. [42] performed DFT calculations based on the local density approximation (LDA) where they analyzed the adsorption strength of Gr on several metals. They found chemisorbed systems with BE > 0.1 eV except Pd (0.084 eV) and small Gr-metal distances (< 2.31 Å) for Ti, Ni, Co, and Pd. Much weaker bonding (< 0.043 eV) and larger Gr-metal distances (> 3.26 Å) were calculated for Al, Ag, Cu, Au, and Pt. For the strongly interacting systems the graphene bands are strongly perturbed and the characteristic conical band structure of graphene at K is destroyed. Graphene p_z -states hybridize (relatively) strongly with the metal d -states and the corresponding bands acquire a mixed graphene-metal character. In contrast, for the weakly adsorbed metals

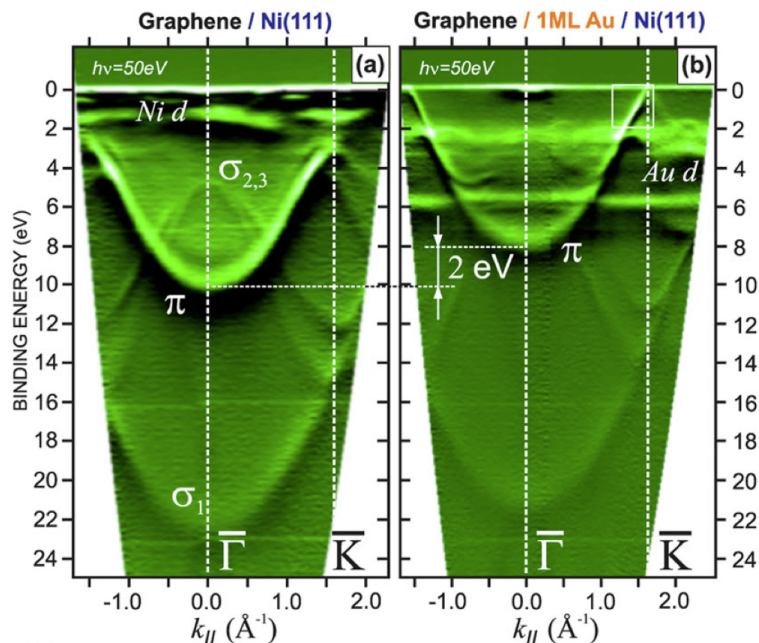


Figure 1.8: Changes of the electronic structure of Gr/Ni(111) along Γ – K before (a) and after (b) the intercalation of 1 ML Au. A shift of the π -band of 2 eV and a preserved Dirac cone are observed after intercalation. Taken from Varykhalov et al. [39]

they found that the graphene bands, including their conical band structure at K , can still be clearly identified. The term physisorption is used to describe this type of bonding. Unlike the case of free-standing graphene where the Fermi level coincides with the conical point, physisorption generally shifts the Fermi level. Even if there is no interaction or the interaction is weak, this does not preclude the transfer of charge between graphene and the metal substrate resulting from the equilibration of the chemical potentials [42].

Although LDA calculations [42] can explain the observed band structures rather well, non-local contributions including vdW forces are only spuriously mimicked by the overbinding of the LDA. Hence, for a detailed analysis of the interaction, more sophisticated methods must be used. Especially, the strong interacting systems Gr/Ni(111) and Gr/Co(0001) unexpectedly were shown to exhibit two energy minima for both of which the BEs are weaker than predicted by LDA calculations [37, 43]. For the weakly interacting systems graphene on Au(111), Ag(111), Pd(111), Cu(111), Pt(111), and Al(111) only one vdW minimum at distances larger than 3 \AA was found [37]. In section 3, the peculiar interaction of graphene with a nickel substrate is studied in more detail.

Part II

**Theoretical Background and
Methods**

Chapter 2

Theoretical Background

2.1 Basic Hamiltonian

Solid materials consist of atomic nuclei, often arranged in a regular (elastic) lattice, and of electrons. As the macroscopic behavior of a solid is determined by these constituents, the description of the system requires the use of quantum mechanics. The Hamiltonian of a system is of fundamental importance, because if the Hamiltonian is known not only the total energy of the system but also the time-evolution of this system can be calculated. In fact one can easily write down the full Hamiltonian of a many-body problem including only electrons and nuclei

$$\hat{H} = \hat{H}_{\text{nuc}} + \hat{H}_{\text{el}} + \hat{V}_{\text{nuc-el}}, \quad (2.1)$$

where the input should be the charge of the nuclei Ze , the mass of the nuclei M , the charge of the electron $-e$, and the mass of the electron m . At the energy range we are interested in, somewhere between zero and keV's, only the Coulomb interaction will play a role. This means that, apart from disregarding gravitation, strong, and weak interactions, one can in general assume that relativistic and retardation effects can be neglected in a first approximation. Therefore, the different parts of the Hamiltonian above, can be written

as follows¹

$$\hat{H}_{\text{nuc}} = \hat{T}_{\text{nuc}} + \hat{V}_{\text{nuc-nuc}} = \sum_{I=1}^K \frac{\hat{P}_I^2}{2M_I} + \frac{1}{2} \sum_{I \neq J} \frac{Z_I Z_J e^2}{|\mathbf{R}_I - \mathbf{R}_J|} \quad (2.2)$$

$$\hat{H}_{\text{el}} = \hat{T}_{\text{el}} + \hat{V}_{\text{el-el}} = \sum_{i=1}^n \frac{\hat{p}_i^2}{2m_i} + \frac{1}{2} \sum_{i \neq j} \frac{e^2}{|\mathbf{r}_i - \mathbf{r}_j|} \quad (2.3)$$

$$\hat{V}_{\text{nuc-el}} = - \sum_{i=1}^n \sum_{J=1}^K \frac{e^2 Z_J}{|\mathbf{r}_i - \mathbf{R}_J|}. \quad (2.4)$$

The Hamiltonian for both the nuclei and electrons, includes a kinetic energy \hat{T} and potential energy term \hat{V} . The last term (2.4) is the potential energy between nuclei and electrons. The Schrödinger equation in its most general form reads

$$i\hbar \frac{\partial}{\partial t} \Psi = \hat{H} \Psi. \quad (2.5)$$

If there is no explicit time dependence for the Hamiltonian (2.1), the time-independent Schrödinger equation

$$\hat{H} \Psi = E \Psi \quad (2.6)$$

is used. In this equation we used the many-particle wave function

$$\Psi(\mathbf{r}_1, s_1, \mathbf{r}_2, s_2, \dots, \mathbf{r}_n, s_n, \mathbf{R}_1, I_1, \dots, \mathbf{R}_K, I_K), \quad (2.7)$$

which depends on all electron and nuclear coordinates $\mathbf{r}_i, \mathbf{R}_J$ and spins s_i, I_J . In the following we combine the spatial and spin degree of freedom to one coordinate \mathbf{r} for electrons and \mathbf{R} for nuclei. It is impossible to solve this equation for a large number of particles. Therefore, approximations must be done so that the problem gets solvable. In solid state theory the first step is usually to separate the electronic and ionic motion within the Born-Oppenheimer approximation.

2.2 Born-Oppenheimer Approximation

The Born-Oppenheimer approximation is based on the fact that the typical electronic velocities are much larger than ionic velocities, because the nuclei are much heavier than electrons. Therefore, one supposes that the electrons can follow the motion of the nuclei

¹In this chapter Gaussian units are used.

almost instantaneously. Often one simply assumes that the electrons stay in their ground-state for any configuration of the nuclei. Mathematically speaking, the wave function $\Psi(\mathbf{r}, \mathbf{R})$ can be written as a product of an electronic and a nuclear wave function

$$\Psi(\mathbf{r}, \mathbf{R}) = \chi_{\text{el}}(\mathbf{r}, \mathbf{R}) \cdot \phi_{\text{nuc}}(\mathbf{R}). \quad (2.8)$$

One assumes further that the electronic wave function χ_{el} , depends on the nuclear positions only as parameters. When the full Hamiltonian is applied to (2.8), one gets two expressions: first, a Schrödinger for the electrons

$$\hat{H}_e \chi_{\text{el}}(\mathbf{r}, \mathbf{R}) = E_{\text{el}} \chi_{\text{el}}(\mathbf{r}, \mathbf{R}), \quad (2.9)$$

with an electronic Hamiltonian \hat{H}_e

$$\hat{H}_e = \hat{T}_{\text{el}} + \hat{V}_{\text{el-el}} + \hat{V}_{\text{nuc-nuc}} + \hat{V}_{\text{nuc-el}}. \quad (2.10)$$

And secondly a Schrödinger equation for the nuclei

$$(\hat{T}_{\text{nuc}} + \hat{H}_e(\mathbf{R})) \phi_{\text{nuc}}(\mathbf{R}) = E_{\text{nuc}} \phi_{\text{nuc}}(\mathbf{R}). \quad (2.11)$$

In the following we want to study the electronic properties of materials and treat the ionic motion classically.

2.3 Simple Models in Solid State Physics

In the field of solid state physics a typical number of particles is 10^{23} . With $(3 \cdot n)$ degrees of freedom, not considering the spin, it is impossible to solve the electronic Schrödinger equation (2.9) directly and further approximations must be considered.

A number of different attempts in describing the electronic structure of solids were made, after the quantum theory was established. In 1927, Sommerfeld combined the classical Drude model with quantum mechanical Fermi-Dirac statistics. This model is now known as the *free electron* or *Drude-Sommerfeld model*. Within this model, the valence electrons are completely detached from their ions. The electron-electron interactions are completely neglected and the crystal lattice is not taken into account. As the electrons feel no potential, the respective Schrödinger equation is

$$-\frac{\hbar^2}{2m_e} \nabla^2 \psi(\mathbf{r}, t) = i\hbar \frac{\partial}{\partial t} \psi(\mathbf{r}, t) \quad (2.12)$$

and the plane wave solution

$$\Psi(\mathbf{r}, t) = \frac{1}{\sqrt{\Omega_r}} e^{i\mathbf{k}\cdot\mathbf{r} - i\omega t}, \quad (2.13)$$

with wave vector \mathbf{k} , volume of space occupied by one electron Ω_r , and angular frequency ω . Even though it is such a crude approximation, it explains many experimental phenomena such as the Wiedemann-Franz law, electrical conductivities, the temperature dependence of the heat capacity, and the shape of the electronic density of states surprisingly well. But it could not explain, for example, the existence of insulators.

The next step was the *nearly free electron model*, where a weak periodic potential is included to account for the interaction between the ions in the crystalline solid and the conduction electrons, but electron-electron interactions are completely ignored in this model. The periodic crystal is reflected in the solution for the wave function

$$\Psi_{n, \mathbf{k}}(\mathbf{r}) = e^{i\mathbf{k}\cdot\mathbf{r}} u_n(\mathbf{r}), \quad (2.14)$$

which are called Bloch waves, where $u_n(\mathbf{r})$ is a periodic function over the crystal lattice

$$u_n(\mathbf{r}) = u_n(\mathbf{r} - \mathbf{R}). \quad (2.15)$$

Here n is the n -th energy band, \mathbf{r} is the position in the crystal and \mathbf{R} is the location of an atomic site [44]. A result of the weak perturbation by solving the Schrödinger equation, is the introduction of band gaps between interacting bands at the Brillouin zone boundaries. Despite the complete neglect of electron-electron interactions, this model works rather well for materials with small distances between neighboring atoms, e.g. some metals like Al.

The opposite case to the nearly free electron model assumes that the wave function is still closely related to the solution for the constituent atoms. In this *tight-binding (TB) model*, the solution to the time-independent Schrödinger equation Ψ , is approximated by a linear combination of atomic single-electron orbitals $\psi_n(\mathbf{r})$ [44].

$$\Psi(\mathbf{r}) = \sum_{n, \mathbf{R}} b_{n, \mathbf{R}} \psi_n(\mathbf{r} - \mathbf{R}), \quad (2.16)$$

where the coefficients $b_{n, \mathbf{R}}$ are the weights of the atomic orbitals. The TB model is best suited for materials with small overlap between atomic orbitals and potentials of neighboring atoms, e.g. Si, GaAs, SiO₂ and diamond are well described by TB-Hamiltonian on the basis of sp^3 orbitals. The band structure (for p_z electrons) of graphene is also well described with a TB-model (see section 1.3.3).

2.4 Hartree and Hartree-Fock Method

A different attempt to solve the time-independent electronic Schrödinger equation (2.9) is the application of the Rayleigh-Ritz variational principle, which states that the expectation value of the Hamiltonian in any state $|\Psi\rangle$ is always larger than, or equal to the ground-state energy E_0 , i.e.

$$E_0 \leq \frac{\langle \Psi | H | \Psi \rangle}{\langle \Psi | \Psi \rangle}. \quad (2.17)$$

Hartree used this principle and obtained the following equation² [46]

$$\left\{ -\frac{\hbar^2}{2m_e} \nabla^2 + v_{\text{ext}}(\mathbf{r}) + v_{\text{H}}(\mathbf{r}) \right\} \psi_i(\mathbf{r}) = \epsilon_i \psi_i(\mathbf{r}) \quad (2.18)$$

In this so-called *Hartree equation*, the nuclei-electron potential of Eq. (2.4) is incorporated by the external potential

$$v_{\text{ext}}(\mathbf{r}) = -\sum_{J=1}^K \frac{e^2 Z_J}{|\mathbf{r} - \mathbf{R}_J|}, \quad (2.19)$$

and the Hartree potential v_{H} is defined as

$$v_{\text{H}}(\mathbf{r}) = \int d^3 r' n(\mathbf{r}') \frac{e^2}{|\mathbf{r} - \mathbf{r}'|}, \quad (2.20)$$

with the electron density

$$n(\mathbf{r}) = \sum_{i=1}^N |\psi_i(\mathbf{r})|^2. \quad (2.21)$$

The Hartree equations (2.18) have the form of effective one-particle Schrödinger equations. But the solutions $\psi(\mathbf{r})$ enter the effective one-particle Hamiltonian. Therefore, iterative *self-consistent field* methods are used to solve the equations. The expectation value of the Hamiltonian equals the total energy, which reads in the Hartree approximation

$$E_{\text{H}} = \sum_{i=1}^N \epsilon_i - V_{\text{H}} + V_{\text{nuc-nuc}}, \quad (2.22)$$

where the *Hartree energy*

$$V_{\text{H}} = \frac{1}{2} \int d^3 r d^3 r' \frac{e^2 n(\mathbf{r}) n(\mathbf{r}')}{|\mathbf{r} - \mathbf{r}'|}, \quad (2.23)$$

corresponds to the classical electrostatic energy of the electronic charge distribution. This term appears twice in the Hartree eigenvalue, thus it is subtracted in Eq. (2.22). Because

²For a detailed derivation see, e.g. Gross [45].

the Hartree equations are solved self-consistently, the total energy is not simply the sum over non-interacting particle energies, but the interaction is included to some extent.

Thus, the Pauli principle is in some way included in the Hartree ansatz, however the anti-symmetry of the wave function is not taken into account. This can be done by using Slater determinants to construct the wave function, which leads to the *Hartree-Fock equations* [47]

$$\left\{ -\frac{\hbar^2}{2m_e} \nabla^2 + v_{\text{ext}}(\mathbf{r}) + v_{\text{H}}(\mathbf{r}) \right\} \psi_i(\mathbf{r}) - \sum_{j=1}^N \int d^3r' \frac{e^2}{|\mathbf{r} - \mathbf{r}'|} \psi_j^*(\mathbf{r}') \psi_i(\mathbf{r}') \psi_j(\mathbf{r}) \delta_{\sigma_i \sigma_j} = \epsilon_i \psi_i(\mathbf{r}). \quad (2.24)$$

An additional term appears in comparison with the Hartree equation (2.18), the so-called *exchange term*. The total energy in the Hartree-Fock approximation is given by

$$E_{\text{HF}} = \sum_{i=1}^N \epsilon_i - V_{\text{H}} - E_{\text{x}} + V_{\text{nuc-nuc}}, \quad (2.25)$$

Similar to Eq. (2.22), the Hartree energy V_{H} and the exchange energy E_{x} are subtracted, because they appear twice in the Hartree-Fock eigenvalues. While in the Hartree approximation the electrons are not correlated, the anti-symmetry of the wave functions in the Hartree-Fock approach leads to the so-called *exchange hole* – electrons of the same spin avoid each other. The exchange energy corresponds to the repulsive Coulomb interaction between electrons of the same spin and decreases the total energy. However, electrons of opposite spin are still not correlated. The energy can be further decreased, if these electrons avoid each other. This additional effect is called *electron correlation* and the *electron correlation energy* is defined as the difference between the exact total energy of the system and the Hartree-Fock energy [45].

2.5 Post Hartree-Fock Methods

In the Hartree-Fock method, several assumptions and shortcomings are incorporated such as: (i) the Born-Oppenheimer approximation is assumed, (ii) relativistic effects are neglected, (iii) the basis set is incomplete, (iv) the effects of electron correlation is only partially included. *Post-Hartree-Fock* methods mainly focus on the fourth item by adding electron correlation. Some frequently used methods are presented in the following.

The configuration interaction (CI) method adds determinants to the wave function by replacing occupied orbitals. If only single (S) and double (D) excitations are included in the sum, the method is called CISD with the wave function

$$\Psi_{\text{CISD}} = \Psi_{\text{HF}} + \sum c_i^{(1)} \Psi_i^{(1)} + \sum c_i^{(2)} \Psi_i^{(2)}. \quad (2.26)$$

The coefficients $c_i^{(j)}$ are varied to find an optimized wave function Ψ_{CISD} . If all possible determinants are added (in the given basis set), the method is referred as full-CI (FCI), which exactly solves the Schrödinger equation within the spanned one-particle basis set. However, FCI calculations are limited to rather small systems. One issue with this approach is that the scaling of the energy is not linear with the number of electrons. The size consistency is recovered with the *coupled cluster* (CC) method, where the exponential of the excitation operators is taken. For single and double excitations only (CCSD) the wave function can be written as

$$\Psi_{\text{CCSD}} = \exp(\hat{T}_1 + \hat{T}_2) \Psi_{\text{HF}}, \quad (2.27)$$

where \hat{T}_i is the i -fold cluster operator. Higher order excitations are often incorporated perturbatively, because of computational limitations. The present “gold-standard” for quantum chemistry reference calculations is CCSD(T), where triple excitations are accounted perturbatively.

A different approach is to incorporate the excitations perturbatively in the *Møller-Plesset perturbation theory*, where the difference between the true many-body Hamiltonian and the Hartree-Fock Hamiltonian is treated perturbatively. Hartree-Fock theory is correct to first order. In many cases only the second-order term is treated, which is referred as MP2 method and is cheaper but less accurate than CCSD(T) calculations.

For large system sizes post-Hartree-Fock methods are too expensive. Another method is needed which can handle large systems efficiently with the required accuracy. In recent years one method that is not based on a representation of the many-body wave function, but on the electron density has proven to be the best choice for this requirements: density functional theory (DFT).

2.6 Density Functional Theory

The basic principle of density functional theory is to work with a quantity that is easier to handle, namely the electron density $n(\mathbf{r})$, which is reduced in coordinate space, instead of trying to solve the electronic Hamiltonian (2.10) through complicated many-body wave functions. The idea of using the electron density to calculate the electronic structure was already used by L. Thomas and E. Fermi in 1927 [48, 49]. However, the application of this *Thomas-Fermi model* for real systems yields poor quantitative predictions. Furthermore, this model is not based on a solid theory which relates the electron density to the corresponding many body wave function [8].

In fact, the *Hohenberg-Kohn theorem* provides the missing connection and thereby is the foundation of DFT. This theorem states that the ground-state density $n(\mathbf{r})$ of a system of interacting electrons in an external potential uniquely determines this potential, which can be proven in an elegant way [8]. Whereas the variational principle of Hohenberg and Kohn proves that the correct ground-state density n_0 minimizes the energy functional $E[n]$

$$E_{\text{tot}} = \min_{n(\mathbf{r})} E[n] = \min_{n(\mathbf{r})} (T[n] + V_{\text{ext}}[n] + V_{\text{H}}[n] + E_{\text{xc}}[n]). \quad (2.28)$$

The functional of the external potential $V_{\text{ext}}[n]$ and of the classical electrostatic interaction energy, which corresponds to the Hartree energy $V_{\text{H}}[n]$, can be easily expressed through the electron density. All quantum mechanical many-body effects are hidden in the so-called *exchange correlation energy* $E_{\text{xc}}[n]$. However, this non-local functional is not known and it is probably impossible to determine its exact form. Also the kinetic energy functional for non-interacting electrons $T[n]$ is not well-known, thus the formulation (2.28) is usually not directly used to solve for the ground-state energy.

One rather expresses the electron density as a sum over single-particle orbitals

$$n(\mathbf{r}) = \sum_{i=1}^N |\psi_i(\mathbf{r})|^2, \quad (2.29)$$

and uses the variational principle for the energy functional to minimize $E[n]$ in a similar way as in the derivation of Hartree and Hartree-Fock to derive single-particle equations, the so-called *Kohn-Sham equations* [9]

$$\left\{ -\frac{\hbar^2}{2m_e} \nabla^2 + v_{\text{ext}}(\mathbf{r}) + v_{\text{H}}(\mathbf{r}) + v_{\text{xc}}(\mathbf{r}) \right\} \psi_i(\mathbf{r}) = \epsilon_i \psi_i(\mathbf{r}). \quad (2.30)$$

This equation is again a Schrödinger equation for non-interacting electrons in an effective potential

$$v_{\text{eff}}(\mathbf{r}) = v_{\text{ext}}(\mathbf{r}) + v_{\text{H}}(\mathbf{r}) + v_{\text{xc}}(\mathbf{r}), \quad (2.31)$$

which generates the same density as any given system of interacting electrons. The exchange-correlation potential $v_{\text{xc}}(\mathbf{r})$ in Eq. (2.31) can be written as functional derivative of the *exchange-correlation functional* $E_{\text{xc}}[n]$

$$v_{\text{xc}}(\mathbf{r}) = \frac{\delta E_{\text{xc}}[n]}{\delta n}. \quad (2.32)$$

The ground-state energy in the Kohn-Sham formalism can now be expressed as

$$E = \sum_{i=1}^N \epsilon_i + E_{\text{xc}}[n] - \int d^3r v_{\text{xc}}(\mathbf{r})n(\mathbf{r}) - V_{\text{H}} + V_{\text{nuc-nuc}}, \quad (2.33)$$

where the term $V_{\text{nuc-nuc}}$ is added in order to get the correct total energy of the electronic Hamiltonian (2.10). The single-particle energies ϵ_i serve just as Lagrange multipliers and have no physical meaning except for the highest occupied state, but are often interpreted as one-particle energies. Furthermore, the Kohn-Sham eigenvalues cannot be strictly taken as excitation energies [50] although done in practice in many cases. However, for a correct evaluation of excited state properties like band gaps or quasiparticle energies as measured e.g. by spectroscopy, more advanced theories like *GW* [51] have to be applied (see section 2.10).

The Kohn-Sham theory may be seen as an extension of the Hartree theory, because if the exchange-correlation terms are neglected, the Hartree formulation is recovered. In contrast to the total energies in the Hartree and Hartree-Fock approximation, the ground-state energy (2.33) is in principle exact. However, the exchange-correlation functional $E_{\text{xc}}[n]$ is not known, and to find an accurate expression for $E_{\text{xc}}[n]$ is of crucial importance to give reliable results in the framework of DFT calculations.

2.7 Exchange Correlation Functional

In principle, the exchange-correlation energy functional $E_{\text{xc}}[n]$ can be expressed as

$$E_{\text{xc}}[n] = \int d^3r n(\mathbf{r})\epsilon_{\text{xc}}[n], \quad (2.34)$$

where the exchange-correlation energy density $\epsilon_{\text{xc}}[n]$ is a functional of n and therefore depends on the whole electron density distribution $n(\mathbf{r})$. However, the exact form of E_{xc} and $\epsilon_{\text{xc}}[n]$ is not known in general, but the exchange-correlation energy for the homogeneous electron gas can be calculated [52]. This exchange-correlation energy is then used in the so-called local density approximation (LDA) also for non-homogeneous situations,

$$E_{\text{xc}}^{\text{LDA}}[n] = \int d^3r n(\mathbf{r}) \epsilon_{\text{xc}}^{\text{LDA}}(n(\mathbf{r})). \quad (2.35)$$

Therefore, the local exchange-correlation energy of the homogeneous electron gas $\epsilon_{\text{xc}}^{\text{LDA}}$ is used at every single point in space for the corresponding density, despite the non-locality of the real exchange-correlation energy $\epsilon_{\text{xc}}[n]$.

LDA calculations were surprisingly successful for a wide range of bulk and surface problems [53], which is still not fully understood but probably due to a cancellation of errors in the exchange and correlation expression of LDA. For systems where the electron density is rapidly changing, such as atoms or molecules, LDA performs poorly. Furthermore, LDA shows usually overbinding, i.e. binding and cohesive energies are too large compared to experiment.

The first step to improve for systems with large spatial variations of the electron density, is the addition of a term adding information on the semi-local surrounding. The gradient of the density is a good choice and leads to the so-called *generalized gradient approximation* (GGA) for the exchange-correlation energy

$$E_{\text{xc}}^{\text{GGA}}[n] = \int d^3r n(\mathbf{r}) \epsilon_{\text{xc}}^{\text{GGA}}(n(\mathbf{r}), |\nabla n(\mathbf{r})|). \quad (2.36)$$

The energies with GGA calculation yield better results than LDA for many systems. There are different flavors of GGA functionals, but most widely used in the surface physics community is the Perdew-Burke-Ernzerhof (PBE) functional [54]. Despite its success for many material classes, DFT calculations on the level of LDA and PBE-GGA still fail in several aspects [45]: (i) van der Waals (vdW) forces cannot be described, (ii) electron affinities are too small, so that negative ions are usually not bound, (iii) an exponential decay of the Kohn-Sham potential instead of $\propto 1/r$, (iv) band gaps are considerably underestimated in both, LDA and GGA, (v) cohesive energies are overestimated with LDA and underestimated with GGA, (vi) the ground-state of strongly correlated solids (CoO, FeO) is predicted wrong.

There are different attempts to correct these failures and to get more accurate results. One possibility is to include higher-order powers of the gradient or the local kinetic energy in the so-called *meta-GGA*'s [55]. Another ansatz are *hybrid functionals*, that incorporate a portion of exact exchange from Hartree-Fock theory with exchange and correlation from DFT. The most popular hybrid functionals in use nowadays are B3LYP [56, 57] and HSE [58]. Other methods which are based on orbital functionals, such as the optimized potential method and the optimized effective potential method, give very accurate results for small molecules [59]. However, the high computational efficiency of DFT is lost by using this methods. Relativistic effects become important for heavy elements such as Au [60] and the Hohenberg-Kohn theorem can be extended to the relativistic regime [61]. For spin-polarized calculations the electron density $n(\mathbf{r})$ is substituted by $n^\uparrow(\mathbf{r}) + n^\downarrow(\mathbf{r})$ which leads to the Kohn-Sham spin density functional theory [9].

2.8 Performing a DFT Calculation in Practice

Only a very limited number of problems can be solved analytically with the above mentioned theories. In practice one uses numerical methods to solve the equations. Throughout this work, the Vienna ab initio simulation package (VASP) [62, 63] is utilized to perform DFT calculations. In practice, the Kohn-Sham equations are solved self-consistently, where an initial guess for the charge density is made. This guess is used to calculate the respective potentials and to solve the Kohn-Sham equations. A new charge density is calculated from the resulting wave function and compared to the initial charge density. If a certain criterion is fulfilled the cycle stops, otherwise a new charge density by combining the old ones is generated and the cycle starts again. A second loop is performed if the ions are allowed to relax into to their equilibrium positions. Here the forces acting on the ions are evaluated and new position are calculated according to one of several possible algorithms, e.g. the RMM-DIIS quasi-Newton algorithm [64] or the conjugate-gradient algorithm [65].

With VASP, the wave functions are expanded in a plane wave basis³, which is the

³A detailed discussion of the plane wave approach in DFT can be found, e.g. in the review of Payne et al. [53]

common basis to describe periodic systems because a plane wave

$$\Psi_{\mathbf{k}}^{\mathbf{G}}(\mathbf{r}) = \frac{1}{\sqrt{V}} e^{i(\mathbf{k}+\mathbf{G})\cdot\mathbf{r}}, \quad (2.37)$$

has the form required by the Bloch theorem [66]. In Eq. (2.37) \mathbf{G} is a reciprocal lattice vector and \mathbf{k} is a wave vector inside the first Brillouin zone. The computation of many quantities, e.g. the charge density and the total energy require the integration over the Brillouin zone but in practice, a finite k-point grid is used to sample the Brillouin zone, e.g. in the form of a Monkhorst-Pack grid [67].

The expansion in plane waves is computationally very efficient due to the fact that the plane waves are eigenfunctions of the momentum operator and that the kinetic energy operator is diagonal in momentum space. Thus, the kinetic energy can be easily evaluated in momentum space, whereas the potential energy is evaluated in real space. The switching between real and momentum space is done via Fast-Fourier-Transformation (FFT) techniques. The expansion in plane waves usually requires a three-dimensional periodicity, which is naturally given for perfect 3D crystals but a somewhat artificial concept for finite or aperiodic systems. However, this can be achieved by the so-called supercell approach, where the respective systems are placed in large 3D supercells in order to avoid interactions between repeated images. In the case of surfaces, on the one hand the vacuum between the slabs must be sufficiently large to minimize the interaction between the slabs, and on the other hand the slabs have to be thick enough to be a reasonable model for a surface. Fortunately, both requirements can be easily checked by convergence tests through increasing the vacuum and the number of layers.

However, for the description of strongly localized electrons with rapid oscillations, such as electrons close to the core, a large number of plane waves is needed which is computationally very demanding. The size of the plane wave basis set is usually defined by the so-called cutoff energy

$$E_{\text{cutoff}} = \max_{\mathbf{G}} \frac{\hbar^2(\mathbf{k} + \mathbf{G})^2}{2m}. \quad (2.38)$$

In fact, the effect of core electrons is often negligible and the main influence comes from the valence electrons. Various methods have been proposed to utilize this, e.g. the pseudopotential method [68], and the very efficient projector augmented-wave method

(PAW) [69, 70] which is used in VASP. Here the space is divided into spherical areas around the nuclei (muffin-tin potential) and an interstitial region. In the region around the nuclei, the wave function is projected onto a pseudo-wave function orthogonal to the core states. In combination with the frozen core approximation (fixed core-states) the cutoff energy E_{cutoff} and thus the number of plane waves can be significantly reduced allowing an efficient treatment even of large systems.

2.9 Including van der Waals Interactions in DFT

The standard exchange-correlation functionals employed in DFT use only local physical quantities such as the electron density or its derivative. Thus, non-local effects as London dispersion⁴ are ignored with these functionals. London dispersion forces are one part of the vdW forces besides Keesom forces⁵ and Debye forces⁶, but are often referred as vdW forces in the DFT community. The London dispersion force is a weak intermolecular force due to an instantaneous polarization, which is even present between neutral atoms. In a simple picture, quantum fluctuations induce a dynamic multipole in adjacent particles which leads to a small attractive interaction between the particles.

The quantum mechanical explanation, first given by London in 1930 [71, 72], is based on second-order perturbation theory. The perturbation is the Coulomb interaction between the electrons and nuclei of atoms. After the expansion in a Taylor series, a substitution into second-order perturbation theory yields the following approximation for the dispersion interaction between two atoms A and B

$$E_{\text{AB}}^{\text{disp}} \approx -\frac{3}{2} \frac{I_{\text{A}} I_{\text{B}}}{I_{\text{A}} + I_{\text{B}}} \frac{\alpha^{\text{A}} \alpha^{\text{B}}}{R^6}, \quad (2.39)$$

where α^{J} and I_{J} are the dipole polarizability and first ionization potential of atom J.

In the beginning of DFT, mainly solid state materials were studied where dispersion interactions are negligible in most cases. But in recent years, a growing interest for systems where vdW forces are important like biomolecules or physisorbed molecules is arising. Furthermore, vdW forces have been proposed to play a role even in materials

⁴The term dispersion reflects the similarity to the quantum mechanical theory of light dispersion.

⁵Force between two permanent dipoles.

⁶Force between a permanent dipole and a corresponding induced dipole.

where their influence was not expected, such as ionic and semiconducting solids [73]. Furthermore vdW interaction are crucial for the materials studied in this work, such as graphene on metals [7, 41, 43] and layered materials like graphite [74]. Therefore, there is a clear demand to account for dispersion forces in the framework of DFT calculations. Different approaches were proposed in the past with promising candidates, but there is still enough space for improvements in this current research field.

2.9.1 Force-field Corrections

A pragmatic method to include vdW dispersion has been given by the DFT-D approach [75], where a semi-empirical vdW term E_{vdW} is simply added to the conventional Kohn-Sham DFT energy $E_{\text{KS-DFT}}$

$$E_{\text{DFT-D}} = E_{\text{KS-DFT}} + E_{\text{vdW}}. \quad (2.40)$$

The vdW term is an pairwise interatomic $C_6 R^{-6}$ term and represents an attractive interaction

$$E_{\text{vdW}} = -\frac{1}{2} \sum_{A,B} f_{\text{damp}}(R_{AB}, R_A^0, R_B^0) C_{6AB} R_{AB}^{-6}, \quad (2.41)$$

where R_{AB} is the distance between atoms A and B, C_{6AB} is the corresponding C_6 coefficient, and R_A^0 and R_B^0 are the vdW radii. The short-ranged damping function f_{damp} satisfies that the vdW corrections are minimized within typical bonding distances so that the R_{AB}^{-6} divergence is eliminated. This type of force-field correction was originally proposed for the Hartree-Fock method which is also missing the vdW dispersion [76] and several types have been proposed in DFT [75, 77–81]. The DFT-D2 method of Grimme [78] (as one of those methods) is employed for some calculations in the present work. The C_6 coefficient for an atom A in this method is given as $C_6^A = 0.05 N I_p^A \alpha^A$, where N has value 2, 10, 18, 36, and 54 for atoms from rows 1-5 of the periodic table. The atomic ionization potential I_p^A and the static dipole polarizability α^A of atom A are provided by parameter free density functional model PBE0 calculations [82]. The composed coefficients are expressed as $C_{6AB} = \sqrt{C_6^A C_6^B}$.

The advantage of the DFT-D approach is a very fast computation of E_{vdW} compared to the rest of the Kohn-Sham energy. However, the major drawback are the empirically obtained dispersion coefficients used by these methods. They are kept constant for each

pair of elements, however, the actual coefficients may change due to the bonding environment or depending on the hybridization of the atom [83]. More recently proposed methods try to overcome this shortcomings [83, 84] by reducing the empiricism with using reference polarizability data. The starting point for both mentioned studies is the exact expression (Casimir-Polder integral [85]) for the leading isotropic C_6 term between two atoms or molecules A and B

$$C_{6AB} = \frac{3}{\pi} \int_0^\infty \alpha_A(i\omega) \alpha_B(i\omega) d\omega, \quad (2.42)$$

where $\alpha_A(i\omega)$ is the polarizability of atom A at the imaginary frequency $i\omega$. Tkatchenko and Scheffler [83] further got an expression for C_{6AB} only depending on homonuclear parameters C_{6AA} , C_{6BB} , α_A^0 , and α_B^0 ,

$$C_{6AB} = \frac{2C_{6AA}C_{6BB}}{\frac{\alpha_B^0}{\alpha_A^0}C_{6AA} + \frac{\alpha_A^0}{\alpha_B^0}C_{6BB}}. \quad (2.43)$$

For the free-atom reference values of α_A^0 and C_{6AA} , accurate reference values were taken. The C_6 coefficients for an atom inside a molecule or solid is scaled according to the change of volume occupied by the atom, where the direct relation between polarizability and volume is used [86]. A disadvantage of this method is that atomic forces are not readily available, which is not the case for the second mentioned method, which was also proposed by Grimme et al. [84]. Again, more accurate polarizability data from time-dependent DFT computations are employed. Yet, here the different chemical environment is accounted through dispersion coefficients that are dependent on the number of neighboring atoms. Moreover, higher-order coefficients and a three-body term which substantially weakens the interlayer binding in graphene were also included in this method. The total errors are decreased with both methods compared to formerly mentioned methods with constant coefficients.

However, there are several weaknesses for all DFT-D approaches [87]. First, the interaction is a pure force-field correction and is not derived from the electron density, therefore large changes in density are difficult to address. Although very accurate dispersion corrections may be obtained, the $1/r^6$ interaction at small distances needs to be removed by using a damping function. The damping is in a region where the effect of repulsion is strong and therefore the damping function alters the position of the minimum on the

binding curve. This implies that for different functionals (with different binding curves) the damping function must be adapted to give the same binding minima. Finally, it is obvious that the additional dispersion term E_{disp} is always attractive and increases the binding. Therefore this approach improves total energies only for functionals which are not overbinding.

2.9.2 The Adiabatic-Connection Fluctuation-Dissipation Theory in its Random Phase Approximation (RPA)

In DFT the actual Coulomb electron-electron interaction operator is exchanged by the more easily treatable exchange-correlation energy E_{xc} and the problem of interacting electrons is reduced to non-interacting electrons in an effective potential E_{eff} . In the adiabatic-connection fluctuation-dissipation theory (ACFDT) one can find an exact expression of the exchange-correlation energy E_{xc} by smoothly switching the electron-electron interaction from a non-interacting KS system to a fully interacting system⁷. The electronic Hamiltonian of Eq. (2.3) in the adiabatic connection is modified to

$$\hat{H}(\lambda) = \hat{T}_{\text{el}} + \hat{V}(\lambda) + \lambda \hat{V}_{\text{el-el}}, \quad (2.44)$$

where \hat{T}_{el} and $\hat{V}_{\text{el-el}}$ are the kinetic energy and the electron-electron potential defined in Eq. (2.3). The coupling constant λ determines how much of the electron-electron interaction is turned on, and at the same time influences the potential energy $V(\lambda)$ to keep the ground-state density at the value of the fully interacting system. For $\lambda = 1$ the fully interacting system is recovered with $V(\lambda) = V_{\text{ext}}$, and $\lambda = 0$ represents the Kohn-Sham system with $V(\lambda) = V_{\text{ext}} + V_{\text{xc}}$.

By performing a thermodynamic integration over λ and using the Hellman Feynman theorem, the Hartree-exchange-correlation energy E_{xc}^{H} can be expressed as

$$E_{\text{xc}}^{\text{H}} = \int_0^1 d\lambda \langle \Psi(\lambda) | V_{\text{el-el}} | \Psi(\lambda) \rangle, \quad (2.45)$$

where $\Psi(\lambda)$ is the ground-state wave function of the λ interaction system. This expression is free of the kinetic energy operator, therefore the explicit construction of the one-particle density matrix is entirely avoided.

⁷For a more detailed discussion of the ACFDT in the RPA see Ref. [88]

Next, the fluctuation-dissipation theorem is applied. This theorem states that the response of a system to a small perturbation is the same as its response to a spontaneous fluctuation, which is a density fluctuation in our case. A small time-dependent additional potential generates a density response which can be described by the density-density response function χ . After applying the FDT theorem one can derive the following expression for the exchange-correlation energy

$$E_{\text{xc}} = -\frac{e^2}{2} \int_0^1 d\lambda \int d^3r d^3r' \frac{1}{|\mathbf{r} - \mathbf{r}'|} \left\{ n(\mathbf{r})\delta(\mathbf{r} - \mathbf{r}') + \frac{1}{\pi} \int_0^\infty d\omega \chi^\lambda(\mathbf{r}, \mathbf{r}', i\omega) \right\}, \quad (2.46)$$

where the first term is the Hartree energy and χ^λ is the response function of the λ interacting system. One can rewrite Eq. (2.46) (after some algebraic transformations, see Ref. [88]) to separate the exchange and correlation part

$$E_{\text{xc}} = E_{\text{x}} \left[\left\{ \Psi^{\text{KS}} \right\} \right] - \int_0^1 d\lambda \int d^3r d^3r' \frac{e^2}{|\mathbf{r} - \mathbf{r}'|} \int_0^\infty \frac{d\omega}{2\pi} \left\{ \chi^\lambda(\mathbf{r}, \mathbf{r}', i\omega) - \chi^{\text{KS}}(\mathbf{r}, \mathbf{r}', i\omega) \right\}, \quad (2.47)$$

with the response function of the Kohn-Sham system χ^{KS} . The Hartree-Fock exchange energy is evaluated for the wave functions of the Kohn-Sham system. The response function for the λ interacting system χ^λ appearing in the correlation energy (right hand side of Eq. (2.47)) is not known exactly but is linked by the Dyson equation to χ^{KS}

$$\begin{aligned} \chi^\lambda(\mathbf{r}, \mathbf{r}', i\omega) &= \chi^{\text{KS}}(\mathbf{r}, \mathbf{r}', i\omega) + \\ &+ \int d^3r_1 d^3r_2 \chi^{\text{KS}}(\mathbf{r}, \mathbf{r}_1, i\omega) \left(\frac{\lambda e^2}{|\mathbf{r}_1 - \mathbf{r}_2|} + f_{\text{xc}}^\lambda(\mathbf{r}_1, \mathbf{r}_2, i\omega) \right) \chi^\lambda(\mathbf{r}_2, \mathbf{r}', i\omega). \end{aligned} \quad (2.48)$$

In the random phase approximation (RPA) the exchange-correlation kernel f_{xc} is set to zero. After a transformation to reciprocal space and some algebra where the explicit λ integration can be avoided, the correlation term of Eq. (2.47) in the ACFDT-RPA can be written as

$$E_{\text{c}}^{\text{RPA}} = \int_0^\infty \frac{d\omega}{2\pi} \text{Tr} \left\{ \ln [1 - \chi^{\text{KS}}\nu] + \chi^{\text{KS}}\nu \right\}, \quad (2.49)$$

with the Coulomb-kernel ν . The total energy with ACFDT-RPA is now given as a sum of the Hartree-Fock energy expression evaluated for the Kohn-Sham wave functions and the RPA correlation energy

$$E = E \left[\left\{ \psi^{\text{KS}} \right\} \right] + E_{\text{c}}^{\text{RPA}}. \quad (2.50)$$

The self-consistent solution for RPA energies is in principle possible, but for practical reasons (high computational costs) Eq. (2.50) is usually evaluated using DFT wave-functions.

RPA calculations reproduce lattice constants, bulk moduli, heats of formations and surface energies in excellent agreement with experiments for various materials, while atomization energies are less accurately described [89, 90]. A major advantage of RPA is that vdW interactions are seamlessly incorporated and that it allows to analyze the correlation and exchange energy contributing to the total energy. Therefore, systems where the bonding is dominated by weak vdW forces are well described with RPA [87, 91]. Furthermore, it was shown that RPA reproduces the correct interlayer dispersion in graphite [74]. A drawback of this method is that forces are not directly accessible in the present implementation and secondly, it is computationally much more demanding than LDA or GGA. Therefore the system size for RPA calculations is limited to about 100 atoms nowadays [90].

2.9.3 vdW-DF

A related route to include vdW interactions in DFT calculations, however on a lower level but with less computational effort, was proposed by Dion et al. [92]. In this so-called vdW-DF the exchange-correlation energy is calculated as

$$E_{\text{xc}} = E_{\text{x}}^{\text{GGA}} + E_{\text{c}}^{\text{LDA}} + E_{\text{c}}^{\text{nl}}, \quad (2.51)$$

where $E_{\text{x}}^{\text{GGA}}$ is the GGA exchange energy. In the original proposed vdW-DF the revised PBE functional from Zhang and Yang (revPBE) [93] was used. The correlation energy is divided into $E_{\text{c}}^{\text{LDA}}$, which accounts for the local correlation energy obtained with LDA, and a non-local correlation energy E_{c}^{nl} that accounts approximately for the non-local electron correlation effects. The expression for E_{c}^{nl} is based on electron densities interacting via a model response function. However, the particular form of E_{c}^{nl} is still a subject of research [94, 95]. In the originally proposed derivation [92], the starting point is the correlation energy in the ACFDT formalism and (after some tricky algebra) E_{c}^{nl} can be expressed as a simple double space integral

$$E_{\text{c}}^{\text{nl}}[n(\mathbf{r})] = \frac{1}{2} \int d^3r_1 d^3r_2 n(\mathbf{r}_1)n(\mathbf{r}_2)\phi(q_1, q_2, r_{12}), \quad (2.52)$$

where $\phi(q_1, q_2, r_{12})$ is a function depending on $r_{12} = |\mathbf{r}_1 - \mathbf{r}_2|$ and a universal function $q_0[n(\mathbf{r}), |\nabla n(\mathbf{r})|]$ evaluated at \mathbf{r}_1 and \mathbf{r}_2 . The form of ϕ should guarantee that (i) for

a system with constant density E_c^{nl} is zero, and (ii) a correct r^{-6} dependence of the interaction energy for large separations r [96]. For a detailed derivation and the exact expression of ϕ , see Ref. [92].

First implementations of vdW-DF were not accurate enough with errors of ≈ 60 meV for the S22 dataset⁸ [97] compared to CC data [98]. Since the interaction energies obtained with vdW-DF depend on the incorporated exchange functional one can simply try to improve the resulting energies by choosing an optimum exchange functional. In doing so Klimeš et al. [94, 99] proposed three new functionals “optPBE-vdW”, “optB88-vdW” and “optB86b-vdW” with significantly lower errors in interaction energy. Because the “optB88-vdW” and “optB86b-vdW” functionals are employed in this work, the optimization procedure leading to this functionals is summarized in the following.

Klimeš et al. [94] considered various alternative GGA functionals for the exchange functional E_x^{GGA} in Eq. (2.51). They observed that in contrast to revPBE-vdW⁹, PBE-vdW systematically overbinds the dimers in the S22 dataset. The different performances for various functionals can be understood by analyzing the enhancement factors of PBE and revPBE.

The exchange energy density for GGA is given by

$$\epsilon_x(n, s) = \epsilon_x^{\text{LDA}}(n)F_x(s), \quad (2.53)$$

where $\epsilon_x^{\text{LDA}}(n)$ is the LDA exchange energy density and the enhancement factor $F_x(s)$ depends on the reduced density gradient $s(\mathbf{r})$

$$s(\mathbf{r}) = \frac{1}{2(3\pi^2)^{1/3}} \frac{|\nabla n(\mathbf{r})|}{n(\mathbf{r})^{4/3}}. \quad (2.54)$$

The enhancement factors of PBE and revPBE differ only in the value of parameter κ in

$$F_x^{\text{PBE}}(s) = 1 + \kappa - \frac{\kappa}{1 + \frac{\mu s^2}{\kappa}}. \quad (2.55)$$

The value for κ with revPBE is larger than with PBE leading to a steeper F_x vs. s curve for revPBE than PBE (see Fig. 2.1). Therefore, in regions with low density gradients, e.g. in the center of a molecule, functionals with flat F_x curves (PBE) are preferred, i.e.

⁸The S22 dataset is a set of 22 weakly interacting dimers which is mostly of biological importance.

⁹A combination of an exchange functional X with vdW correlation is denoted X-vdW in Ref. [94] and also used throughout this work.

the interaction is stronger for PBE than for revPBE (see Ref. [100] for a more detailed discussion). In the following, an exchange functional with a κ value between the extrema of PBE (underbinding) and revPBE (overbinding) was shown to reduce the mean absolute deviations (MAD) to 21 meV with respect to the reference data for a S22 set. Furthermore, by varying both, κ and μ the MAD could be further reduced to 15 meV yielding the optPBE-vdW functional.

The B88-vdW functional (proposed by Becke in 1988 [101]) performs slightly better than revPBE in terms of MADs for the S22 set but outperforms in the mean deviation of hydrogen bonded and dispersion bonded subsets. The exchange enhancement factor for the B88 functional can be written as

$$F_x^{\text{B88}}(s) = 1 + \frac{\mu s^2}{1 + \beta s \operatorname{arcsinh}(cs)}, \quad (2.56)$$

with a constant c and parameters μ and β . After the optimization of μ/β the MAD could be decreased to 10 meV. The functional with the new parameter set is called ‘‘optB88’’.

In a more recent paper Klimeš et al. [99] proposed a new functional based on the B86b functional by Becke from 1986 [102]. The goal was to find a functional that is less repulsive than revPBE, which is assured if F_x rises less steeply for small s . In addition, for large s it should have a $s^{2/5}$ behavior to give binding curves similar to Hartree-Fock [103]. This requirements are fulfilled for the optB86b-vdW functional with an exchange enhancement factor $F_x^{\text{B86b}}(s)$

$$F_x^{\text{B86b}}(s) = 1 + \frac{\mu s^2}{(1 + \frac{\mu s^2}{\kappa})^{4/5}}, \quad (2.57)$$

with $\mu = 0.1234$ leading to similar MAD as for optB88-vdW. The exchange enhancement factors for different functionals are compared in Fig. 2.1. The optimized functionals are less steep for small values of s and keep rising for large s . Functionals with steeply increasing F_x for small s are more repulsive than functionals with F_x less steep or flat (LDA). A flat F_x curve for large s leads to a more attractive functional. Therefore, the least repulsive functional is optB86b-vdW, followed by optB88-vdW and optPBE-vdW. In the asymptotic region on the other hand, optPBE-vdW is more attractive than optB86b-vdW, and optB88-vdW¹⁰. In general the vdW correlation overestimates the interaction for long range. This effect is thus reduced by using the optB88-vdW exchange.

¹⁰This trends in interaction energies are also observed for graphene on Ni(111), see Fig. 3.4.

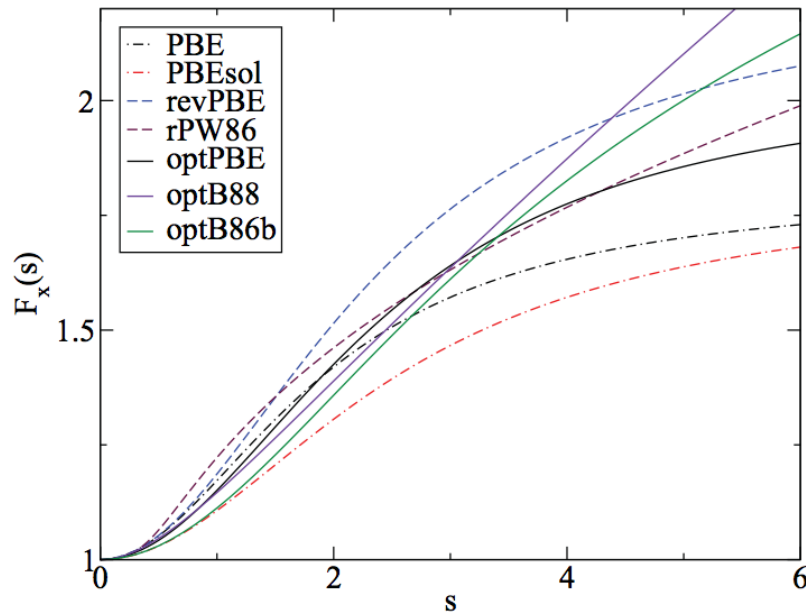


Figure 2.1: Exchange enhancement factors F_x as a function of the reduced gradient density s for different functionals. PBE, PBEsol, and revPBE share the same functional forms but have different parameters. The three functionals “opt” were optimized for the use with vdW correlation. The optimized functionals rise less steeply for small s than the original functionals which decreases repulsion for hydrogen bonded systems. Moreover for large s , optB88 and optB86b keep rising which decreases the overestimation of the binding caused by vdW correlation [87]. Taken from Klimeš et al. [99]

The vdW-DF method was implemented in the VASP code by J. Klimeš using the algorithm of Roman-Perez and Soler [96]. Calculations with vdW-DF are only slightly more expensive than regular GGA calculations making them an attractive choice for large system sizes. However, the dependence of the interaction energies on the actual function is unsatisfactory. In practice, one should compare the results of vdW-DF calculations with reference calculations and select a proper functional.

2.10 Quasiparticle Energies in the *GW* Approximation

While DFT has been very successfully applied to obtain ground-state properties such as total energies and structural properties, the Kohn-Sham eigenvalues cannot be directly viewed as quasiparticle energies as measured, e.g. in photoemission spectroscopy. A widely used approach to study quasiparticle energies is a Green's function based method, the *GW* approximation. In order to calculate the Green's function, the non-local and energy dependent self-energy operator is required. In the *GW* approximation [51] only the lowest order in the expansion of the self-energy Σ in terms of the single-particle Green's function G and the dynamical screened Coulomb potential W

$$\Sigma = iGW - GWGWG + \dots \quad (2.58)$$

is used. Therefore, the self-energy in the *GW* approximation is given by

$$\Sigma \approx iGW. \quad (2.59)$$

In practice, first DFT calculations are performed and from the obtained orbitals and eigenvalues a first guess of the Green's function G_0 and of the potential W_0 is constructed. In the next step, the self-energy $\Sigma = iG_0W_0$ can be used to calculate a new Green's function in a Dyson equation, which is then the input for a new self-energy and so forth, until self-consistency is reached. However, often one stops after the first iteration, which is known as the G_0W_0 approximation. The band gaps for semiconductors and insulators provided with the *GW* approximation are in good agreement with experimental data [51] and thus improve the systematic underestimation of band gaps predicted with DFT.

Furthermore, the calculated quasiparticle energies allow for a direct comparison of the calculated band structure with experimental angle-resolved photoelectron spectroscopy data.

Part III

Results

Chapter 3

Graphene on Ni(111)

The main results of this chapter were published in Phys. Rev. B, 84, 201401 (2011), *Graphene on Ni(111): Strong interaction and weak adsorption* [43], where the present author contributed to the DFT calculations.

Graphene grown on Ni(111) is a good model system to study the growth and interaction of graphene on a transition metal substrate, because the lattice mismatch between graphene and the nickel substrate is small. Therefore, graphene usually grows epitaxially in 1×1 structures on the nickel substrate, keeping additional strain-induced contributions small and makes it easy to model with periodic slabs, in contrast to weakly interacting systems with large moiré unit cells. Consequently adsorption, interaction and changes in the electronic structure have been already the subject of quite a few theoretical studies [37, 42, 104–107].

The potential usage as spin-filtering devices boosted the interest in Gr/Ni(111) even more. Karpan et al. [108, 109] predicted an ideal spin-filtering for interfaces between graphite and (111) face-centered cubic (fcc) or (0001) hexagonal close-packed (hcp) Ni or Co. The effectiveness of spin-filtering was tested in a current-perpendicular-to-the-plane configuration for a ferromagnet|Gr_{*n*}|ferromagnet sandwich-like structures with *n* graphene layers. The prerequisite for the spin-filter effect is an almost perfect lattice match so that they share a common two-dimensional reciprocal space. However, the striking point is the unique overlap in the reciprocal space for only one spin direction (Fig. 3.1). In graphene or graphite, the only states at or near the Fermi surface are at the corners of the hexagonal Brillouin zone where Co and Ni have states of minority spin character only.

For only one graphene layer, the strong Gr-metal interaction will partially quench the spin-filtering effect in the sandwich-like structure. However by using other combination of ferromagnetic materials, a sizeable effect is predicted [110].

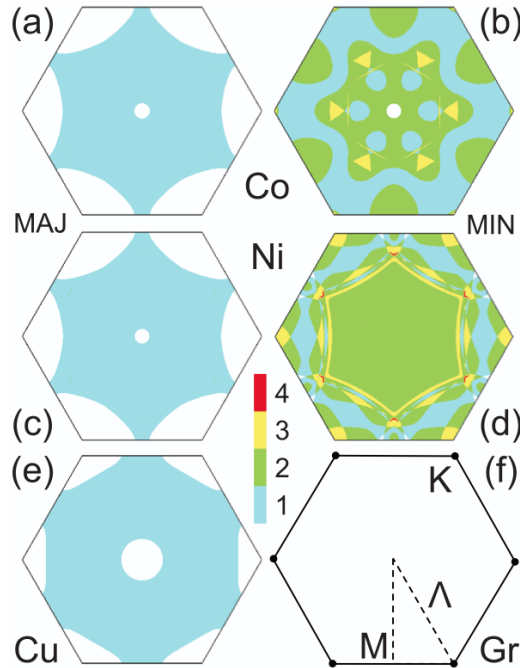


Figure 3.1: Fermi surface projections onto the (111) plane for (a,b) fcc Co majority and minority spins, (c,d) fcc Ni majority and minority spins and (e) for fcc Cu. For graphene and graphite (f), the constant-energy surface is reduced to a single point, i.e. the K -point. Taken from Karpan et al. [108]

Graphene on Ni(111) is difficult to treat from a theoretical point of view. Both, an accurate description of the metallic surface and the nonlocal correlation effects is needed. Several authors have investigated this system with standard DFT approaches [42, 104–106] where the vdW contributions are completely neglected. A gradient-corrected GGA exchange-correlation functional yields too repulsive energy vs. distance curves with a local minimum corresponding to endothermic, i.e. no bonding. The LDA approximation yields a minimum at approximately the correct distance but with completely wrong long-range asymptotic behavior and to strong binding (see section 3.1.3). Furthermore, even the recently proposed vdW-DF [92] fails to predict an appropriate structure for the graphene-metal interfaces. In a recent paper, Hamada and Otani showed that the

originally proposed vdW functionals (vdW-DF, vdW-DF2) also lead to no binding at all [111].

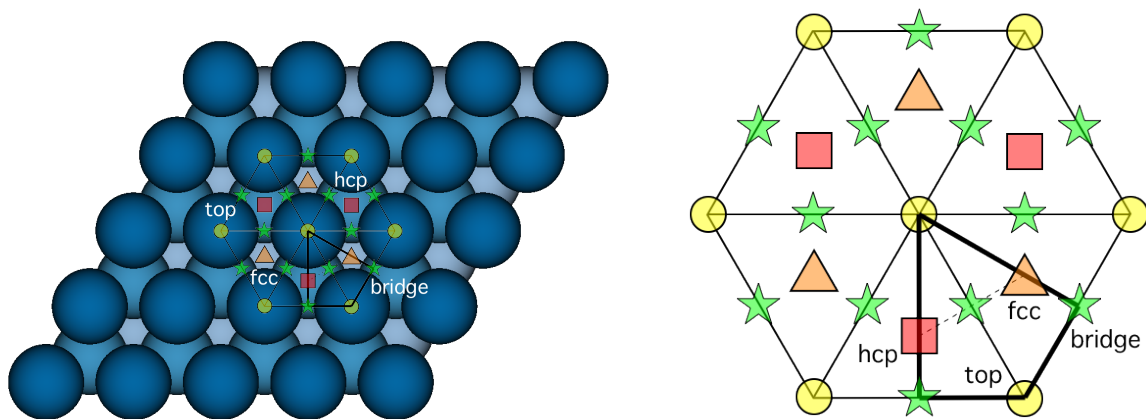
Although the use of recently proposed vdW-DF exchange functionals leads to more reasonable results, the wide spread of the computed adsorption energies using different functionals underlines the need for a reference calculation. Benchmark calculations for Gr/Ni(111) using the adiabatic-connection dissipation-fluctuation theorem (ACFDT) in the random-phase approximation (RPA) are presented in this chapter and are compared to computationally cheaper vdW functionals.

3.1 Structure of Gr/Ni(111)

3.1.1 State of the Art

The “high-symmetry” adsorption sites for an adatom on a fcc(111) surface are shown in Fig. 3.2. For a single adatom the three-fold coordinated fcc and hcp “hollow” sites are usually the most stable adsorption positions. The adatom is at an fcc-site, when it continues the fcc stacking sequence ABCABC and is therefore above a substrate atom of the third layer. If it breaks up the fcc stacking sequence and is instead above a substrate atom of the second layer, the adsorption configuration is the so-called hcp-site. A position directly above a substrate atom, which has only one-fold coordination, is commonly referred as top-site. The two-fold coordinated bridge site is located in the middle of two adjacent top-sites what is equivalent to the middle of an fcc and hcp-site (Fig. 3.2).

With respect to Gr/Ni(111), two adsorption sites per unit cell are occupied by carbon atoms. First, there are the three “high-symmetry” configurations: top-fcc, top-hcp, and hcp-fcc (Fig. 3.3a, 3.3c, and 3.3e), where e.g. top-fcc means that one carbon atom is on the top-site and the other one on the fcc-site. Three additional “low-symmetry” configurations were considered by Fuentes-Cabrera et al. [106], which were labeled bridge-top, bridge-fcc and bridge-hcp by the authors (Fig. 3.3b, 3.3d, and 3.3f). In these structures, the carbon atoms are not placed at hollow or top sites, but in the center of two of these sites, respectively. However, only the center of hcp and fcc is the before mentioned bridge-



(a) Hexagonal fcc(111) surface structure with adsorption sites

(b) Enlarged figure of adsorption positions from (a)

Figure 3.2: Adsorption sites on a fcc(111) surface with marked adsorption sites top, fcc, hcp, and bridge.

site, the other two are usually not specifically labeled in the literature. The notation might therefore be misleading as there is indeed one atom at a bridge site for bridge-hcp and bridge-fcc, but none for the bridge-top configuration. The notation rather indicates that the middle of a C-C bond (the bridge) is located above a top, hcp, or fcc-site for bridge-top, bridge-hcp, and bridge-fcc, respectively.

Different stable adsorption positions for Gr/Ni(111) were proposed in experimental as well as theoretical studies (table 3.1). From a theoretical point of view, Bertoni et al. [104] as well as Kalibaeva et al. [105] performed DFT-PBE calculations, which yielded the top-fcc structure as the most stable configuration. However, Fuentes-Cabrera et al. [106] showed that for the PBE functional, hcp-fcc is the only stable structure. They included three additional “low symmetry” configurations bridge-top, bridge-hcp, and bridge-fcc and surprisingly found bridge-top to be the most stable one for using LDA. While Khomyakov et al. [42] did not include bridge configurations and got top-fcc as the favorite geometry, Zhao et al. [107] performed a combined high-resolution X-ray photoelectron spectroscopy (HR-XPS) and DFT study to investigate the favorite adsorption position. The latter employed the PBE functional plus dispersion corrections [80] to take care of van der Waals

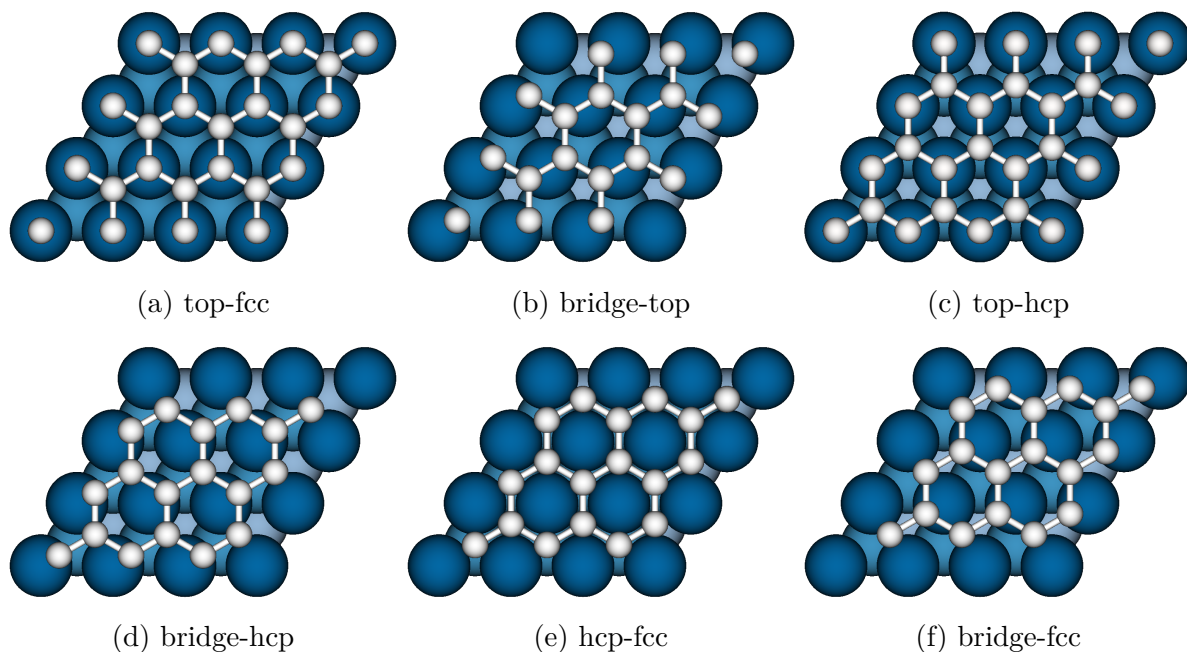


Figure 3.3: Adsorption sites of graphene on Ni(111).

(vdW) interactions. Their calculations again showed that a bridge-top configuration has slightly larger binding energy (BE) than a top-fcc configuration. The favorite adsorption sites could be distinguished by measured and calculated core level (CL) shifts, which suggested a coexistence of both phases with relative fractions probably depending on minor defect concentrations. The most expensive and nowadays state-of-the-art calculation was performed by Mittendorfer et al. [43] in 2011, using ACFDT in the RPA (see section 2.9.2), where the vdW interactions are intrinsically included. The bridge structures were not considered in this study but two minima were found for the top-fcc configuration at 2.17 Å and 3.3 Å corresponding to a chemisorbed and physisorbed state (see section 3.1.3). Also in 2011, Olsen et al. [112] used the same method to study graphene on Ni(111), Cu(111), and Co(0001). For Gr/Ni(111) they did not find two distinct minima but rather a broad flat minimum extending roughly from 2.2 to 3.2 Å. However, their global minimum is located at 3.25 Å with a 8 meV larger BE than at the chemisorption state at 2.3 Å. This discrepancy was solved in a more recent paper of Olsen and Thygesen [37], where they ascribed the divergent results to an insufficient k-point sampling in Ref. [112] and reproduced the two minima found by the present author [43].

From an experimental side, Rosei et al. [113] and Klink et al. [114] assigned hcp-

Ref.	method	site	BE [meV]	$d_{\text{Gr-Ni}}$ [Å]
[113]	SEELFS ^a	hcp-fcc	-	2.80 ± 0.08
[114]	STM ^b	hcp-fcc	-	-
[115]	LEED ^c	top-fcc	-	$2.11/2.16 \pm 0.07$
[104]	GGA-PBE	top-fcc	-	2.122/2.130
[105]	GGA-PBE	top-fcc	-	2.13
[106]	LDA	bridge-top	205	1.95
[42]	LDA	top-fcc	125	2.05
[107]	HR-XPS, PBE ^d	bridge-top (top-fcc)	≈ 130	≈ 2.07
[43]	RPA	top-fcc	67	2.17
[37]	RPA	top-fcc	70	2.19

Table 3.1: Experimental and calculated literature values of the preferred adsorption site, BE, and Gr-Ni distance of Gr/Ni(111).

^a Surface extended energy loss fine structure (SEELFS) spectroscopy

^b Scanning tunneling microscope (STM)

^c Low-energy electron diffraction (LEED)

^d Zhao et al. combined high-resolution X-ray photoelectron spectroscopy (HR-XPS) and dispersion corrected DFT-PBE studies

fcc as the most stable structure, whereas a top-fcc configuration was found by Gamo et al. [115] and Kawanowa et al. [116]. In the early study of Rosei et al. surface extended energy loss fine structure spectroscopy was used, and a bonding distance of $2.80 \pm 0.08 \text{ \AA}$ was determined. This result is in contradiction with DFT results, where the binding distance is around 2.1 \AA for top-fcc and around 3.4 \AA for fcc-hcp (Fig. 3.7) geometries. More recent low-energy electron diffraction (LEED) measurements of Gamo et al. [115] stated a distance of $2.11/2.16 \pm 0.07$, i.e. 2.11 \AA for the nearby carbon atom and a small corrugation of 0.05 \AA . The obtained value of Gamo et al. is in accordance with the theoretical studies.

Thus, a proper functional that takes the vdW interactions into account is crucial to get the correct bonding behavior of Gr/Ni(111). Therefore, the adsorption energies for various functionals are studied in more detail in section 3.1.3 after a summary of the lattice constants for the employed potentials.

3.1.2 Interface Lattice Constants

The lattice constant of nickel bulk a_{Ni} is 3.520 \AA . The lateral analogue for the Ni(111) surface is

$$a_{\text{Ni}}^{\text{lat}} = \frac{a_{\text{Ni}}}{\sqrt{2}} \approx 2.49 \text{ \AA}.$$

The calculated lattice constants for the used potentials in the following discussion are compared with the experimental ones in table 3.2. The calculated values for the graphene lattice constant are in good agreement with the experimental one. However, the LDA lattice constant for nickel is smaller than the experimental one by approximately 3%, which is in agreement with values reported by Fuentes-Cabrera et al. [106]. Usually LDA shows overbinding, i.e. binding and cohesive energies turn out to be too large compared to experiment. This overbinding also leads to lattice constants and bond lengths that are smaller than the experimental values [45]. The PBE lattice constant on the other hand, is in very good agreement with experiment. The effect of Grimme force-field vdW corrections is an additional attractive interaction so that the nickel lattice constant is 1.6% smaller than the experimental one. Both vdW-DF which are implemented in VASP are close to the experimental lattice constant. They also reproduce the experimental

lattice mismatch of 1.30% better than the PBE-Grimme potential, where the graphene lattice constant is 0.6% larger than the nickel lattice constant.

	a_{Gr} [Å]	$a_{\text{Ni}}^{\text{lat}}$ [Å]	$(a_{\text{Ni}}^{\text{lat}} - a_{\text{Gr}}) / a_{\text{Gr}}$ [%]
experimental	2.46 [19]	2.492	1.30
LDA	2.447	2.424	-0.09
PBE	2.468	2.493	1.01
PBE+Grimme	2.468	2.451	-0.07
optB88-vdW	2.463	2.484	0.09
optB86b-vdW	2.465	2.479	0.06

Table 3.2: Experimental and calculated lattice constants of graphene and lateral Ni(111). The lattice mismatch in the last column is very small for Gr/Ni(111).

3.1.3 Adsorption Energies for different Functionals

As discussed in section 3.1.1, previous studies of Gr/Ni(111) suggest that the choice of a proper functional that includes vdW interactions is essential to accurately describe the bonding behavior. In this section a comparison of different functionals is given.

In Fig. 3.4 the adsorption energies as a function of the graphene-nickel distance for certain potentials are shown. The carbon atoms are in a top-fcc configuration, which is one of two favorite adsorption geometries (see section 3.1.4).

In the present work the sign convention by Groß [45] is adopted, meaning that positive adsorption energies, which are equivalent to negative BEs represent repulsion. When PBE is used, the adsorption energy is positive for all distances which represent a repulsive interaction. This would cause graphene not to stick on nickel as already pointed out by Fuentes-Cabrera et al. [106]. Nevertheless, with PBE a local minimum is present at a binding distance of 2.15 Å, which is close to the experimental value of $2.11/2.16 \pm 0.07$ [115], however with an “endothermic” adsorption energy of 20 meV. The PBE functional is therefore an unfortunate choice for this system.

The binding situation is better described with LDA. A distinct minimum is present at

a Gr-Ni distance of 2.00 Å. The BE at the minimum (191 meV) is larger than for any other presented functional, but is still in the range of physisorption, where vdW interactions are important. Despite the small Gr/Ni bonding distance, it is questionable if the adsorption can be viewed as traditional (covalent) chemisorption, because of the small BEs. It should be mentioned that the BE at the LDA lattice constant of nickel is even decreased by a factor of two.

Furthermore, it can be seen in Fig. 3.4 that for the local LDA and semi-local PBE functionals the interaction decays exponentially with distance and has nothing in common with the correct long-range vdW behavior that is expected to be of polynomial form ($C_3 \times 1/d^3 - C_4 \times 1/d^4$) [74]. Clearly, both semi-local and local functionals are missing these vdW like contributions: the deep LDA minimum is a true artifact and related to the wrong decay of the Kohn-Sham potential and orbitals from the surface into the vacuum [43].

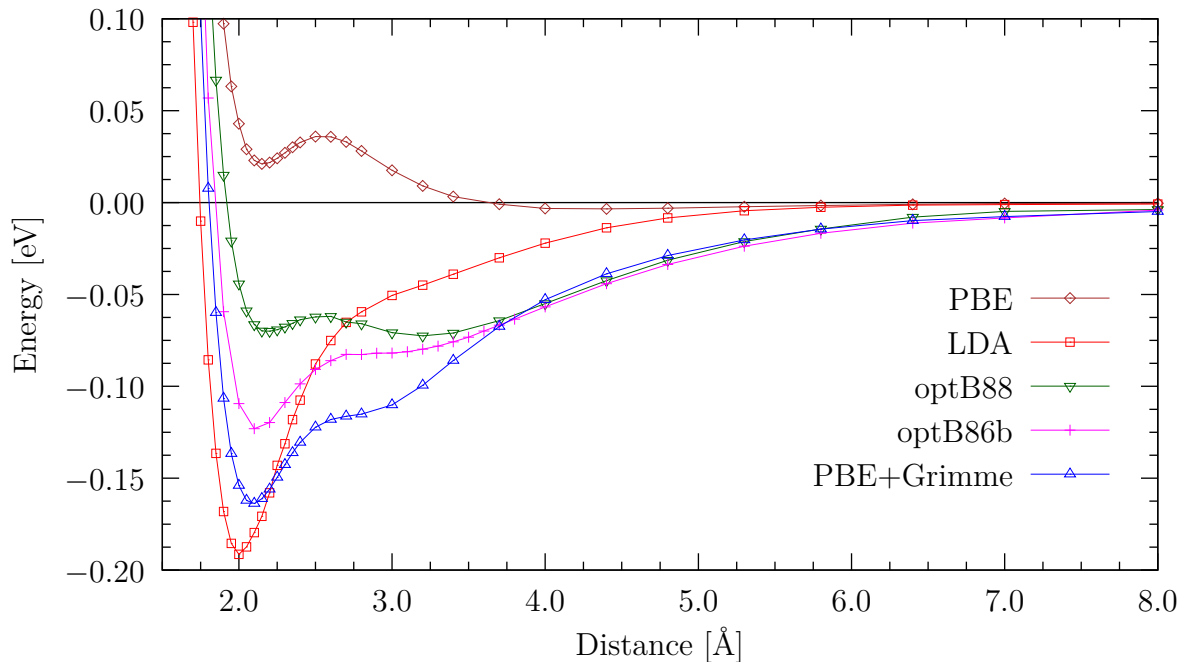


Figure 3.4: Adsorption energy per carbon atom as a function of the Gr/Ni distance for different functionals at the RPA lattice constant of 2.493 Å. The graphene layer is adsorbed at a top-fcc configuration on Ni(111).

There are several approaches to include vdW interactions in the framework of DFT

(see section 2.9). In this thesis, two approaches are used namely the PBE+Grimme (DFT-D2 [78]) and vdW-DF in the flavor of optB88 and optB86b [92], besides RPA calculations performed by F. Mittendorfer [43]. In the DFT-D2 method of Grimme [78], the van der Waals interactions are described via a simple pair-wise force-field, while the vdW-DF proposed by Dion et al. [92] is a nonlocal correlation functional that approximately accounts for dispersion interactions. There are multiple proposed versions of this method in usage, which are compared to the reference RPA calculations [43] in Fig. 3.5 (for details of the ACFDT RPA method see section 2.9.2). The original functionals, vdW-DF and vdW-DF2, lead to a nonbonding behavior in the vicinity of the surface, which was already discussed by Hamada and Otani [111]. The vdW functionals (“opt”), which were recently developed by Klimeš and Michaelides [94, 99], lead to improved binding at short distances. The binding energies at the local energy minima for the optB88-vdW functional are in good agreement with our RPA results. This functional replicates the RPA curves very well. The optB88-vdW is more repulsive at low distances (the repulsive curve on the left of Fig. 3.5 is shifted to the right compared to optB86b-vdW) and optB86b-vdW is more attractive at larger distances. This is due to the construction of the respective functionals (see section 2.9.3 for a detailed discussion). The barrier between the chemisorption and physisorption minima is more pronounced with RPA than optB88-vdW. The binding energies in the chemisorption region are decreased (increased) for the optPBE (optB86b-vdW) functional.

At Gr-Ni distances of more than 4 Å both PBE+Grimme and vdW-DF curves are almost identical with the RPA curve, while they behave differently when graphene is close to the nickel substrate (Fig. 3.4, 3.5). A pronounced energy minimum at 2.1 Å is obtained with PBE+Grimme that is even more pronounced than for optB86b. For these two functionals, instead of a second minimum like for optB88-vdW and RPA, the energy-distance curve is just flattened and no distinct minimum can be detected.

RPA results

The results of our RPA calculations of Mittendorfer et al. [43] are summarized in the following. RPA predicts a weak adsorption at a distance of 2.17 Å with a BE of 67 meV per carbon atom (Fig. 3.5, 3.6). It should be noted that this value is slightly higher than

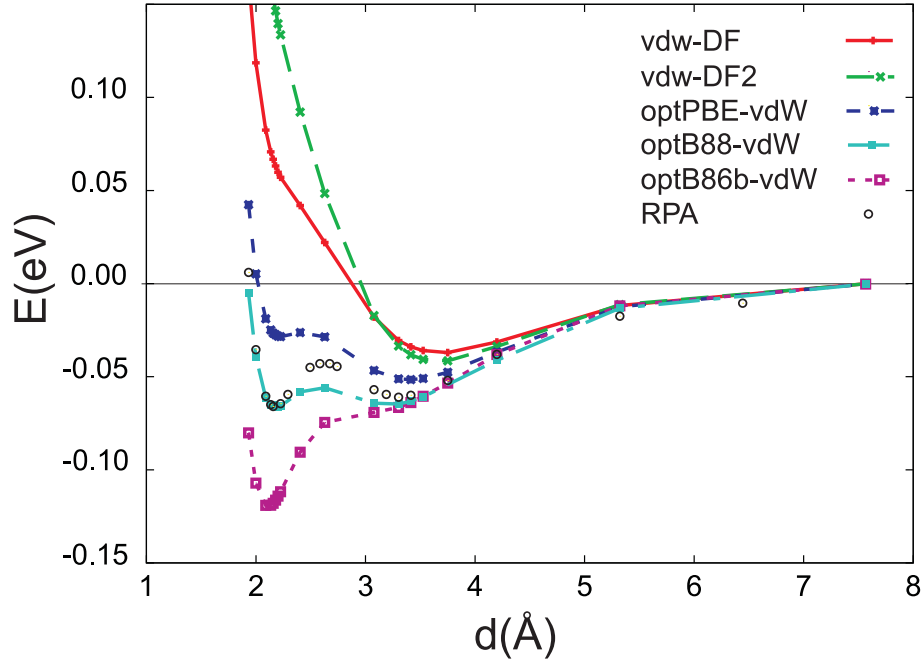


Figure 3.5: Adsorption of graphene on Ni(111) in top-fcc configuration as a function of the exchange-correlation functional. Taken from Mittendorfer et al. [43]

the calculated BE of 48 meV for the graphene sheets in graphite [74], indicating that the graphene sheet will wet the surface, in agreement with experiment. A second minimum at a typical vdW distance for graphene on a transition metal [117], of 3.3 Å is slightly more weakly bound with a BE of 60 meV.

A split-up of the total energy in the correlation and exchange contribution illustrates the origin of the double peak. At large distances down to 2.8 Å, the exchange interaction is purely repulsive (and the band structure is hardly modified, see section 3.2), and the correlation follows essentially a vdW like behavior: the long-range contributions of the correlation energy can be fitted well by a curve following $d^{-3.84}$ (Fig. 3.6, pink line). The value of the exponential is rather close to -4 indicative of a simple additive pairwise interaction between two sheets [74].

At distances shorter than 2.8 Å, the graphene band structure starts to be modified with a hybridization setting in (see section 3.2), and most importantly, with a breakup of symmetry between the top-site and hollow-site carbon atoms. For the related adsorption of graphene on Ir(111), a small hybridization has been predicted even for a slightly larger distance of 3.2 Å, presumably due to the less localized Ir $5d$ -states [11]. The symmetry

reduction by the hybridization abruptly changes the exchange energy (EXX), resulting in a strong interaction even on the level of exact exchange. Part of the reason for this decrease of the exchange energy is that Hartree-Fock prefers a symmetry-broken solution for the free-standing graphene layer, i.e., an insulating charge density wave ground state with disproportionated carbon atoms is preferred over the metallic ground state. Such a charge density wave is induced by the metal slab, lowering the exchange energy. However, correlation restores the correct symmetric ground state for free-standing graphene, and concomitantly on the surface, the correlation rises almost as steeply as the exchange energy decreases. The resulting total energy is smooth, with a slight barrier between the physisorption minimum, characterized by a graphene band structure that is hardly modified compared to free-standing graphene, and the second “chemisorption” minimum, where the graphene band structure is strongly modified compared to the free-standing layer (see section 3.2).

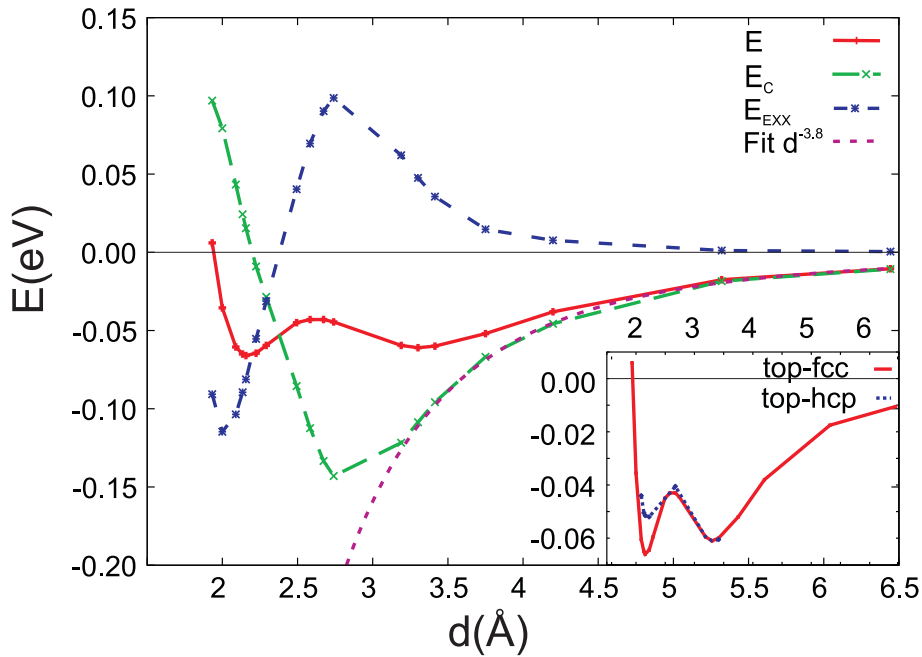


Figure 3.6: RPA adsorption energies for the adsorption of graphene on Ni(111) in the top-fcc (red line) and top-hcp (inset) configuration. The total adsorption energy is separated into the exchange- (blue line) and correlation contributions (green line). The pink line indicates an analytic fit to the long-range correlation contributions. Taken from Mittendorfer et al. [43]

3.1.4 Influence of the Adsorption Configuration

The adsorption energies per carbon atom as a function of the Gr/Ni distance for all six adsorption configurations (Fig. 3.3) are shown in Fig. 3.7. The calculations employ the vdW-DF optB88-vdW at the Ni RPA lattice constant of 2.493 Å, very close to the experimental value of 2.492 Å. This functional mimics the reference RPA calculations best as discussed in section 3.1.3.

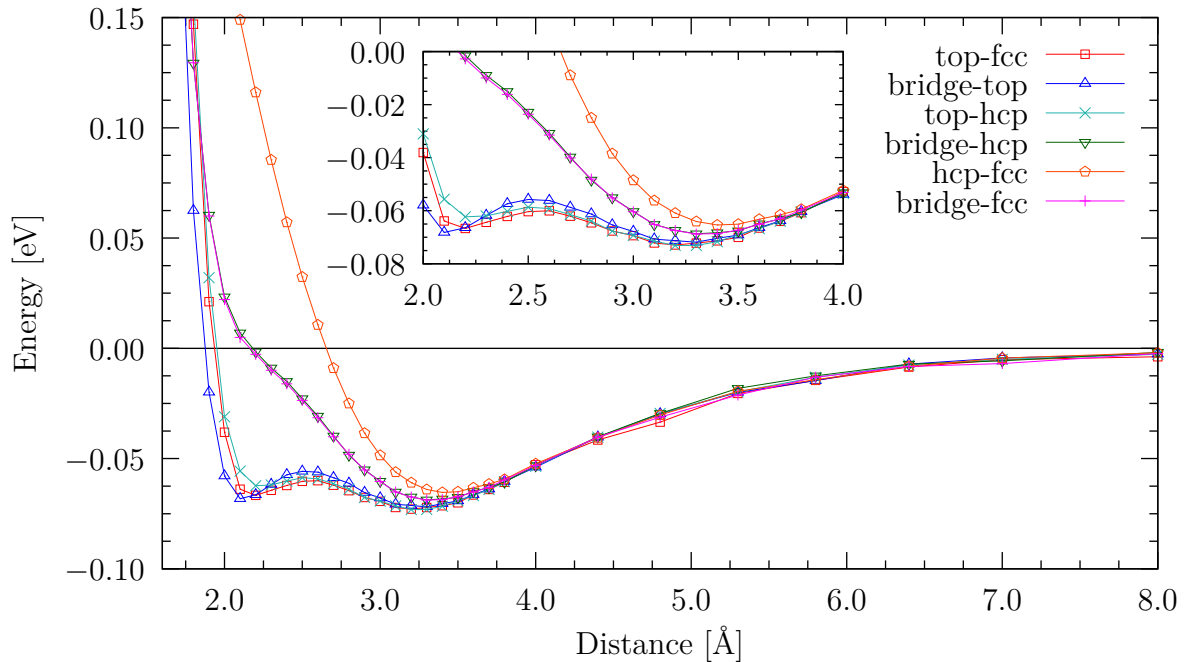


Figure 3.7: Adsorption energy per carbon atom as a function of the Gr/Ni distance for various adsorption sites with the optB88-vdW functional at the RPA Ni lattice constant.

A physisorption minimum at typical vdW distances of about 3.4 Å is present for all configurations, whereas a second minimum at approximately 2.2 eV exists only for the top-fcc, bridge-top, and top-hcp configurations. The adsorption energies for this chemisorption minimum are of the same order of magnitude for all three systems, but the top-fcc valley is slightly smaller. The highest BE is found for the top-fcc arrangement with 71 meV. The bridge-top configuration not calculated with RPA, yields almost the same binding energy as top-fcc.

The physisorption minima for top-fcc, bridge-top, and top-hcp are all at the same level ($\Delta \text{BE} \leq 1$ eV), whereas there are slightly higher BEs at the minimum of the three

remaining configurations, bridge-hcp, hcp-fcc, and bridge-fcc. Notice that the energy-distance curve of the hcp-fcc configuration in the chemisorption range is much steeper than for bridge-hcp and bridge-fcc, which are almost identical due to a similar local adsorption geometry.

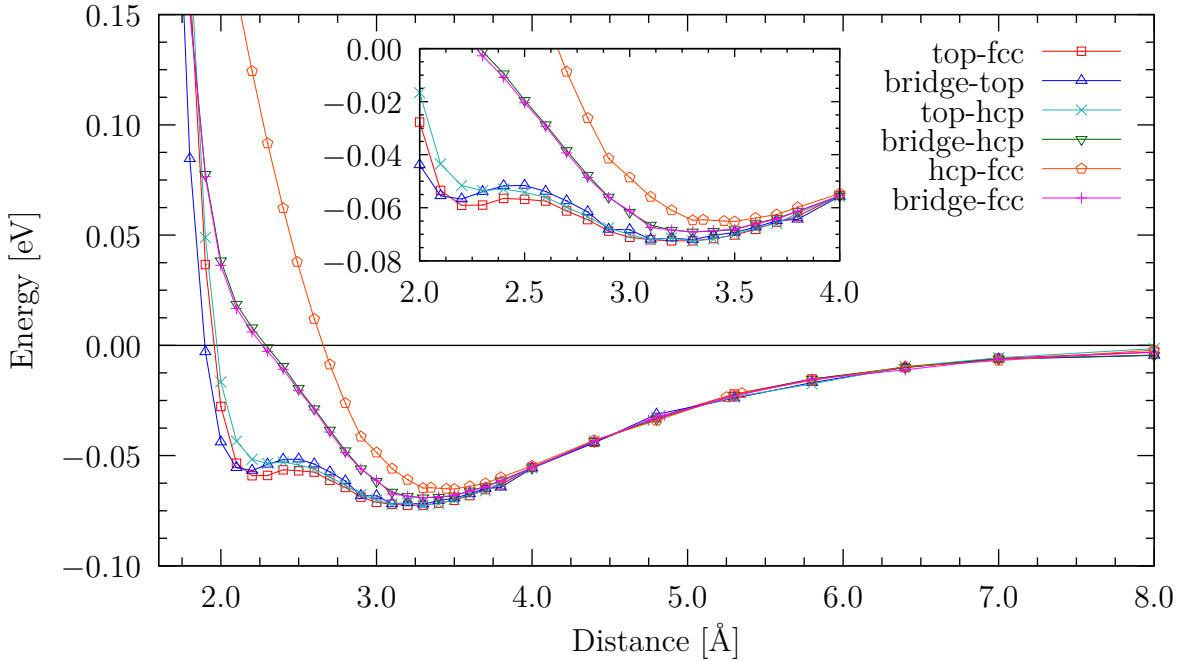


Figure 3.8: Adsorption energy per carbon atom as a function of the Gr/Ni distance for various adsorption sites with the optB88-vdW functional at the optB88 Ni lattice constant.

If instead of the RPA, the optB88-vdW lattice constant is used, a distinct chemisorption minimum is no longer present as illustrated in Fig. 3.8. Although the optB88-vdW lattice constant is only 0.4% smaller than the RPA one, the curves are clearly changing. While the vdW minima are nearly the same, the chemisorption minima are ≈ 11 meV (or 15%) lower in BE.

The adsorption energies as a function of the Gr/Ni separation when graphene is in a top-fcc arrangement was already shown in Fig. 3.4 and is replotted in Fig. 3.9 as well as the respective curves of the other adsorption configurations for the optB86b-vdW functional. The three chemisorption states found for the optB88-vdW functional have a minimum around 2.1 Å also for the optB86b-vdW functional. The highest BE of 126 meV

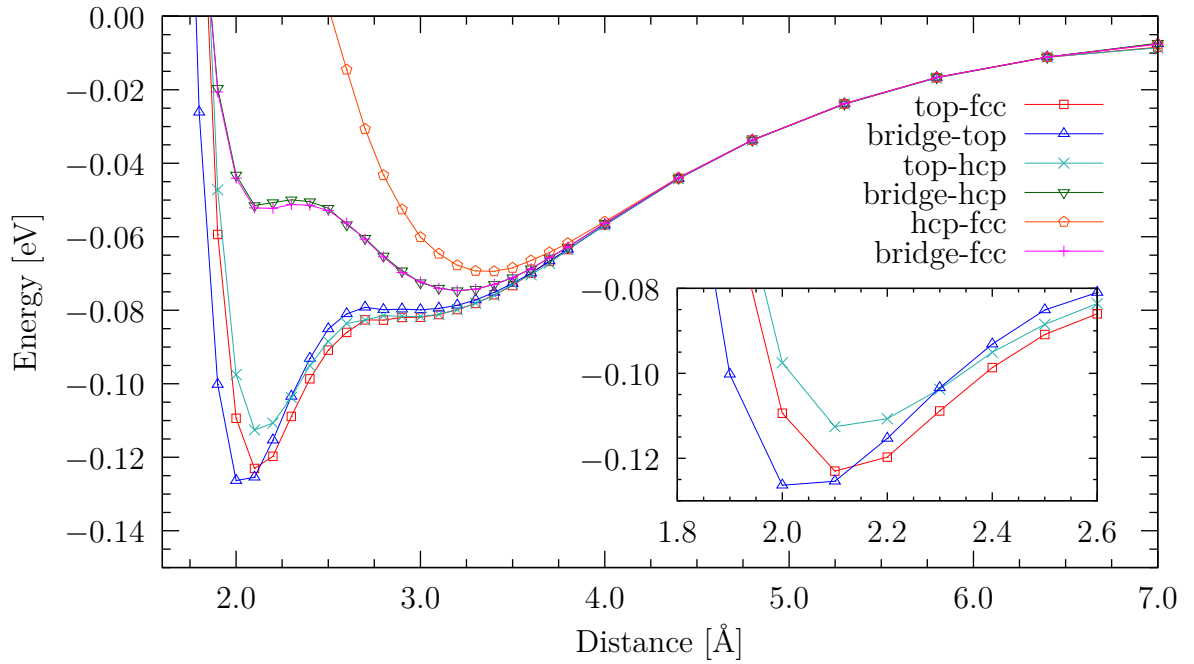


Figure 3.9: Adsorption energy per carbon atom as a function of the Gr/Ni distance for various adsorption sites with the optB86b-vdW functional at the RPA Ni lattice constant.

is reached for the bridge-top configuration at 2.0 Å. While for optB88-vdW, there was a quite linear curve with a small kink at 2.1 Å for bridge-hcp and bridge-fcc at small distances (Fig. 3.7, 3.8), with optB86b-vdW there is a flat region from 2.1 Å to 2.4 Å. It becomes a definite minimum if a larger lattice constant is employed. For the extreme case of using the optB86b-vdW Ir lattice constant which is 9.7% larger than the RPA Ni lattice constant, even the hcp-fcc configuration develops a minimum (Fig. 3.10). This is an unrealistic scenario on its own as the graphene is stretched by 11%, which costs 0.61 eV per carbon atom compared to results with the RPA Ni lattice constant. Nevertheless, the results are useful with respect to nickel intercalated Ir(111) where one monolayer of nickel is stretched to the Ir lattice constant (see section 7). However, due to the strong σ -bonds graphene is not stretched but forms a moiré. The calculations with the Ir lattice constant shows the tendency of stronger adsorption energies at the chemisorption minima in general, and the binding for bridge-hcp and bridge-fcc geometries mimics rather top-fcc, top-hcp and bridge-top, than hcp-fcc in this case. Furthermore, the minima are shifted to smaller Gr-Ni distances: the largest absolute adsorption energy is found for the bridge-top

configuration at 1.90 Å.

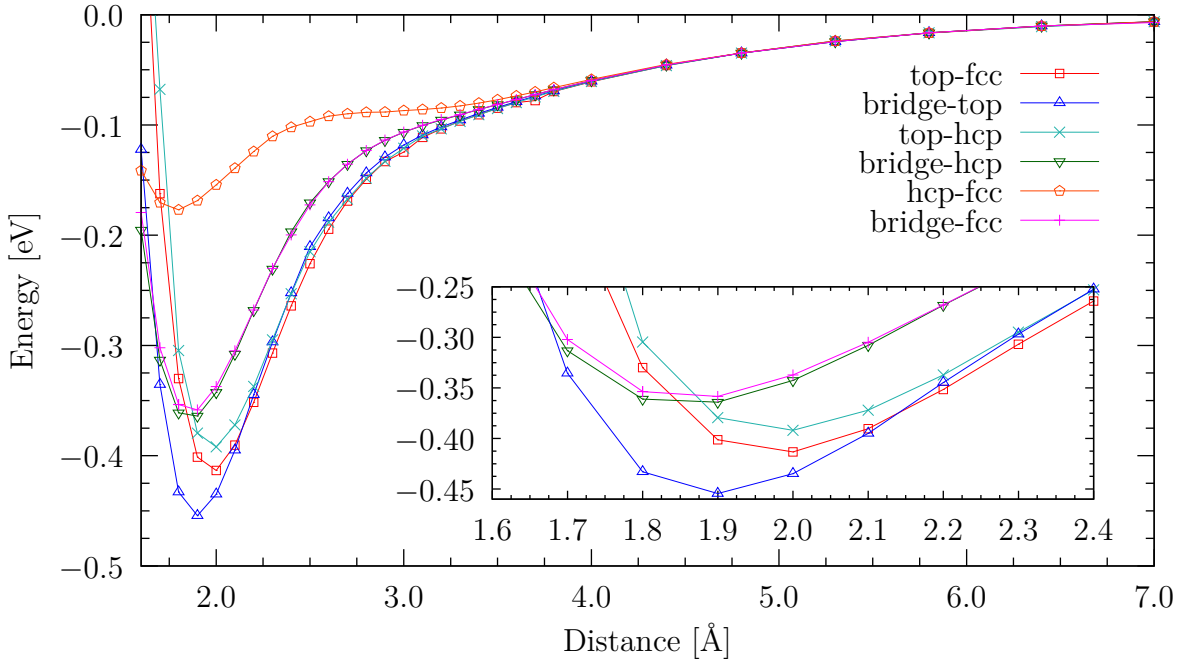


Figure 3.10: Adsorption energy per carbon atom as a function of the Gr/Ni distance for various adsorption sites with the optB86b-vdW functional at the optB86b Ir lattice constant.

3.1.5 Relaxation Effects

No relaxations were allowed for the energy-distance calculations showed in Fig. 3.7-3.10. For each local energy minima an additional calculation where the atoms can relax, are presented in table 3.3. The optB88-vdW functional at the RPA lattice constant is used. The two bottom Ni layers are kept fixed and all other atoms are allowed to relax.

The BEs in table 3.3 show that the relaxation does not change the order of energies, and the BEs are quite similar compared to the unrelaxed calculations. The maximum BEs are found for top-hcp and bridge-top arrangements and differ by only 3 meV. The physisorption and chemisorption minima are practically at the same energy. The BE for top-fcc with RPA is slightly lower (67 meV) [43]. The Gr-Ni distance for all three chemisorbed states are at distances ranging from 2.11 Å to 2.26 Å, which is in good agreement with the RPA results (2.17 Å for top-fcc and top-hcp) [43] and the experimen-

	BE [meV]	$d_{\text{Gr-Ni}}$ [Å]
top-fcc	71	2.20
	73	3.21
bridge-top	72	2.11
	72	3.22
top-hcp	64	2.26
	73	3.20
bridge-hcp	69	3.35
hcp-fcc	65	3.42
bridge-fcc	69	3.34

Table 3.3: BEs and Gr-substrate distance for different adsorption configurations with RPA lattice constant and optB88-vdW functional.

tal value of $2.11/2.16 \pm 0.07$ [115]. The physisorption minima of the also chemisorbed configurations are almost at the same distances (3.20 - 3.22 Å), which is in good agreement with RPA [43] (3.3 Å for top-fcc and top-hcp). The other three configurations, bridge-hcp, hcp-fcc, and bridge-fcc have slightly lower BEs and the equilibrium Gr-Ni distance is larger.

3.1.6 STM Simulation

The STM simulations within the Tersoff-Hamann approach [118] for top-fcc, top-hcp, hcp-fcc, and bridge-top are illustrated in Fig. 3.11. The occupied states in the energy range $E_{\text{F}} - 0.5$ eV to E_{F} are plotted. While for the hcp-fcc and bridge-top configuration both carbon atoms are visible as white spots (smeared out for bridge-top), only one white spot per unit cell is detected for top-fcc and top-hcp. The bright spot for top-fcc (top-hcp) is located at the fcc- (hcp-) site. The symmetry breaking is mirrored in the STM images because of a stronger interaction for the top-site carbon atom with the underneath lying nickel atom which pushes reactant states above E_{F} (see section 3.2). Therefore, it is possible to distinguish between a bridge-top and top-hollow configuration, but it is

not possible to distinguish between top-fcc and top-hcp. Graphene adsorbed in a hcp-fcc configuration has a lower BE and should not be observed in experiments anyway.

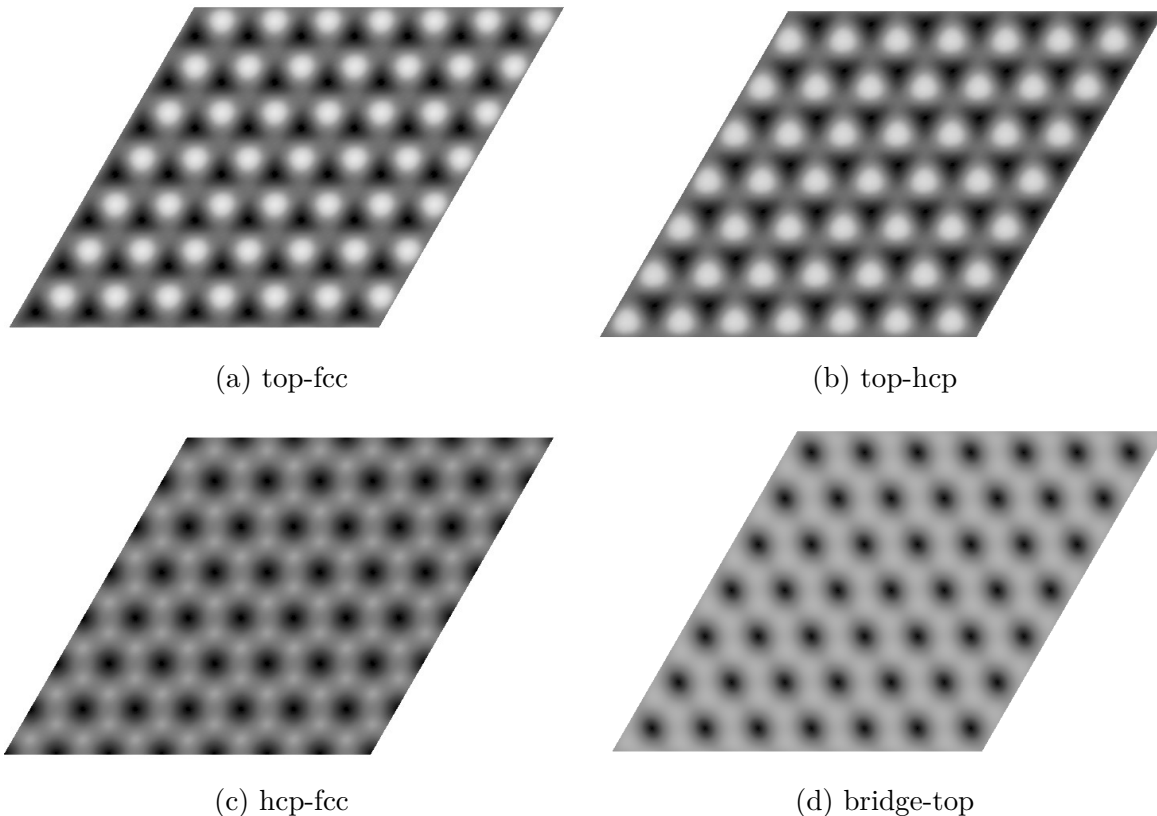


Figure 3.11: Simulated STM image of graphene on Ni(111) in the (a) top-fcc (b) top-hcp (c) hcp-fcc and (d) bridge-top configuration in a 7×7 unit cell.

3.2 Band Structure

The bonding at short Gr-Ni distances indicates a strong covalent interaction, which is reflected in the band structure already on the level of semi-local functionals. The PBE band structure for graphene in the top-fcc configuration on Ni(111) projected at the carbon atoms is shown in Fig. 3.12a. At a distance of 2.1 Å a pronounced band-splitting of the π -bands (green dots) at the (Dirac) K -point is observed, while the lower-lying σ -bands remain unchanged compared to free-standing graphene. A similar nonrigid downward shift was observed also in previous studies [39, 104, 119, 120]. The interaction between graphene and nickel layers implies a hybridization of the graphene π -bands with the nickel

d -bands. In the graphene band structure there are only two states at the Dirac point. Since the symmetry is broken, the double degeneracy of the π -band is lifted as well and four states near the Fermi energy appear. A similar splitting is also observed for the interaction of graphene with, e.g. Ru surfaces [121].

The energies of the calculated states for Gr/Ni(111) are compared with literature data in table 3.4. The main contribution of the two lower bands can be related to the fcc carbon p_z minority state at -2.9 eV. It is the bonding state between the fcc hollow carbon and the interface nickel atom and corresponds to the interfaces state I_1 described by Bertoni et al. [104] and the experimentally found state at -2.9 eV, -2.8 eV, and -2.65 eV, respectively (table 3.4). The top site carbon p_z orbitals interact strongly with the nickel states (predominantly d_{z^2} , d_{xz} and d_{yz}) leading to strong bonding resonance at -2.2 (-1.9) eV for the majority (minority) state at the Dirac points. This state can be assigned as the I_2 state [104] and the experimentally found state at -1.6 eV to -1.7 eV (table 3.4). The hollow site carbon p_z also exhibits an anti-bonding state close to the Fermi-level at -0.3 ($+0.2$) eV for majority (minority) states. Using a many-electron (G_0W_0) approach, only a small shift of the bonding states to values of -2.5 (-1.9) eV for the top C atoms and -0.7 ($+0.3$) eV for the hollow atoms is predicted [43]. The density functional theory predictions are very accurate in this case. The values obtained by experiment for occupied states near the Fermi-level (-0.15 to -0.7 eV) are in good agreement with the calculated energies.

The strong hybridization of carbon p_z and nickel d -states are clearly related to the vicinity to the surface, as moving the graphene layer to a larger distance of 3.0 Å restores the band structure of free standing graphene with the usual crossing of the π -bands at the Fermi level (Fig. 3.12a, bottom). Previous DFT calculations showed, that for a hcp-fcc configuration with a Gr-Ni distance of $3.1/3.3$ Å, graphene bands are restored indicating a small graphene-substrate interaction. Only a small downward shift of the graphene bands with respect to E_F , and a small upward shift of the nickel surface state was observed [104, 108].

The differential charge density induced by the adsorption at the chemisorption minimum is shown in Fig. 3.12b. Due to the strong hybridization between top site carbon p_z orbitals and nickel d_{z^2} orbitals, the nickel d_{z^2} orbitals are partly pushed above the

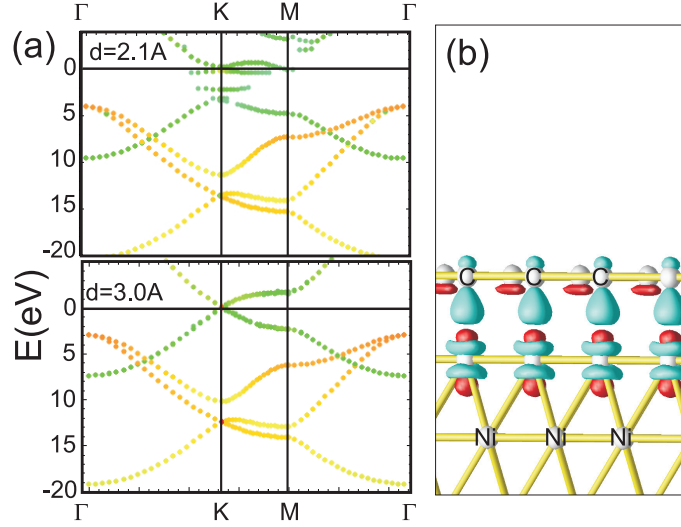


Figure 3.12: (a) PBE band structure of graphene/Ni(111) at a distance of 2.1 Å and 3.0 Å projected at the carbon atoms. (b) Differential charge induced by the adsorption of graphene on Ni(111) for a distance of 2.1 Å: blue (red) areas mark an increase (decrease) of the charge density. No significant changes in the differential charge distribution can be observed at a distance above 3 Å. Taken from Mittendorfer et al. [43]

(*)		Bertoni et al. [104]		Experimental				
Spin ↑	Spin ↓	Spin ↑	Spin ↓	[119]	[39]	[120]		
fcc	-0.3/-0.7 ¹	0.2/0.3 ¹	fcc (I ₃)	-0.2	0.18	-0.6	-0.2	-0.15
top	-2.2/-2.5 ¹	-1.9/-1.9 ¹	top (I ₂)	-2.4	-1.96	-1.7	-1.6	-0.7
fcc	-3.2 ²	-2.9	fcc (I ₁)	-3.37	-3.24	-2.9	-2.8	-1.65
top	-3.4 ²	-3.1 ²						-2.65

Table 3.4: Energies in eV of graphene states close to the Fermi energy at the K -point of the Brillouin zone.

(*) Augmented analysis of Mittendorfer et al. [43]

¹The second value is obtained with the many-electron (G_0W_0) approach.

²Only small contributions.

Fermi-level resulting in a depletion of charge in the nickel d_{z^2} states (graphene-surface anti bonding linear combinations), and an increase of the charge density on the carbon p_z orbitals (graphene-surface bonding linear combinations at -2.0 eV). There is a slight loss of charge from the fcc carbon p_z orbitals induced by the minority fcc carbon p_z orbitals being pushed above the Fermi-level to $+0.2$ eV, and an increase of charge on the nickel d_{xz} and d_{yz} orbitals.

The interaction is reminiscent of classical molecule-surface interaction, to some extent. There is the (back-)donation from the surface nickel d_{z^2} states into the top-site carbon p_z orbitals on one hand, and the hollow-site carbon p_z orbitals donate charge to the nickel d_{xz} and d_{yz} states, on the other hand. However the second interaction is fairly weak for sterical reasons. The donation to the surface nickel d_{xz} and d_{yz} orbitals is mainly necessitated by the requirement of charge neutrality for the graphene sheet. In fact, a Bader analysis shows that the net charge flow from the surface to graphene is zero [43]. The weak hybridization of the hollow-site carbon atoms with the surface could be a reason for the small total interaction energies. The nickel d_{xz} and d_{yz} states are pushed to lower energies (below the Fermi-surface) as a result of electrostatics related to the loss of charge on the nickel d_{z^2} states [43].

3.3 Computational Methods

The presented calculations were performed with the Vienna Ab Initio Simulation package (VASP) [62, 63] using the PAW method [70]. Ni $3s$ and $3p$ -electrons were included for the RPA calculations. The Ni(111) surface was modeled by a slab consisting of five layers and a vacuum width of ≈ 14 Å thickness. The RPA calculations of Mittendorfer et al. [43] were performed at an RPA lattice constant of 3.526 Å, which is very close to the experimental value of 3.524 Å. The lattice constants used in other calculations is given in the respective sections. The Brillouin zone integration was done on a $19 \times 19 \times 1$ k-point mesh for RPA and on a $15 \times 15 \times 1$ for all other calculations. Further technical details concerning the RPA method can be found in Schimka et al. [122] and Harl et al. [90]

3.4 Conclusion

Ab initio studies of graphene on ferromagnetic Ni(111) show that PBE and LDA disagree significantly about the trend in BEs. While PBE leads to no binding at all, LDA finds a minimum at 2.0 Å. However, both functionals are (semi-)local and are missing vdW interactions, which are crucial for a correct description of Gr-metal interactions. An explicit evaluation of the correlation energy in the framework of the ACFDT in the RPA leads to a natural inclusion of the nonlocal vdW contributions. The most remarkable result gained from the RPA calculations is the presence of two minima, one at a typical physisorption distance of 3.3 Å, and a second chemisorption minimum at 2.17 Å. The analysis of the interaction indicates that the common concepts of adsorption cannot be applied to this system, as we observe both, strong signs of chemisorption at short distances, but also an adsorption energy that remains in the typical range of weak physisorption. The broken symmetry induced by the adsorption of the graphene layer on Ni(111), e.g. for a top-fcc adsorption configuration, results in a decreased exchange energy at shorter distances. The small BEs are related to the lack of an efficient hybridization mechanism for donation of charge from the carbon overlayer to the surface, for instance via the hollow-site carbon p_z orbitals. Band structure calculations show a strong hybridization in the chemisorption regime but almost intact graphene bands at typical vdW adsorption distances.

The use of the accurate RPA data allows to assess the quality of the computationally significantly cheaper vdW-DF functionals. The long-range behavior is in accordance with the RPA curves for both, PBE+Grimme (DFT-D2) and the vdW-DF calculations. In the short range the optB88-vdW results are in best agreement with the RPA calculations, making this vdW functional a promising choice for the treatment of larger systems. Within the computationally demanding RPA approach only the two top-hollow configurations are considered, where top-fcc has a bit higher binding energies than top-hcp. More adsorption configurations are analyzed with optB88-vdW and optB86b-vdW functionals, yielding top-fcc and bridge-top as the favorite adsorption configurations and top-fcc with slightly lower BEs, whereas for hcp-fcc, bridge-hcp, and bridge-fcc only physisorption minima are present. However, the actual BEs strongly depend on nickel lattice constant and the specific functional.

Chapter 4

Defect Structures and Defect Healing of Nickel-supported Graphene

The main results of this chapter were published in *J. Phys. Chem. Lett.*, 3, 136 (2012), *Disorder and Defect Healing in Graphene on Ni(111)* [123], where the present author performed the DFT calculations.

In previous chapters, only perfect graphene and nickel structures were considered which can be described by a two-dimensional periodic lattice. The atoms occupy sites determined by repeating fixed distances as given by the two-dimensional unit cell. However, most real materials are not perfectly periodic, but rather the regular patterns are interrupted by crystallographic defects [124]. Point defects are defects that occur only at or around one single lattice point and are not repeated in space in any dimension. In this chapter, two types of point defects are studied: single vacancies (SV) and Stone-Wales (SW) defects, first for free-standing graphene and secondly, for nickel-supported graphene. It will be shown that with aid of the nickel support, diffusion barriers are decreased so that the healing of defects is facilitated.

Defects in Graphene

A recent review article of Banhart et al. [125] gives an overview of structural defects in graphene. According to Banhart, it is intuitively clear that defects associated with dangling bonds should enhance the reactivity of graphene. Indeed, numerous simulations indicate that hydroxyl, carboxyl, or other groups can easily be attached to vacancy-type defects. The controlled creation of defects can be used, e.g. for the local functionalization of graphene samples, the development of electrical contacts with metal electrodes, and for the creation of graphene ribbons with the designed properties by various chemical methods [125].

The electronic properties of graphene are affected by defects and bond lengths in the strain field of defects are altered. Defects can lead to a local rehybridization of σ and π -orbitals which further changes the electronic structure. A local deformation of the graphene lattice around defects influences the rehybridization as well. In summary, all defects lead to scattering of the electron waves and change the electron trajectories [126, 127].

4.1 Single Vacancies

The simplest type of a defect is a single vacancy – a missing carbon atom at one specific lattice point. SVs have been observed via transmission electron microscopy (TEM) [128, 129] (Fig. 4.1a), and STM measurements [130]. Point defects give rise to localized states near the Fermi energy in sp^2 -bonded materials like graphene, leading to the protrusions that appear bright in STM images [130] (Fig. 4.1c).

First the single vacancies are studied on free-standing graphene. In pristine graphene there are two equivalent carbon atoms in the unit cell. To create a SV any of the carbon atoms is replaced by a hole. To model a single vacancy in graphene, larger supercells must be used instead of the regular 1×1 unit cell. For two-dimensional systems, one simply repeats the two-dimensional unit cell in the two lateral directions. On the one hand the supercell must be large enough to minimize the defect-defect interactions and to allow the system to relax the atoms close to the defect. On the other hand it must be small enough

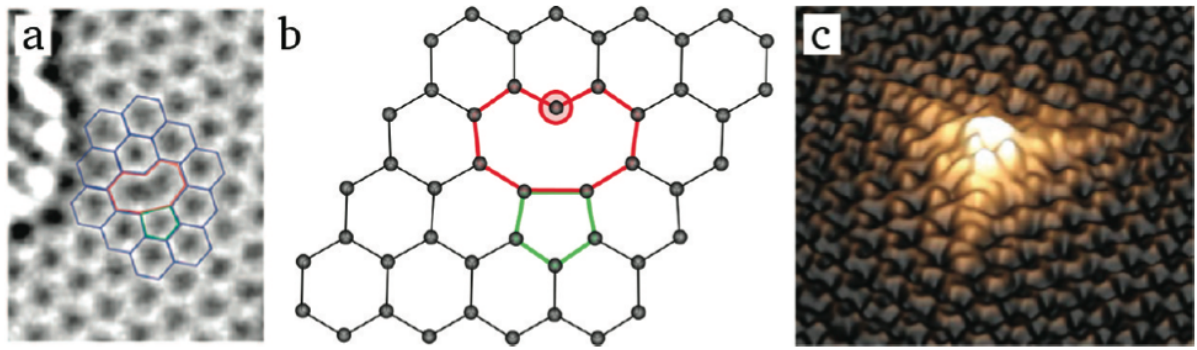


Figure 4.1: (a) Single vacancy as seen in an TEM image, taken from Meyer et al. [128]; (b) atomic structure obtained with DFT, taken from Banhart et al. [125]; (c) experimental STM image of an artificially generated SV, appearing as a protrusion due to an increase in the local density of states at the dangling bond (marked with a circle in panel b), taken from [130].

to make the system computationally treatable in reasonable time. Usually 5×5 cells, as used in this section, are a good compromise between these two requirements [131]. However, the convergence of the calculations depends on the particular system and computational details and must be checked for each calculation.

Three different structures are compared in the following. First, all atomic positions are fixed at the positions of the ideal graphene lattice with one carbon atom removed. In the second and third case, the atoms are allowed to relax. A metastable symmetric configuration is found for the second case. Earlier theoretical studies found a symmetric structure where the three carbon atoms next to the vacancy each move away by 0.4 \AA [132] or move symmetrically closer to the vacancy [133], although the possibility of a Jahn-Teller (JT) distortion¹ for SVs in graphite was already put forward in 1963 [135]. Indeed, the asymmetric third configuration (Fig. 4.2) due to JT distortion is the preferred configuration in our calculations, in agreement with more recent studies [125, 136, 137]. Due to the JT distortion two of the three dangling bonds pointing toward the missing atom are saturated. The one remaining dangling bond, shows a local magnetic moment of $0.52 \mu_B$.

¹The theorem named after H. A. Jahn and E. Teller states that any nonlinear molecule with a spatially degenerate electronic ground state will undergo a geometrical distortion that removes that degeneracy, because the distortion lowers the overall energy of the species [134].

The magnetic moments can be identified by the color code in Fig. 4.2 and shows that the atom with the dangling bond is the only one contributing effectively to the total magnetic moment of the magnetic solution as found first by Ma et al. [138].

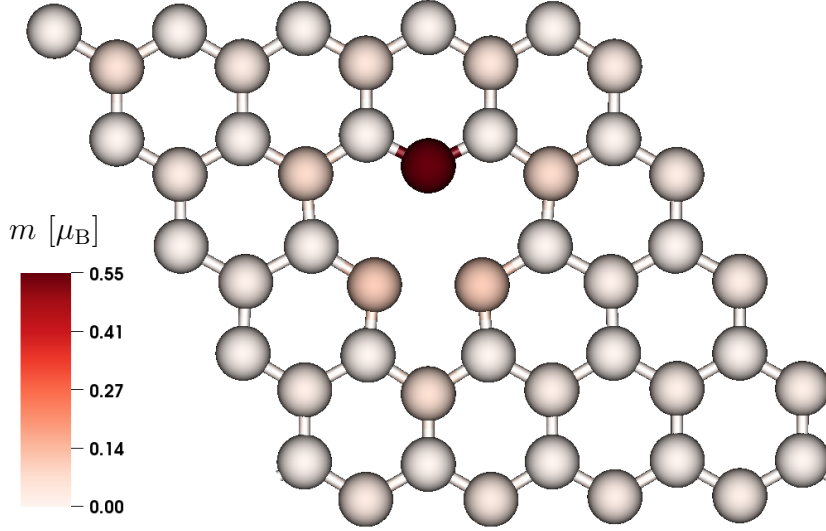


Figure 4.2: Free-standing graphene with a SV in the most stable asymmetric configuration. The carbon atom next to the vacancy with shorter bonds is the only one with a considerable magnetic moment.

The formation energy is defined as

$$E_{\text{form}} = E_{\text{def}} - E_{\text{perfect}} - n\mu$$

where E_{def} is the total energy of the supercell with the defective site and E_{perfect} is the total energy of the supercell in the perfect graphene structure. The chemical potential μ is taken as the energy per carbon atom in perfect graphene and n denotes the number of atoms that are added ($n > 0$) to or removed ($n < 0$) from the supercell when an impurity or defect is created [139], e.g. for a SV $n = -1$. The asymmetric configuration has the lowest formation energy with 7.789 eV (table 4.1), which compares well with the experimental value of 7.0 ± 0.5 eV, and the value of Ma et al. (7.7 eV). These numbers are large compared to formation energies in other materials (usually less than 3 eV in most metals [140]). The formation energy of the metastable symmetric configuration and the rigid model is 0.287 eV and 0.545 eV larger, respectively.

Other theoretical studies calculated formation energies of the same order of magnitude. They are all found in the range of 7.4 to 7.7 eV (table 4.1). However, the studies of El-Barbary et al. [136], Kaxiras and Pandey [141], and Li et al. [132] use a symmetric configuration, which is not the most stable one according to [138]. The activation barrier for removing a single carbon atom is calculated as the formation energy plus a migration barrier, which is relatively small compared to the formation energy (1.7 eV [136], 1.6 eV [141], 1.3/1.4 eV [137]) which allows a measurable migration of the SV already slightly above room temperature (100-200 °C) [125].

The concentration c of an impurity, defect, or complex is related to the respective formation energy. In thermodynamic equilibrium the expression

$$c = N_{sites} N_{config} e^{-\frac{E_{form}}{k_B T}}$$

is valid [139], where k_B is Boltzmann's constant and T is the temperature. N_{sites} is the number of sites in the lattice where the defect can be incorporated and N_{config} gives the number of equivalent configurations in which the defect can be incorporated. For vacancies on unsupported graphene where no symmetry breaking occurs, N_{config} equals one. But for supported graphene, which will be discussed in the following section, the symmetry is broken and there are two non-equivalent sites (with different formation energies). Because of a high formation energy for a SV defect (≈ 9 eV), the SV density is usually small in experiments.

4.2 Single Vacancies in Nickel-supported Graphene

In this section the effect of a nickel support on graphene with a SV is studied. The top-fcc and bridge-top are the most stable configurations for Gr/Ni(111), as discussed in section 3.1.4 and hence calculations presented in this section use the top-fcc adsorption geometry with a five layer nickel slab underneath, within a 5×5 two-dimensional unit cell. More computational details are described in section 4.6.

The initial structure before relaxation is a perfect Gr/Ni(111) system with one carbon atom removed. Due to the broken symmetry, caused by the nickel substrate, there are two different choices to remove a carbon atom. The vacancy can be either above a nickel

Ref.	method	configuration	E_{form} [eV]	E_{act} [eV]
(*)	DFT PBE+Grimme	no relaxation	8.334	-
(*)	DFT PBE+Grimme	symmetric	8.076	-
(*)	DFT PBE+Grimme	asymmetric	7.789	-
[141]	DFT LDA	symmetric	7.6	9.2
[136]	DFT LDA	symmetric	7.4	9.1
[138]	DFT PBE	asymmetric	7.7	-
[132]	DFT PBE	symmetric	7.6	-
[137]	DFTB/DFT ^a	asymmetric	7.6/7.7	8.9/9.1
[142]	exp.	-	7.0 ± 0.5 eV	-

Table 4.1: Formation energies of unsupported graphene with a SV. The activation barrier is calculated as $E_{\text{act}} = E_{\text{form}} + E_{\text{migr}}$ where E_{migr} is the migration energy.

(*) Present results, partially published in [123].

^a Krasheninnikov et al. performed DFT-based tight binding (DFTB) as well as DFT calculations.

atom or above a fcc-hollow position, which are labeled top- and fcc-vacancy, respectively. Therefore, the three carbon atoms next to the top- (fcc)-vacancy are at fcc- (top)-sites, respectively. In the relaxed structure, the three adjacent carbon atoms at fcc-sites are 0.60 \AA closer to the nickel substrate than the other mainly unaffected other carbon atoms (Fig. 4.3) so that the C-C bond lengths are stretched to 1.43 \AA compared to a bond length of pristine graphene of 1.425 \AA . The nickel atom below the vacancy site is lifted by 0.58 \AA . Thus, the C-Ni bond length to the interface nickel atom at the vacancy site is decreased to 1.85 \AA , whereas the bond lengths to the other two nickel atoms is 2.14 \AA , which is 0.06 \AA less than the Gr-Ni separation.

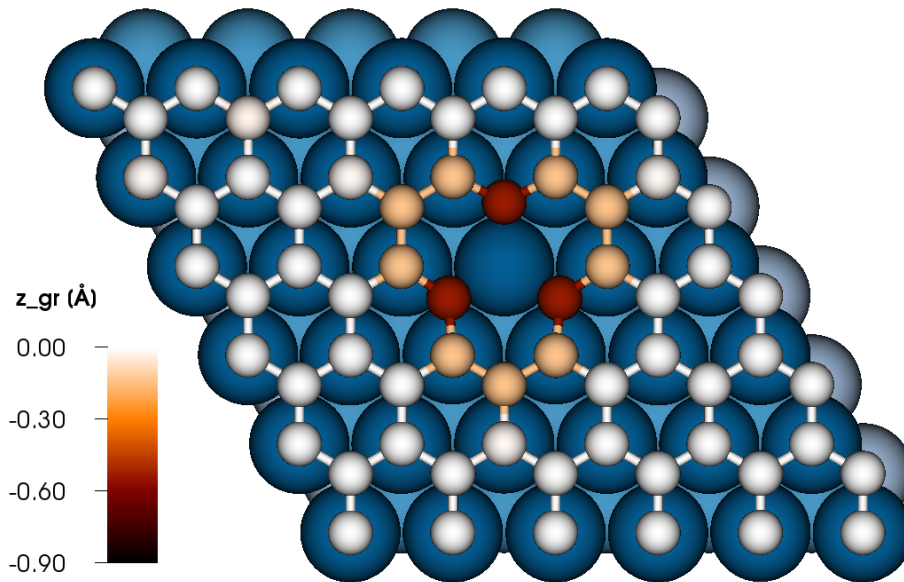


Figure 4.3: Graphene with a single vacancy at the top-site. The color code indicates the height of the C atoms. The three C atoms around the vacancy are 0.60 \AA closer to the nickel substrate than the C atoms away from the vacancy.

The relaxation effects for the fcc-vacancy configuration are less distinctive (Fig. 4.4). The three carbon atoms next to the vacancy move 0.23 \AA downwards, the C-C bond lengths are only slightly decreased by 0.02 \AA .

The formation energies are drastically lowered compared to free-standing graphene, whereupon the top-vacancy configuration (2.817 eV) is by far more stabilized than the fcc-vacancy configuration (5.553 eV). The three carbon atoms at fcc-hollow sites in the top-vacancy geometry are higher coordinated than the top-site carbon atoms in the other

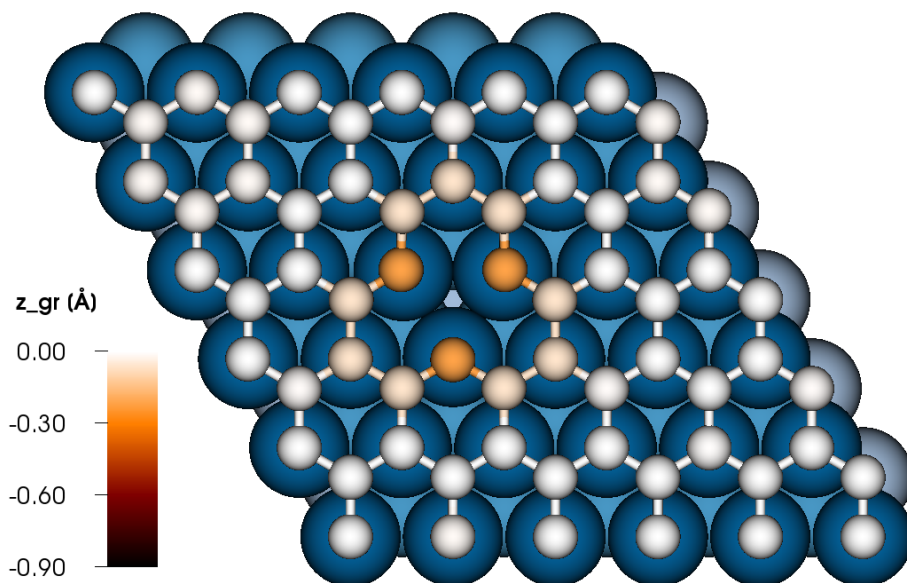


Figure 4.4: Graphene with a single vacancy at the fcc-site. The three C atoms around the vacancy are 0.23 \AA closer to the nickel substrate, indicated by the color code.

case. A single carbon adatom on Ni(111) gains 2.20 eV BE when it is adsorbed on a fcc-hollow site instead of a top-site². For the top-vacancy geometry, the energy gain per carbon atom is still 0.912 eV . In contrast to the unsupported structures, smaller magnetic moments $< 0.35 \mu_B$ are calculated for the preferred structure. No dangling bonds are found and both configurations are symmetric with respect to the SV.

A migration barrier is not calculated here, since a barrier that must be larger than the difference of the two formation energies ($> 2.736 \text{ eV}$) is unlikely to be overcome in reality.

4.3 Stone-Wales Defects in Pristine Graphene

The Stone-Wales defect is a 90° rotation of two carbon atoms with respect to the midpoint of the bond and does not require any removal or addition of carbon atoms. This type of defect was described in 1986 by A. J. Stone and D. J. Wales [143] on the isomerization of fullerenes. More precisely, the truncated icosahedron C_{60} molecule with carbon arranged

²The favorite adsorption position for a single carbon atom on Ni(111) is the hcp-site that has 0.03 eV more BE. However, there is a strong driving of the carbon atom to segregate into the bulk or contribute to a nickel surface carbide layer (see section 5).

in pentagons and hexagons was studied. By rotating a C-C bond by 90° , the orientation of the pentagons and hexagons can be locally changed which influences the electronic and vibrational levels of C_{60} . SW defects have been extensively studied in carbon nanotubes for their effect on the electronic, chemical, and mechanical properties. They can act as preferred adsorption sites, e.g. for transition metal atoms [144], which is of certain interest for gas-sensor applications [145].

SW defects also appear in planar graphene and frequently occur during electron bombardment in TEM. In graphene, it is a transformation of four hexagons of pristine graphene into two pentagons and two heptagons (Fig. 4.5a,b). Thus, the formation of a SW defect does not involve any removed or added atoms. But besides changing the structure in real space also the electronic structure is altered [146]. DFT studies reported on a band gap opening at the K -point due to the symmetry breaking of a single graphene layer on SiC [147] as well as the adsorption due to atomic hydrogen [148].

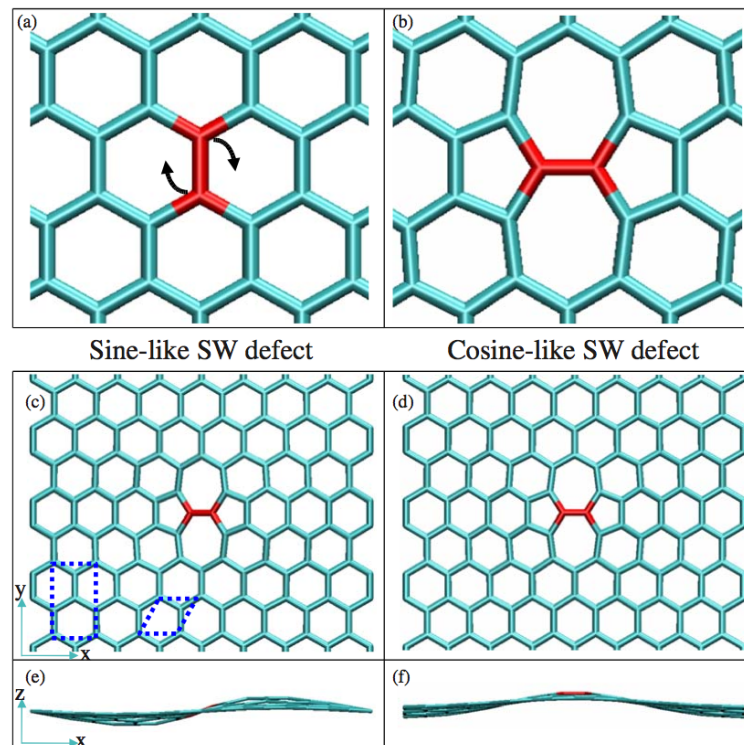


Figure 4.5: The 90° bond rotation is indicated for perfect graphene in (a). A flat SW-defect (b) is unstable, whereas the sine-like (c),(e) and cosine-like (d),(f) buckled conformations are lower in energy. Taken from Ma et al. [149]

Previous studies discussed the configuration of SW defects as planar defects [132, 141, 146], where the formation energies vary from 4.8 to 10.4 eV (table 4.2). Yet, Ma et al. [149] proposed that the planar configuration is rather a saddle point that separates two lower-energy buckled defect structures (Fig. 4.5c-f). The buckling height (difference between the highest and lowest carbon atom) was reported to be pronounced: $\approx 1.4 \text{ \AA}$ and $\approx 1.7 \text{ \AA}$ for the cosine- and sine-like waves, respectively. The explanation why a SW defect in graphene buckles is simple and merely related to strain relief [149]. The C-C bond lengths upon making the SW defect flat are compressed to 1.31 \AA . Since the in-plane motion of carbon atoms in graphene is much stiffer than out-of-plane motion, the flat structure cannot release the compression efficiently. To expand the compressed bond, the carbon atoms instead move out of plane [149]. The C-C bond length for the sine- and cosine-like structures are increased to 1.33 \AA and 1.32 \AA , respectively. The sine-like configuration was found to be most stable by Ma et al. [149]. A sine-like configuration is confirmed as the most stable structure by means of PBE+Grimme calculations which take into account vdW interactions in a simple way (table 4.2). The large formation energy clearly demonstrates a huge thermodynamic driving force for the healing of the defect.

Ref.	method	configuration	E_{form} [eV]	E_{act}
(*)	DFT PBE+Grimme	flat	5.410	-
(*)	DFT PBE+Grimme	cosine	5.320	-
(*)	DFT PBE+Grimme	sine	5.183	9.279
[141]	DFT LDA	sine	10.4	13.7
[132]	DFT PBE/LDA	sine	4.8/5.2	9.2/9.4
[149]	DFT PBE/QMC	sine	≈ 5	-

Table 4.2: Comparison of formation energies and activation energies needed to get a SW-defect in free-standing graphene. A sine-like configuration has a lower formation energy than a flat configuration.

(*) Present results partially published in [123].

When a SW defect is already present, an energy $E_{\text{rem}} = E_{\text{act}} - E_{\text{form}}$ is needed to remove the defect (Fig. 4.6). This barrier and the corresponding transition state (TS) configuration has not been calculated by Ma et al. for the buckled configurations and the values obtained by Kaxiras and Pandey [141] and Li et al. [132] are not reliable. In the first place, because they only considered planar structures and secondly because, either already the formation energies were by a factor two to large [141], or a rather small supercell (3×3) was used [132].

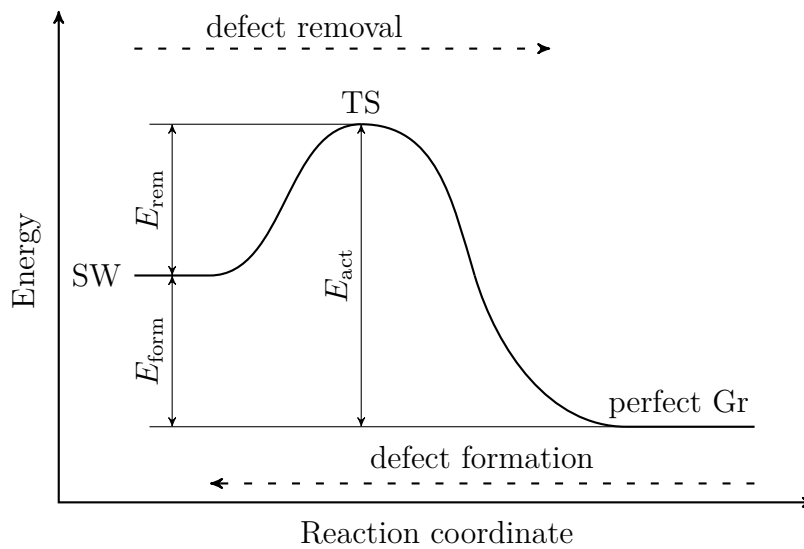


Figure 4.6: Schematic representation of the energies involved in the removal and the formation of a SW defect. First, for the healing of a SW defect an energy barrier E_{rem} must be overcome. And secondly the reverse process, when the initial state is a perfect graphene sheet and we want to generate a SW defect, an activation energy E_{act} is needed. The formation energy is the energy difference of the initial configuration (SW defect) to the final configuration (perfect graphene).

Because of a high energy barrier E_{rem} of 4.10 eV [123], the defects are stabilized and the healing process is hindered. The mechanism of the healing process is illustrated in Fig. 4.7a-c. The high reaction barrier is due to an unfavorable transition state configuration (Fig. 4.7b). The healing reaction proceeds via an out-of-plane rotation of a C-C pair, so that two corner atoms of the neighboring graphene rings have lost one bonding atom.

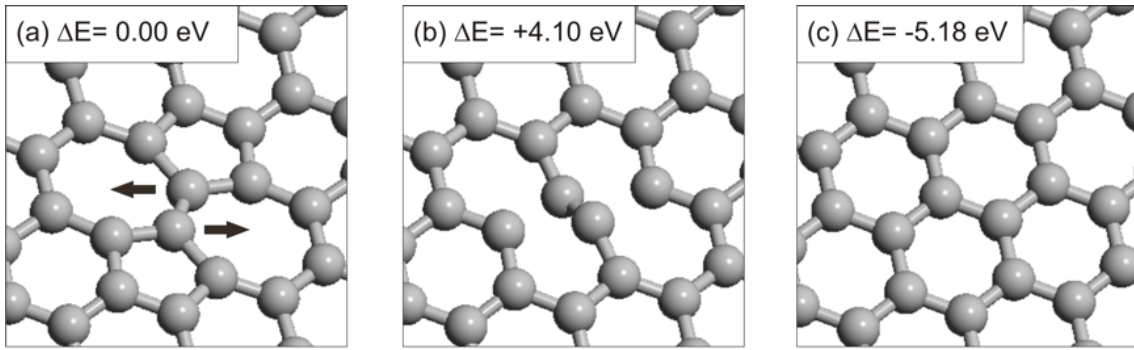


Figure 4.7: Calculated reaction pathway for the healing of a SW defect in pristine graphene (a-c). Panel b displays the transition state configuration. Taken from Jacobson et al. [123]

4.4 SW Defects on Nickel-supported Graphene

In this section the influence of a nickel support for the healing of a SW defect is studied. The graphene is adsorbed in a 1×1 top-fcc arrangement on the nickel substrate, similar to the SV supported case in section 4.2. For the three high-symmetry configurations top-fcc, top-hcp, and hcp-fcc, the middle of the two C-C bonds in the unit cell are at equivalent positions, respectively (e.g. bridge for hcp-fcc, see Fig. 3.2). Therefore, it does not matter which of the two C-C bonds is rotated to form a SW defect.

The relaxed defect structure shows a pronounced buckling (1.2 \AA) of the carbon atoms (Fig. 4.8). A sine-like configuration analog to unsupported graphene is not possible because of geometrical restrictions. A cosine-like structure is found as the most stable configuration. The two rotated carbon atoms are close to the interface nickel. Notice, that the determined final structure is not symmetric. The carbon atoms to the right of the defect (in top view) are higher than the left ones. The three top-site carbon atoms to the right of the defect are $\approx 0.3 \text{ \AA}$ higher than the lowest carbon atoms. The bonding to the nickel atoms induces a small corrugation in the interface nickel layer of 0.2 \AA (dashed circles in Fig. 4.8). The enhanced bonding due to the nickel support is also reflected in an decreased formation energy of 4.18 eV with respect to the unsupported defect.

The crucial point, however, is that the energy barrier E_{rem} is reduced to 2.88 eV , from 4.10 eV for unsupported graphene. Even though such barrier still implies that high temperatures of more than $700 \text{ }^\circ\text{C}$ for a thermal healing of the SW defects on the Ni(111)

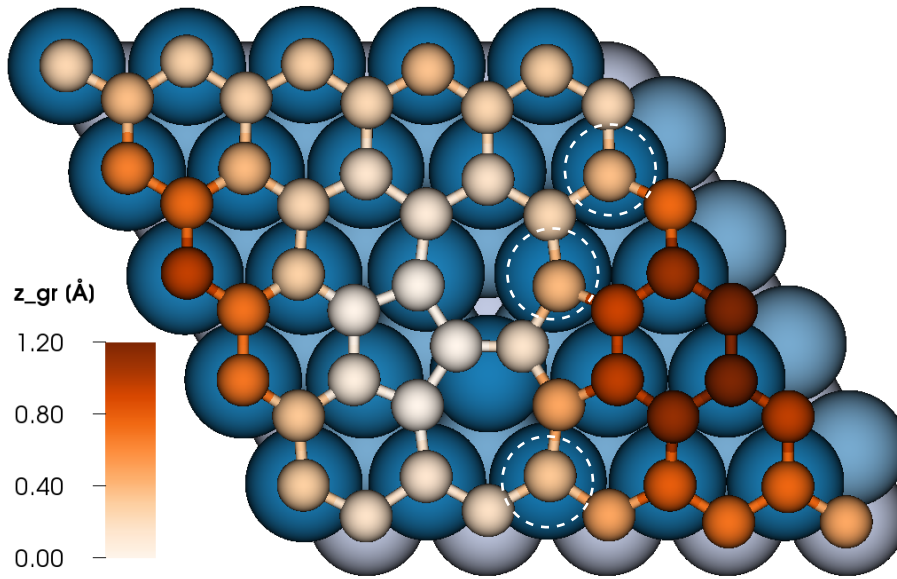


Figure 4.8: Configuration of Gr/Ni(111) with SW defect. The carbon atoms are colored to denote the corrugation. The dashed circles label the three nickel atoms that are lifted by $\approx 0.2 \text{ \AA}$.

surface are required, a barrier of 4.10 eV for pristine graphene would completely suppress this process at these temperatures [123].

The reaction mechanism for the removal of a SW defect proceeds differently when a nickel substrate is involved (Fig. 4.9a-c). The presence of the nickel surface breaks the symmetry of the process. In contrast to the symmetric out-of-plane tilting of the bond at the transition state in the unsupported graphene layer (Fig. 4.7b), the steric restriction prevents moving the lower carbon atom closer to the nickel surface (Fig. 4.9b). Consequently, while both five-fold rings are opened simultaneously for the unsupported graphene, one of the five-fold rings remains closed at the transition state for the Ni-supported graphene. The bond between the substrate and the edge of the pentagon is especially pronounced, leading to a C-Ni distance of 1.94 \AA and a corrugation of 0.37 \AA in the uppermost Ni layer (Fig. 4.9d). The large increase in corrugation below the SW defect at the transition state indicates a strong chemical bonding between the SW defect and nickel, despite the low adsorption energies for Gr/Ni(111) found in section 3.1.3. Therefore, during the reaction the surface corrugation increases when compared to the unsupported SW defect. Importantly, we find that all but one under-coordinated edge

atom of the reaction intermediate binds to the surface (Fig. 4.9b), leading to a stabilization of the reaction barrier.

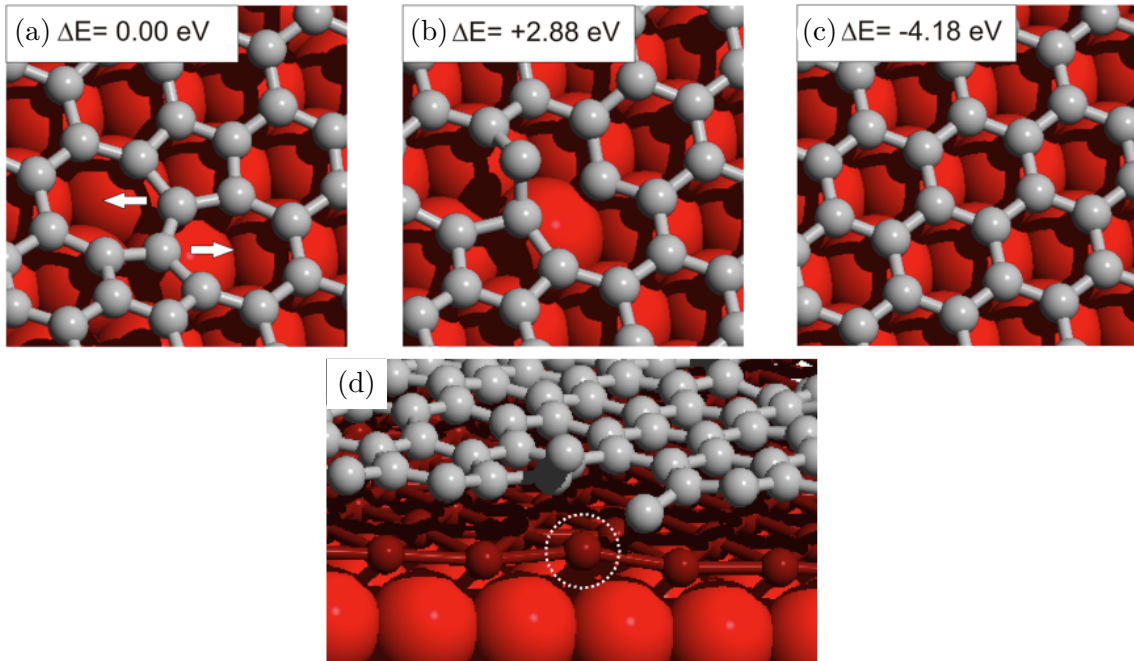


Figure 4.9: Calculated reaction pathway for the healing of a SW defect for nickel-supported graphene (a-c). One of the two carbon atoms is rotated out-of-plane at the transition state (b). Panel d shows a side-view cutaway at the transition state and the 0.37 Å increase in nickel surface corrugation; the affected Ni atom is circled in white. The top nickel layer is shown as a ball and stick model (dark red) to better visualize the corrugation. Taken from Jacobson et al. [123]

4.5 STM Measurements of defective Graphene

Peter Jacobson et al. [123] did STM measurements on the structural evolution of graphene on Ni(111) as a function of the growth temperature. A detailed description of the experimental methods is found in [123]. At a low temperature of 400 °C (Fig. 4.10a), the film is highly defective. The graphene honeycomb structure and SW-type defect structures are clearly visible (Fig. 4.10a,e). With increasing growth temperature the disordered domains shrink, leaving small clusters of defects alongside epitaxially matched graphene

(Fig. 4.10b-d). Annealing the film grown at 450 °C to 650 °C results in epitaxial graphene that is still highly disordered (Fig. 4.10f).

While graphene grown at 650 °C on Ni(111) is largely perfect, defects such as grain boundaries occur (Fig. 4.11a), where SW defects may be created. A single carbon vacancy appears as dark three-fold feature in a different region of the rotated graphene grain (Fig. 4.11b). The STM images simulated with DFT of the top-vacancy configuration from section 4.2 reproduce the experimental image (Fig. 4.11c). Although a single carbon vacancy is the simplest structural defect in graphene, isolated carbon vacancies were rarely observed on graphene on Ni(111) grown at high temperature (650 °C). A recent study of isolated carbon vacancies in graphene on Pt(111) required post growth ion bombardment to create carbon vacancies, indicating that these defects are not prevalent in epitaxially grown graphene [150].

4.6 Computational Methods

All results in this chapter were obtained by spin-polarized DFT calculations using PAW-VASP. The PBE functional including vdW corrections proposed by Grimme [78] is used together with an energy cutoff of 400 eV. The defect energies have been evaluated for a 5×5 graphene surface cell supported by five layers of nickel using a nickel lattice constant of 3.47 Å (i.e., a nearest-neighbor distance of 2.45 Å), where two nickel layers next to the interface were allowed to relax, resulting in residual forces < 0.02 eV/Å. A $4 \times 4 \times 1$ k-point mesh was employed for the integration of the Brillouin zone except for free-standing graphene with a SV where a $7 \times 7 \times 1$ k-point mesh was used. The transition states have been identified with the improved dimer method [151], and verified by a subsequent relaxation to the initial (final) state minimum.

4.7 Conclusion

In this chapter SVs and SW defects both, on unsupported and nickel-supported graphene were studied. A huge formation energies of 7.8 eV prevents a noteworthy concentration of SVs in pristine graphene at least at typical experimental temperatures. The symmetry is

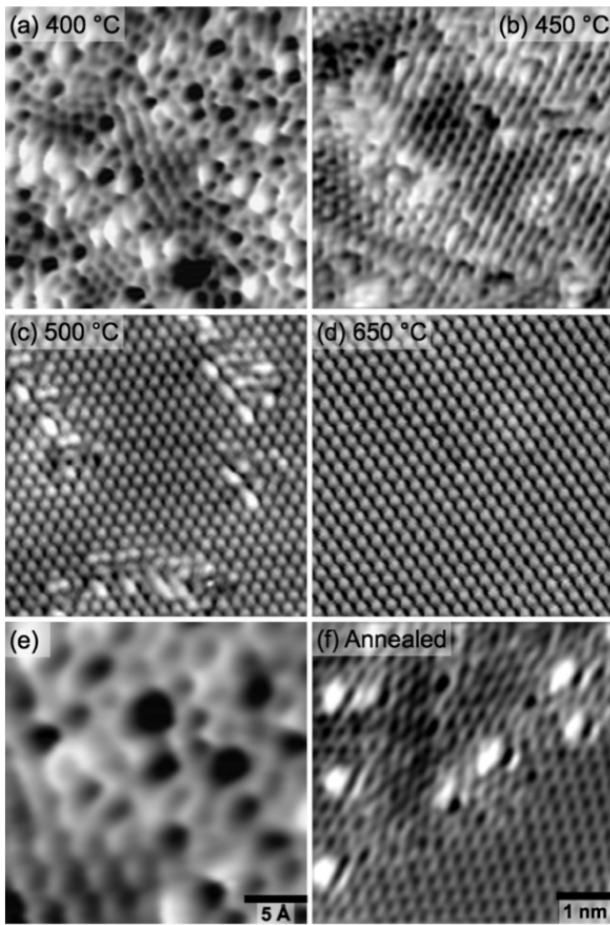


Figure 4.10: STM images ($6 \times 6 \text{ nm}^2$) of graphene grown at different temperatures: (a) 400 °C, (b) 450 °C, (c) 500 °C, (d) 650 °C. (e) Close up ($2.4 \times 2.4 \text{ nm}^2$) of the structure in panel a. (f) Graphene film grown at 450 °C then annealed at 650 °C for 15 min. Taken from Jacobson et al. [123]

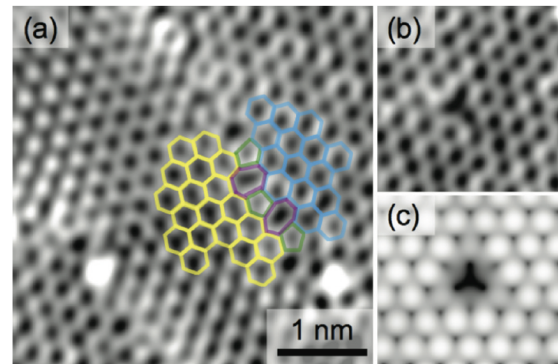


Figure 4.11: (a) High-resolution image of a graphene grain boundary ($4 \times 4 \text{ nm}^2$). Five- and seven-membered rings observed at the grain boundary and are colored with green and magenta, respectively. (b) An isolated carbon vacancy on a graphene sheet rotated 21.8° ($2 \times 2 \text{ nm}^2$). (c) Simulated STM image of a single carbon vacancy in a supported ($1 \times 1 \text{ nm}^2$) graphene sheet. Taken from Jacobson et al. [123]

broken for nickel-supported graphene. If the vacancy is at a top-site the formation energy is drastically decreased to 2.8 eV, whereas a vacancy at fcc-site is less favorable. The lower energy configuration shows no considerable magnetic moment in contrast to unsupported graphene but the strong carbon-nickel bonds of the carbon atoms next to the vacancy at fcc sites stabilize the defect.

A planar SW defect in free-standing graphene comes along with small C-C bonds and high surface stress. A sine-like configuration where the C-C bonds are expanded can release the stress induced by the SW defect and was confirmed as the lowest energy solution. For the healing of the defect a barrier (4.1 eV) of the same order of magnitude as the formation energy (5.2 eV) was calculated. Therefore, once the defect is formed under non-equilibrium conditions, a high reverse transformation barrier ensures its stability at room temperatures. The formation energy is reduced to 4.2 eV for a SW defect on nickel-supported graphene. However, the most remarkable result is the decrease of the barrier to remove the defect to 2.8 eV. While for unsupported graphene both five-fold rings are opened at the transition state, for the supported graphene all but one atom binds to the surface, which induces a corrugation of the nickel interface layer of 0.37 Å.

Chapter 5

Surface Carbide induced Changes on Graphene/Ni(111)

The main results of this chapter were published in ACS Nano, 6, 3564 (2012), *Nickel Carbide as a Source of Grain Rotation in Epitaxial Graphene* [152], where the present author performed the DFT calculations.

Graphene grown by chemical vapor deposition (CVD) is utilized to produce large-sized graphene sheets of high quality [29, 153]. While CVD-grown epitaxial graphene has been investigated on numerous transition metals [7] (e.g. Ru, Pt, Ir, Rh, Co, Ni, and Cu), nickel and copper are primarily utilized in applied research. Because graphene on copper has no preferred epitaxial growth orientation, grain orientations cannot be easily controlled [154]. Epitaxial graphene on Ni(111), on the other hand, adsorbs in one of several possible 1×1 structures due to a small lattice mismatch (see section 3.1.2). E.g. the adsorption energies for top-fcc and bridge-top adsorption configurations are rather similar (see section 3.1.4), and it has been shown recently that both phases can coexist on Ni(111) [107].

In addition to these 1×1 structures, several local moiré structures have been observed [120, 155, 156], but the existence of such moiré structures is unexpected due to the overwhelming preference of 1×1 configurations. The source of the grain rotations was found by a combined study using STM and DFT [152, 157]. Local regions with excess carbon in the form of a surface-confined nickel carbide (Ni_2C) prevent graphene from adopting its preferred 1×1 epitaxial relationship on Ni(111). Graphene has no epitaxial relationship with the surface carbide, resulting in a range of grain rotations (6.6-23.8°).

5.1 Nickel Carbide on Ni(111)

When Ni(111) is exposed to hydrocarbons above 300 °C, the surface reconstructs into a monolayer surface carbide with stoichiometry Ni₂C [114, 158, 159]. Atomic carbon strongly chemisorbs on Ni(111), penetrating the topmost layer and becoming nearly coplanar with nickel. As the carbon forces itself into the top nickel layer, the nickel-nickel distance is increased $\approx 3\%$ and the local structure is distorted, effectively changing the hexagonal symmetry of the (111) surface into a square mesh similar to the (100) face (Fig. 5.1). This reconstruction includes clockwise and counterclockwise rotations of the square carbon lattice; hence, this surface carbide is known as the “clock reconstruction”. The distortion to a square lattice on a hexagonal surface results in an incommensurate surface overlayer. Two supercells were suggested in the past, to model the system. The originally proposed structure by McCaroll et al. [158] is a $(\sqrt{39}R16.1^\circ \times \sqrt{39}R16.1^\circ)$ cell while Klink et al. [114] claimed that a $(\sqrt{39}R16.1^\circ \times \sqrt{37}R-34.7^\circ)$ cell is closer to a coincidence cell. The notation indicates the carbide unit cell orientation with respect to the Ni(111) unit cell; specifically, rotations of 16.1 and -34.7° from the $[1\bar{1}0]$ direction and with 110.8° between basis vectors.

Both models are simulated with DFT calculations using LDA to relax the structures. However, LDA predicts a BE that is too strong for graphene/Ni(111). Especially for the Gr/Ni₂C/Ni(111) system discussed in next section the inclusion of vdW interactions is needed. Therefore, vdW-DF calculations employing the optB88-vdW functional are performed for the relaxed LDA geometry. It turned out that the surface energy of both proposed configurations is almost the same (< 0.01 eV/Å² difference) for both, LDA and optB88-vdW functionals. The $(\sqrt{39}R16.1^\circ \times \sqrt{37}R-34.7^\circ)$ cell proposed by Klink et al. [114] is used for the following discussions, since it is a better approximation to the experimentally observed structure [114].

In STM measurements, large areas of carbon-induced reconstructions are observed (Fig. 5.2b). The presence of the carbide phase is indicated by parallel lines (highlighted in yellow) with a spacing of 1.65 nm and an apparent height modulation of 20 pm. The local structure of Ni₂C is shown in Fig. 5.2c, where carbon atoms are imaged as depression (black dots) and the line structure in (Fig. 5.2b) is now recognizable as regions with more

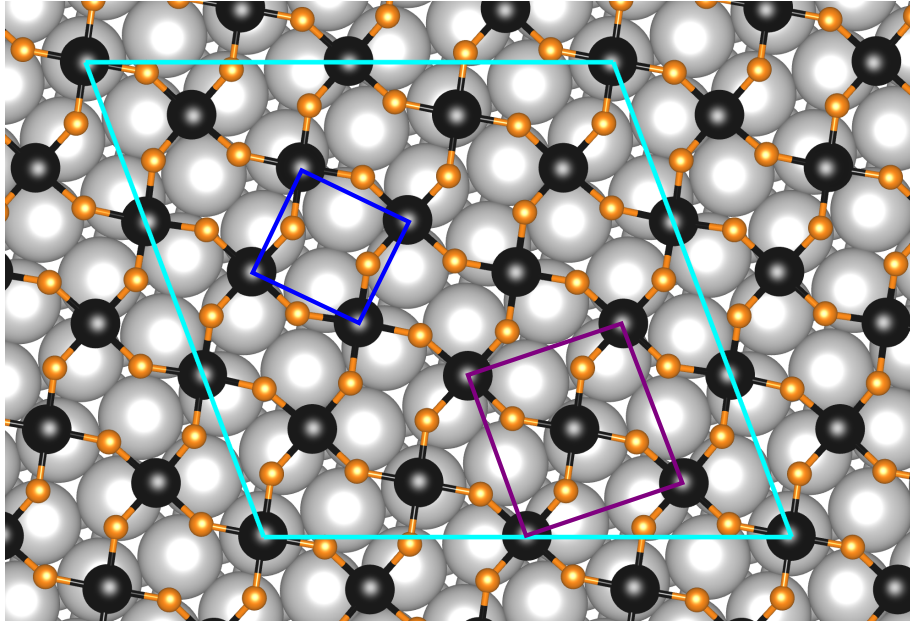


Figure 5.1: Clock reconstruction of the Ni_2C surface carbide at the LDA nickel lattice constant. The $(\sqrt{39}R_{16.1^\circ} \times \sqrt{37}R_{-34.7^\circ})$ unit cell is marked with turquoise lines. The nickel atoms of the surface layer are pictured as small orange balls, the surface carbon atoms are colored black, and the bulk nickel atoms are grey. The carbon square-like structures are rotated clockwise and counterclockwise. The small square units in blue are slightly irregular (average side length 3.41 \AA) while the large square units (purple) are even less distorted ($4.72 \text{ \AA} \times 4.76 \text{ \AA}$)

or less pronounced depressions. A fast Fourier transform (FFT) of the Ni_2C domain (Fig. 5.2d) shows spots of the underlying Ni(111) surface, marked with black circles. The square-like carbon lattice of the clock reconstruction unit cell shows periodicities of 3.6 Å (blue circles in Fig. 5.2d and corresponding blue square in Fig. 5.2c and Fig. 5.1) and 5.2 Å (purple circles in Fig. 5.2d, purple square units in Fig. 5.2c and Fig. 5.1) in the FFT image. The stripes observed in large-scale images (Fig. 5.2b) are also present in the FFT and indicate a periodicity of 16.5 Å. These characteristic features allow Ni_2C to be readily identified, in effect acting as fingerprint for the presence of Ni_2C . The STM image simulated with DFT of the ($\sqrt{39}R16.1^\circ \times \sqrt{37}R-34.7^\circ$) Ni_2C reconstruction reproduces the experimentally observed square-like structure very well (Fig. 5.2e).

5.2 Graphene on Nickel Carbide

5.2.1 DFT Calculations

For the calculations of Gr/ Ni_2C /Ni(111) the same $\sqrt{39}R16.1^\circ \times \sqrt{37}R-34.7^\circ$ cell as for Ni_2C /Ni(111) is used with graphene on top, aligned to the Ni(111) substrate in the top-fcc configuration. Thus, graphene is not rotated in contrast to the STM measurements (see below). The BE per carbon atom is weak (LDA: 0.022 eV, vdW-DF: 0.068 eV) with respect to 1×1 graphene on Ni(111) for which the BE of Gr/Ni(111) per carbon atom is calculated as 0.101 eV for LDA, and 0.062 eV for vdW-DF at the respective optimal nickel lattice constant. Therefore, standard DFT (LDA) predicts that the adhesion of graphene on the Ni_2C is significantly weaker compared to the bare Ni(111) surface. Although the vdW-DF calculations (with the optB88-vdW functional) predict a similar BE of graphene on a Ni_2C and a bare nickel covered surface (almost the same as in bulk graphite), the adsorption energies show a strong dependency on the choice of the vdW-DF functional (see section 3.1.3) which renders a reliable qualitative comparison doubtful. Nevertheless, the average (LDA) distance of 3.16 Å (vdW-DF: 3.23 Å) between graphene and Ni_2C is significantly larger than the 2.21 Å for graphene on Ni(111), indicating only van der Waals bonding of graphene on Ni_2C . The weak interaction with the Ni_2C enables a wide range of grain rotations. Rotation angles of 16.1° and 25° would result from alignment

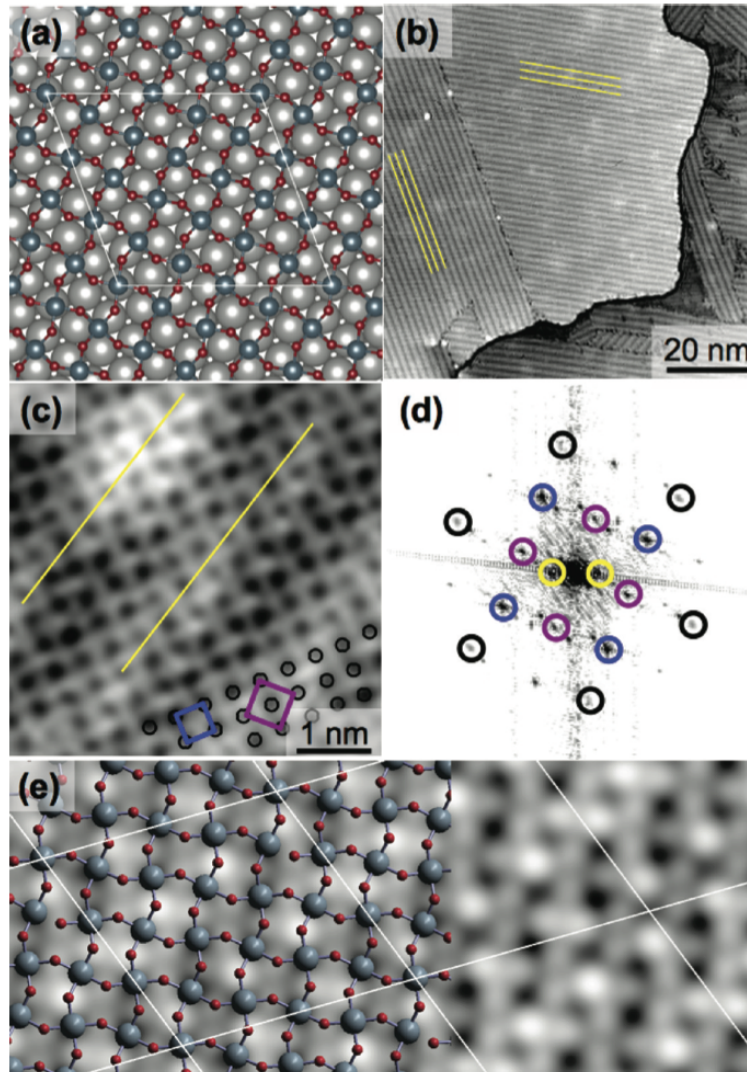


Figure 5.2: (a) Top view model of the $(\sqrt{39}R16.1^\circ \times \sqrt{37}R-34.7^\circ)$ Ni_2C reconstruction (C, dark gray; surface Ni, red; bulk Ni, light gray) determined by DFT; white lines indicate the carbide unit cell. (b) Large-scale STM image of the Ni(111) surface covered with the Ni_2C reconstruction. The parallel stripes (marked in yellow) are indicative of Ni_2C . (c) High-resolution STM image of the Ni_2C surface. Black dots denote the position of individual carbon atoms. The yellow lines indicate the stripes observed in panel b. The square-like structures from Fig. 5.1 are marked in purple and blue again. (d) FFT of the Ni_2C domain in panel c. Black circles correspond to the Ni(111) substrate; purple and blue circles highlight the non-hexagonal Ni_2C reconstruction; yellow circles indicate the stripes in panel b. (e) Simulated STM of Ni_2C overlaid with the model (C, dark gray; Ni, red). Taken from Jacobson et al. [152]

of the graphene lattice with the sides of the Ni₂C superstructure cell. Since the unit cell of Gr/Ni₂C/Ni(111) is already very large, rotated graphene would require even larger supercells, which are not tractable by the given computational resources.

5.2.2 STM Results

In STM measurements (Fig. 5.3a) graphene grown on the Ni₂C covered Ni(111) surface as well as epitaxial graphene and rotated graphene was observed. In the color-coded map of Fig. 5.3a, the central triangular region in yellow contains a moiré pattern that turns into 1 × 1 graphene (red) and graphene on Ni₂C (blue in Fig. 5.3b). A high-resolution image of the area indicated by the black box in Fig. 5.2a shows the boundary between the moiré patterned graphene and graphene on Ni₂C (Fig. 5.3c). The upper half of Fig. 5.3c contains a moiré pattern indicating rotation of the graphene sheet away from the expected 1 × 1 binding sites. In the FFT image of this region hexagonal spots corresponding to graphene (Fig. 5.3e, green circles) and the nickel substrate (black circles) are observed. Inside the primary graphene spots, a series of satellite spots (yellow circles) correspond to the 9.5 Å periodicity of the moiré unit cell, and a rotation of 14.6° with respect to 1 × 1 graphene. The lower half of Fig. 5.3c contains a more complex structure with no obvious moiré cell (see detail in Fig. 5.3d). In the FFT of Fig. 5.3d again the same primary spots attributable to graphene are observed. However, the satellite features correspond to Ni₂C i.e. graphene is adsorbed on Ni₂C and not Ni(111) with graphene rotations ranging from 6.6° to 23.8°.

Depressions and protrusions in STM measurements are preferentially found at the grain boundary where 1 × 1 graphene meets the rotated graphene (Fig. 5.4a,b). In FFTs, 1 × 1 graphene in top and right regions of panel b (Fig. 5.4c), as well as rotated graphene in the central region of panel b (Fig. 5.4d) are confirmed. Line profiles along the hexagonal features in panel b show a decrease in apparent height by 2 Å (blue curve in Fig. 5.4e) and more than 2.5 Å (red curve in Fig. 5.4e). As the interplane distance of Ni(111) is 2 Å, these line profiles indicate that for the red line profile one nickel layer and for the blue line profile two nickel layers have been (partially) removed under the graphene sheet.

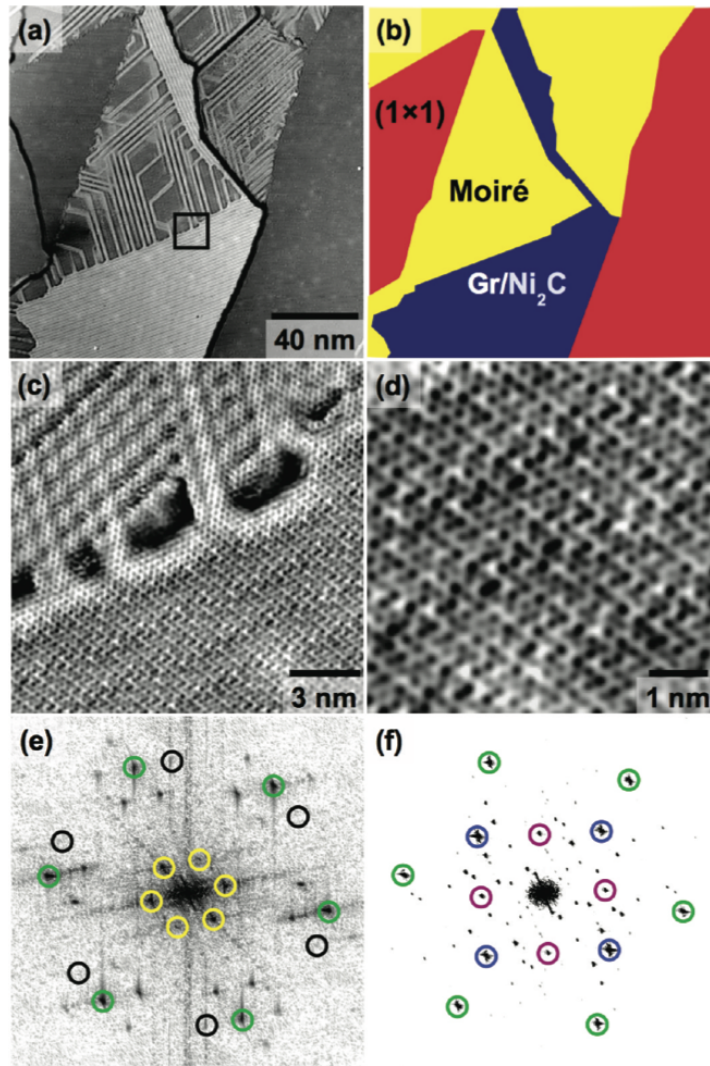


Figure 5.3: (a) Morphology of graphene grown on the surface in Fig. 5.2b. Three distinct regions are found in this image and are marked in panel b for clarity. (b) Red indicates 1×1 epitaxial graphene on Ni(111); yellow represents graphene rotated away from 1×1 epitaxy; blue marks graphene residing on Ni_2C . (c) Zoom in on the boundary, marked with a black box in panel a. (d) Graphene adsorbed on the Ni_2C reconstruction (blue in panel b). (e) FFT of the upper half of panel c; green circles indicate the graphene lattice, black circles indicate the Ni(111) substrate, and yellow circles indicate the moiré unit cell. (f) FFT from the lower half of panel c; green circles indicate the graphene lattice, while purple and blue are non-hexagonal elements. The non-hexagonal features are the same as observed in Fig. 5.2c. Taken from Jacobson et al. [152]

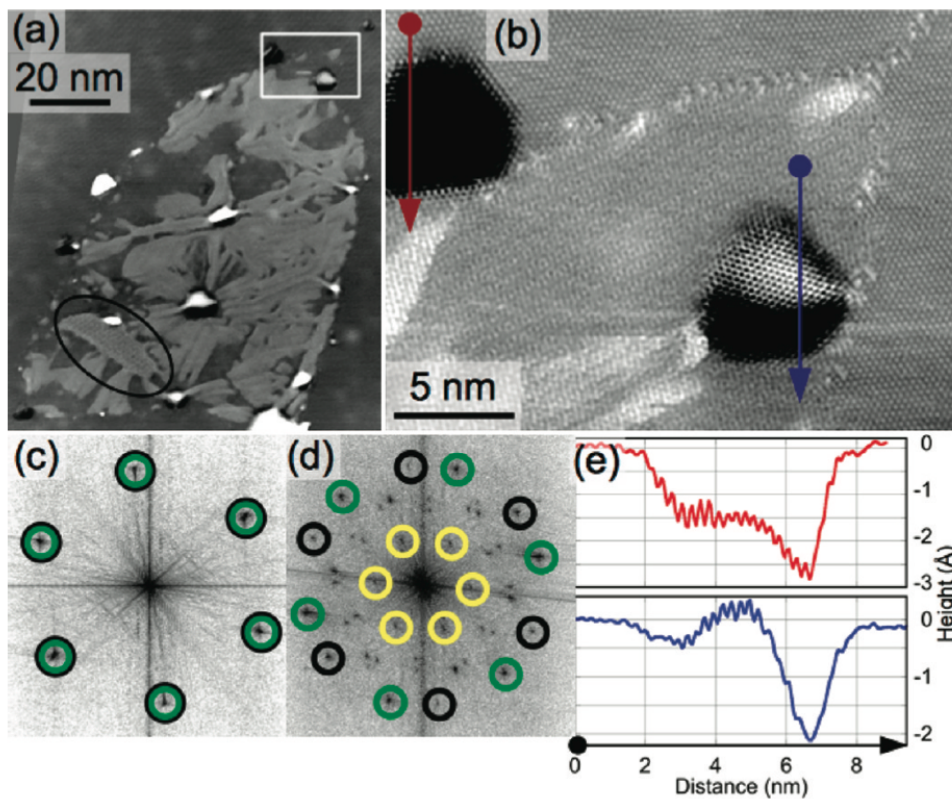


Figure 5.4: (a) Rotated graphene grain surrounded by 1×1 graphene. Inside the central region, a small domain of Ni_2C is circled in black. Protrusions, hexagonal depressions, and ripples are found in the central region. A close-up of the white box (b) shows two hexagonal features at a tilt grain boundary. (c) FFT of the 1×1 graphene of panel b, excluding the hexagonal areas at the grain boundaries; green and black circles mark the graphene features and $\text{Ni}(111)$, respectively. (d) FFT of the rotated grain; the green circles mark the rotated graphene, black circles mark the $\text{Ni}(111)$ substrate, and yellow circles show the moiré unit of the rotated region. (e) Line profiles taken from panel b over the hexagonal features show the removal of nickel below the graphene sheet. Taken from Jacobson et al. [152]

5.3 Surface Phase Diagram

In order to find the most stable structure for phases with different amounts of carbon and nickel atoms, a mere comparison of total energies is not sufficient. The stability also depends on the reservoir from where, e.g. carbon atoms are supplied. The method of choice is to calculate surface phase diagrams [160], where the surface free energies as a function of the chemical potential are plotted and the equilibrium phases at a given chemical potential can be identified. The surface free energy γ in the ab initio thermodynamics framework are calculated as

$$\gamma(\mu_C) = (E_{\text{tot}} - N_{\text{Ni}}\mu_{\text{Ni}} - N_{\text{C}}(\mu_{\text{C}} + E_{\text{C-atom}})) / A - E_{\text{lat}}(\text{Ni}(111)) \quad (5.1)$$

where E_{tot} gives the total energy of the calculations, the chemical potential μ_{Ni} is set to the BE of bulk nickel, and the energy $E_{\text{C-atom}}$ of a single carbon atom is used as a reference value for carbon. The area of the surface unit cell is A , the number of nickel and carbon atoms in the supercell is N_{Ni} and N_{C} , respectively. The surface energy of a bare Ni(111) surface is subtracted due to the bare Ni(111) surface at the back side of the slab geometry used in the calculations.

The surface free energies of Ni(111), the surface carbide Ni₂C/Ni(111), Gr/Ni(111), and Gr/Ni₂C/Ni(111) are compared for LDA and optB88-vdW functionals in Fig. 5.5 and Fig. 5.6, respectively. At the graphite chemical potential ($\mu_{\text{C}} = -9.00$ eV), the LDA calculations predict a small decrease in the surface energy of 0.014 eV/Å² after the formation of Ni₂C, and a further decrease upon the formation of a graphene layer on Ni(111). The choice of graphite as a reference for the chemical potential determines the respective thermodynamic stability after the dosing of hydrocarbons, while the relevant chemical potential of carbon can be significantly higher under growth conditions [161, 162]. The optB88-vdW calculations predict a decreased stability (i.e. higher surface energy) for the Ni₂C, making the surface carbide thermodynamically only metastable (Fig. 5.6, light blue line). Nevertheless, at the chemical potential of graphite, both functionals predict a similar energy gain for the formation of a graphene layer on Ni(111) from a Ni₂C surface carbide, as the surface energy is reduced by ≈ 20 meV/Å² for both functionals.

Evaluation of the free surface energy for the Gr/Ni₂C/Ni(111) system at the chemical

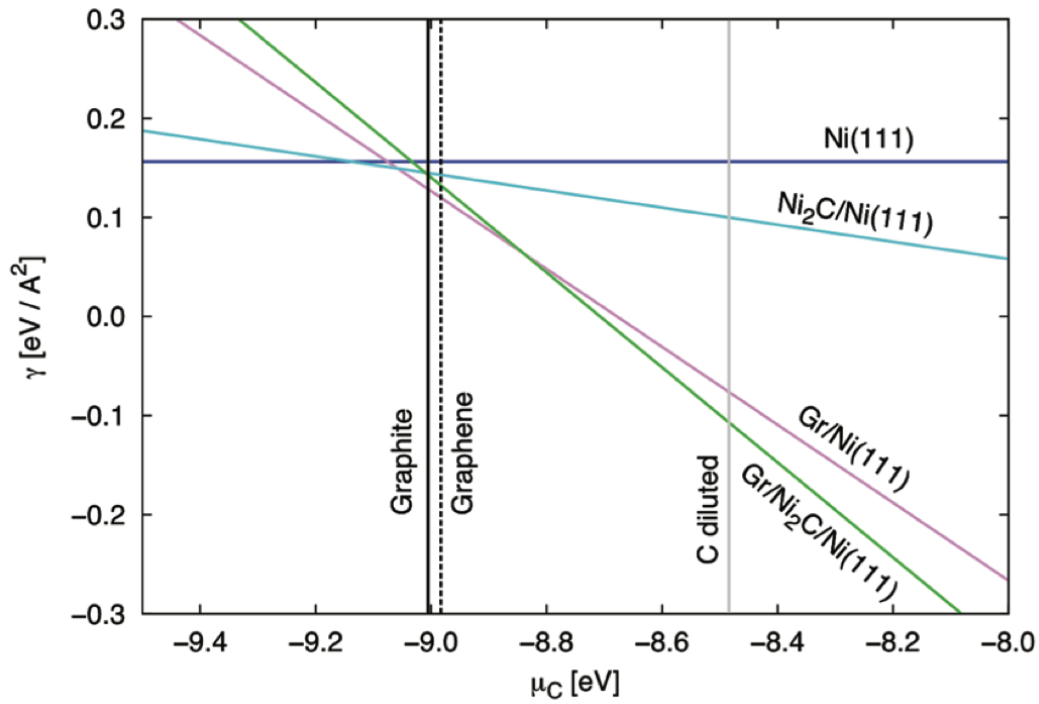


Figure 5.5: Free surface energies (LDA) of Ni(111), Gr/Ni(111), Ni₂C/Ni(111), and Gr/Ni₂C/Ni(111). The vertical lines indicate the specific value of the carbon chemical potential for graphite, graphene, and dissolved carbon; the chemical potential scale is referenced to a single carbon atom. The thermodynamically stable surface termination is given by the lowest energy line (entropy effects are neglected). Taken from Jacobson et al. [152]

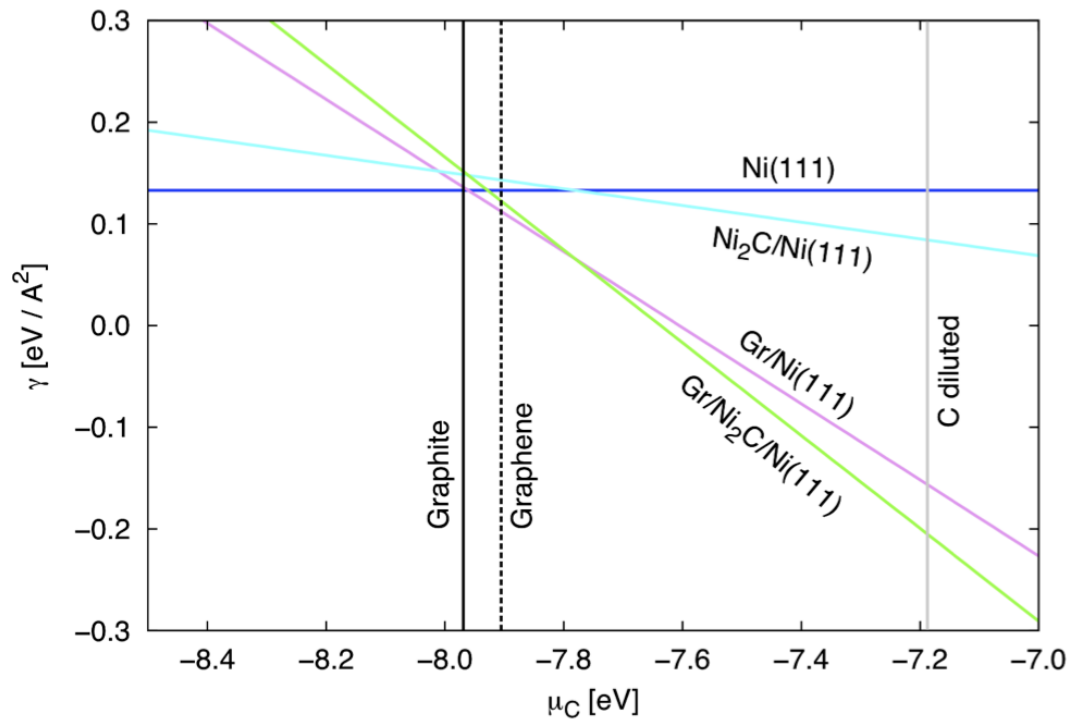


Figure 5.6: Free surface energies of Ni(111), Gr/Ni(111), Ni₂C/Ni(111), and Gr/Ni₂C/Ni(111) using the optB88-vdW DF. The vertical lines indicate the specific value of the carbon chemical potential for graphite, graphene, and dissolved carbon; the chemical potential scale is referenced to a single carbon atom. Taken from Jacobson et al. [152]

potential of graphite yields a value of $0.152 \text{ eV}/\text{\AA}^2$ (vdW-DF) and $0.143 \text{ eV}/\text{\AA}^2$ (LDA), which is about $14 \text{ meV}/\text{\AA}^2$ higher than graphene/Ni(111). On the other hand, under carbon-rich conditions (i.e. at the chemical potential of diluted carbon), the phase diagram indicates a high stability of the graphene-covered surface carbide. Therefore, while the calculations predict the formation of a graphene-covered surface carbide in carbon-rich conditions, the surface carbide is transformed to graphene/Ni(111) due to the higher stability of the graphene sheet on the bare Ni(111) surface at lower chemical potential.

5.4 Growth Model

When clean nickel is exposed to hydrocarbons (e.g., toluene) at $650 \text{ }^\circ\text{C}$, the hydrocarbon is decomposed, allowing atomic carbon to dissolve into the nickel bulk. The incorporation of carbon into nickel at an optimized volume results in an increase of the total energy by 0.44 eV (LDA) and 0.71 eV (vdW-DF) per carbon atom (values at $T = 0 \text{ K}$; with respect to phase separation into pure nickel and graphite). Experimental evidence for this carbon-nickel solid solution comes from a diverse range of experimental techniques [163–165]. When sufficient carbon enters the bulk, the carbon-nickel solid solution reaches supersaturation and carbon segregated to the surface can contribute to the formation of surface carbide Ni_2C and graphene growth.

Graphene grown on a surface containing Ni_2C has not been deliberately investigated before, but due to the relevance of Ni_2C in the methanation reaction much is known about Ni_2C surfaces. Previous studies showed that Ni_2C can survive on nickel surfaces at elevated temperatures similar to that used in the experiments [159, 166]. The conclusion is that Ni_2C is present in the actual experiments when the graphene growth begins. This assumption is strengthened by the observation of vacancy islands. The formation of these features can be understood by first considering the structure of Ni_2C . When hydrocarbons are exposed to the clean Ni(111) surface, or when the bulk has a sufficient reservoir of carbon, the surface reconstructs into the clock reconstruction shown in Fig. 5.1. This reconstruction alters the Ni(111) surface layer into a quasi-square symmetry reminiscent of the Ni(100) surface with a $c(2 \times 2)$ structure of adsorbed carbon. To transform the (111) surface into a (100)-like surface requires a reduction of the surface nickel density by 12%.

The driving force behind this transformation is surface stress induced by the adsorption and incorporation of carbon [114]. Because the formation of Ni_2C occurs at elevated temperatures and the diffusion barrier for nickel adatoms on $\text{Ni}(111)$ is small (0.22 eV [167]), excess nickel can diffuse to step edges. When a carbide domain starts to dissolve at high temperature – by diffusion of carbon into the Ni bulk or through consumption of the carbon in the graphene growth – there is a local deficit of nickel compared to the initial clean $\text{Ni}(111)$ terrace. Dissolution of Ni_2C after graphene formation will therefore result in vacancy islands, as observed in experiments.

The basic steps in the formation of rotated graphene are summarized in Fig. 5.7. After the hydrocarbons are decomposed, atomic carbon can dissolve into the nickel bulk. In these carbon-rich conditions, Ni_2C is formed as predicted by DFT calculations in the previous section. When the Ni_2C layer is completed, graphene nucleation starts with graphene loosely bound by vdW forces to the surface carbide, enabling different rotation angles. With the depletion of carbon in nickel bulk, the $\text{Gr}/\text{Ni}_2\text{C}/\text{Ni}(111)$ is no longer the phase with the lowest surface energy and carbon either contributes to the graphene growth, leaving Ni vacancy islands, or diffuses into nickel bulk so that the lowest surface energy phase $\text{Gr}/\text{Ni}(111)$ for this chemical environment is established. However, the graphene is still rotated with respect to the $\text{Ni}(111)$ substrate (Fig. 5.7).

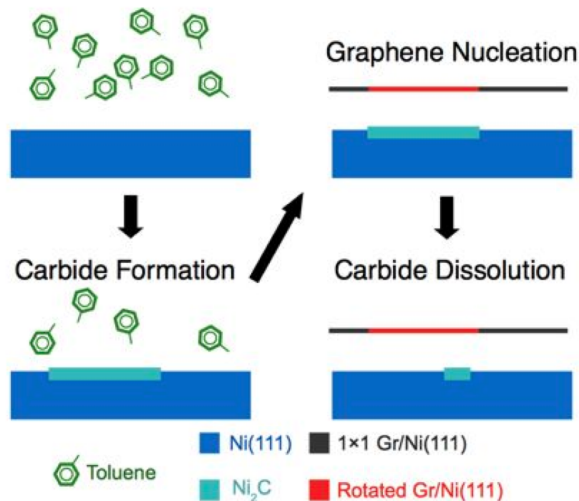


Figure 5.7: Proposed steps in the formation of rotated graphene grains. Taken from Jacobson et al. [152]

Based on observations similar to those shown in Fig. 5.3, Lahiri et al. [155] proposed a different graphene growth model assuming the in-plane transformation of Ni₂C into graphene at low temperatures (< 460 °C). The FFT analysis however, proves that graphene is adsorbed on Ni₂C. Furthermore, the Supporting Information (Fig. S8) in Jacobsen et al. [152] confirms the assumption that Lahiri et al. did not observe the direct transformation of Ni₂C into graphene but also observed graphene on Ni₂C.

5.5 Computational Methods

Spin-polarized DFT calculations were performed with the VASP code using PAW potentials. As standard GGA potentials predict an endothermic adsorption of graphene on Ni(111) due to the neglect of the vdW contributions (see section 3.1.3) the calculations were performed on the basis of vdW-DF using the optB88-vdW exchange-correlation functional [99], which offers a good description of the interaction of graphene and nickel as compared with gold-standard-RPA calculations [43], and also with the LDA functional. The energy cutoff employed for both functionals was 400 eV. The nickel lattice constant was optimized for the respective functional, 3.43 Å for LDA calculations and 3.51 Å for optB88-vdW (which is close to the experimental lattice constant of 3.52 Å). The system was modeled with a ($\sqrt{39}R16.1^\circ \times \sqrt{37}R-34.7^\circ$) slab consisting of three supportive layers of nickel and a vacuum of more than 10 Å. The geometry of the two bottom nickel layers was fixed. The graphene sheet was adsorbed on the Ni₂C surface in the orientation of the Ni(111) substrate leading to a slight deformation of the graphene sheet, which introduces an error of less than 0.008 (vdW-DF: 0.007) eV/C atom. A $2 \times 2 \times 1$ k-point mesh was employed for the integration of the Brillouin zone. The formation energies of the diluted carbon were evaluated from a bulk cell of 32 nickel atoms both at a fixed volume (LDA: 0.52 eV, vdW-DF: 0.78 eV/C atom) and at an optimized volume (LDA: 0.44 eV, vdW-DF: 0.71 eV/C atom). All LDA structures were relaxed to forces lower than 0.02 eV/Å. The same geometries rescaled with the optB88-vdW nickel bulk lattice constants were used for the vdW-DF calculations.

5.6 Conclusion

In a combined STM/DFT study, the surface carbide Ni_2C was identified as the source of rotated graphene grains observed on the Ni(111) surface by STM. These rotated grains are unexpected given the widely reported 1×1 epitaxial match between Ni(111) and graphene. Ni_2C is only found below rotated graphene grains, and nickel vacancy islands are found within and at the periphery of rotated grains – a clear indicator of carbide dissolution. DFT calculations predict that the graphene/ Ni_2C /Ni(111) phase is stable when the carbon chemical potential is determined by the dilute carbon reservoir and predict a transformation to the graphene/Ni(111) as the dilute carbon reservoir (i.e., the Ni bulk) is depleted. Grain rotation is facilitated by the weak BE of graphene on Ni_2C , and calculations indicate that adsorption is dominated by the vdW interaction.

Chapter 6

Graphene on Ir(111)

The main results of section 6.2 were published in *Sci. Rep.*, 3 (2013), *Electronic structure and imaging contrast of graphene moiré on metals* [168], where the present author contributed to the DFT calculations.

Graphene on Ir(111) is a typical example of a weakly interacting Gr-metal system. In a study by N'Diaye et al. [33] using STM and DFT methods, the structure of graphene on Ir(111) was identified on an atomistic level. Due to the mismatch of the lattices a long-range moiré with three local high-symmetry regions (*FCC*, *HCP*, and *ATOP*) was found which may serve as sample surface for growing small metal clusters of well defined size into the moiré, allowing experiments on charge carrier manipulation through periodical potentials [169]. However, standard DFT functionals like LDA and GGA (used by [33]) are (semi-)local and lack the nonlocal-correlation effects responsible for vdW interaction [170]. GGA calculations showed very weak binding (20 meV/C) and a large Gr-Ir distance of ≈ 3.9 Å [11] while with LDA the binding is stronger, reflecting mainly the well known tendency of LDA to overbind. Busse et al. [11] included vdW forces on the level of force-field vdW corrections (PBE+Grimme) [78] to relax the structures and obtained the total energy with vdW-DF [171] using the relaxed PBE+Grimme geometry. It was further shown that GGA alone does not bind graphene for vdW corrected distances which have been determined with a mean value of 3.41 Å, close to an experimental value of 3.38 ± 0.04 Å [11].

The band structure of Gr/Ir(111) was studied by Pletikosić et al. [10] with angle-resolved photoelectron spectroscopy (ARPES) exhibiting a graphene Dirac cone only

slightly shifted to smaller binding energies due to a marginal p -doping by the substrate. Furthermore, the moiré structure imposes a superperiodic potential giving rise to Dirac cone replicas and the opening of minigaps [10].

In this chapter the Gr/Ir(111) structure calculated with optB86b vdW-DF is presented and compared with previous results. Furthermore, the results of a joint experimental theoretical study on the electronic structure and imaging contrast on Gr/Ir(111) [168] are discussed. By applying a combination of DFT calculations, STM and atomic force microscopy (AFM) measurements, a deeper insight into the electronic and topographic contributions to the imaging contrast of the epitaxial Gr/Ir(111) system is gained. In STM imaging the electronic contribution is found to prevail over the topographic one, and in AFM a variation of the interaction strength between the tip and graphene for the different high-symmetry areas of the graphene moiré supercell is observed [168].

6.1 Lattice Mismatch and Moiré Unit Cell

The lateral lattice constants of graphene and Ir(111) summarized in table 6.1 show the large lattice mismatch of more than 10 % between graphene and Ir(111). The overbinding of LDA is less pronounced for an iridium substrate as compared to nickel (see section 3.1.2) leading to a lattice constant (2.706 Å) which is in good agreement with the experimental value of 2.71 Å. The iridium lattice constants obtained with the other functionals are all less than 1.5 % larger than the experimental lattice constant.

	a_{Gr} [Å]	$a_{\text{Ir}}^{\text{lat}}$ [Å]	$(a_{\text{Ir}}^{\text{lat}} - a_{\text{Gr}}) / a_{\text{Gr}}$ [%]
experimental	2.46 [19]	2.71	10.16
LDA	2.447	2.706	10.58
PBE	2.468	2.747	11.30
PBE+Grimme	2.468	2.670	11.30
optB88-vdW	2.463	2.747	11.53
optB86b-vdW	2.465	2.735	10.95

Table 6.1: Experimental and calculated lattice constants of Gr and Ir.

If graphene would grow in 1×1 structures an enormous strain would be induced due to the large lattice mismatch. Therefore it is energetically favorable to form a moiré structure instead of the epitaxial 1×1 , as observed in experiments [33, 172, 173].

In Gr/Ir(111) the graphene and iridium lattices are often not rotated against each other [33, 172], therefore the distance between two moiré maxima $a_{\text{moiré}}$ can be expressed as

$$\frac{2\pi}{a_{\text{moiré}}} = \frac{2\pi}{a_{\text{Gr}}} - \frac{2\pi}{a_{\text{Ir}}^{\text{lat}}}. \quad (6.1)$$

The value measured for $a_{\text{moiré}}$ is $25.3 \pm 0.4 \text{ \AA}$, which equals 9.32 ± 0.15 times the iridium nearest neighbor distance, $a_{\text{Ir}}^{\text{lat}}$ [33, 172].

For DFT calculations, a 10×10 graphene ad-layer on a 9×9 Ir(111) slab is a very good approximation to the experimentally found moiré structure. The supercell shows three high-symmetry regions (Fig. 6.1), top-fcc, top-hcp, and hcp-fcc. The nomenclature is in line with previous chapters, e.g. in top-fcc, one carbon atom is on top of an interface nickel and the other carbon is above a nickel atom of the third layer, slightly different than the nomenclature used by N'Diaye et al. [33] who designate *ATOP*: hcp-fcc, *FCC*: top-hcp and *HCP*: top-fcc. In addition to the high-symmetry regions, the lower-symmetry sites¹ bridge-top, bridge-hcp, and bridge-fcc appear three times in each case because of the three-fold symmetry.

The Gr-Ir distances in the relaxed structure are in very good agreement with the PBE+Grimme calculations by Busse et al. [11] and by Voloshina et al. [168] (table 6.2). The maximum graphene height is reached in the hcp-fcc region with 3.65 \AA and the minimum height at top-hollow sites (top-fcc and top-hcp nearly identical). The average distance of 3.42 \AA is within the experimental range $3.38 \pm 0.04 \text{ \AA}$ [11]. The large Gr-Ir separation indicates a weak interaction with small BEs.

The average BE per carbon atom for the relaxed structure is 80 meV for the optB86b vdW-DF, which is larger than the value obtained by Busse et al. (50 meV/C) [11], but still a typical adsorption energy for physisorbed systems. Computationally highly demanding RPA benchmark calculations like for Gr/Ni(111) are not available because of the too large unit cell. However, Olsen et al. [37] studied weakly interacting systems with smaller lattice

¹The 1×1 adsorption configurations illustrated in Fig. 3.3 for graphene on fcc-Ni(111) are similar for graphene on fcc-Ir(111).

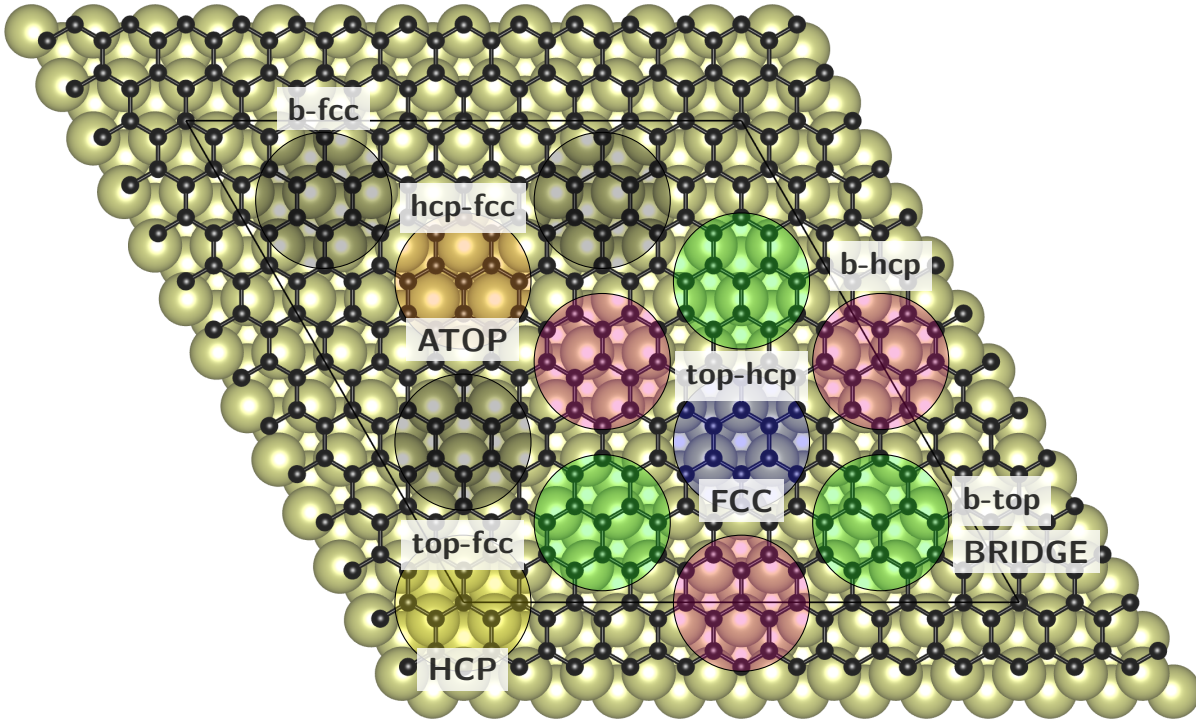


Figure 6.1: Structure of the Gr/Ir(111) moiré cell used in DFT calculations. A 10×10 graphene layer is above a 9×9 iridium substrate. The high-symmetry regions are indicated as circles filled with orange (fcc-hcp | *ATOP*), blue (top-hcp | *FCC*), and yellow color (top-fcc | *HCP*). The notation written in capital letters, where the center of a graphene hexagon is at a top, fcc, and hcp-site for *ATOP*, *FCC*, and *HCP*, respectively is used in this section. The lower symmetry regions bridge-top | *BRIDGE*, bridge-hcp, and bridge-fcc are indicated with circles filled with green, magenta, and black, respectively. All low symmetry regions occur three times in the unit cell. Replicas at the boundary of the unit cell are not plotted. In the fcc-hcp region the carbon atoms cover the threefold coordinated hollow sites. In the top-fcc and top-hcp regions every second atom is located above an iridium surface atom and every second atom at fcc and hcp sites, respectively.

Ref.	d_{\max} [Å]	d_{\min} [Å]	\bar{d} [Å]	Δd [Å]
(*)	3.65	3.30	3.42	0.35
[11]	3.62	3.27	3.41	0.35
[168]	3.58	3.27	-	0.31

Table 6.2: Comparison of the maximum height, minimum height, average height, and corrugation $\Delta d = d_{\max} - d_{\min}$ for Gr/Ir(111).

(*) Present results (optB86b vdW-DF)

mismatch such as Gr/Al(111), Gr/Ag(111), and Gr/Au(111) by using RPA on a $\sqrt{3} \times \sqrt{3}$ unit cell. On the one hand, the largest BEs at typical vdW distances ≈ 3.4 Å were found to be about double the values obtained with LDA and vdW-DF². On the other hand, the BE for an artificial 1×1 structure at the lattice constant of unsupported graphene (i.e. iridium lattice constant compressed by 11 %) and optimized for optB86b-vdW yields 75 meV, while the corresponding BE for optB88-vdW is only 66 meV. Hence, although here the optB86b-vdW functional might overestimate the interaction strength, vdW-DF functionals may underestimate it in general. Therefore, the value of the true BE remains an open question and its determination must be postponed to future studies.

Despite the small BEs Busse et al. [11] showed that the binding is not pure physisorption, but is chemically modulated. In the top-fcc and top-hcp³ regions a small charge redistribution from graphene toward the iridium substrate, caused by the adsorption, takes place. The p_z orbital of a top-site carbon atom hybridizes with the underlying Ir $5d_{3z^2-r^2}$ orbital. The charge is provided from the neighbor carbon atom, which explains their tendency to bind additionally deposited metal atoms [33]. This charge transfer is intimately related to the nonlocal part of the BE density [11], which is missing in LDA and PBE. As a result a slight p -doping where the Dirac point is shifted by ≈ 100 meV above the Fermi level [168] is predicted, which is close to the data obtained by photoelectron spectroscopy [10].

²The original vdW-DF proposed by Dion et al. [92] was used.

³In the original notation of Busse et al. [11], top-fcc corresponds to the *HCP* region and top-hcp to the *FCC* region.

Further insights in the electronic structure of Gr/Ir(111) by analyzing the band structure and core level shifts is postponed to chapter 7, where the results for Gr/Ir(111) are compared to nickel intercalated Gr/Ir(111).

6.2 Electronic Structure and imaging Contrast

In the joint experimental and theoretical study of Voloshina et al. [168], the moiré pattern of Gr/Ir(111) is easily recognizable in LEED and the large-scale STM images in Fig. 6.2a. The distance between two moiré maxima $a_{\text{moiré}}$ is 25.5 Å and 25.2 Å, obtained by LEED and STM respectively, in good agreement with previously published data [33, 172]. The STM structure is imaged in the so-called *inverted contrast* [172] (Fig. 6.2a,b), where topographically highest *ATOP* places are imaged as dark and topographically lowest *HCP* and *FCC* ones as bright regions. By performing “on-the-fly” switching between constant current (CC) STM and constant frequency shift (CFS) AFM imaging during scanning (Fig. 6.2c), an inversion of the topographic contrast $z(x, y)$ is observed. This is clearly seen in Fig. 6.2c around areas marked with an arrow: darkest contrast in CC STM becomes the brightest one in CFS AFM for the *ATOP* position. The imaging contrast strongly depends on the experimental conditions.

6.2.1 Contrast Inversion in CC STM

The inversion of the imaging contrast was also detected in CC STM images when the bias voltage is changed from -0.5 V to -1.8 V during scanning (Fig. 6.2a). The simulated STM image [168] (Fig. 6.3b) using the Tersoff-Hamann formalism [118] is in good agreement with the experimental image. The inverted contrast arises because of the dominant role of certain peaks in the local DOS (see Fig. 6.3c) for specific regions in the moiré unit cell [168].

The electron density difference induced by the adsorption (lower inset in Fig. 6.3c) shows an increase of charge in *FCC*, *BRIDGE*, and *HCP* regions between graphene and interface iridium atoms indicating the stronger binding in this regions compared to *ATOP*.

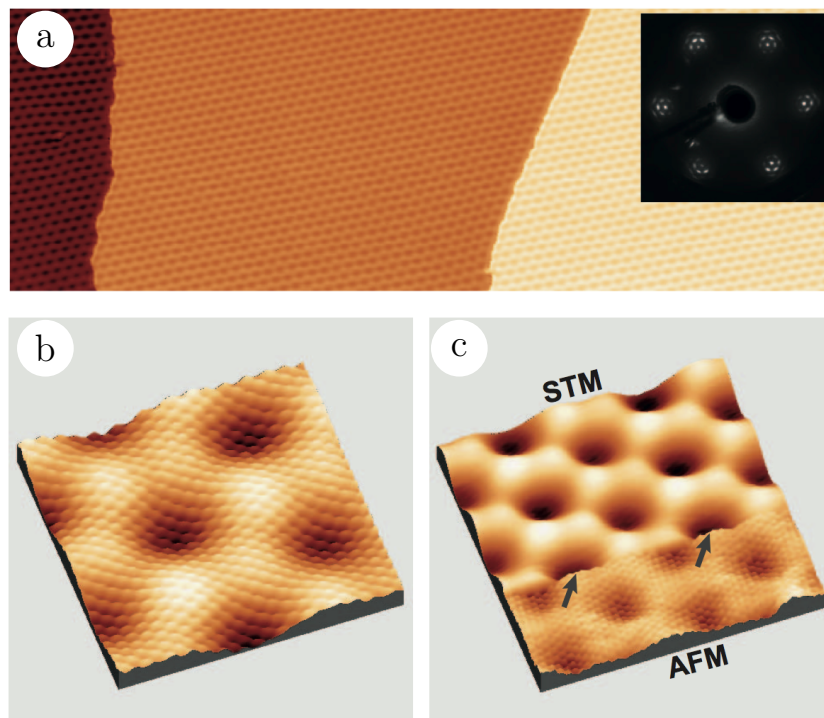


Figure 6.2: (a) Large scale STM image of Gr/Ir(111) and the corresponding LEED image as inset. (b) Atomically resolved STM image showing the inverted contrast. (c) A combined STM/AFM image with a switching “on-the-fly” between CC STM and CFS AFM image during scanning. Taken from Voloshina et al. [168]

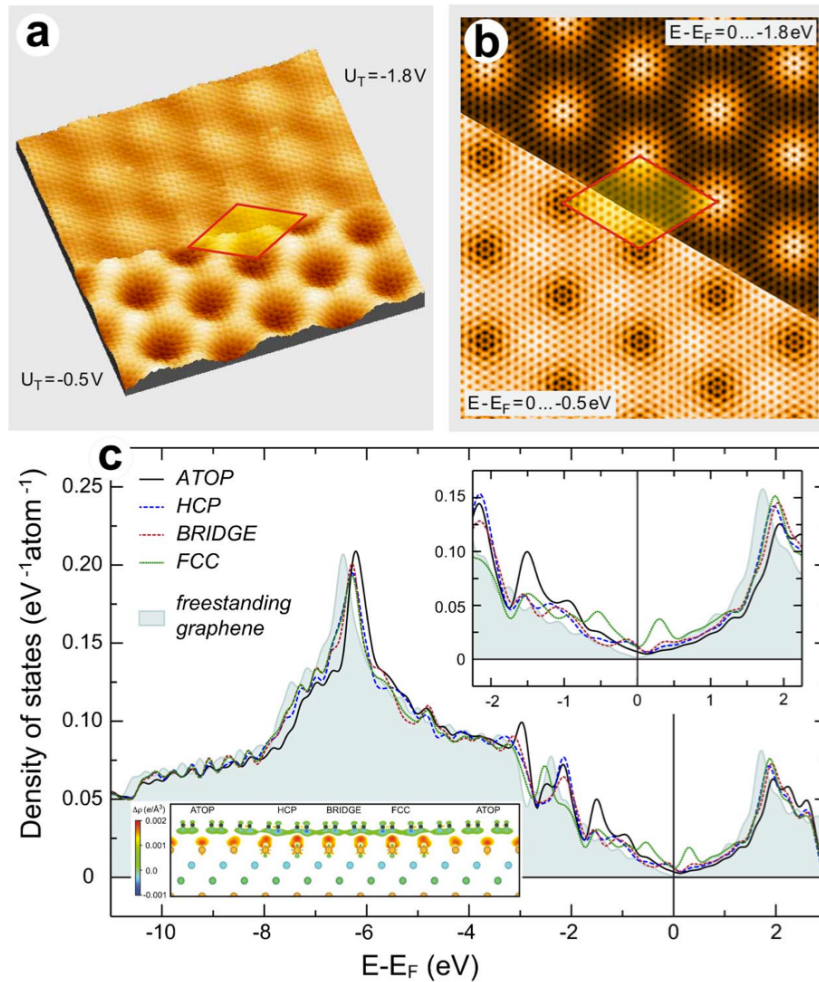


Figure 6.3: Experimental (a) and calculated (b) CC STM images of Gr/Ir(111) obtained at -0.5 V (bottom) and -1.8 V (top) bias voltage. (c) DOS projected on carbon atoms for all high-symmetry regions of Gr/Ir(111) with a zoom-in around the Fermi energy in the top-right inset and the electron density difference induced by adsorption in the lower inset. Taken from Voloshina et al. [168]

6.2.2 Contrast Inversion in AFM

The contrast in the AFM measurements depends on the tip-sample distance, the local region in the moiré and the used bias voltage, which will be discussed in the following. The frequency shift $\Delta f(d)$ of an oscillating sensor as a function of the distance from the surface is shown in Fig. 6.4a,b. The corresponding tunneling current (Fig. 6.4c) is needed to get the relative z-positions. The frequency shift is related to the interaction energy E and the vertical force F_z through following expressions

$$\Delta f(d) = -\frac{f_0}{2k_0} \frac{\partial F_z(d)}{\partial d} \quad (6.2)$$

$$F_z(d) = -\frac{\partial E(d)}{\partial d}. \quad (6.3)$$

The frequency shift is proportional to the negative derivative of the force and to the second derivative of the interaction energy, f_0 and k_0 are the resonance frequency and the spring constant of the sensor. Repulsive, attractive, and long-range electrostatic and vdW contributions can be separated in AFM imaging [174]. At large tip-sample distances ($> 5 \text{ \AA}$) the imaging contrast is insensitive to the local atomic structure of sample and scanning tip because the long-range vdW interactions are dominant. In the short-range around the minimum of the Δf curves, the interactions are dominated either by repulsive (left-hand side) or attractive (right-hand side) forces and define the atomically-resolved site-selective chemical contrast. The site-selective interaction is clearly observable in the $\Delta f(d)$ curves of Fig. 6.4a,b. On the one hand the absolute value of the maximum frequency shift is larger in the *FCC* and *HCP* region than in the *ATOP* region and on the other hand the minima of the $\Delta f(d)$ curves are shifted by 0.97 \AA compared to a corrugation of Gr/Ir(111) in CC STM of 0.67 \AA , reflecting the different interaction strength for different regions in the moiré cell.

Furthermore, DFT simulations by Ondráček et al. [174] of two different tips interacting with graphene showed that the imaging contrast also depends on the tip reactivity. The vdW contributions are dominating for a weakly reactive silicon tip whereas short-range forces are only small. Here the contrast between different sites appears in the repulsive region while for a tungsten tip the short-range forces dominate and therefore determine the atomic contrast in the attractive regime. Therefore, a hexagonal pattern of bright

spots was observed for the weakly interacting silicon tip but the honeycomb pattern with inverted contrast in the repulsive regime is seen for a strongly interacting tungsten tip.

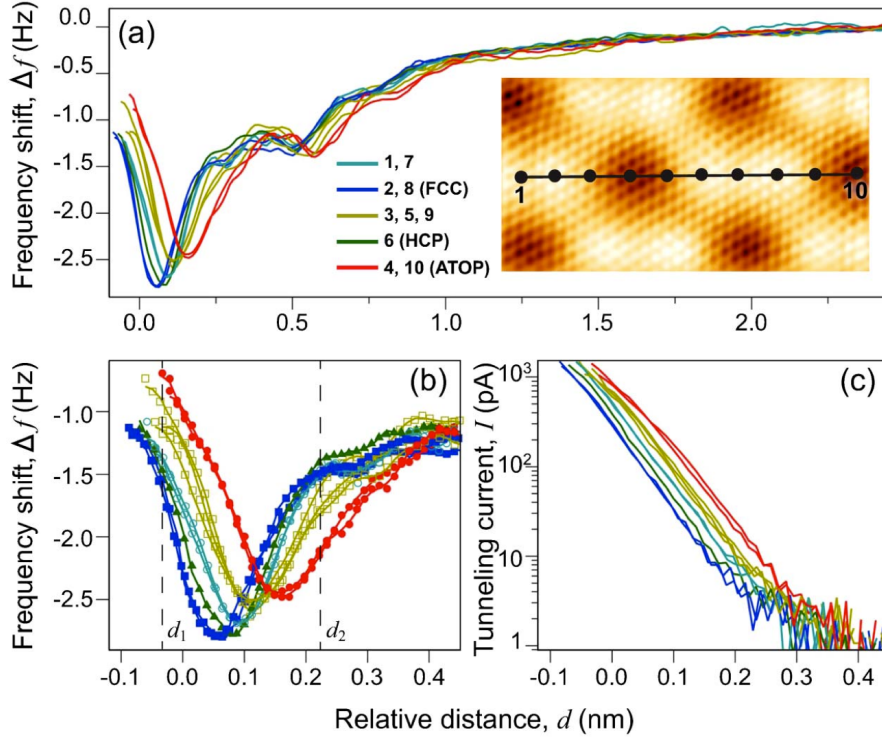


Figure 6.4: Experimental frequency shift obtained in AFM measurements (a,b) and the corresponding tunneling current (c) as a function of the relative distance between tip and the Gr/Ir(111) sample. The inset of (a) shows the corresponding STM image with the path where Δf and I data were measured. Taken from Voloshina et al. [168]

In constant height (CH) AFM experiments⁴ the contrast in $\Delta f(d)$ images is changing for different heights and completely inverted for two limit z -positions ($d_1 = -0.033$ nm and $d_2 = +0.227$ nm, Fig. 6.5). In the vicinity of the surface, the interaction has more repulsive character leading to a smaller frequency shift in *ATOP*, and larger shifts in *FCC* and *HCP* regions. At larger distances the interaction is more attractive and frequency shifts in *FCC* and *HCP* regions are smaller and correspondingly the shifts are larger in the *ATOP* region. The modified frequency shifts at different distances is again founded in a different interaction strength depending on the actual position. The contrast in tunneling current images otherwise, shows the same *inverted* contrast for both distances (lower row

⁴In constant height AFM experiments the z -coordinate of the oscillating sensor is fixed during scanning.

in Fig. 6.5). Furthermore, the change of bias voltage during CH AFM imaging does not lead to any changes in the imaging contrast for Δf or I . Thus, taking into account the contrast inversion in CC STM for different bias voltages and a similar variation of the distances of CC STM and CH AFM (when U_T is changed from -0.5 V to -1.8 V), one can separate the topographic and electronic contributions for imaging at different biases and distances.

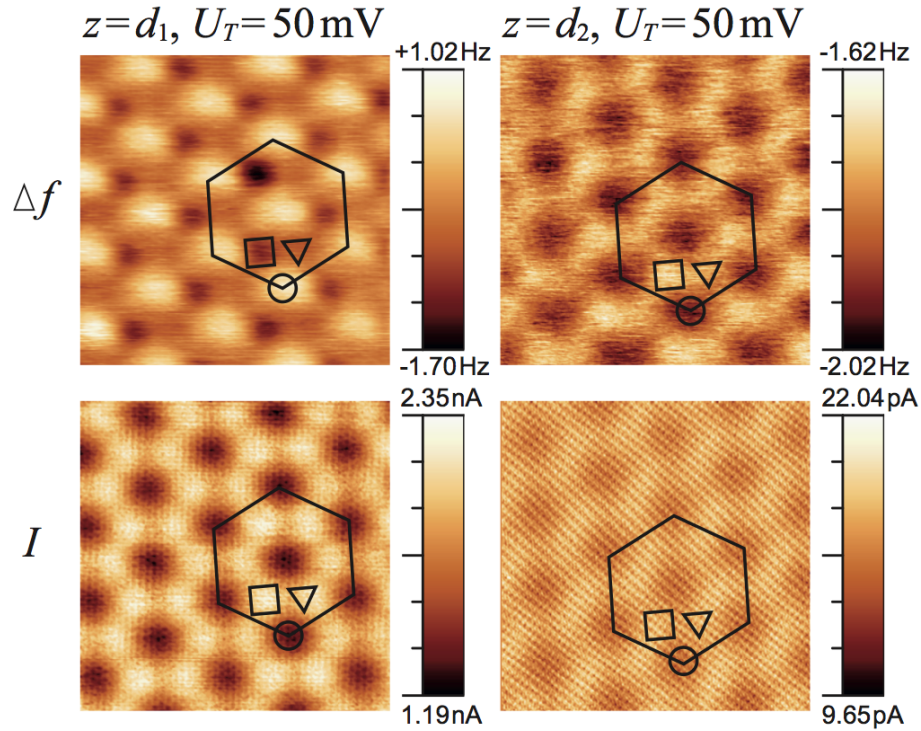


Figure 6.5: Frequency shift (upper row) $\Delta f(x, y)$, and tunneling current $I(x, y)$ (lower row) of constant height AFM measurements of Gr/Ir(111), obtained at two different sensor-substrate distances d_1 and d_2 . High symmetry regions are indicated with a circle (*ATOP*), square (*FCC*), and triangle (*HCP*). For different distances the contrast in the frequency shift is inverted whereas the contrast in the tunneling current is not inverted. Taken from Voloshina et al. [168]

A first approximation via DFT calculations of the experimentally obtained AFM images can be given by expressing the tip-sample force as a function of the potential $V_{ts}(\mathbf{r})$ on the tip $F_{ts} \propto -\nabla[|\nabla V_{ts}(\mathbf{r})|^2]$ [175]. The results of such DFT simulations [168] (Fig. 6.6a) can sometimes offer an initial view on the expected topography. However, the interaction

of the scanning tip with the sample is not taken into account and therefore the results of this analysis should be assessed by other methods.

Within another more quantitative approach, the W-tip is explicitly included in the calculations. In the present study, it was approximated by a five-atom pyramid as shown schematically in Fig. 6.6b and the interaction energy was explicitly calculated for varying tip-surface distances [168]. The interaction energy for the two limiting positions of the W-tip, *ATOP* and *FCC*, is shown in Fig. 6.6c. The Morse potential was used to fit the calculated data as this was shown to be the most suitable for graphene-metal systems [176]. The resulting curves are shown by solid lines in the same figure. The force and frequency shift are calculated according to Eqs. 6.2 and 6.3.

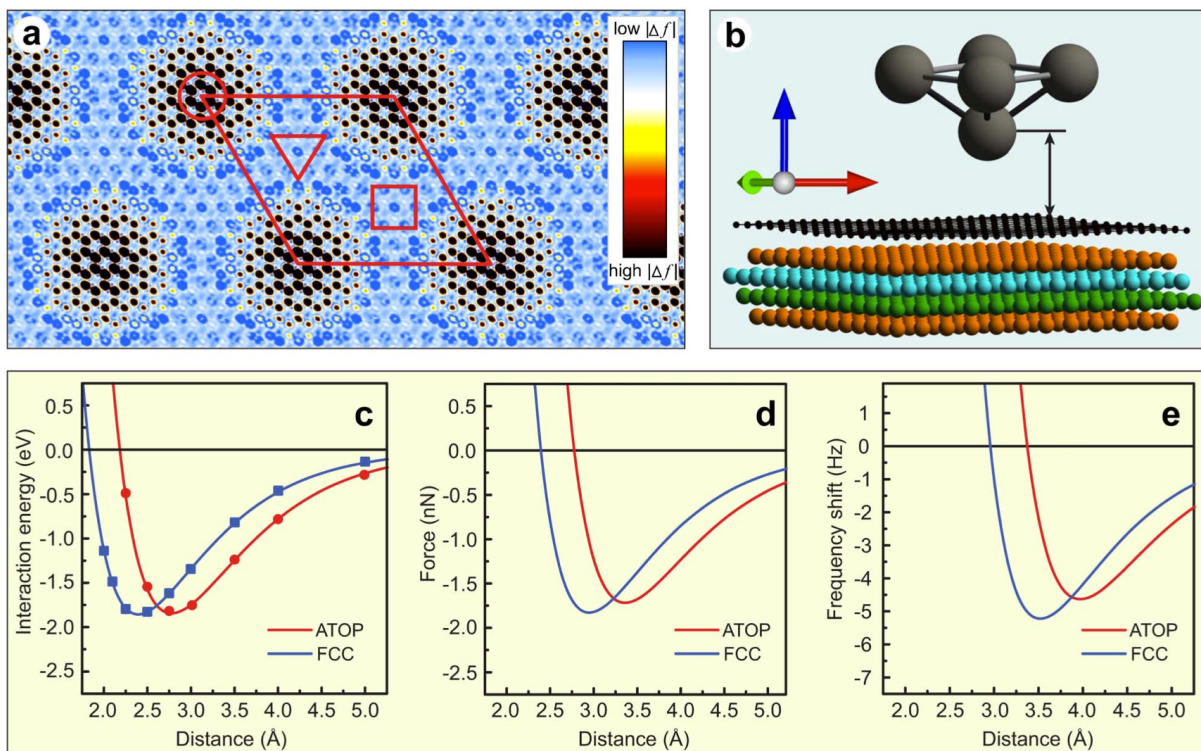


Figure 6.6: (a) Simulated CH AFM image of the Gr/Ir(111) system according to the approach suggested by [175]. (b) Schematic representation of the geometry of the 5-atom-W-tip/Gr/Ir(111) model [168]. Interaction energy (c) force (d) and frequency shift (e) for the system illustrated in panel b as a function of the distance between the model tip and Gr/Ir(111). Taken from Voloshina et al. [168]

The interaction energy curves from DFT calculations [168] (Fig. 6.6c) for both high-symmetry regions are very similar but shifted by 0.40 \AA with respect to each other reflecting the height difference between *ATOP* and *FCC* regions. The maximal absolute value of energy is slightly higher for *FCC* by 0.015 eV . The minima in the force and frequency shift curves are more distinct at larger distances. The *ATOP* and *FCC* extrema in the frequency shift curve are separated by 0.45 \AA , which is approximately two times larger than the experimental values. Nevertheless, the shape and trend for the inversion of the imaging contrast are clearly reproducible with the calculated data. Also the larger absolute value of the frequency shift in the *FCC* compared to *ATOP* is correctly reflected in the calculated curves.

However, relaxations of Gr/Ir(111) and the W-tip are not taken into account by these calculations. Therefore, to get more reliable results, in a more realistic DFT model a ten atom tungsten tip (10W-model) was used (with a geometry similar to the tip used in Ref. [174]) where the five tungsten atoms of the tip nearer to the surface as well as the top-most layer of the iridium substrate were allowed to relax. In this calculations the tip is in the *FCC* region of the moiré cell. In addition to the Grimme method [78], where the vdW interactions are accounted for by a simple force-field correction, the more advanced optB86b-vdW functional [92] was applied. Differences to the former model (5W-model, blue curves in Fig. 6.6) are visible already in the static calculations (green curves and red plus symbols in Fig. 6.7), due to the larger tip and the different functional. While the shapes of all three curves are similar for both models the absolute values and the positions of the minima differ slightly. The minima in the interaction energies are found at $\approx 2.3 \text{ \AA}$ for both cases, but the absolute values of the energy are larger for the 10W-model. At the minimum the interaction energies differ by 0.4 eV which reflects the additional binding contributions for the larger tip but may also be related to the different used exchange-correlation functionals. The minimum for the force is shifted to a larger tip-sample distance for the 10W-model and the absolute force is about 0.7 nN larger compared to the 5W-model. Each of the five additional tungsten atoms in the 10W tip experiences an additional force which increases the total force accordingly. The most noticeable difference is a three times larger frequency shift for the 10W-model compared to the 5W-model.

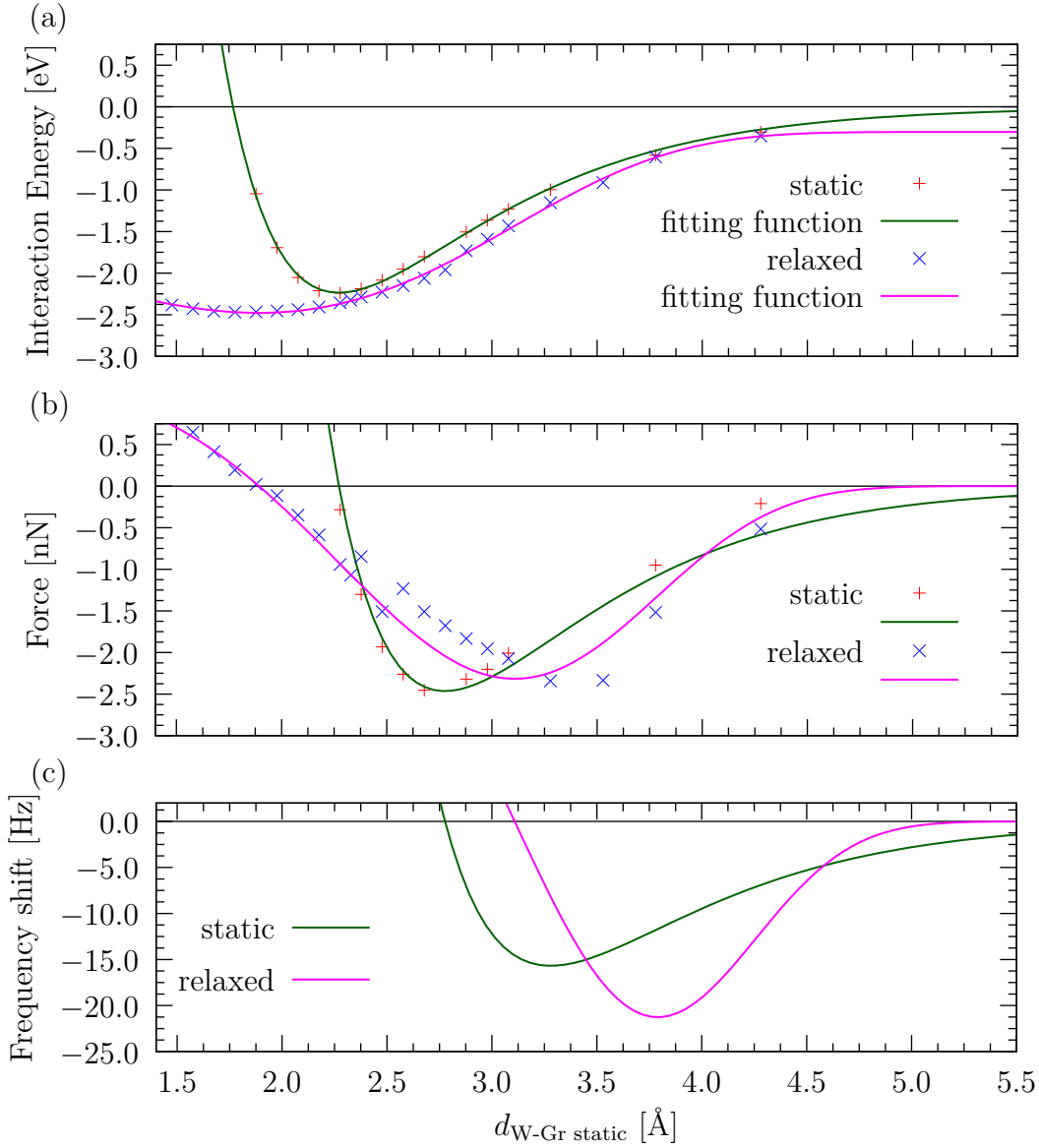


Figure 6.7: Interaction energy (a), force (b), and frequency shift (c) as a function of the distance for the rigid system $d_{\text{W-Gr static}}$ (see Fig. 6.6) for a tungsten tip consisting of ten atoms at the *FCC* region in the moiré unit cell. The calculated interaction energies and forces as marked by plus symbols and crosses, respectively. The Morse potential was used to fit the energy curve for static calculations (green line in panel a). The fitting function for the energy of the relaxed system is a more complex function (magenta line in panel a). The curves in panel b and c displaying the force and frequency shift are evaluated from the fitted interaction energy curve (a) according to Eqs. (6.3) and (6.2), respectively. The crosses in (b) correspond to the values directly determined by the DFT calculation.

When the five lower tip atoms and the top-most iridium layer are allowed to relax, the curves are drastically changing compared to the static calculations. The interaction energy is increased at all tip-surface distances (Fig. 6.7a) but instead of a sharp minimum at 2.3 Å for the unrelaxed system, the minimum is flat with almost the same interaction energies of ≈ 2.5 eV between 1.5 and 2.25 Å distance. Therefore, the system gains 0.2 eV binding energy due to the relaxation. The force curve on the other hand is almost linear in the range of 1.5 to 3.25 Å tip-sample distance (Fig. 6.7b) and the extremum is reached at 0.4 Å larger distance compared to the static calculations. The absolute value of the force, however, is only slightly reduced. A considerably larger frequency shift is calculated for the relaxed system due to a more rapid decrease of the force curve. This is partially an artifact of an unfavorable fitting function for the interaction energy, which is parallel to the x-axis at distances of more than 4.3 Å. Moreover, the minimum of the frequency shift is shifted to a 0.5 Å larger Gr-substrate distance. However, the discrepancy between the small experimentally obtained frequency shifts (< 3 Hz) and the calculated values is probably due to the oscillation amplitude of the sensor (1-3 Å). For the interpretation of these curves, it should be noticed that the x-coordinate in Fig. 6.7 is the tip-sample distance of the rigid model $d_{\text{W-Gr static}}$ for both, static and relaxed calculations (Fig. 6.8b).

The reasons for the anomalous relaxation curves can be understood by considering the evolution of the relaxed structures (Fig. 6.8a) when starting at a large tip-sample distance and in the following continuously approaching the surface. The energies and forces are very similar to the unrelaxed (static) ones for large distances (> 4.3 Å) where forces are very small, indicating that relaxation effects are negligible, i.e. the Gr/Ir(111) moiré structure is intact and the forces acting on the tip lead to only minor changes of the tip shape. Indeed, the actual distance between the tip and graphene $d_{\text{W-Gr}}$ is almost the same compared to the static tip-Gr distance $d_{\text{W-Gr static}}$ in Fig. 6.8a while the local distance between graphene and the top-most iridium layer is approximately the unperturbed C-Ir distance of this specific region in the moiré unit cell (FCC).

If the distance is further decreased (from 4.3 Å to 3.5 Å), the attractive forces (mainly vdW) acting on the carbon atoms of the weakly coupled graphene sheet lead to a local deformation so that the graphene iridium distance (at the tip position) is increased (blue curve in Fig. 6.8a) reaching its maximum at $d_{\text{W-Gr static}} = 3.5$ Å. Furthermore, the W-tip

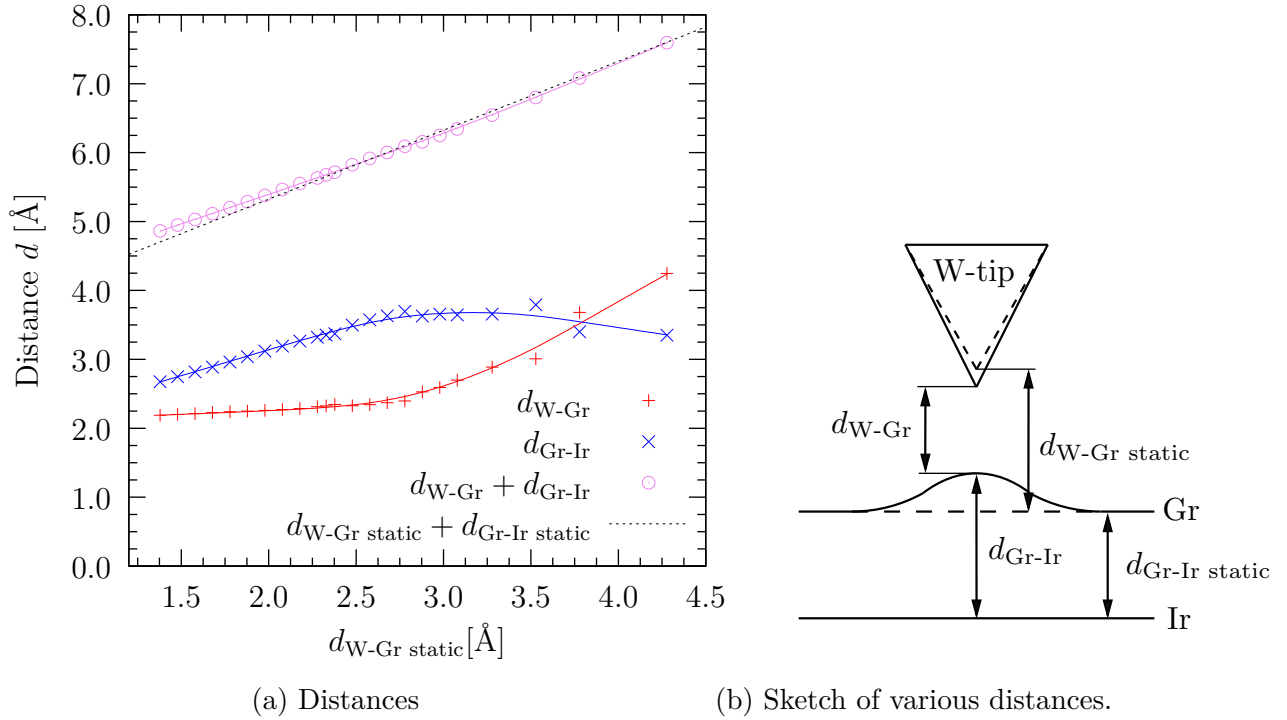


Figure 6.8: (a) Different distances sketched in panel b as a function of the static tip-surface distance $d_{W-Gr\ static}$, which is equivalent to the distance between the unrelaxed W-tip and the unrelaxed graphene sheet (dashed lines in panel b). The actual distance between the tip and graphene including relaxation effects d_{W-Gr} plus the actual Gr-Ir distance d_{Gr-Ir} is almost a linear function of the distance $d_{W-Gr\ static}$. The difference to the perfectly linear $d_{W-Gr\ static} + d_{Gr-Ir\ static}$ function is due to the relaxation of the W-tip, while the corrugation of the iridium layer is negligible.

is also slightly deformed, which is seen in the difference of the dashed line and the violet line in Fig. 6.8a. At distances around 3.5 Å the violet line is about 0.05 Å lower than the dashed line, which means that the W-tip is slightly stretched toward the surface. Both effects result in a larger reduction of the actual tip-surface distance $d_{\text{W-Gr}}$ and consequently in a rapid increase of the forces between 4.3 Å and 3.5 Å where the maximum is already reached at 3.5 Å⁵.

Between 3.5 Å and 2.8 Å tip distance ($d_{\text{W-Gr static}}$) the Gr-Ir distance of approximately 3.7 Å is almost constant, i.e. a local outwards deformation of graphene by 0.3 Å compared to Gr/Ir(111) without tip, while the tip is constantly getting closer to the graphene surface, which is observable by a linear red curve in this region with a similar gradient as the unrelaxed distance $d_{\text{W-Gr static}} + d_{\text{Gr-Ir static}}$ in Fig. 6.8a. When the distance between the W-tip and graphene $d_{\text{W-Gr}}$ is smaller than 2.4 Å a repulsive interaction between carbon atoms of graphene and tungsten atoms of the tip prevents a further decrease of the tip-Gr distance. From that point on, the Gr-Ir distance is linearly reduced, i.e. the deformation is first reduced until the equilibrium structure of Gr/Ir(111) without tip is reached again at $d_{\text{W-Gr static}} = 2.3$ Å. Thereafter, graphene is deformed in the other direction, i.e. toward the iridium substrate. The equilibrium position (total force on tip equals zero) for the tip is reached at $d_{\text{Gr-Ir}} = 3.0$ Å, however, the tip is compressed in this region. On the left side of Fig. 6.8a the force is still in a linear relation to the distance $d_{\text{W-Gr static}}$. It is expected that this linearity is lost for $d_{\text{Gr-Ir}}$ smaller than ≈ 2.3 Å when the repulsion between the carbon atoms of the depression and the iridium substrate becomes stronger and the interaction energies are decreasing. Further calculations must be performed to prove this assumption.

Therefore, the relaxation of the system has a strong influence of the actual shape of the measured frequency shift curves. However, for a detailed analysis, other tip positions in the moiré cell, e.g. *ATOP*, *HCP*, must be considered, as well as different local positions, e.g. top-site vs. hollow-site in each high-symmetry reason. Consequently, the present calculations already sketch the changes stemming from the relaxation of the tip, but for a complete analysis of the experimental curves further calculations must be per-

⁵The minimum of the forces predicted by the fitting curve is shifted to the left, however the actual minimum can be identified by the crosses in Fig. 6.7

formed. Moreover, the actual atomic structure of the tip is not known and there is a small uncertainty in the tip position during the measurements of the Δf curves which makes a rigorous simulation difficult. Nevertheless, the basic mechanism of the contrast inversion can already be understood on the basis of DFT simulations using the rigid 5W-tip model.

6.3 Methods

Spin-polarized DFT calculations were performed with the VASP code using PAW potentials and an energy cutoff of 400 eV. Standard (semi-)local LDA and GGA functionals do not account for vdW interactions, which is crucial for weakly interacting systems such as Gr/Ir(111) [11]. Therefore, the calculations in section 6.1 and AFM simulations with the relaxed 10W tip in section 6.2 were performed using the optB86b-vdW functional [99] to account for the long-range vdW interaction. The Gr/Ir(111) structure is modeled using a supercell with a (9×9) lateral periodicity of three iridium layers and (10×10) graphene adsorbed on top with a lattice constant of 2.735 Å (2.725 Å) for calculations in section 6.1 (in Ref. [168]). The Brillouin zone is sampled with a $3 \times 3 \times 1$ Γ -centered k-point mesh. The details of the experimentally used equipment and settings for the STM and AFM measurements can be found in Voloshina et al. [168].

6.4 Conclusion

In conclusion, the ab initio calculations give an accurate description of the structure of the graphene mesh supported on Ir(111), and allow to identify the origin of the experimentally observed contrast inversion in STM and AFM measurements. The lattice mismatch between graphene and iridium and the weak Gr-Ir interaction lead to a moiré pattern with a large average Gr-Ir separation of 3.42 Å and a small corrugation of the graphene film of 0.35 Å. The maximum Gr-Ir distance is reached in the hcp-fcc (ATOP) region whereas top-hollow and bridge-like configurations are closer to the surface, reflecting a stronger and weaker interaction in the respective regions. The structure was relaxed by using the optB86b-vdW functional which gives similar results to the data obtained with PBE+Grimme [11], but an average binding energy per carbon atom of 80 meV is con-

siderably larger than the PBE+Grimme value of 50 meV [11]. Nevertheless, the Gr-Ir system can be considered as weakly interacting system which is also confirmed by a linear dispersion relation in the band structure and in only one peak obtained by core level measurements and calculations in the following chapter.

A combination of DFT calculations and scanning probe microscopy/spectroscopy allowed to distinguish between topographic and electronic contribution of the imaging contrast observed in STM and AFM experiments on Gr/Ir(111) [168]. The electronic contribution is predominant in STM imaging compared to the topographic one and can explain the contrast inversion for different bias voltages. The contrast in constant height AFM measurements is changing for different tip-sample heights and also depends on the specific region of moiré cell. The AFM images were simulated on the basis of DFT calculations with different levels of sophistication. The site specific contrast could be reproduced already by analyzing the potential [168]. However, for a quantitative comparison with the experiments the interaction energy, force, and frequency shift have to be included in the calculations. Still, additional corrections stemming from the size of the tip and the relaxation effects can play an important role. The contrast inversion can be explained with the rigid 5W-tip model. A stronger interaction strength at the *FCC* site compared to *ATOP* shifts the frequency shift minima to smaller distances and therefore leads to a different imaging contrast depending on the tip-position in the moiré cell as well as to a contrast inversion for different heights [168]. Within the second model, the effect of the relaxation employing the optB86b-vdW functional instead of PBE+Grimme was analyzed for a tip located in the *FCC* region. The relaxation considerably affects the shape of the interaction energy curves and consequently also the force and the frequency shift curves where the minimum of the frequency shift is at larger distances and the absolute value is increased.

Chapter 7

Graphene on intercalated Ni/Ir(111)

The main results of section 7.1 were published in Phys. Rev. B, 87, 035420 (2013), *Artificially lattice-mismatched graphene/metal interface: Graphene/Ni/Ir(111)* [41], where the present author performed the DFT calculations, while the main results of section 7.2 are submitted with the title *Intercalation Mechanism of Nickel in G/Ir(111)* [177], where the present author also performed the DFT calculations.

Graphene on Ir(111) (see section 6) is a weakly interacting system with a large Gr-Ir distance and only small perturbations of the graphene bands. The large lattice mismatch between graphene and iridium leads to a moiré pattern with a small corrugation [11]. Graphene on Ni(111), on the other hand is a strongly interacting system with very small lattice mismatch. Although the BE between graphene and nickel is relatively weak (typical for physisorption), the π -band of graphene is no longer preserved due to a strong hybridization between nickel d -bands and graphene π -bands (see section 3). In section 7.1 an artificially lattice mismatched Gr-Ni interface with one single epitaxial nickel layer in Gr/Ir(111) is studied by STM (Uni Konstanz), ARPES (Elettra Trieste) and DFT including vdW interactions (Vienna), providing a wide characterization of electronic and structural properties [41]. For this system, the lattice mismatch between graphene and the nickel layer is increased, while the local chemical environment is similar to Gr/Ni(111) defining the doping level of the graphene layer. Indeed, the intercalation leads to a *locally* enhanced interaction, resulting in a strong corrugation of the graphene layer. The comparison between Gr/Ni/Ir(111) and Gr/Ni(111) allows to determine the influence of two important factors, lattice mismatch and chemical interaction, which affect the graphene-

metal adsorption.

A study of the intercalation mechanism is presented in section 7.2 [177]. Experimentally, nickel is deposited on Gr/Ir(111) and subsequently annealed at 510-550 °C. As seen in the STM images, nickel clusters are preferentially adsorbed at step edges and also the intercalated nickel is found most often at step edges. This is in agreement with DFT calculations which predict the favorite position for a single adsorbed or intercalated nickel atom at the step edge. The DFT calculations also show that a low diffusion barrier for the nickel between graphene and Ir(111) facilitates the accumulation at step edges. Bordering fcc-hcp regions are avoided by intercalated nickel because the Gr-Ni bonds are weaker in that regions due to the large Gr-Ni separation. Diffusion barriers for nickel passing through the graphene layer are studied for different scenarios. The actual process may involve point defects like single vacancies to explain the high diffusion rates observed in experiments.

7.1 Graphene adsorbed on one Monolayer Ni/Ir(111)

7.1.1 Experimental Background: STM Results

In the STM images performed in the group of M. Fonin [41] the Gr/Ir(111) surface displays large fully graphene covered terraces with several hundreds of nanometers width and straight steps following the direction of the graphene moiré, with distinct fcc-hcp regions and virtually indistinguishable top-hollow (top-fcc and top-hcp) sites. The STM images of Gr/Ir(111) show an inverted contrast as described in Ref. [172], where topographically higher fcc-hcp regions appear as dark depressions in the middle of bright rings. Upon nickel intercalation, the nickel film starts to grow at the step edges, and the STM images show no contrast inversion. In Fig. 7.1a three different regions can be distinguished: Graphene-covered iridium areas (A, C) with inverted contrast and an intermediate area with non-inverted contrast (B) following the geometrical topology, as well as two remaining nickel clusters (in white) on top of graphene with a height in the nanometer range. From the morphology of the sample after intercalation it becomes clear that areas A and C display pristine graphene on adjacent iridium substrate levels, whereas area B corre-

sponds to graphene on a nickel-intercalated region. The area depicted in Fig. 7.1c is analyzed and line profiles across the terraces and histograms showing the distribution of apparent height values are evaluated (Fig. 7.1b).

The moiré pattern of area C continues the pattern of area A whereas the moiré in area B is rotated against the others (Fig. 7.1c). Therefore two line profiles are displayed, where line profile 1 is aligned to the Gr/Ir(111) moiré pattern of area A and C and crosses fcc-hcp positions of Gr/Ir(111), which appear as dark depressions. The second height profile crosses the bright protrusions of terrace B. The STM measurements indicate a significantly enhanced corrugation on terrace B compared to terraces A and C. The histogram in Fig. 7.1b shows the frequency of apparent height values for equally sized areas on terrace A, B and C, respectively, as well as for the complete area in Fig. 7.1c. The distribution for Gr/Ir(111) on terrace A and C is narrow (0.45 Å peak width) and features a distribution maximum reflecting the top-hollow sites and a distinct shoulder at lower apparent height corresponding to the fcc-hcp regions. For nickel intercalated graphene on terrace B the distribution is much wider (0.8 Å peak width) with a maximum 0.6 Å below the maximum of Gr/Ir(111) and a shoulder extending far into the Gr/Ir(111) region. The reason for this change will be discussed on the basis of DFT calculations in the next section. If the intercalated nickel atoms arrange pseudomorphically on the Ir(111) surface with a similar interplane distance, then the distance between equivalent sites in the measurements (e.g. lowest heights on terrace A and B in Fig. 7.1c) reflects to a large extent the difference in the Gr-metal distance. This would mean that graphene on intercalated nickel is on average 0.6 Å closer to the substrate compared to the pristine Gr/Ir(111) with a much larger graphene corrugation. The almost unaffected continuation of the graphene moiré on the intercalated nickel patches – albeit with increased corrugation – already indicates a pseudomorphic arrangement of the intercalated nickel atoms.

7.1.2 DFT Calculations

In agreement with the experimentally observed (10×10) periodicity of the graphene moiré, the nickel intercalated system is modeled by a (10×10) graphene sheet adsorbed on a (9×9) Ni/Ir(111) substrate, consisting of three iridium layers and one nickel layer on top of iridium. Table 7.1 shows a comparison of the experimental and the theoretical

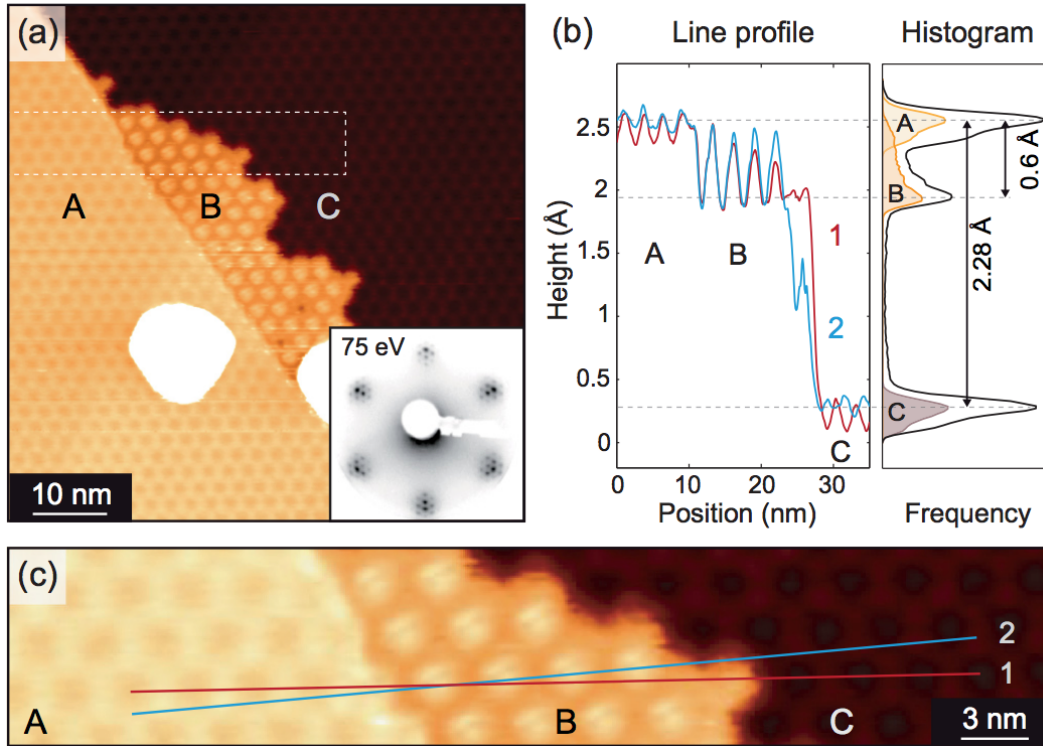


Figure 7.1: (a) Topographic STM overview showing the morphology of graphene with a partially intercalated nickel sub-monolayer. Nickel accumulates at step edges (B area) showing increased moiré corrugation in STM as compared to Gr/Ir(111) (A and C areas). Corresponding LEED image in the inset. (b) Areas with nickel intercalated underneath graphene (B areas) show reduced mean apparent height in the line profiles and the histogram. The histogram shows the frequency of apparent height values appearing in the magnification depicted in (c) (black curve) and within areas on terrace A, B or C (yellow, orange and brown curves, respectively). (c) Magnification of the dotted square in (a). Taken from Pacilé et al. [41]

lattice constants. The experimental iridium lattice constant is 8.75% larger than the nickel lattice constant and the lattice mismatch for the calculated equilibrium lattice constants are even larger ($> 10\%$). Therefore the nickel layer is significantly stretched on the iridium substrate. There are two possible (hollow) adsorption sites for the nickel atoms. First, when they continue the fcc iridium stacking sequence and the nickel atom is above an iridium atom of the third layer and in the second position, when the nickel atom is above an iridium atom of the second layer. In the following the first case is called FCC site and the second one HCP site. A calculation of one ML nickel on Ir(111) shows that the FCC arrangement is preferred over HCP by 30 meV/Ni atom. Therefore, the pseudomorphical FCC arrangement is preferred for Ni/Ir(111), but also with a graphene layer on top, the calculations produce the same stacking sequence.

	$a_{\text{Ir}}^{\text{lat}}$ [Å]	$a_{\text{Ni}}^{\text{lat}}$ [Å]	$(a_{\text{Ir}}^{\text{lat}} - a_{\text{Ni}}^{\text{lat}}) / a_{\text{Ni}}^{\text{lat}}$ [%]
experimental	2.71 [178]	2.492	8.75
LDA	2.706	2.424	11.63
PBE	2.747	2.493	10.19
optB88-vdW	2.747	2.484	10.59
optB86b-vdW	2.735	2.479	10.33

Table 7.1: Experimental and calculated lateral lattice constants of Ir and Ni.

The relaxed geometry of Gr/1 ML Ni/Ir(111) (in the most stable pseudomorphic nickel arrangement) is illustrated in Fig. 7.2a,b. The intercalation of the nickel layer leads to a pronounced corrugation of $\Delta h = 1.51$ Å in the graphene layer, significantly larger than for Gr/Ir(111) (Fig. 7.2b). However, more than 70% of the carbon atoms in the graphene layer are adsorbed at a close distance of about 2.0-2.2 Å from the nickel layer, which is in the same range as the interplane distance of Gr/Ni(111) (2.1 Å). Hence, the binding of graphene to the intercalated nickel layer in these regions is similar to the binding in 1×1 Gr/Ni(111), despite the expansion of roughly 11% due to pseudomorphic growth of the nickel lattice in Gr/1 ML Ni/Ir(111). Therefore we can conclude that the strong interaction of graphene/Ni(111) is not a result of the small lattice mismatch, but

rather related to the chemical properties of the surface layer, which also drives the strong corrugation of the graphene layer in the mismatched structure.

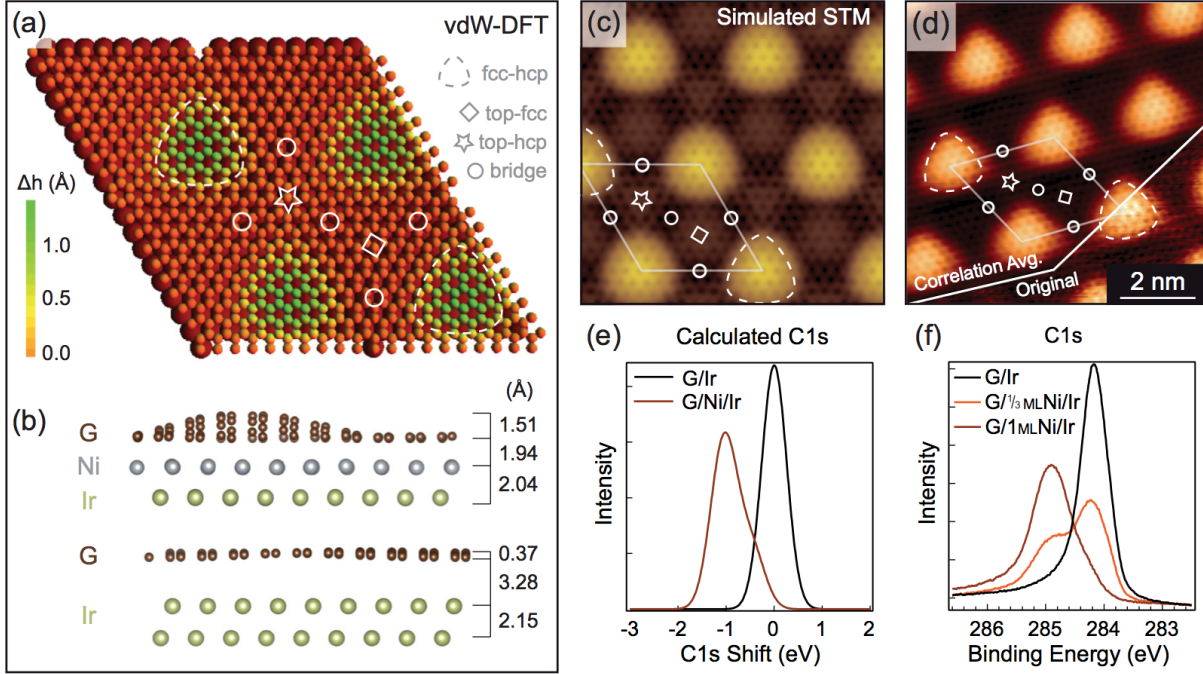


Figure 7.2: (a) Structural model for a single layer of graphene on Ni/Ir(111). The color coding indicates the height of the corrugation Δh in the graphene layer. (b) Comparison of the corrugation in the optimized structure of graphene/Ni/Ir(111) (upper panel) and graphene/Ir(111) (lower panel). (c) Simulated STM image for the states between E_F and $E_F + 0.2$ eV. (d) Atomically resolved STM topography of graphene/Ni/Ir(111). Theoretical (e) and experimental (f) C1s core level shifts of Gr/Ni/Ir(111) compared to Gr/Ir(111). Taken from Pacilé et al. [41]

In the flat regions of the moiré structure, the magnetic moment of the nickel atoms is completely quenched by the interaction with the graphene sheet, while the nickel atoms under the graphene bubbles yield a small magnetic moment ($< 0.4 \mu_B$). Nevertheless, the remaining magnetic moment in the surface layer is too small to induce a magnetic moment in the graphene sheet, opposite to the graphene/Ni(111) system showing an induced magnetic moment of carbon atoms [179].

Seen from an atomistic point of view, a close adsorption configuration of the graphene layer is reached not only for a top-fcc configuration preferred on Ni(111), but also for

adsorption in a bridge-like configuration¹. Both configurations yield a close adsorption distance reaching values as low as 1.94 Å. In contrast, the weak interaction in the fcc-hcp sites (green regions in Fig. 7.2a) leads to the formation of local protrusions, with a maximal distance of 3.45 Å to the nickel layer common for physisorbed graphene. Nevertheless, this distance is still smaller than the calculated maximal (vdW-DF) separation 3.7 Å ($\Delta h = 0.37$ Å) for the adsorption of graphene on the bare Ir(111) surface (Fig. 7.2b).

A stronger bonding at bridge-like and top-hollow positions was also seen in calculations of 1×1 graphene on Ni(111) in section 3.1.4. The binding energies at the chemisorption minimum are overestimated with optB86b-vdW compared to RPA. Nevertheless, only if graphene is adsorbed in a top-fcc, bridge-top, or top-hcp configurations a distinct minimum around 2.1 Å is found at the RPA nickel lattice constant (Fig. 3.9). At the iridium lattice constant (also used for Gr/Ni/Ir(111) calculations) the minima in adsorption energy are at smaller Gr-Ni distances of about 1.9 Å and the BEs for all adsorption sites are strongly increased (Fig. 3.10). An average BE per carbon atom of 0.19 eV for the Gr/1 ML Ni/Ir(111) system indicates a strong interaction if compared to the largest 1×1 Gr/Ni(111) BE at the RPA lattice constant of 0.13 eV (0.45 eV at the Ir lattice constant).

A direct comparison of the obtained STM data (Fig. 7.2d) and a simulated STM image (Fig. 7.2c) reflects the structure of the adsorbed graphene sheet: the elevated fcc-hcp regions appear brightest, while the low-lying areas with top-hollow configuration appear as a dark background. In agreement with the structure recently reported for Gr/Ru(0001) [180] and Gr/Rh(111) [181–183], the regions where the graphene sheet is adsorbed in a local bridge configuration is the area of the smallest distance to the surface. These areas appear as faintly visible depressions in STM topographies. A peak-to-valley corrugation of up to 1 Å fits well the corrugation of 1.3 Å in the simulated image. On the atomic level, Gr/Ni/Ir(111) shows both carbon atoms of a graphene ring everywhere within the moiré supercell in Fig. 7.2d. However, inside the strongly bound areas a difference in intensity between neighboring carbon atoms is observed indicating a broken sublattice symmetry.

The corrugation and hybridization of graphene with the metallic substrate is also

¹The bridge-like configuration is labeled by a circle in Fig. 7.2a and corresponds to a bridge-top configuration in Fig. 3.3b and Fig. 6.1

reflected in the C1s line-shape [34, 35]. The C1s core level energies taken at 445 eV of Gr/Ir(111), Gr/(1/3) ML Ni/Ir, and Gr/1 ML Ni/Ir are compared in Fig. 7.2f. According to the existing literature [11, 34], in the Gr/Ir(111) system the C1s BE is found at 284.10 ± 0.20 eV. After the intercalation of 1/3 ML of nickel, a second peak at higher BE is observed, which turns into the only component for 1 ML intercalated nickel. The main peak centered at 284.90 ± 0.20 eV close to the value found for graphene grown on bare Ni(111) [164]. There a single peak at 284.7 ± 0.18 eV was measured, with an intrinsic line width of 216 meV.

The calculated CL energies (Fig. 7.2e) are in good agreement with the experimental ones and display a similar shift toward higher BEs for the main peak. For both curves, a strong asymmetry toward lower BE of the line-shapes for Gr/1 ML Ni/Ir is observed, which is due to different CL shifts in different regions of the moiré unit cell. In the strongly interacting top-hollow and bridge-like positions the C1s CL shift is stronger whereas the weakly interacting fcc-hcp region give rise to only a minor CL shift compared to Gr/Ir(111). The dominant contribution however comes from the lower regions of the moiré leading to the detected intensity shape with only one peak (Fig. 7.2e) and thus do not exhibit a double C1s peak as observed for Gr/Re(0001), Gr/Rh(111) or Gr/Ru(0001) [34, 35].

7.1.3 Band Structure of Gr/Ni/Ir(111)

In order to get a better insight into the overall interaction of graphene with the mismatched nickel layer, the band structure was studied both experimentally by ARPES measurements and theoretically by DFT calculations. Figures 7.3a-d show the electronic band structure along the ΓK direction obtained with ARPES on (a) Gr/Ir(111); (b) Gr/0.33 ML Ni/Ir(111); (c) Gr/1 ML Ni/Ir(111); (d) Gr/thick Ni/Ir(111). The graphene π and σ -band in Gr/Ir(111) show similar features as the free-standing graphene bands with an intact Dirac cone. However, the π -band approaches the K -point at a BE of 70 meV and replica bands of both, π - and σ -states due to the moiré superpotential are seen close to the K -point according to the literature [10, 34, 184]. After the intercalation of about 1/3 ML of nickel atoms (Fig. 7.3b), new π - and σ -states appear at higher BE together with the d -states of nickel. The co-existence of double π - and σ -bands reflects

an inhomogeneous surface with clean areas of Gr/Ir(111) and patches where nickel atoms are in between.

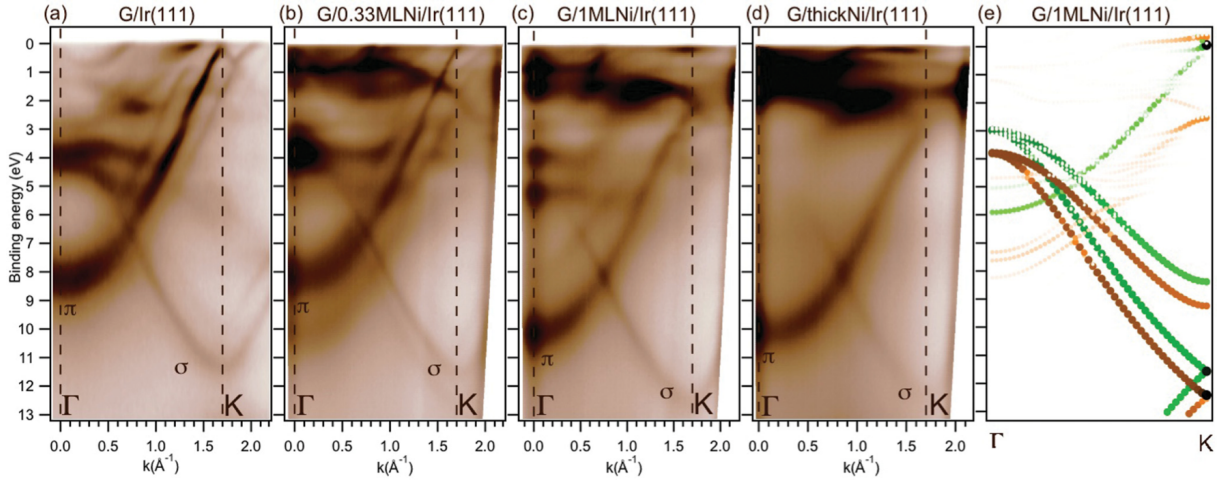


Figure 7.3: (a-d) ARPES dispersions along ΓK as a function of the amount of nickel atoms intercalated underneath graphene (G) on Ir(111). (a) and (d) show extreme cases of 0 ML and thick nickel, respectively. (e) Carbon projected band structure of a 1×1 model system of graphene/Ni/Ir(111). The band structure was evaluated at a Gr-Ni distance of 2.0 \AA (brown-dark gray dots) and 3.4 \AA (green-light gray dots). Taken from Pacilé et al. [41]

The band structure for a full monolayer Ni intercalated (Fig. 7.3c) clearly shows the new bands at higher binding energies, while the lower-lying of the double-bands of Gr/0.33 ML Ni/Ir(111) have vanished. The π -band no longer shows a linear dispersion, but reaches a maximum of 2.16 eV at the K -point. The electronic states of iridium disappear when several monolayers of nickel (above five) are intercalated via annealing (Fig. 7.3d) and the band structure is identical to Gr/Ni(111) [120]. The BE at the K -point for the σ -state is independent of the number of nickel layers. Yet, the π -state is shifted toward higher BEs at the K -point when more nickel layers are intercalated (Fig. 7.3d). In case of a Ni bulk substrate the maximum is found at 2.65 eV [120]. This finding is related to the differences in the width of the Ni d -states of a single intercalated nickel layer compared to a surface of bulk nickel: narrowing of the Ni $3d$ -band upon the decreasing of the nickel layer thickness. Taking into account that the position of the graphene-derived π -band at the Γ -point is the same for both thick and thin (1 ML) intercalated nickel layers,

we can conclude that the energy shift of π -band with respect to free-standing graphene is purely defined by the charge transfer between nickel and carbon atoms at the closest distance through the donation/back-donation mechanism [185]. The broken symmetry for two carbon atoms in the graphene unit cell in this system, accompanied by a strong hybridization between nickel $3d$ and graphene π -states determine the presence as well as the width of the band gap between π - and π^* -graphene-derived states.

Theoretical band structures were evaluated for a comparison with experiment. However, due to the large supercell the bands are multiply folded and the unfolding of the entire Brillouin zone would require heavy post-processing [186]. Therefore, the local interactions are modeled with a smaller (1×1) cell of Gr/Ni/Ir(111) in a top-fcc configuration, where the nickel monolayer continuous the fcc stacking sequence and graphene at an average distance of the flat regions (2.0 Å) and at the maximal height of the bubbles (3.4 Å). The resulting band structure is shown in Fig. 7.3e. The calculations clearly show that the interactions at the elevated regions of the bubbles (green-light gray dots in Fig. 7.3e) are rather weak, resulting in a nearly unperturbed graphene band structure. On the other hand, a much stronger interaction can be expected for the dominant flat regions in the vicinity of the surface, leading to a large splitting of the π -band at the Dirac point (brown-dark gray dots in Fig. 7.3e). These findings agree with the experimentally observed opening of a band gap in the ARPES data. Furthermore, in the experiments no π -band-splitting is observed for Gr/Ni/Ir(111), due to the metallic nature of graphene [187], in contrast to the electronic behavior of h -BN grown on selected transition metals [188], where the dielectric nature of the overlayer allows to observe double σ - and π -states corresponding to higher and lower regions in the moiré cell.

7.2 Intercalation Mechanism of Gr/Ni/Ir(111)

7.2.1 Experimental Evidence: Intercalated Nickel at Gr/Ir

Figure 7.4 shows the surface of graphene samples after nickel intercalation for various pre-deposited nickel thicknesses and annealing times. Remaining nickel clusters with apparent heights in the nm range on top of the surface are rendered in white color and decorate

most frequently step edges as well as terraces after intercalation.

For low pre-deposited nickel amounts of 0.8 \AA Ni (Fig. 7.4a,b), the intercalation progress is slow. The nickel clusters occupy an area of 5.4% of the sample surface and intercalated areas cover only 1.8% of the sample in Fig. 7.4a after two annealing periods of all together 17 minutes at $510 \text{ }^\circ\text{C}$. Further annealing does not significantly increase the fraction of intercalated material underneath the surface. Intercalated areas are observed mostly in the vicinity of substrate steps.

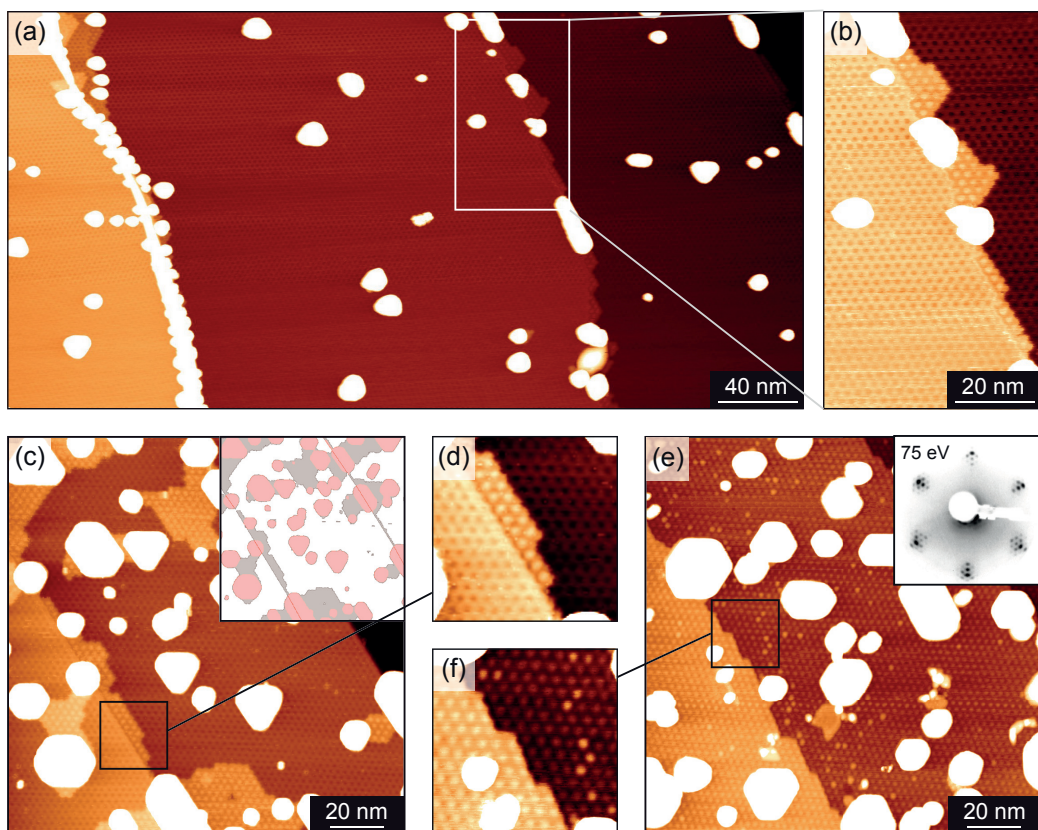


Figure 7.4: (a) Topographic STM overview showing a Gr/Ir(111) sample with low nickel coverage (0.8 \AA) after annealing for 17 minutes at $510 \text{ }^\circ\text{C}$. (b) Magnification of the intercalated areas in panel a. (c) High nickel coverage sample (6.1 \AA) after annealing for three minutes at $525 \text{ }^\circ\text{C}$. (d) Magnification of the intercalated areas in panel c. (e) Sample surface of the high nickel coverage sample after prolonged annealing for a sum of 17 min showing more than one full monolayer of intercalated material. (f) Magnification of the surface in panel e. Taken from Leicht et al. [177]

In Fig. 7.4c,d the surface of a Gr/Ir(111) sample with an increased nickel amount of 6.1 Å nominal nickel deposition is shown after a subsequent annealing process of three minutes at 525 °C. As compared to the lower coverage graphene sample, the surface area covered by intercalated material has now increased to 17.3% (excluding the potentially intercalated areas underneath nickel clusters) after roughly 1/5 of the annealing time, however still exhibiting less than one monolayer of intercalated graphene after the first annealing step. In addition to intercalation at steps, intercalated nickel now also forms isolated patches within flat terraces. After prolonged annealing of 14 minutes at 550 °C in addition to the initial three minutes at 525 °C the surface features intercalated Gr/Ni/Ir on 100% of the sample (Fig. 7.4e). In comparison to the initially straight Gr/Ir(111) steps, kinks along the step edge are observed now. Furthermore single moiré positions become extensively bulged marking the onset of intercalation of more than one monolayer of nickel (Fig. 7.4e,f).

In LEED no qualitative change is found for Gr/Ir(111), partly intercalated surfaces and intercalation with greater coverages than one monolayer (inset in Fig. 7.4e). Therefore no change in the periodicity of Gr/Ni/Ir(111) moiré superstructure parameters below the resolution limits of LEED is found.

Given the comparable annealing temperatures used for samples in Fig. 7.4 one can assume, that the intercalation rate depends significantly only on the deposited nickel amount. In the low nickel coverage sample, a nickel surface coverage of 5.4% is measured and from the intercalated surface fraction an intercalation rate of 0.001 monolayer/min is found. Comparing these values with the higher nickel coverage sample (surface nickel coverage: 25% and intercalation rate: 0.058 monolayer/minute) an increase of the intercalation rate around a factor of 50 is found, whereas the nickel covered surface fraction increases only by a factor of roughly five. An intercalation yield of hundred percent of the deposited nickel appeared to be unobtainable within the annealing periods and temperatures investigated. This appears to be connected to the 3D growth of nickel clusters on graphene and the thereby reduced surface coverage with decreased nickel amounts.

7.2.2 Adsorption and Intercalation of a Single Nickel Atom

To address the accumulation of the nickel atoms, the adsorption and intercalation of single nickel adatoms on both, flat Gr/Ir(111) and Gr/Ir(111) with step edges, was investigated with DFT calculations. In the moiré geometry the favorite adsorption site for a nickel adatom is on top of a carbon atom, whereas an adsorption in the center of a carbon hexagon is 0.13 eV lower in BE (table 7.2). The adsorption of the nickel adatom in the middle of the terrace in the smaller step edge structure (pos. C in Fig. 7.5) yields a slightly decreased BE (3.080 eV) compared to the full cell calculations (3.116). However, including the step edge calculation, the highest BE is reached when the nickel atom is located above the iridium step atom (position A in Fig. 7.5). A configuration where the nickel adatom is located in the middle of the terrace (pos. C in Fig. 7.5) or at the lower side of the step edge (pos. B in Fig. 7.5) decreases the BE by 0.04 eV and 0.16 eV, respectively (table 7.2). Thus, nickel adatoms will preferentially accumulate at step edges, in good agreement with the experimental observations of the previous section.

site	BE [eV]	Δ BE [eV]
top	2.982	-
ring	3.116	0.134
pos. A	3.042	-
pos. B	3.201	0.160
pos. C	3.080	0.038

Table 7.2: BEs of a single nickel adatom on top and in the middle of a carbon hexagon at the moiré unit cell of Gr/Ir(111) (first two rows), and BEs of an adsorbed single nickel atom on stepped Gr/Ir at different positions (A-C) illustrated in Fig. 7.5.

Once a single nickel atom has penetrated through the graphene sheet (the intercalation mechanism is subject of section 7.2.5) it is captured between the graphene layer and the iridium substrate. BEs calculated for different positions of the intermediate nickel atom on both, flat and stepped Gr/Ir, are summarized in table 7.3. There are two possible hollow positions where the nickel atom can find a local energy minimum. First, when it

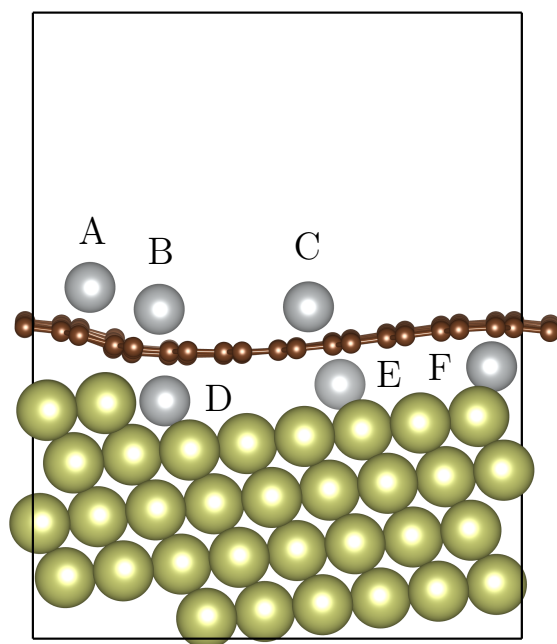


Figure 7.5: Adsorption positions A-C and intercalation positions D-F for nickel atoms at a stepped graphene covered Ir surface. Nickel atoms are colored in grey, Ir in green, and C in brown. The unit cell is indicated as box with black lines.

continues the fcc iridium stacking sequence (pseudomorphic arrangement) and is located above an iridium atom of the third layer (FCC position) or when it is above an iridium atom of the second layer (HCP position). The favorite adsorption configuration for a single nickel adatom on Ir(111) (without Gr) is HCP with 12 meV larger binding energy than FCC. The surface diffusion barrier for nickel on Ir(111) is 0.208 eV.

When the nickel atom is between graphene and flat Ir(111), the different local configuration with respect to the moiré unit cell alters the respective bonding situation. But the graphene-substrate interaction is small for Gr/Ir(111) leading to a large Gr-Ir separation and a small corrugation in the graphene layer and hence, to rather uniform Gr-Ni distances. Therefore, the BEs and surface diffusion barriers are expected not to differ significantly for the various intercalation sites in the moiré cell. In table 7.3 BEs for intercalated nickel in high-symmetry regions of the moiré unit cell for both, FCC and HCP positions are summarized. The high-symmetry regions are labeled according to the Gr/Ir(111) notation in Fig. 6.1. The minimum energy configuration is found in the fcc-hcp region. HCP and FCC nickel positions in this region have a similar local geometry (see Fig. 6.1). For both cases, a carbon atom is on top of a nickel. In top-hollow regions otherwise, for one configuration (either FCC or HCP) a carbon atom is on top of nickel, but for the other one the nickel is at the center of a carbon hexagon. Therefore, the BEs are similar for FCC and HCP in the preferred fcc-hcp region with a slightly larger BE of 0.02 eV for HCP, but are different for FCC and HCP in the top-hollow regions. The configurations where the nickel atom is at the center of a carbon hexagon (pos. e and pos. h in Fig. 7.6) are more stable than the configurations where a nickel atom is under a carbon atom (pos. f and pos. g in Fig. 7.6), which have ≈ 0.4 eV lower BEs (table 7.3).

The enhanced bonding in fcc-hcp region can be understood from geometrical arguments. The highest BEs are reached in the region within the moiré unit cell where the Gr-Ir distance has its maximum value and the additional nickel atom is stretching the graphene locally only by 0.25 Å (Fig. 7.8a). In top-fcc and top-hcp regions, the additional nickel atom causes a stretching of the carbon atoms near the nickel atom perpendicular to the surface of 0.44 Å and 0.50 Å, respectively, which results in higher total energies.

The diffusion barrier of an intercalated nickel atom for hopping from one hollow position over a bridge site to an adjacent hollow site is 0.37 eV in the top-fcc region, 0.34 eV

site	BE [eV]	Δ BE [eV]
HCP	0.556	-
FCC	0.568	0.012
BRIDGE	0.764	0.208
fcc-hcp HCP (pos. b)	-0.003	-
fcc-hcp FCC (pos. a)	0.020	0.023
fcc-hcp BRIDGE	0.209	0.212
bridge HCP (pos. c)	0.019	0.022
bridge FCC (pos. d)	0.072	0.075
top-hcp HCP (pos. f)	0.409	0.412
top-hcp FCC (pos. e)	0.049	0.052
top-hcp BRIDGE	0.393	0.396
top-fcc HCP (pos. h)	0.077	0.080
top-fcc FCC (pos. g)	0.416	0.419
top-fcc BRIDGE	0.448	0.451
pos. D	-0.573	-
pos. E	-0.004	0.569
pos. F	0.163	0.736

Table 7.3: In the first three rows, BEs of nickel adatoms on 5×5 Ir(111) (without Gr) at FCC, HCP, and BRIDGE position are shown. The following rows are BEs of intercalated single nickel atoms between graphene and the flat iridium substrate. The position fcc-hcp_FCC e.g., is also found as pos. a in Fig. 7.6, which is located in a fcc-hcp high-symmetry region (in terms of Gr/Ir(111)) and in FCC stacking sequence, thus the nickel atom is above a third layer iridium substrate atom. In the last three rows, the BEs of intercalated nickel atoms in a step edge structure are compared. The nickel positions D-F are illustrated in Fig. 7.5.

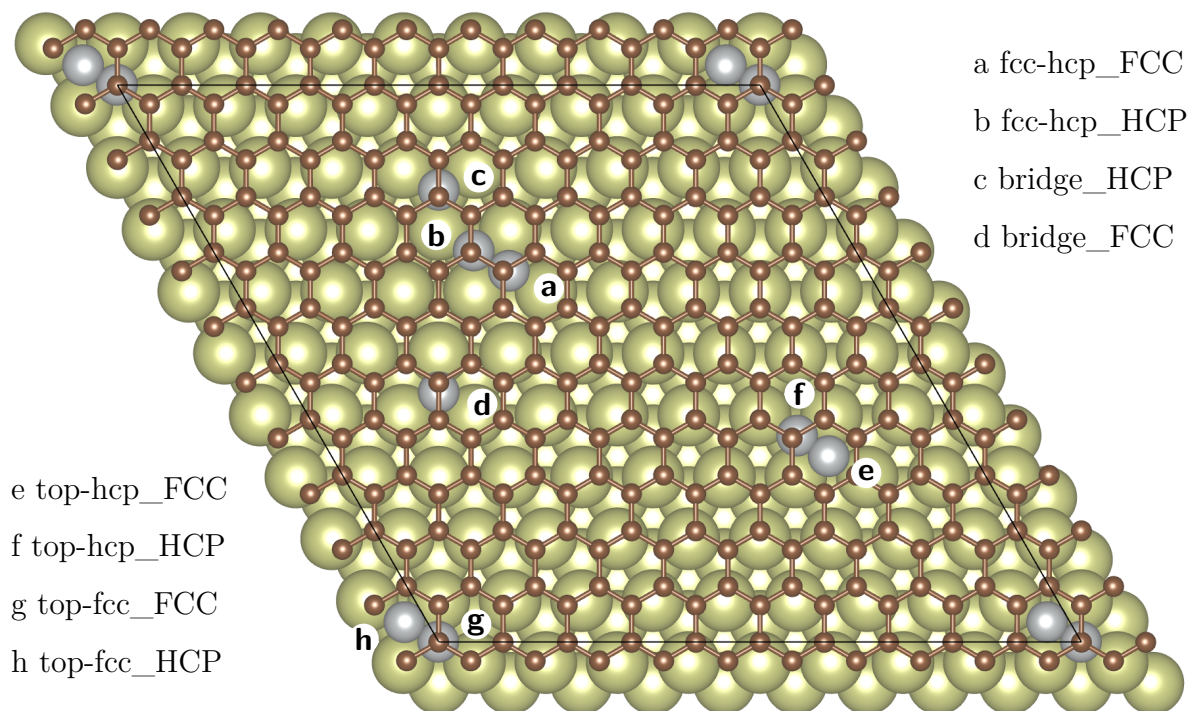


Figure 7.6: Gr/Ir(111) structure with intercalated nickel atoms at various adsorption sites. The positions a-h mark the different adsorption positions, which are also indicated in table 7.2

in the top-hcp, and 0.21 eV in the fcc-hcp region. Thus, also the diffusion barrier is the lowest in the fcc-hcp region. Because of these low diffusion barriers throughout the moiré cell, the nickel atoms in the graphene-iridium interface have a high mobility and can find minimum energy sites relatively fast.

When considering also a step edge, the nickel atom can gain additional 0.57 eV when it gets close to the step edge (from pos. E to pos. D in Fig. 7.5, table 7.3). The coordination at this site is enhanced whereas at a configuration on the opposite side of the terrace (pos. F) the BE is decreased by 0.17 eV. The final adsorption site D is a FCC site while HCP sites are not favored nearby a step edge. Therefore, the Ni atoms are predicted to accumulate at the step edges in a fcc stacking sequence. Because of the small diffusion barrier in the layer, the nickel atom between graphene and iridium can find the minimum energy position at the step edge fast and growth of the intermediate nickel layer is predicted to start at the step edges, which is in good agreement with STM measurements.

7.2.3 Preferred Configurations of Intercalated Nickel

In Fig. 7.7a the STM image in atomic resolution of a Gr/Ni/Ir(111) to Gr/Ir(111) terrace is shown. In Gr/Ni/Ir(111) a moiré superstructure is formed due to the pseudomorphic growth of nickel underneath graphene, as described in section 7.1.1. Fcc-hcp moiré sites appear as bright protrusions in contradiction to Gr/Ir(111) where fcc-hcp sites appear as dark depressions in the experiments. The top-hollow sites as well as bridge sites on the other hand form a quite flat terrace interconnecting the fcc-hcp sites as displayed in Fig. 7.7a. The overlaid grid connecting the Gr/Ni/Ir(111) fcc-hcp sites extends beyond the edge of the intercalated material, clearly showing the local configuration of carbon atoms with respect to delimiting nickel atoms. Whilst the growth of intercalated islands away from steps occurs, new fcc-hcp sites are suppressed until the fcc-hcp position is completely surrounded by material (Fig. 7.7a, grid and circles). A similar behavior is found in the middle of intercalated nickel patches: Randomly scattered fcc-hcp sites collapse (Fig. 7.7c, dashed circles) marking missing nickel atoms which arrange underneath graphene such that the fcc-hcp configurations are avoided.

The main reason is the locally weaker Gr-Ni interaction in fcc-hcp regions of the moiré cell due to the large Gr-Ni separation in these regions. To estimate the weakening of the

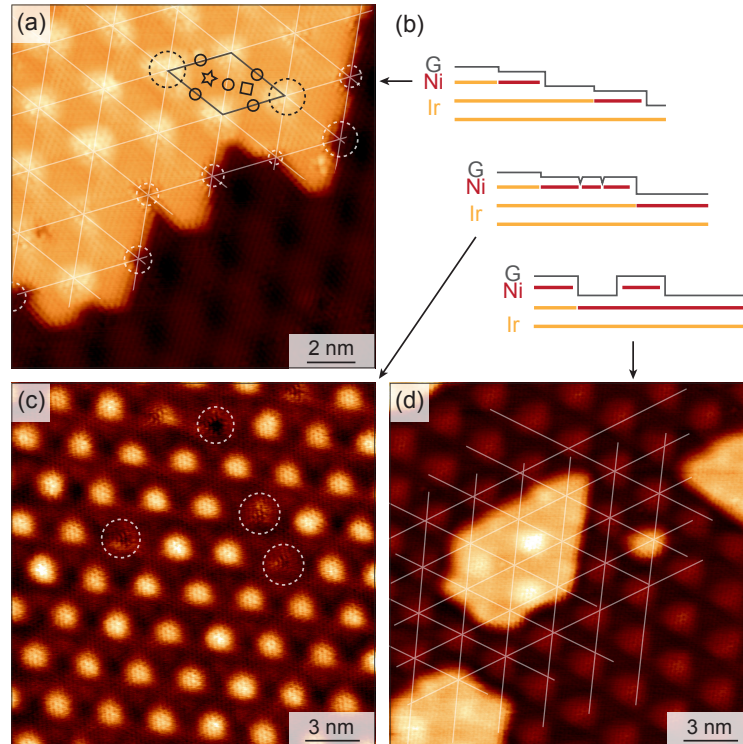


Figure 7.7: (a) Atomically resolved topographic STM image of a Gr/Ni/Ir(111) to Gr/Ir(111) step. The symbols label high-symmetry regions in the moiré unit cell according to Fig. 7.2a. (b) Schematic of the intercalated regions (c) Atomically resolved topography of a large intercalated area with occasionally collapsed moiré atop sites (d) Atomically resolved topographic STM of multilayer intercalated nickel in between graphene and Ir(111). Taken from Leicht et al. [177]

interaction in this area, DFT calculations for a single nickel atom between the iridium substrate and a fixed graphene layer, in the structural configuration of Gr/Ni/Ir(111), for different nickel sites are compared. The weakest bonding occurs for a nickel atom in the fcc-hcp region due to a large Gr-Ni separation. The energy difference to the preferential top-fcc region is 0.65 eV. In the ideal case, the nickel atoms at the Gr/Ni/Ir(111) to Gr/Ir(111) boundary region are at a top-hollow or bridge configuration as schematically pictured in Fig. 7.8c. Here, the geometry of the graphene film fits perfectly to the Ni-Ir substrate. Whereas in the case of bordering nickel atoms at fcc-hcp sites, the graphene would have to buckle at the most unfavorable position, decreasing the BE in this region as roughly estimated in above mentioned calculations (Fig. 7.8d). The nickel atoms will rather locate in higher BE regions like top-hollow or bridge like and omit the fcc-hcp region.

7.2.4 Multilayer Nickel Intercalated in Gr/Ir(111)

In Fig. 7.7d the sample surface of few monolayers of intercalated material is shown. The lower terrace features Gr/Ni/Ir(111) as observed for a submonolayer of intercalated material in Fig. 7.7a. Furthermore the second terrace visible in topography features isolated islands. In contrast to observations in the submonolayer regime we now find intercalated islands which are scattered across terraces and not connected to substrate steps. Again the fcc-hcp configurations play a special role in respect to preferential occupation with additional intercalated material. However the arrangement of the topmost intercalated layer seems to contradict the arrangement of one submonolayer on Gr/Ir(111) at first glance – as for intercalation in the multilayer regime an arrangement of nickel at protruded fcc-hcp sites appears to be favorable. Similar behaviors are visible for the shape of intercalated islands, which feature straighter edges now as compared to intercalated islands of submonolayer intercalated nickel.

DFT calculations were performed to study the favorite adsorption positions for nickel atoms forming a second intercalated layer. The Gr-Ni distance for Gr/1 ML Ni/Ir(111) in the fcc-hcp region is the largest (3.45 Å) whereas in top-hollow and bridge regions the distance is only 2.0 Å (see Fig. 7.2a). An additional nickel atom above the intermediate nickel layer in the fcc-hcp region is covered under a graphene bubble and the distortion of

the graphene layer is small (0.24 Å). But when the nickel atom is in any other region, the single nickel atom finds no stable position between the nickel and graphene layer but would rather contribute to the stretched nickel layer. Thus the additional nickel atom would create an interstitial defect in the nickel layer which is energetically favorable compared to an nickel atom adsorbed on the nickel layer, at which the graphene sheet would be considerably deformed. However, this is by far a worse configuration compared to the fcc-hcp site considered before (1.46 eV less BE). A second intermediate nickel layer will therefore start to grow in the fcc-hcp regions of Gr/1 ML Ni/Ir(111).

Experimentally only small patches of Gr/2 ML Ni/Ir(111) are observed. However, when a full second intercalated nickel layer is formed, former fcc-hcp positions convert to top-hollow configurations. If one assumes, that also the second nickel layer follows the fcc stacking sequence, fcc-hcp regions convert to top-fcc, top-fcc to top-hcp, and top-hcp to fcc-hcp. Therefore, the second nickel layer starts to grow in a top-fcc region where the bonding is enhanced. The graphene-nickel interface (without other substrate layers) is equivalent for Gr/1 ML Ni/Ir(111) and Gr/2 ML Ni/Ir(111). Thus, a similar corrugation of the graphene layer with a weaker bonding and larger distances in fcc-hcp regions also for Gr/2 ML Ni/Ir(111) is most likely. The difference in the structure occurs at the second substrate layer and will probably change the graphene structure only slightly. Furthermore, the STM image in Fig. 7.7d clearly shows brighter regions (presumably at fcc-hcp regions in terms of Gr/2 ML Ni/Ir(111)) on multilayer intercalated nickel, indicating a similar corrugation for Gr/2 ML Ni/Ir(111) and Gr/1 ML Ni/Ir(111).

7.2.5 Intercalation Mechanism

Based on the observations of the previous sections, the intercalation appears to comprise two steps: penetration of nickel from the cluster (preferred at step edges) through the graphene layer and subsequent diffusion of nickel in the graphene-iridium interface with final agglomeration at step edges. This intercalation mechanism favors the development of intercalated material patches connected to substrate steps. A comparison to intercalation studies of nickel underneath graphene on Rh(111) [182] shows distinctly different morphology of intercalated material where intercalation leads to isolated intercalated islands scattered across substrate terraces. The comparison of nickel intercalated in Gr/Rh

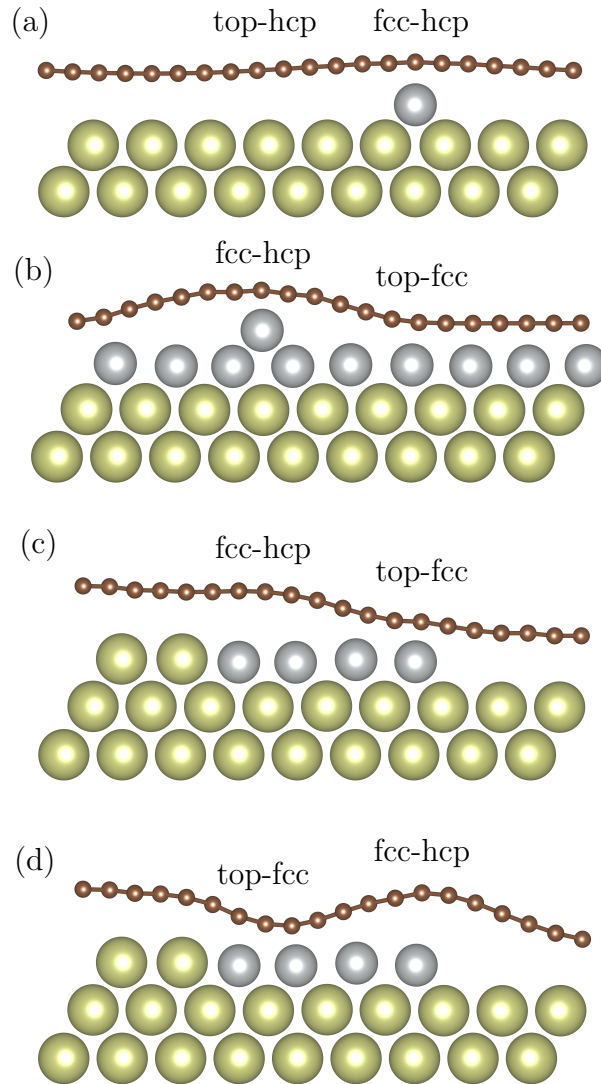


Figure 7.8: Schematic structural profile of Gr/Ir(111) with one intercalated nickel atom in the fcc-hcp region (a), Gr/1 ML Ni/Ir(111) with one additional intercalated nickel atom (b). Notice that the fcc-hcp region for Gr/Ni/Ir(111) is the top-hcp region in terms of Gr/Ir(111). (c) Schematic picture of a preferential configuration of a graphene covered Ir step with intercalated nickel nearby the step edge. The nickel atoms opposite from the step edge are in the top-hollow region with small Gr-Ni distance so that the graphene can smoothly encase the substrate atoms. (d) Hypothetical picture similar to (c) where the outer part of Gr/Ni/Ir(111) is a fcc-hcp region so that the Gr-Ni distance is enhanced in this region. The graphene-substrate interaction is smaller than in (c) and the graphene sheet is additionally stretched which costs an additional amount of BE.

and Gr/Ir, yields a stronger interaction and increased electronic and topographic modulation of the moiré pattern for Gr/Ni/Ir(111). It has been shown in Ref. [182] that nickel patches underneath Gr/Rh(111) are formed, due to high diffusion barriers at strongly bound bridge sites. Graphene/Ir(111) on the other hand shows decreased substrate interaction and diffusion barriers of nickel underneath graphene are low throughout the whole moiré unit cell, as described in section 7.2.2. Therefore, nickel diffusion is less hindered, which is strengthened by the observed intercalation morphology of samples with more than one monolayer of intercalated nickel. As discussed earlier, graphene performs a transition from weakly bonded to strongly bonded graphene upon intercalation and hence the morphology of intercalated nickel changes. Here single bumps at the position of the fcc-hcp sites within the moiré are found (bulged areas in Fig. 7.4f and Fig. 7.7d). These bulged areas appear to be filled by only few additional atoms per bump and underline the hindered diffusion underneath graphene as in Gr/Rh(111), once the graphene strongly interacts with the substrate.

Different types of diffusion processes are also studied with DFT calculations. A nickel atom that starts at the favorite adsorption position above a step edge (pos. A) and gets to the most stable position (pos. D) due to diffusion through the graphene sheet gains about 3.62 eV. On a flat terrace the energy gain is decreased to 3.00 eV. There is a strong driving force for nickel to intercalate though. However, the nickel atom must pass the graphene layer in some way, which means that an energy barrier has to be overcome. This energy barrier depends on the actual intercalation mechanism and is defined as the energy difference of the transition state and the initial state – which is in this case the configuration where nickel is adsorbed on graphene. The configuration where the energy has its maximum during the diffusion process is the transition state. The final state is reached when the nickel atom is completely intercalated and has found a local energy minimum under the again intact graphene sheet.

Various energy barriers were calculated using a 4×4 cell and are shown in Fig. 7.9. The energy barrier for direct diffusion of a single nickel atom through perfect free-standing graphene is 9.94 eV. Here, the initial and final state are equivalent and reached for an equilibrium Ni-Gr distance of 1.52 Å. This huge barrier is reduced to 5.70 eV including the iridium support. The values of the 4×4 model are compared with full cell calculations

for the latter case, where the energy barrier is further decreased to 5.04 eV. This result also shows that the actual energy barriers might be lower than the values of the 4×4 cell calculated in the following.

The transition state of the full cell calculations is shown in Fig. 7.10. The nickel atom is close to the iridium surface atoms and the energy is strongly decreased compared to the free-standing graphene transition state, because of the formation of Ni-Ir and C-Ir bonds. However, it is still not likely to overcome such a barrier at typical annealing temperatures and alternative diffusion mechanisms must be considered.

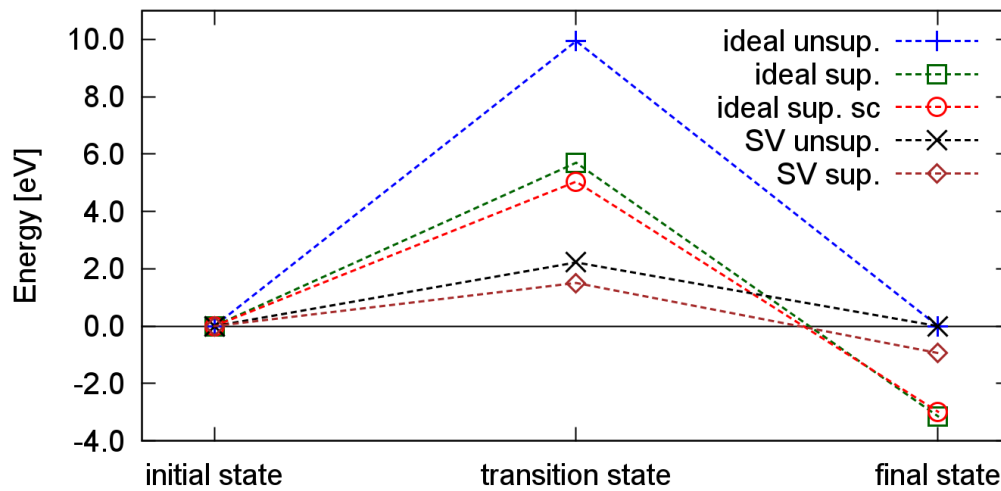


Figure 7.9: Energies of the initial state, transition state, and final state for a nickel atom diffusing through graphene for various systems. The energy barrier for free-standing graphene (ideal unsp.) is the largest and is decreased with Ir support (ideal sup.). The 4×4 calculation is compared to the full supercell (sc) calculation for the latter case. The barriers are smaller when a single vacancy (SV) is present.

When diffusing at step edges, the barrier is decreased by 0.90 eV compared to the ideal flat graphene surface. In addition, defects like single vacancies (SV) can lower the energy barriers significantly. A nickel atom passing the graphene sheet at the vacancy site decreases the barrier to 2.22 eV for unsupported graphene with a SV (Fig. 7.9). The energy barrier is further decreased if the graphene is supported with iridium substrate to 1.51 eV. This low barrier may explain the experimentally observed high diffusion rate, when enough vacancies are available. In general the vacancy density is low in graphene

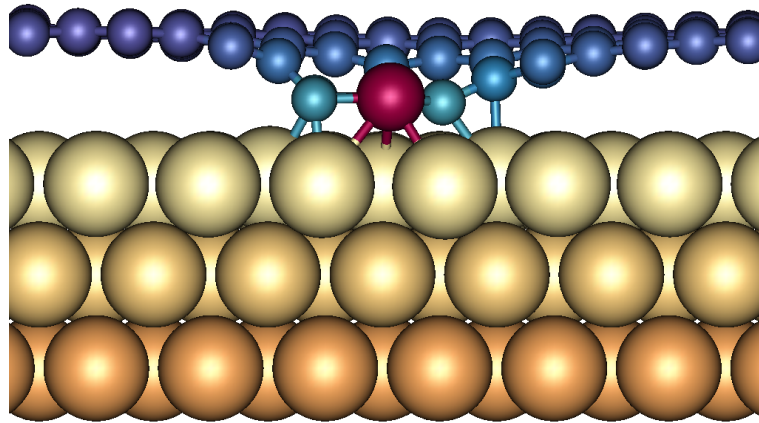


Figure 7.10: Transition state of nickel (purple) diffusing through Gr/Ir(111) in the moiré unit cell.

because of high formation energies, but in the presence of supporting transition metals the formation energies of single vacancies can be drastically reduced (see section 4.2). Furthermore, a recent DFT study showed that the formation energies of single and double vacancies are decreased when transition metal impurities (Fe, Ni, Co) are present at the surface [189]. The experiments moreover imply that the barriers are decreased with an increasing portion of nickel deposited. The nickel clusters on top of graphene and the higher concentration of nickel at step edges might lower the barriers as well, but further calculations have to be done in order to quantify this prediction.

7.3 Computational Methods

The spin-polarized DFT calculations were performed with VASP using the PAW method. Because (semi-)local functionals do not describe the Gr-Ni interaction correctly (see section 3.1.3), the calculations were performed using vdW-DF with the optB86b-vdW functional [99]. For the calculations with a flat Ir(111) surface, a (10×10) graphene sheet was adsorbed on a (9×9) (Ni)Ir(111) substrate with a lateral lattice constant of 2.735 \AA , consisting of a three layer slab where the two bottom layers were kept fixed and all other atoms allowed to relax. For the step edge calculations, a fcc(19,17,17) plane was used with 9 iridium atoms along the step edge, giving 72 iridium atoms in one layer and 200 carbon atoms on top. The iridium substrate consists of four layers with the two bottom

layers fixed and all other atoms allowed to relax.

The diffusion of the nickel atom through graphene is modeled using a 4×4 unit cell. For the iridium-supported case, the graphene layer is in top-fcc arrangement above three fixed iridium layers at the graphene lattice constant. The single vacancy is at a top site. All structures were relaxed to forces lower than $0.01 \text{ eV}/\text{\AA}$. A Γ -centered $3 \times 3 \times 1$ k-point mesh was used for both, flat Ir(111) structures and step edge configurations and a Γ -centered $7 \times 7 \times 1$ k-point mesh for diffusion calculations. The C1s core level shifts were calculated in the initial state approximation. For the graphical visualization, the resulting total core level spectra are displayed as a sum over Gaussian functions with a standard deviation of 0.25. The STM simulations were performed using the Tersoff-Hamann approximation [118] using the integrated charge density between E_F and $E_F + 0.2 \text{ eV}$.

7.4 Conclusion

The results of this chapter clearly show that one can use the adsorption of graphene on epitaxial layers to study the influence of the lattice mismatch between graphene and the substrate, while keeping the chemical environment similar. When one ML nickel is intercalated in Gr/Ir(111), the nickel layer is pseudomorphically arranged at the Ir(111) interface. The large lattice mismatch between nickel and iridium leads to a stretched nickel layer with iridium lattice constant and graphene on top. The structure of Gr/Ni/Ir(111) was investigated with STM measurements and DFT methods and shows a moiré pattern with strong corrugation of about 1.5 \AA and a minimum Gr-Ni distance of about 2 \AA due to a locally strongly enhanced interaction for specific adsorption configurations similar to Gr/Rh(111) and Gr/Ru(0001). About 70 % of the nickel atoms are adsorbed at a distance of about $2.0\text{-}2.2 \text{ \AA}$ from the substrate in top-hollow or bridge-like configurations. The Gr-Ni interaction in the fcc-hcp regions is dominated by weak vdW at larger distances, similar to the findings for 1×1 graphene on Ni(111). The graphene band structure probed by ARPES shows a clear transition with increasing amount of intercalated nickel from almost free-standing to strongly perturbed graphene bands similar to graphene on nickel bulk. The hybridization between nickel *d*-states and graphene π -states for Gr/1 ML Ni/Ir(111) is

a result of the strongly interacting regions in the moiré unit cell. The electronic interaction in Gr/Ni/Ir(111) determines the strongly interacting regions, while the lattice mismatch is responsible for the ratio between strongly and weakly interaction regions.

The intercalation of nickel comprises two steps: penetration of nickel through the graphene layer and subsequent diffusion of nickel in the graphene-iridium interface with final agglomeration at step edges. The diffusion through the graphene layer occurs probably with the aid of point defects such as single vacancies. Low diffusion barriers for the nickel between graphene and Ir(111) enables to find the higher coordinated preferred positions at the step edge. With larger amounts of intercalated nickel the moiré pattern of Gr/Ni/Ir(111) is formed, whereupon fcc-hcp regions are avoided as long as neighboring regions can be filled up, because of a lower Gr-Ni interaction in this region. When one monolayer nickel is completed, additional nickel atoms accumulate in the bubbles of the Gr/1 ML Ni/Ir(111) structure (fcc-hcp region), but the diffusion across the nickel interface is hindered by the strongly interacting top-hollow and bridge-like regions of the moiré cell.

Chapter 8

Silver intercalated in Gr/Re(0001)

The main results of this chapter are submitted in a joint paper with the title *Hybridization of Graphene and a Ag Monolayer Supported on Re(0001)* [190], where the present author contributed to the DFT calculations.

To gain further insight into the interaction of graphene with metal substrates the influence of a noble metal layer intercalated in a strongly interacting Gr-metal system is studied. This study uses the opposite setup as for Gr/Ni/Ir(111) where a strongly interacting metal was intercalated in a weakly interacting system. The graphene-substrate interaction is strong for graphene adsorbed on Ni [115], Rh [181], and Ru [191, 192], with a minimum Gr-metal distance of $\approx 2.1 \text{ \AA}$, where the hybridization between carbon and metal leads to a loss of the linear dispersion of the graphene bands [119, 187]. However, in many cases the electronic properties can be restored by the intercalation of noble metal layers, as shown by several ARPES studies [39, 40, 193–195]. The intercalated noble metal layers do not merely act as spacer layers, but also decrease the hybridization between the metal d -states and the graphene π -band. Indeed, a stiffening of the graphene phonon modes after the intercalation of noble metals (Cu, Ag, Au) [196–198] and the recovered linear dispersion relation for the π -band of graphene have been taken as indication that graphene is decoupled from the substrate. However, the role of an intercalated noble metal is still not clarified on a fundamental level.

In this section a combined study is presented where ARPES experiments and DFT calculations were used to investigate the electronic structure of graphene-supported on Re(0001) before and after the intercalation of one ML silver to assess the decoupling

of the graphene sheet [190]. Because of a large (lateral) lattice mismatch of about 12%, Gr/Re(0001) exhibits a moiré structure which can be approximated by a (10×10) graphene layer over a (9×9) rhenium unit cell [35]. A large corrugation of about 1.6 Å and a minimum Gr-Re distance of about 2.1 Å in the closely bound top-hollow and bridge-like regions [35] indicate a strong Gr-metal interaction. Similar to Gr/Ru(0001) and Gr/Rh(111) [34] a strong graphene-substrate interaction is also indicated by a splitting of the graphene C1s photoemission peak for graphene on bare rhenium. In addition, ARPES measurements of Gr/Ru(0001) show strongly perturbed graphene bands which are again signs of a strong Gr-metal interaction. The intercalation of one ML silver restores the linear dispersion relation of the graphene π -band close to the Dirac point. This weakening of the interaction is confirmed by DFT calculations and C1s core level measurements. However, in agreement with experimental measurements, band structure calculations still predict a hybridization of graphene π -bands with Ag-states, leading to the formation of a band gap 4-7 eV below E_F .

8.1 Band structure and Core Level Shifts

The experimental electronic band structure for bare rhenium is shown in Fig. 8.1a. For Gr/Re, the π - and σ -state of graphene are clearly visible in Fig. 8.1b. In contrast to the linear dispersion relation observed for a weakly interaction system, e.g. Gr/Ir(111) (Fig. 7.3a), for Gr/Re(0001) a parabolic dispersion of the π -band with a maximum at the K -point 3.90 eV below the Fermi level is visible. Similar to Gr/Ru(0001) [40, 187], the hybridization of graphene with the metal d -states leads to a diffuse π^* -band (Fig. 8.1b,f). These findings clearly point toward a strong interaction between graphene and the rhenium substrate.

After the intercalation of one monolayer of silver the graphene π -band is shifted by about 1.60 eV toward E_F at the Γ -point and the linear dispersion relation is restored at the K -points (Fig. 8.1c). The π -band shift is an indicator for a reduced graphene-substrate interaction [39, 40, 194]. A weak adsorption is also predicted by vdW DFT calculations carried out for a (9×9) graphene layer supported on a (8×8) Ag/Re substrate in contrast to the experimentally found (10×10) Gr on (9×9) Ag/Re structure due to the

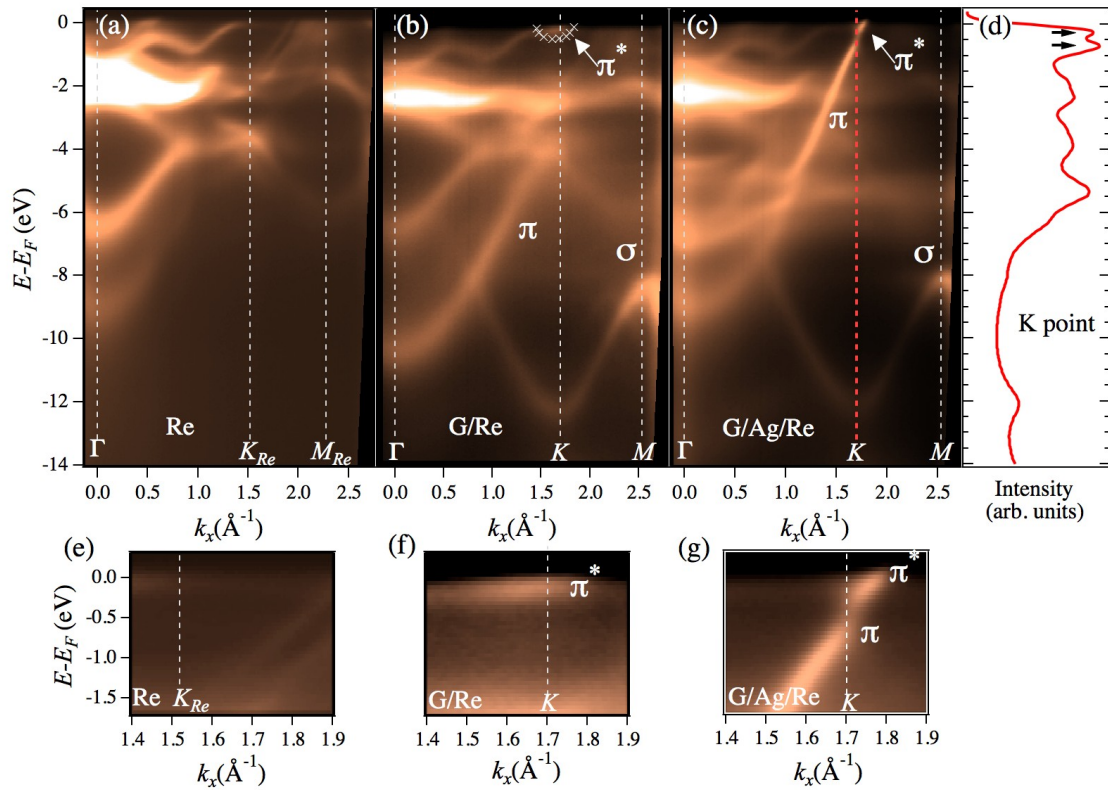


Figure 8.1: ARPES band structure of (a) Re(0001), (b) graphene on rhenium, and (c) after intercalation of a full single Ag layer (Gr/Ag/Re). (d) Energy distribution curve measured at the K -point of Gr/Ag/Re surface (red dashed curve in panel c evidences a band gap highlighted by arrows). Panels (e), (f), and (g) display magnified views of the low energy region near to the K -point of panels a, b and c, respectively. Taken from Papagno et al. [190]

slightly different ratio of the theoretical lattice constants compared to the experimental ones. The average Gr-Ag distance is at 3.47 Å with a small corrugation of 0.21 Å in the graphene layer and the average adsorption energy is 60 meV per carbon atom, which are all typical values for weakly coupled Gr-metal systems. The π^* -band is clearly visible for Gr/Ag/Re (Fig. 8.1c,g) because the experimental data show that the Dirac point is shifted 0.4 eV below Fermi level due to the electron charge transfer from Ag to graphene. The calculated energy shift is slightly lower with a value of 0.1 eV. A similar shift has been predicted by DFT for the adsorption of graphene on a bare Ag surface [31]. The energy distribution curve measured at the K-point for Gr/Ag/Re reveals an energy gap of 0.45 eV, marked by the arrows in Fig. 8.1d. The DFT calculations in the large cell do not show a band gap, although small gaps have been predicted for graphene adsorbed on Au/Ru(0001) [40].

The intercalation of noble metal atoms is also reflected in the core states of both graphene and rhenium. For graphene on bare rhenium a splitting of the C1s core level into two main contributions centered at binding energies 285.05 and 284.45 eV (black curve in Fig. 8.2a) has been reported already by Miniussi et al. [35] as a consequence of the strong buckling of the graphene film (about 1.6 Å according to DFT calculations [35]). A similar splitting was found for the strongly corrugated Gr/Ni/Ir(111) for the same reasons (see section 7.1.2 and Fig. 7.2e,f). The strongly interacting regions of the moiré cell at low Gr-Re distances contribute to a peak at higher binding energy and the weakly interacting region at larger separations define the peak at lower binding energy. The two main C1s peaks are separated by 0.6 eV as compared to 0.53 eV for Gr/Rh(111) and 0.6 eV for Gr/Ru(0001) [34]. Therefore, the energy splitting of the C1s peaks reveals that the corrugation of graphene on Re(0001) is comparable to that of Gr/Rh(111) and Gr/Ru(0001).

After the intercalation of silver (red curve in Fig. 8.2a) the width of the whole C1s structure is decreased by about 140 meV and only one peak with a slight asymmetry is observed. Furthermore, the center of the peak is shifted by \sim 400 meV toward lower binding energies. The calculated C1s binding energies for Gr/Ag/Re(0001) are shown in Fig. 8.3. The spectral distribution (blue rectangle) reveals a very small spread of binding energies ($<$ 0.1 eV) which leads to an almost perfectly symmetric C1s spectrum.

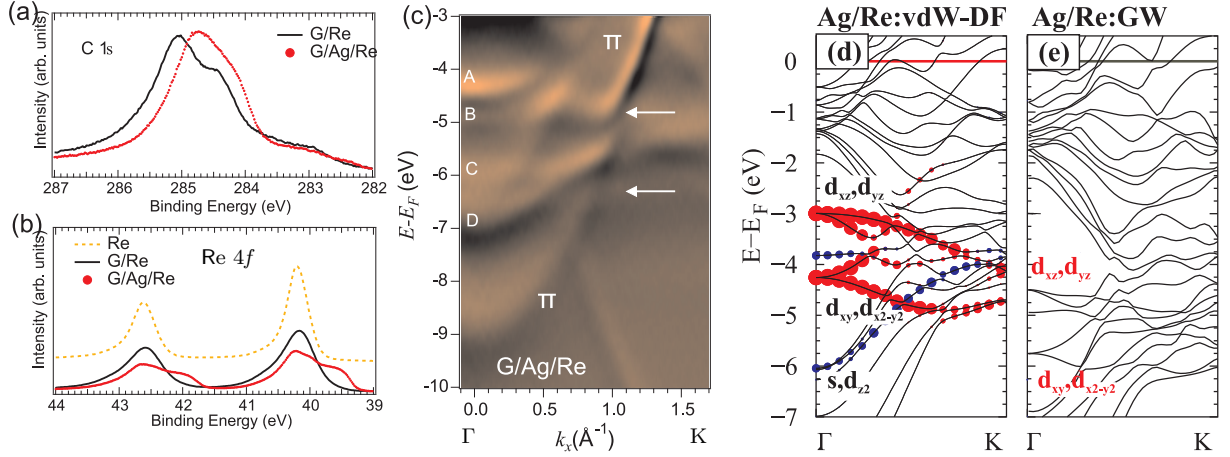


Figure 8.2: (a) C1s photoemission peak measured at normal emission with photon energy of 410 eV for Gr/Re (black curve) and Gr/Ag/Re (red curve). (b) Re 4f states for clean Re (yellow curve), Gr/Re (black curve), and Gr/Ag/Re (red curve) collected with a photon energy of 650 eV at normal emission. (c) First derivative ARPES map of Gr/Ag/Re along the ΓK direction in the energy range 3-10 eV below E_F . A, B, C and D denote new features in the electronic band structure due to Ag intercalation. The arrows highlight the induced electronic gap in the graphene π -band. (d) Calculated (optB88-vdW) band structure of a monolayer Ag/Re along the ΓK direction (dot size indicates the localization in the Ag layer), and (e) G_0W_0 band structure along the ΓK direction for Ag/Re. Taken from Papagno et al. [190]

Nevertheless, a major peak shifted to smaller binding energies is observed which can be assigned to the larger amounts of strongly interacting regions in the moiré cell, compared to a broad distribution at lower energies, which are due to a weaker interaction in the hcp-fcc region of the moiré cell. However, the resulting asymmetry in the simulated spectrum cannot explain the size of the experimentally observed asymmetry with a shoulder toward lower binding energies (Fig. 8.2a). An incompletely intercalated silver film with patches of Gr/Re(0001) in between could explain the asymmetric shape of the C1s curve. However, both experimental and theoretical C1s spectra indicate a reduced corrugation of the graphene film and a weaker Gr-substrate interaction induced by the intercalated silver layer and therefore confirm the DFT and ARPES result.

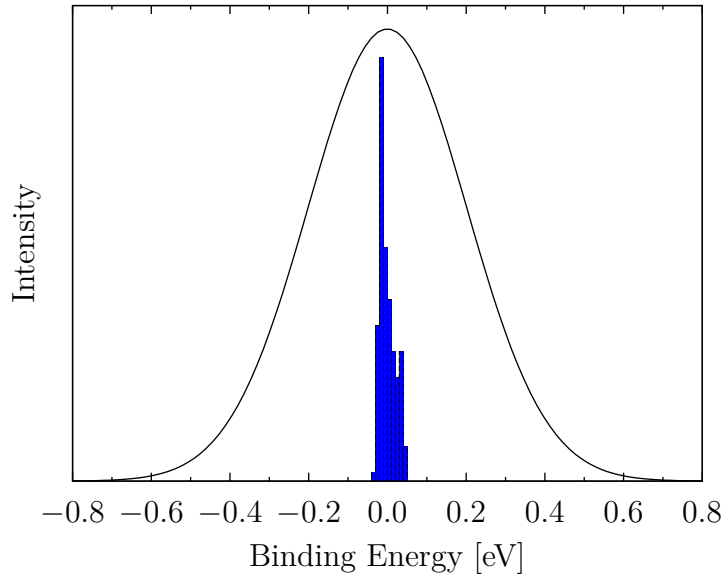


Figure 8.3: Calculated C1s core level spectrum and spectral distribution (blue rectangles) for Gr/Ag/Re(0001).

The photoemission spectrum for the clean surface of the Re $4f$ states (yellow curve in Fig. 8.2b) shows a splitting into the doublet $4f_{7/2}$ and $4f_{5/2}$ at 40.22 eV and 42.64 eV binding energy respectively, in agreement with earlier studies [199]. The surface core level shift is due to the half filled $5d$ band of rhenium [199]. The graphene covered surface leads to an increase of the peak widths (black curve in Fig. 8.2b) due to the C-Re interaction. The intercalation of silver promotes Ag-Re chemical bonds, resulting in a shift of the interface Re $4f$ peaks by 0.6 eV with respect to the bulk components (red

curve in Fig. 8.2b) indicating a charge transfer from silver to rhenium.

Nevertheless, the most intriguing features induced by silver intercalation are the changes in the graphene bands due to the interaction with the silver d states. Figure 8.2c shows the first derivative ARPES map in a close-up of Fig. 8.1c. At the Γ -point, four features (labeled A, B, C, and D) are observed. In addition, a band gap in the graphene π -states (highlighted by the two arrows) is seen, similar to Gr/Au/Ni [39] and Gr/Ir(111) [200, 201].

The character of the features A-D in Fig. 8.2c is determined by DFT calculations, performed for a single pseudomorphic silver layer on the Re(0001) surface, i.e. the experimentally observed structure [202]. Around the Γ -point in Fig. 8.2d there are several dispersing silver d bands of different symmetry located within the band gap of rhenium. At the Γ -point, the calculations predict two degenerate d_{xz} and d_{yz} states (E1) at -3.0 eV, a s, d_{z^2} hybrid state at -3.8 eV, two degenerate d_{xy} and $d_{x^2-y^2}$ states (E2) at -4.3 eV and another s, d_{z^2} hybrid state at -6 eV below E_F . The two-fold degeneracy is lifted as one proceeds toward the K -point and the $d_{x^2-y^2}$ mixes into the s, d_{z^2} hybrid, opening a gap of ≈ 1 eV about midway between ΓK . Quite evidently, the DFT Ag d -like single-particle DFT eigenvalues are located at significantly higher values compared to the experimental states. Including many body self-energy effects on the level of G_0W_0 calculations lead to a shift of the bands to lower energies (Fig. 8.2e). However, the shift for the silver E1 and E2 bands (-1.4 eV) is significantly more pronounced than for the Ag s, d_{z^2} hybrid states (-1.1 eV), a fact already predicted for bulk silver [203]. Thus, the experimentally observed features are assigned as follows: A and C correspond to the Ag E1 (d_{xz} , d_{yz}) and Ag E2 (d_{xy} , $d_{x^2-y^2}$) states, while the experimental bands B and D correspond to the two Ag s, d_{z^2} bands.

The interaction of the graphene states with the substrate is analyzed with the aid of three DFT models: first, graphene on an unsupported single silver layer, secondly, graphene on epitaxial (1×1) Ag/Re, and thirdly, (9×9) graphene on (8×8) Ag/Re. The band structure for the first model, a pseudomorphic graphene film adsorbed at 3.4 \AA on an unsupported single Ag layer at the Re lattice constant is illustrated in Fig. 8.4a. The π -band of graphene shows a nearly linear dispersion close to the Fermi level but is shifted toward lower energies. Furthermore, the graphene π -band evidently hybridizes with Ag

d_{xz} states at -4 eV (highlighted by the black circle) and with the $d_{x^2-y^2}$ and d_{z^2} states at about -3 eV (pink circle), leading to the formation of two band gaps. This hybridization is modified when a Re substrate is present. In the band structure of Gr/Ag/Re (Fig. 8.4b) the silver d_{xz} and d_{z^2} states already hybridize with the rhenium states which results in only a single band gap (cyan circle) in the energy region 3-5 eV below E_F , in accordance with the experimental observations (Fig. 8.4d). The graphene band width and the size of the band gap are underestimated in the (1×1) model structure due to the expanded graphene lattice which is clearly seen compared to the more realistic (9×9) model (Fig. 8.4c). The Dirac point is shifted to lower energies (0.07 eV and 0.18 eV for (9×9) and (1×1) model, respectively), therefore both simulations predict a marginal n -doping. Consequently, the smaller band width in the (1×1) leads to a 2 eV higher binding energy of the π -band at the Γ -point. Nevertheless, the hybridization of the graphene π -band with the proper Ag d states and the resulting band gap is already captured on the level of the (1×1) model.

8.2 Computational Methods

DFT calculations were performed with PAW-VASP with an energy cutoff of 400 eV. The optB88-vdW functional [99] was applied to approximate the exchange-correlation potential, as it was shown to capture the non-local contributions to the adsorption of graphene on a metal surface [43]. The DFT lattice constants of $a = 2.777 \text{ \AA}$ and $c = 4.482 \text{ \AA}$ were used for the rhenium substrate. Due to the slightly different ratio of the theoretical lattice constants compared to the experimental ones, the calculations were carried out for a (9×9) -graphene layer supported by three (8×8) -Re layers and an epitaxial silver layer, resulting in a strain of only 0.2 % in the graphene layer ($a = 2.463 \text{ \AA}$). Additional band structure calculations were performed using a smaller model, consisting of a (1×1) unit cell using a six layer slab with the uppermost three layers relaxed. To integrate the Brillouin zone a Γ -centered $(15 \times 15 \times 1)$ k -point mesh was used for the primitive cell and a $(3 \times 3 \times 1)$ mesh for the larger cell. In addition, the role of many-body effects on the band structure of the intercalated noble metal has been explored in the framework of the G_0W_0 approximation. The details of the experimental methods can be found in [190].

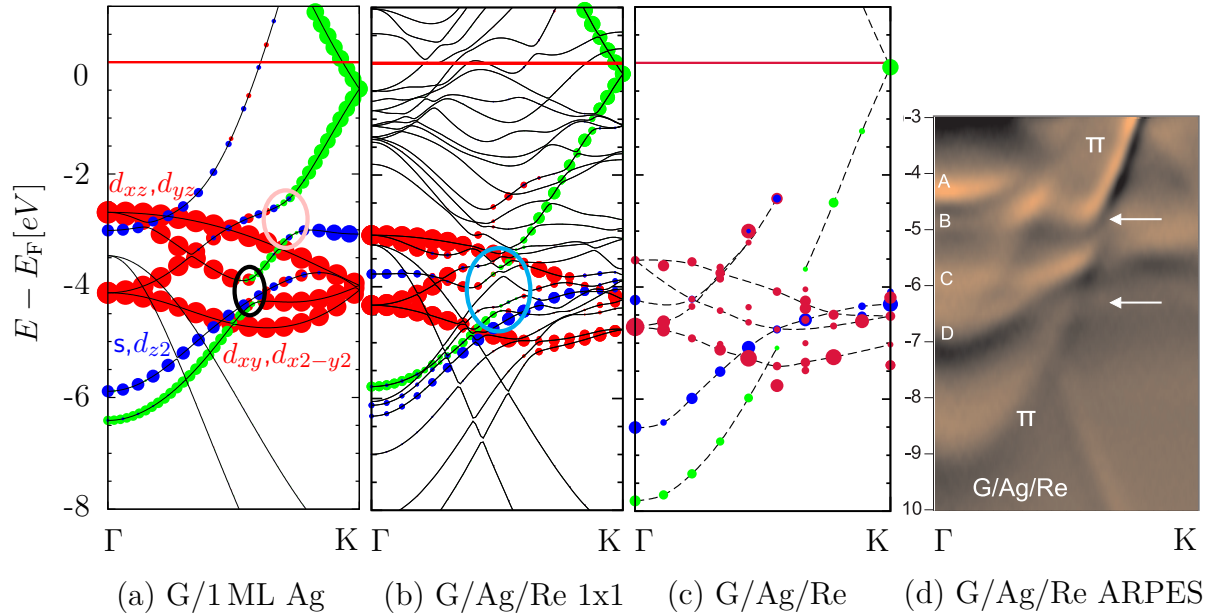


Figure 8.4: DFT band structure (optB88-vdW functional) along the ΓK direction for (a) graphene on a single ML Ag, (b) graphene/Ag/Re using a (1×1) model system and (c) the unfolded band structure of the large (9×9) Gr on (8×8) Ag/Re model (bulk Re bands not shown). Bands localized in the Ag layer with symmetries d_{xz} , d_{yz} , d_{xy} , and $d_{x^2-y^2}$ are shown in red and with s and d_{z^2} like character in blue. The localization in the respective layer is indicated by the dot-size. The π -band of graphene is displayed in green. Circles identify distinct electronic band gaps of graphene bands. Taken from Papagno et al. [190]

8.3 Conclusion

In conclusion, the changes in the electronic structure induced by the intercalation of a monolayer silver in Gr/Re(0001) was studied by means of DFT calculations. While Gr/Re is a strongly interacting system with a large graphene corrugation, the intercalation of silver leads to a weaker graphene-substrate interaction with an average Gr-Ag/Re distance of 3.47 Å and only a minor buckling of 0.21 Å. However, the effects of the silver layer on the electronic band structure is twofold. On the one hand, the linear character of the π -band in proximity of E_F is restored, but on the other hand, a significant hybridization with the Ag d -bands is observed at lower energies resulting in the formation of a band gap in the graphene π -band. The results clearly indicate that the “weakly” interacting graphene sheet on the intercalated noble metal layer is still electronically not completely decoupled. Therefore the electronic structure of graphene adsorbed on a noble metal can still deviate significantly from the structure of free-standing graphene.

Chapter 9

Summary and Conclusion

Ab initio calculations on the basis of density functional theory (DFT) and post-DFT approaches (GW, RPA) were performed to study the properties of various graphene (Gr)-metal interfaces. Late transition metals are of special interest as supporting material because the epitaxial growth of graphene on transition metals allows the fabrication of high-quality graphene sheets of large sizes. However, the unique electronic properties of free-standing graphene can be extensively altered when graphene is interacting with a metal substrate. Depending on the particular choice of the supporting material, the interaction can either lead to large changes compared to the electronic structure of free-standing graphene, e.g. for Gr/Ni(111) discussed in chapter 3 or to only minor alterations, e.g. for Gr/Ir(111) discussed in chapter 6 and 7.

The theoretical treatment of graphene on metal surfaces is a difficult task as both, an accurate description of the metallic surface and nonlocal correlation effects in the Gr-metal interface must be taken into account. DFT is a commonly used tool to handle such systems, despite the fact that the prevalently used (semi-)local LDA and GGA functionals do not account for nonlocal van der Waals (vdW) interactions. As shown for Gr/Ni(111) in chapter 3, LDA and GGA functionals fail to describe the non-local character of the Gr-Ni interactions, but approaches which take care of vdW interactions reveal their true nature. The inclusion of vdW interactions is even more important, when graphene is weakly coupled to the substrate, e.g. for Gr/Ir(111). Therefore a functional taking proper care of vdW interactions turns out to be crucial for both, weakly and strongly interacting systems.

Graphene on Ni(111) is usually considered as a system with strong Gr-metal interactions indicated by a small Gr-substrate separation and a strong hybridization of the graphene π -bands with nickel d -states. Due to a small lattice mismatch graphene usually grows in (1×1) structures, which makes Gr/Ni(111) a perfect model system for theoretical studies because of the resulting small lateral cell size in a supercell approach. However, DFT calculations using LDA and PBE fail to give a proper description of the Gr-nickel interaction. While PBE leads to no binding at all, a minimum at 2.0 Å is found by LDA. As shown in section 2.9.2 the vdW interaction is naturally included when applying ACFDT in the RPA. These calculations predict two energetical minima, one at a typical physisorption distance of 3.3 Å, and a second chemisorption minimum at 2.17 Å. The graphene π -bands strongly hybridize with the metal d -states in the chemisorption regime although the adsorption energy remains in the typical range of weak physisorption. The results of the accurate RPA data allows to assess the quality of computationally significantly cheaper vdW-DF functionals. Especially the optB88-vdW functional is in good agreement with RPA calculations making this vdW-DF functional a promising candidate for the treatment of larger systems where the graphene-metal interaction has to be described accurately. The influence of a substrate on the stability of defects in graphene was studied for single vacancies and Stone-Wales (SW) defects. The calculations revealed that these common defects have a high formation energy, but are still stabilized by large kinetic barriers. A supporting nickel layer breaks the symmetry, i.e. the carbon atoms around the defect are no longer equivalent as in free-standing graphene which results in a drastically reduced formation energy for a single vacancy at the Ni top site. In this configuration the carbon atoms next to the vacancy form strong carbon-nickel bonds, which stabilizes the defect. A SW defect is the 90° rotation of C-C bond leading to two pentagons and two heptagons instead of hexagons. A sine-like configuration was confirmed as the most stable structure because the surface stress is lowered as compared to a planar configuration. The calculations show that the energy barrier for healing a SW-defects in pristine graphene is of the same order of magnitude as its formation energy (4.2 eV), while in the presence of a nickel substrate, the formation energies for a SW-defect is reduced by 1.0 eV. However, the most striking result is a reduction of the energy barrier to remove the defect down to 2.8 eV. While for unsupported graphene both five-fold rings are opened at the transition

state, for supported graphene all but one atom binds to the surface. The strong C-Ni interaction at the transition state is also indicated by a 0.37 Å corrugation of the surface nickel layer. Due to the small lattice mismatch, graphene usually grows epitaxially on Ni(111). However, experimentally Gr/Ni(111) is also observed in moiré structures, indicating a rotated graphene phase. DFT calculations, show that the nickel surface is prone to the formation of a Ni₂C surface carbide, weakening the graphene-substrate interaction, thus enabling different graphene rotations. The Gr/Ni₂C/Ni(111) phase is stable in carbon rich conditions while a transformation to Gr/Ni(111) is predicted as the dilute carbon reservoir (i.e. the Ni bulk) is depleted, leaving rotated graphene grains on Ni(111). The structure of graphene on Ir(111) is determined by a large lattice mismatch and a weak vdW interaction, which results in a moiré graphene pattern with a large average Gr-substrate separation of 3.42 Å. In spite of the weak interactions, the local configuration within the moiré cell leads to a modulation of the interaction strength and a small corrugation of the graphene layer (0.35 Å). However, the maxima and minima in the moiré cell cannot be unambiguously assigned via AFM or STM experiments, because the measured contrast depends on the bias voltage in STM and on the tip-surface distance in AFM. The correct assignment and the reason of the contrast inversion was clarified by DFT calculations. The measured frequency shifts in AFM were simulated by explicitly evaluating the interaction energy and forces between a model tip and the Gr-iridium surface and produced the correct dependency on the particular regions of the moiré as well as inversion for different distances between tip and surface.

In order to identify the role of the mismatch compared to chemical interactions, an artificially modified system obtained by the intercalation of a strongly interacting nickel monolayer at the weakly interacting Gr/Ir(111) interface was studied. In contrast to the small corrugation of Gr/Ir(111), the stronger C-Ni interactions lead to a large corrugation of about 1.5 Å in Gr/Ni/Ir(111). The minimal distances, and hence the strongest interactions, are predicted for local configurations which are also most stable configurations for Gr/Ni(111). The enhanced interaction for Gr/Ni/Ir(111) is further confirmed by a strong hybridization of the graphene π -bands and nickel d -states, a C1s core level shift and the good agreement of simulated and experimental STM images. Thus, the electronic interaction in Gr/Ni/Ir(111) determines the strongly interacting regions, while the lattice

mismatch is responsible for the ratio between strongly and weakly interaction regions.

The formation of an intercalation layer includes the diffusion of nickel atoms through graphene and a diffusion of nickel atoms between graphene and Ir(111) with a final agglomeration at step edges. On the one hand, the diffusion of nickel atoms through an unperturbed, ideal graphene lattice was shown to have a prohibitively high energetic barrier, which can only be reduced at defect and vacancy sites. On the other hand, the calculations show that after the intercalation process, the nickel atoms are rather mobile underneath the graphene sheet, facilitating the growth of a well-ordered nickel ad-layer.

In contrast to Gr/Ni/Ir(111), the intercalation of a weakly interacting silver in a strongly interacting Gr/Re(0001) system, leads to a reduced interaction strength expressed by a smaller buckling and a recovered linear π -band dispersion at the Dirac point. However, a detailed analysis of the electronic structure revealed that the graphene π -band hybridizes with Ag d -states resulting in the formation of a band gap at about 6.5 eV below the Fermi level. Therefore, the electronic structure of graphene adsorbed on a noble metal can still deviate significantly from the one of free-standing graphene.

A final word: The manifold and complex interactions at Gr-metal interfaces are accurately described by the theoretical methods employed in the present thesis leading to a good agreement with experimental findings for a variety of Gr-metal systems.

List of Abbreviations

ACFDT	adiabatic-connection fluctuation-dissipation theory
AFM	atomic force microscopy
ARPES	angle-resolved photoelectron spectroscopy
BE	binding energy
CC	constant current
CFS	constant frequency shift
CL	core level
CVD	chemical vapor deposition
DFT	density functional theory
DOS	density of states
fcc	face-centered cubic
FFT	fast Fourier transform
GGA	generalized gradient approximation
Gr	graphene
hcp	hexagonal close-packed
JT	Jahn-Teller
LDA	local density approximation

LEED	low-energy electron diffraction
MAD	mean absolute deviation
ML	monolayer
PAW	projector augmented-wave
PBE	Perdew-Burke-Ernzerhof
RPA	random phase approximation
STM	scanning tunneling microscopy
SV	single vacancy
SW	Stone-Wales
TB	tight-binding
TEM	transmission electron microscopy
TS	transition state
VASP	Vienna ab initio simulation package
vdW	van der Waals

Bibliography

- [1] K. S. Novoselov, A. K. Geim, S. V. Morozov, D. Jiang, Y. Zhang, S. V. Dubonos, I. V. Grigorieva, and A. A. Firsov. *Science*, 306, 666 (2004).
- [2] I. Janowska, F. Vigneron, D. Bégin, O. Ersen, P. Bernhardt, T. Romero, M. Ledoux, and C. Pham-Huu. *Carbon*, 50, 3106 (2012).
- [3] K. S. Novoselov, A. K. Geim, S. V. Morozov, D. Jiang, M. I. Katsnelson, I. V. Grigorieva, S. V. Dubonos, and A. A. Firsov. *Nature*, 438, 197 (2005).
- [4] A. K. Geim and K. S. Novoselov. *Nature Mater.*, 6, 183 (2007).
- [5] A. H. Castro Neto, F. Guinea, N. M. R. Peres, K. S. Novoselov, and A. K. Geim. *Rev. Mod. Phys.*, 81, 109 (2009).
- [6] Y. Zhang, Y.-W. Tan, H. L. Stormer, and P. Kim. *Nature*, 438, 201 (2005).
- [7] J. Wintterlin and M.-L. Bocquet. *Surf. Sci.*, 603, 1841 (2009).
- [8] W. Kohn. *Rev. Mod. Phys.*, 71, 1253 (1999).
- [9] W. Kohn and L. J. Sham. *Phys. Rev.*, 140, A1133 (1965).
- [10] I. Pletikosić, M. Kralj, P. Pervan, R. Brako, J. Coraux, A. T. N'Diaye, C. Busse, and T. Michely. *Phys. Rev. Lett.*, 102, 056808 (2009).
- [11] C. Busse, P. Lazić, R. Djemour, J. Coraux, T. Gerber, N. Atodiresei, V. Caciuc, R. Brako, A. T. N'Diaye, S. Blügel, J. Zegenhagen, and T. Michely. *Phys. Rev. Lett.*, 107, 036101 (2011).
- [12] N. D. Mermin and H. Wagner. *Phys. Rev. Lett.*, 17, 1133 (1966).

- [13] J. C. Meyer, A. K. Geim, M. I. Katsnelson, K. S. Novoselov, T. J. Booth, and S. Roth. *Nature*, 446, 60 (2007).
- [14] O. A. Shenderova, V. V. Zhirnov, and D. W. Brenner. *Crit. Rev. Solid State Mater. Sci*, 27, 227 (2002).
- [15] S. F. Braga, V. R. Coluci, S. B. Legoas, R. Giro, D. S. Galvão, and R. H. Baughman. *Nano Letters*, 4, 881 (2004).
- [16] J. Sakamoto, J. van Heijst, O. Lukin, and A. D. Schlüter. *Angewandte Chemie International Edition*, 48, 1030 (2009).
- [17] J. M. Carlsson. *Nature Mater.*, 6, 801 (2007).
- [18] A. Fasolino, J. H. Los, and M. I. Katsnelson. *Nature Mater.*, 6, 858 (2007).
- [19] R. Heyrovska. arXiv:0804.4086 [physics.gen-ph] (2008).
- [20] P. R. Wallace. *Physical Review*, 71, 622 (1947).
- [21] S. Reich, J. Maultzsch, C. Thomsen, and P. Ordejón. *Phys. Rev. B*, 66, 035412 (2002).
- [22] G. W. Semenoff. *Phys. Rev. Lett.*, 53, 2449 (1984).
- [23] N. W. Ashcroft and N. D. Mermin. *Solid state physics*. Holt, Rinehart and Winston, New York (1976).
- [24] J. P. Hobson and W. A. Nierenberg. *Physical Review*, 89, 662 (1953).
- [25] R. Saito, M. Fujita, G. Dresselhaus, and M. S. Dresselhaus. *Appl. Phys. Lett.*, 60, 2204 (1992).
- [26] R. Saito, M. Fujita, G. Dresselhaus, and M. S. Dresselhaus. *Phys. Rev. B*, 46, 1804 (1992).
- [27] K. S. Novoselov, D. Jiang, F. Schedin, T. J. Booth, V. V. Khotkevich, S. V. Morozov, and A. K. Geim. *Proceedings of the National Academy of Sciences of the United States of America*, 102, 10451 (2005).

- [28] J. Shelton, H. Patil, and J. Blakely. *Surf. Sci.*, 43, 493 (1974).
- [29] K. S. Kim, Y. Zhao, H. Jang, S. Y. Lee, J. M. Kim, K. S. Kim, J.-H. Ahn, P. Kim, J.-Y. Choi, and B. H. Hong. *Nature*, 457, 706 (2009).
- [30] G. Giovannetti, P. A. Khomyakov, G. Brocks, P. J. Kelly, and J. van den Brink. *Phys. Rev. B*, 76, 073103 (2007).
- [31] G. Giovannetti, P. A. Khomyakov, G. Brocks, V. M. Karpan, J. van den Brink, and P. J. Kelly. *Phys. Rev. Lett.*, 101, 026803 (2008).
- [32] M. Batzill. *Surf. Sci. Rep.*, 67, 83 (2012).
- [33] A. T. N'Diaye, S. Bleikamp, P. J. Feibelman, and T. Michely. *Phys. Rev. Lett.*, 97, 215501 (2006).
- [34] A. B. Preobrajenski, M. L. Ng, A. S. Vinogradov, and N. Mårtensson. *Phys. Rev. B*, 78, 073401 (2008).
- [35] E. Miniussi, M. Pozzo, A. Baraldi, E. Vesselli, R. R. Zhan, G. Comelli, T. O. Mentès, M. A. Niño, A. Locatelli, S. Lizzit, and D. Alfè. *Phys. Rev. Lett.*, 106, 216101 (2011).
- [36] Q. J. Wang and J. G. Che. *Phys. Rev. Lett.*, 103, 066802 (2009).
- [37] T. Olsen and K. S. Thygesen. *Phys. Rev. B*, 87, 075111 (2013).
- [38] B. Hammer and J. Nørskov. In *Advances in Catalysis*, volume 45, pp. 71–129. Academic Press (2000).
- [39] A. Varykhalov, J. Sánchez-Barriga, A. M. Shikin, C. Biswas, E. Vescovo, A. Rybkin, D. Marchenko, and O. Rader. *Phys. Rev. Lett.*, 101, 157601 (2008).
- [40] C. Enderlein, Y. S. Kim, A. Bostwick, E. Rotenberg, and K. Horn. *New J. Phys.*, 12, 033014 (2010).
- [41] D. Pacilé, P. Leicht, M. Papagno, P. M. Sheverdyeva, P. Moras, C. Carbone, K. Krausert, L. Zielke, M. Fonin, Y. S. Dedkov, F. Mittendorfer, J. Doppler, A. Garhofer, and J. Redinger. *Phys. Rev. B*, 87, 035420 (2013).

- [42] P. A. Khomyakov, G. Giovannetti, P. C. Rusu, G. Brocks, J. v. d. Brink, and P. J. Kelly. arXiv:0902.1203 (2009).
- [43] F. Mittendorfer, A. Garhofer, J. Redinger, J. Klimeš, J. Harl, and G. Kresse. *Phys. Rev. B*, 84, 201401 (2011).
- [44] C. Kittel. *Introduction to solid state physics*. Wiley, Hoboken, NJ (2005).
- [45] A. Groß. *Theoretical Surface Science: A Microscopic Perspective*. Springer, 2nd ed. 2009 edition (2009).
- [46] D. R. Hartree. *Proc. Cambridge. Philos. Soc.*, 24, 89 (1928).
- [47] V. Fock. *Zeitschrift für Physik*, 61, 126 (1930).
- [48] L. H. Thomas. *Mathematical Proceedings of the Cambridge Philosophical Society*, 23, 542 (1927).
- [49] E. Fermi. *Zeitschrift für Physik*, 48, 73 (1928).
- [50] L. J. Sham and M. Schlüter. *Phys. Rev. Lett.*, 51, 1888 (1983).
- [51] F. Aryasetiawan and O. Gunnarsson. *Rep. Prog. Phys.*, 61, 237 (1998).
- [52] D. M. Ceperley and B. J. Alder. *Phys. Rev. Lett.*, 45, 566 (1980).
- [53] M. C. Payne, M. P. Teter, D. C. Allan, T. A. Arias, and J. D. Joannopoulos. *Rev. Mod. Phys.*, 64, 1045 (1992).
- [54] J. P. Perdew, K. Burke, and M. Ernzerhof. *Phys. Rev. Lett.*, 77, 3865 (1996).
- [55] J. P. Perdew, S. Kurth, A. Zupan, and P. Blaha. *Phys. Rev. Lett.*, 82, 2544 (1999).
- [56] A. D. Becke. *J. Chem. Phys.*, 98, 1372 (1993).
- [57] C. Lee, W. Yang, and R. G. Parr. *Phys. Rev. B*, 37, 785 (1988).
- [58] J. Heyd, G. E. Scuseria, and M. Ernzerhof. *J. Chem. Phys.*, 118, 8207 (2003).
- [59] T. Grabo and E. Gross. *Chem. Phys. Lett.*, 240, 141 (1995).

- [60] R. Wesendrup, J. K. Laerdahl, and P. Schwerdtfeger. *J. Chem. Phys.*, 110, 9457 (1999).
- [61] A. K. Rajagopal and J. Callaway. *Phys. Rev. B*, 7, 1912 (1973).
- [62] G. Kresse and J. Hafner. *Phys. Rev. B*, 47, 558 (1993).
- [63] G. Kresse and J. Furthmüller. *Comput. Mat. Sci.*, 6, 15 (1996).
- [64] P. Pulay. *Chem. Phys. Lett.*, 73, 393 (1980).
- [65] M. R. Hestenes and E. Stiefel. *J. Res. Natl. Bur. Stand.*, 49 (1952).
- [66] F. Bloch. *Zeitschrift für Physik*, 52, 555 (1929).
- [67] H. J. Monkhorst and J. D. Pack. *Phys. Rev. B*, 13, 5188 (1976).
- [68] J. C. Slater. *Physical Review*, 51, 846 (1937).
- [69] P. E. Blöchl. *Phys. Rev. B*, 50, 17953 (1994).
- [70] G. Kresse and D. Joubert. *Phys. Rev. B*, 59, 1758 (1999).
- [71] R. Eisenschitz and F. London. *Zeitschrift für Physik*, 60, 491 (1930).
- [72] F. London. *Zeitschrift für Physik*, 63, 245 (1930).
- [73] G.-X. Zhang, A. Tkatchenko, J. Paier, H. Appel, and M. Scheffler. *Phys. Rev. Lett.*, 107, 245501 (2011).
- [74] S. Lebègue, J. Harl, T. Gould, J. G. Ángyán, G. Kresse, and J. F. Dobson. *Phys. Rev. Lett.*, 105, 196401 (2010).
- [75] X. Wu, M. C. Vargas, S. Nayak, V. Lotrich, and G. Scoles. *J. Chem. Phys.*, 115, 8748 (2001).
- [76] C. Douketis, G. Scoles, S. Marchetti, M. Zen, and A. J. Thakkar. *J. Chem. Phys.*, 76, 3057 (1982).
- [77] Q. Wu and W. Yang. *J. Chem. Phys.*, 116, 515 (2002).

- [78] S. Grimme. *J. Comput. Chem.*, 27, 1787 (2006).
- [79] U. Zimmerli, M. Parrinello, and P. Koumoutsakos. *J. Chem. Phys.*, 120, 2693 (2004).
- [80] F. Ortmann, F. Bechstedt, and W. G. Schmidt. *Phys. Rev. B*, 73, 205101 (2006).
- [81] P. Jurečka, J. Černý, P. Hobza, and D. R. Salahub. *J. Comput. Chem.*, 28, 555 (2007).
- [82] C. Adamo and V. Barone. *J. Chem. Phys.*, 110, 6158 (1999).
- [83] A. Tkatchenko and M. Scheffler. *Phys. Rev. Lett.*, 102, 073005 (2009).
- [84] S. Grimme, J. Antony, S. Ehrlich, and H. Krieg. *J. Chem. Phys.*, 132, 154104 (2010).
- [85] H. B. G. Casimir and D. Polder. *Physical Review*, 73, 360 (1948).
- [86] T. Brinck, J. S. Murray, and P. Politzer. *J. Chem. Phys.*, 98, 4305 (1993).
- [87] J. Klimeš. *Towards an accurate theoretical description of surface processes*. Ph.D. thesis, University College London (2011).
- [88] J. Harl. *The linear response function in density functional theory: Optical spectra and improved description of the electron correlation*. Ph.D. thesis, University of Vienna (2008).
- [89] J. Harl and G. Kresse. *Phys. Rev. Lett.*, 103, 056401 (2009).
- [90] J. Harl, L. Schimka, and G. Kresse. *Phys. Rev. B*, 81, 115126 (2010).
- [91] M. Rohlfing and T. Bredow. *Phys. Rev. Lett.*, 101, 266106 (2008).
- [92] M. Dion, H. Rydberg, E. Schröder, D. C. Langreth, and B. I. Lundqvist. *Phys. Rev. Lett.*, 92, 246401 (2004).
- [93] Y. Zhang and W. Yang. *Phys. Rev. Lett.*, 80, 890 (1998).
- [94] J. Klimeš, D. R. Bowler, and A. Michaelides. *J. Phys.: Condens. Matter*, 22, 022201 (2010).
- [95] O. A. Vydrov and T. Van Voorhis. *Phys. Rev. Lett.*, 103, 063004 (2009).

- [96] G. Román-Pérez and J. M. Soler. *Phys. Rev. Lett.*, 103, 096102 (2009).
- [97] P. Jurečka, J. Šponer, J. Černý, and P. Hobza. *Phys. Chem. Chem. Phys.*, 8, 1985 (2006).
- [98] A. Gulans, M. J. Puska, and R. M. Nieminen. *Phys. Rev. B*, 79, 201105 (2009).
- [99] J. Klimeš, D. R. Bowler, and A. Michaelides. *Phys. Rev. B*, 83, 195131 (2011).
- [100] B. Hammer, L. B. Hansen, and J. K. Nørskov. *Phys. Rev. B*, 59, 7413 (1999).
- [101] A. D. Becke. *Physical Review A*, 38, 3098 (1988).
- [102] A. D. Becke. *J. Chem. Phys.*, 85, 7184 (1986).
- [103] Ā. D. Murray, K. Lee, and D. C. Langreth. *J. Chem. Theory Comput.*, 5, 2754 (2009).
- [104] G. Bertoni, L. Calmels, A. Altibelli, and V. Serin. *Phys. Rev. B*, 71, 075402 (2005).
- [105] G. Kalibaeva, R. Vuilleumier, S. Meloni, A. Alavi, G. Ciccotti, and R. Rosei. *J. Phys. Chem. B*, 110, 3638 (2006).
- [106] M. Fuentes-Cabrera, M. Baskes, A. Melechko, and M. Simpson. *Phys. Rev. B*, 77, 035405 (2008).
- [107] W. Zhao, S. M. Kozlov, O. Höfert, K. Gotterbarm, M. P. A. Lorenz, F. Viñes, C. Papp, A. Görling, and H.-P. Steinrück. *J. Phys. Chem. Lett.*, 2, 759 (2011).
- [108] V. M. Karpan, G. Giovannetti, P. A. Khomyakov, M. Talanana, A. A. Starikov, M. Zwierzycki, J. van den Brink, G. Brocks, and P. J. Kelly. *Phys. Rev. Lett.*, 99, 176602 (2007).
- [109] V. M. Karpan, P. A. Khomyakov, A. A. Starikov, G. Giovannetti, M. Zwierzycki, M. Talanana, G. Brocks, J. van den Brink, and P. J. Kelly. *Phys. Rev. B*, 78, 195419 (2008).
- [110] O. V. Yazyev and A. Pasquarello. *Phys. Rev. B*, 80, 035408 (2009).
- [111] I. Hamada and M. Otani. *Phys. Rev. B*, 82, 153412 (2010).

- [112] T. Olsen, J. Yan, J. J. Mortensen, and K. S. Thygesen. Phys. Rev. Lett., 107, 156401 (2011).
- [113] R. Rosei, M. De Crescenzi, F. Sette, C. Quaresima, A. Savoia, and P. Perfetti. Phys. Rev. B, 28, 1161 (1983).
- [114] C. Klink, I. Stensgaard, F. Besenbacher, and E. Lægsgaard. Surf. Sci., 342, 250 (1995).
- [115] Y. Gamo, A. Nagashima, M. Wakabayashi, M. Terai, and C. Oshima. Surf. Sci., 374, 61 (1997).
- [116] H. Kawanowa, H. Ozawa, T. Yazaki, Y. Gotoh, and R. Souda. Jpn. J. Appl. Phys., 41, 6149 (2002).
- [117] P. Sutter, J. T. Sadowski, and E. Sutter. Phys. Rev. B, 80, 245411 (2009).
- [118] J. Tersoff and D. R. Hamann. Phys. Rev. B, 31, 805 (1985).
- [119] A. Nagashima, N. Tejima, and C. Oshima. Phys. Rev. B, 50, 17487 (1994).
- [120] Y. S. Dedkov and M. Fonin. New J. Phys., 12, 125004 (2010).
- [121] S. J. Altenburg, J. Kröger, B. Wang, M.-L. Bocquet, N. Lorente, and R. Berndt. Phys. Rev. Lett., 105, 236101 (2010).
- [122] L. Schimka, J. Harl, A. Stroppa, A. Grüneis, M. Marsman, F. Mittendorfer, and G. Kresse. Nature Mater., 9, 741 (2010).
- [123] P. Jacobson, B. Stöger, A. Garhofer, G. S. Parkinson, M. Schmid, R. Caudillo, F. Mittendorfer, J. Redinger, and U. Diebold. J. Phys. Chem. Lett., 3, 136 (2012).
- [124] J. H. Crawford and L. M. Slifkin. *Point Defects in Solids: General and ionic crystals*. Plenum Press (1972).
- [125] F. Banhart, J. Kotakoski, and A. Krasheninnikov. ACS Nano, 5, 26 (2010).
- [126] A. Cortijo and M. A. H. Vozmediano. Effects of topological defects and local curvature on the electronic properties of planar graphene. arXiv cond-mat/0612374 [cond-mat.str-el] (2006).

- [127] G. M. Rutter, J. N. Crain, N. P. Guisinger, T. Li, P. N. First, and J. A. Stroscio. *Science*, 317, 219 (2007).
- [128] J. C. Meyer, C. Kisielowski, R. Erni, M. D. Rossell, M. F. Crommie, and A. Zettl. *Nano letters*, 8, 3582 (2008).
- [129] M. H. Gass, U. Bangert, A. L. Bleloch, P. Wang, R. R. Nair, and A. K. Geim. *Nat. Nanotechnol.*, 3, 676 (2008).
- [130] M. M. Ugeda, I. Brihuega, F. Guinea, and J. M. Gómez-Rodríguez. *Phys. Rev. Lett.*, 104, 096804 (2010).
- [131] R. Orlando, R. Dovesi, P. Azavant, N. M. Harrison, and V. R. Saunders. *J. Phys.: Condens. Matter*, 6, 8573 (1994).
- [132] L. Li, S. Reich, and J. Robertson. *Phys. Rev. B*, 72, 184109 (2005).
- [133] C. H. Xu, C. L. Fu, and D. F. Pedraza. *Phys. Rev. B*, 48, 13273 (1993).
- [134] H. A. Jahn and E. Teller. *Proc. R. Soc. A*, 161, 220 (1937).
- [135] C. A. Coulson, M. A. Herraiez, M. Leal, E. Santos, and S. Senent. *Proc. R. Soc. A*, 274, 461 (1963).
- [136] A. A. El-Barbary, R. H. Telling, C. P. Ewels, M. I. Heggie, and P. R. Briddon. *Phys. Rev. B*, 68, 144107 (2003).
- [137] A. Krasheninnikov, P. Lehtinen, A. Foster, and R. Nieminen. *Chem. Phys. Lett.*, 418, 132 (2006).
- [138] Y. Ma, P. O. Lehtinen, A. S. Foster, and R. M. Nieminen. *New J. Phys.*, 6, 68 (2004).
- [139] C. G. Van de Walle and J. Neugebauer. *J. Appl. Phys.*, 95, 3851 (2004).
- [140] K. Maier, M. Peo, B. Saile, H. E. Schaefer, and A. Seeger. *Philos. Mag. A*, 40, 701 (1979).
- [141] E. Kaxiras and K. C. Pandey. *Phys. Rev. Lett.*, 61, 2693 (1988).

- [142] P. A. Throver and R. M. Mayer. *Phys. Status Solidi (a)*, 47, 11 (1978).
- [143] A. Stone and D. Wales. *Chem. Phys. Lett.*, 128, 501 (2011).
- [144] S. H. Yang, W. H. Shin, J. W. Lee, S. Y. Kim, S. I. Woo, and J. K. Kang. *J. Phys. Chem. B*, 110, 13941 (2006).
- [145] J. A. Robinson, E. S. Snow, S. C. Bădescu, T. L. Reinecke, and F. K. Perkins. *Nano Letters*, 6, 1747 (2006).
- [146] J. M. Carlsson and M. Scheffler. *Phys. Rev. Lett.*, 96, 046806 (2006).
- [147] X. Peng and R. Ahuja. *Nano letters*, 8, 4464 (2008).
- [148] E. J. Duplock, M. Scheffler, and P. J. D. Lindan. *Phys. Rev. Lett.*, 92, 225502 (2004).
- [149] J. Ma, D. Alfè, A. Michaelides, and E. Wang. *Phys. Rev. B*, 80, 033407 (2009).
- [150] M. M. Ugeda, D. Fernández-Torre, I. Brihuega, P. Pou, A. J. Martínez-Galera, R. Pérez, and J. M. Gómez-Rodríguez. *Phys. Rev. Lett.*, 107, 116803 (2011).
- [151] A. Heyden, A. T. Bell, and F. J. Keil. *J. Chem. Phys.*, 123, 224101 (2005).
- [152] P. Jacobson, B. Stöger, A. Garhofer, G. S. Parkinson, M. Schmid, R. Caudillo, F. Mittendorfer, J. Redinger, and U. Diebold. *ACS Nano*, 6, 3564 (2012).
- [153] X. Li, W. Cai, J. An, S. Kim, J. Nah, D. Yang, R. Piner, A. Velamakanni, I. Jung, E. Tutuc, S. K. Banerjee, L. Colombo, and R. S. Ruoff. *Science*, 324, 1312 (2009).
- [154] Q. Yu, L. A. Jauregui, W. Wu, R. Colby, J. Tian, Z. Su, H. Cao, Z. Liu, D. Pandey, D. Wei, T. F. Chung, P. Peng, N. P. Guisinger, E. A. Stach, J. Bao, S.-S. Pei, and Y. P. Chen. *Nature Mater.*, 10, 443 (2011).
- [155] J. Lahiri, T. Miller, L. Adamska, I. I. Oleynik, and M. Batzill. *Nano letters*, 11, 518 (2011).
- [156] Y. Murata, V. Petrova, B. B. Kappes, A. Ebnonnasir, I. Petrov, Y.-H. Xie, C. V. Ciobanu, and S. Kodambaka. *ACS Nano*, 4, 6509 (2010).

- [157] P. Jacobson. *Defect Structures in Graphene Grown by Chemical Vapor Deposition on Ni(111)*. Ph.D. thesis, Graduate school of Tulane University (2012).
- [158] J. J. Mccarroll, T. Edmonds, and R. C. Pitkethly. *Nature*, 223, 1260 (1969).
- [159] D. E. Gardin, J. D. Batteas, M. A. Van Hove, and G. A. Somorjai. *Surf. Sci.*, 296, 25 (1993).
- [160] J. Grotendorst and S. Blügel. *Computational Nanoscience: Do It Yourself!* John von Neumann Institute for Computing, NIC Series, Jülich (2006).
- [161] D. Teschner, Z. Révay, J. Borsodi, M. Hävecker, A. Knop-Gericke, R. Schlögl, D. Milroy, S. D. Jackson, D. Torres, and P. Sautet. *Angewandte Chemie International Edition*, 47, 9274 (2008).
- [162] N. Seriani, F. Mittendorfer, and G. Kresse. *J. Chem. Phys.*, 132, 024711 (2010).
- [163] X. Li, W. Cai, L. Colombo, and R. S. Ruoff. *Nano Letters*, 9, 4268 (2009).
- [164] A. Grüneis, K. Kummer, and D. V. Vyalikh. *New J. Phys.*, 11, 073050 (2009).
- [165] R. S. Weatherup, B. C. Bayer, R. Blume, C. Ducati, C. Baetz, R. Schlögl, and S. Hofmann. *Nano letters*, 11, 4154 (2011).
- [166] A. Wiltner and C. Linsmeier. *Surf. Sci.*, 602, 3623 (2008).
- [167] T.-Y. Fu and T. T. Tsong. *Surf. Sci.*, 454–456, 571 (2000).
- [168] E. N. Voloshina, E. Fertitta, A. Garhofer, F. Mittendorfer, M. Fonin, A. Thissen, and Y. S. Dedkov. *Sci. Rep.*, 3 (2013).
- [169] C.-H. Park, L. Yang, Y.-W. Son, M. L. Cohen, and S. G. Louie. *Nature Phys.*, 4, 213 (2008).
- [170] M. Vanin, J. J. Mortensen, A. K. Kelkkanen, J. M. Garcia-Lastra, K. S. Thygesen, and K. W. Jacobsen. *Phys. Rev. B*, 81, 081408 (2010).
- [171] P. Lazić, N. Atodiresei, M. Alaei, V. Caciuc, S. Blügel, and R. Brako. *Comput. Phys. Commun.*, 181, 371 (2010).

- [172] A. T. N'Diaye, J. Coraux, T. N. Plasa, C. Busse, and T. Michely. *New J. Phys.*, 10, 043033 (2008).
- [173] Z. Sun, S. K. Hämäläinen, J. Sainio, J. Lahtinen, D. Vanmaekelbergh, and P. Liljeroth. *Phys. Rev. B*, 83, 081415 (2011).
- [174] M. Ondráček, P. Pou, V. Rozsival, C. González, P. Jelínek, and R. Pérez. *Phys. Rev. Lett.*, 106, 176101 (2011).
- [175] T.-L. Chan, C. Z. Wang, K. M. Ho, and J. R. Chelikowsky. *Phys. Rev. Lett.*, 102, 176101 (2009).
- [176] F. Loske, P. Rahe, and A. Kühnle. *Nanotechnology*, 20, 264010 (2009).
- [177] P. Leicht, L. Zielke, A. Garhofer, F. Mittendorfer, J. Doppler, J. Redinger, and M. Fonin. *Intercalation Mechanism of Nickel in G/Ir(111)* (submitted).
- [178] H. P. Singh. *Acta Crystallogr. Sect. A*, 24, 469 (1968).
- [179] M. Weser, Y. Rehder, K. Horn, M. Sicot, M. Fonin, A. B. Preobrajenski, E. N. Voloshina, E. Goering, and Y. S. Dedkov. *Appl. Phys. Lett.*, 96, 012504 (2010).
- [180] M. Iannuzzi and J. Hutter. *Surf. Sci.*, 605, 1360 (2011).
- [181] B. Wang, M. Caffio, C. Bromley, H. Früchtl, and R. Schaub. *ACS Nano*, 4, 5773 (2010).
- [182] M. Sicot, P. Leicht, A. Zusan, S. Bouvron, O. Zander, M. Weser, Y. S. Dedkov, K. Horn, and M. Fonin. *ACS Nano*, 6, 151 (2012).
- [183] E. N. Voloshina, Y. S. Dedkov, S. Torbrügge, A. Thissen, and M. Fonin. *Appl. Phys. Lett.*, 100, 241606 (2012).
- [184] E. Starodub, A. Bostwick, L. Moreschini, S. Nie, F. E. Gabaly, K. F. McCarty, and E. Rotenberg. *Phys. Rev. B*, 83, 125428 (2011).
- [185] S. M. Kozlov, F. Viñes, and A. Görling. *J. Phys. Chem. C*, 116, 7360 (2012).
- [186] W. Ku, T. Berlijn, and C.-C. Lee. *Phys. Rev. Lett.*, 104, 216401 (2010).

- [187] T. Brugger, S. Günther, B. Wang, J. H. Dil, M.-L. Bocquet, J. Osterwalder, J. Winterlin, and T. Greber. *Phys. Rev. B*, 79, 045407 (2009).
- [188] T. Greber, M. Corso, and J. Osterwalder. *Surf. Sci.*, 603, 1373 (2009).
- [189] D. W. Boukhvalov and M. I. Katsnelson. *Appl. Phys. Lett.*, 95, 023109 (2009).
- [190] M. Papagno, P. Moras, P. M. Sheverdyaeva, J. Doppler, A. Garhofer, F. Mittendorfer, J. Redinger, and C. Carbone. *Hybridization of Graphene and a Ag Monolayer Supported on Re(0001)* (submitted).
- [191] W. Moritz, B. Wang, M.-L. Bocquet, T. Brugger, T. Greber, J. Winterlin, and S. Günther. *Phys. Rev. Lett.*, 104, 136102 (2010).
- [192] D. Stradi, S. Barja, C. Díaz, M. Garnica, B. Borca, J. J. Hinarejos, D. Sánchez-Portal, M. Alcamí, A. Arnau, A. L. Vázquez de Parga, R. Miranda, and F. Martín. *Phys. Rev. Lett.*, 106, 186102 (2011).
- [193] A. G. Starodubov, M. A. Medvetskii, A. M. Shikin, and V. K. Adamchuk. *Physics of the Solid State*, 46, 1340 (2004).
- [194] A. Varykhalov, M. R. Scholz, T. K. Kim, and O. Rader. *Phys. Rev. B*, 82, 121101 (2010).
- [195] A. A. Popova, A. M. Shikin, A. G. Rybkin, D. E. Marchenko, O. Y. Vilkov, A. A. Makarova, A. Y. Varykhalov, and O. Rader. *Physics of the Solid State*, 53, 2539 (2011).
- [196] A. Shikin, D. Farías, V. Adamchuk, and K.-H. Rieder. *Surf. Sci.*, 424, 155 (1999).
- [197] D. Farías, A. M. Shikin, K.-H. Rieder, and Y. S. Dedkov. *J. Phys.: Condens. Matter*, 11, 8453 (1999).
- [198] A. M. Shikin, G. V. Prudnikova, V. K. Adamchuk, F. Moresco, and K.-H. Rieder. *Phys. Rev. B*, 62, 13202 (2000).
- [199] R. Wagner, D. Schlatterbeck, and K. Christmann. *Surf. Sci.*, 440, 231 (1999).

- [200] J. Sánchez-Barriga, A. Varykhalov, D. Marchenko, M. R. Scholz, and O. Rader. Phys. Rev. B, 85, 201413 (2012).
- [201] M. Kralj, I. Pletikosić, M. Petrović, P. Pervan, M. Milun, A. T. N'Diaye, C. Busse, T. Michely, J. Fujii, and I. Vobornik. Phys. Rev. B, 84, 075427 (2011).
- [202] M. Parschau, D. Schlatterbeck, and K. Christmann. Surf. Sci., 376, 133 (1997).
- [203] A. Marini, R. Del Sole, and G. Onida. Phys. Rev. B, 66, 115101 (2002).

Acknowledgments

First of all, I want to thank my supervisor Josef “Sepp” Redinger for his guidance and support during my time at the Center for Computational Material Science (CMS). Starting from computer issues till physics related questions, Sepp always took the time to help me. Moreover, I want to express my gratitude to the chairman of the CMS, Peter Mohn, who provided a homelike working atmosphere in the Makartvilla. Furthermore, I want to thank Florian Mittendorfer, my second supervisor, for his assistance and many fruitful discussions. A special thank also to Maria, who was helping me with all kinds of organizational issues during my PhD. Further on I want to point out, that it has been a real pleasure sharing an office with Robert, “Don” Pedro, “Bürosprecher” Christoph, Michi alias “Mr. Wolk”, Stefan “der Danner”, “Gregsi” Gregor, “Jacky” Jacqueline, “Abi” Abhilash, and Roland “Bliemi”, while I want to express my compassion to all colleagues who had to work at the “Todestrakt der Makartvilla” – the wing where the Austrian painter Makart died, such as “Junior Graphene” Jörg, Wernfried, Marcel, Robert and Philipp.

Many thanks also to Prof. Karsten Horn who kindly agreed to serve on my thesis committee, and to all the people from other groups I have been collaborating with, Peter, Michael and Ulrike from the TU Wien, Philipp and Mikhail from Uni Konstanz, Yuriy and Elena from FHI Berlin, and Daniela, Marco and Carlo from Elettra, Trieste.

I wish to thank the Austrian Science foundation FWF for financial support by the Science College “Computational Materials Science” and by Project I422-N16 within the EuroGraphene Collaborative Research Project *Spingraph*. Financial support by the CMS at the beginning of this thesis is also gratefully acknowledged as well as the generous computer support by the Vienna Scientific Cluster (VSC). Thanks also to the members of the SFB “ViCoM” for many fruitful discussions.

Finally, I sincerely thank my loving family who always supported me, and Doris who stayed with me even during the hard times of writing a thesis.

Curriculum Vitae

Dipl.-Ing. Andreas Garhofer

Personal data

Nationality:	Austrian
Place of Birth	Vienna, Austria
Date of Birth	July 3 rd , 1984
Parents	Eva Garhofer, Dipl.-Ing. Robert Garhofer
Home address	Nattergasse 1-3/2/41, A-1170 Wien
E-mail	andreasgarhofer@yahoo.de

Education

1990-1994	Primary School, VS St. Marien, Liniengasse 21, A-1060 Wien
1994-1998	Secondary School, HS St. Marien, Liniengasse 21, A-1060 Wien
1998-2003	Higher Technical College (HTL) of Mechanical Engineering, Wexstraße 19-23, A-1200 Wien
2004-2009	Diploma studies in Technical Physics, Vienna University of Technology Diploma thesis: "First principles studies of Cobalt adatoms on Platinum (111)" Supervisor: Ao. Univ. Prof. Dipl.-Ing. Dr. techn. Josef Redinger
2009-2013	Doctoral studies in Technical Physics, Vienna University of Technology PhD thesis: "Ab initio studies of Graphene-Metal Interfaces" Supervisor: Ao. Univ. Prof. Dipl.-Ing. Dr. techn. Josef Redinger

Publications

- *Unusual Cluster Shapes and Directional Bonding of an fcc Metal: Pt/Pt(111)*
M. Schmid, A. Garhofer, J. Redinger, F. Wimmer, P. Scheiber, and P. Varga, Phys. Rev. Lett. 107, 016102 (2011)
- *Graphene on Ni(111): Strong interaction and weak adsorption*
F. Mittendorfer, A. Garhofer, J. Redinger, J. Klimeš, J. Harl, and G. Kresse., Phys. Rev. B, 84, 201401 (2011)
- *Disorder and Defect Healing in Graphene on Ni(111)*
P. Jacobson, B. Stöger, A. Garhofer, G. S. Parkinson, M. Schmid, R. Caudillo, F. Mittendorfer, J. Redinger, and U. Diebold., J. Phys. Chem. Lett., 3, 136 (2012)
- *Nickel Carbide as a Source of Grain Rotation in Epitaxial Graphene*
P. Jacobson, B. Stöger, A. Garhofer, G. S. Parkinson, M. Schmid, R. Caudillo, F. Mittendorfer, J. Redinger, and U. Diebold., ACS Nano, 6, 3564 (2012)
- *Electronic structure and imaging contrast of graphene moiré on metals*
E. N. Voloshina, E. Fertitta, A. Garhofer, F. Mittendorfer, M. Fonin, A. Thissen, and Y. S. Dedkov, Sci. Rep., 3 (2013)
- *Artificially lattice-mismatched graphene/metal interface: Graphene/Ni/Ir(111)*
D. Pacilé, P. Leicht, M. Papagno, P. M. Sheverdyaeva, P. Moras, C. Carbone, K. Krausert, L. Zielke, M. Fonin, Y. S. Dedkov, F. Mittendorfer, J. Doppler, A. Garhofer, and J. Redinger, Phys. Rev. B, 87, 035420 (2013)
- *Intercalation Mechanism of Nickel in G/Ir(111)*
P. Leicht, L. Zielke, A. Garhofer, F. Mittendorfer, J. Doppler, J. Redinger and M. Fonin, submitted 2013
- *Hybridization of Graphene and a Ag Monolayer Supported on Re(0001)*
M. Papagno, P. Moras, P. M. Sheverdyaeva, J. Doppler, A. Garhofer, F. Mittendorfer, J. Redinger, and C. Carbone, submitted 2013

Conference contributions

- *Adatoms with character: Co and Pt atoms on Pt (111)*
A. Garhofer, Z. Bortlova, M. Schmid, P. Varga, and J. Redinger, DPG spring conference, Regensburg, Germany, 2010
- *Co and Pt adatoms on Pt (111): Initial stages of growth*
A. Garhofer, R. Hammerling, Z. Bortlova, M. Schmid, P. Varga, and J. Redinger, Psi-k conference, Berlin, Germany, 2010
- *Small metal clusters on Pt(111): Theoretical insights*
A. Garhofer, 10th NFN workshop on Nanoscience and Surfaces, Stadtschlaining, Austria, 2010
- *DFT studies of small metal ad-atom clusters on fcc(111) surfaces*
A. Garhofer, C. Lenauer, F. Wimmer, P. Scheiber, M. Schmid, P. Varga, and J. Redinger, DPG spring conference, Dresden, Germany, 2011
- *DFT studies of Stone-Wales(SW) defects in graphene on Ni(111)*
A. Garhofer, P. Jacobson, B. Stöger, G. S. Parkinson, M. Schmid, R. Caudillo, F. Mittendorfer, J. Redinger, and U. Diebold, ECOSS-28, Wrocław, Poland, 2011
- *DFT studies of defects in graphene on Ni(111)*
A. Garhofer, P. Jacobson, B. Stöger, G. S. Parkinson, M. Schmid, R. Caudillo, F. Mittendorfer, J. Redinger, and U. Diebold, SpinGraph Project Meeting, Konstanz, Germany, 2011
- *DFT studies of Graphene on Ni(111) and Surface Nickel Carbide Ni₂C*
A. Garhofer, P. Jacobson, B. Stöger, G. S. Parkinson, M. Schmid, R. Caudillo, F. Mittendorfer, J. Redinger, and U. Diebold, APS March Meeting, Boston, US, 2012
- *DFT studies of Graphene on Ni(111) and Surface Nickel Carbide Ni₂C*
A. Garhofer, P. Jacobson, B. Stöger, G. S. Parkinson, M. Schmid, R. Caudillo, F. Mittendorfer, J. Redinger, and U. Diebold, DPG spring conference, Berlin, Germany, 2012

- *Surface carbide induced changes on graphene/Ni(111)*
A. Garhofer, P. Jacobson, B. Stöger, G. S. Parkinson, M. Schmid, R. Caudillo, F. Mittendorfer, J. Redinger, and U. Diebold, 29th European Conference on Surface Science, Edinburgh, UK, 2012
- *Ab initio studies of graphene on metal surfaces*
A. Garhofer, J. Doppler, F. Mittendorfer, and J. Redinger, SpinGraph Project Meeting, Vienna, Austria, 2012
- *Ab initio studies of Graphene-Metal Interfaces*
A. Garhofer, Seminar at the Institute of Applied Physics, Vienna University of Technology, Vienna, Austria, 2013